U.PORTO

FEUP FACULDADE DE ENGENHARIA
UNIVERSIDADE DO PORTO

ADVANCED HERMETIC ENCAPSULATION OF PEROVSKITE SOLAR CELLS

Dissertation presented for the degree of

Doctor of Philosophy

In Chemical and Biological Engineering

by

Seyedali Emami

Adélio Miguel Magalhães Mendes, Full Professor – Supervisor

Dzmitry Ivanou, Assistant Researcher – Co-Supervisor

lepabe
Laboratory for Process Engineering, Environment, Biotechnology and Energy

Department of Chemical Engineering,

Faculty of Engineering, University of Porto

2020

This thesis was financially supported by Foundation for Science and Technology (FCT) through the PhD grant SFRH/BD/119402/2016 and by projects: i) BI-DSC under the Specific Program "Ideas" of the European Research Council for research and technological development as part of an Advanced Grant Agreement No.321315 from European Commission through the Seventh Framework Program, ii) “GOTSolar” supported by the European Union's Horizon 2020 Programme, through a FET Open research and innovation action under grant agreement No 687008, iii) “SunStorage -Harvesting and storage of solar energy”, with reference POCI-01-0145-FEDER-016387 funded by European Regional Development Fund (ERDF), through Operational Programme for Competitiveness and Internationalisation (COMPETE 2020- Programme for Competitiveness and Internationalization (OPCI), and by national funds, through FCT, iv) ‘WinPSC’ (POCI-010247-FEDER-017796), co-funded by the ERDF, and COMPETE 2020,under the PORTUGAL 2020 Partnership Agreement’, v) “Sunflow - Solar energy storage into redox flow batteries” with reference PTDC/EQUEQU/ 30510/2017 - POCI-01-0145-FEDER-030510, funded by ERDF, through COMPETE 2020 - (OPCI), and FCT, vi) POCI-01-0145-FEDER-006939, funded by ERDF, through COMPETE2020 –POCI and by FCT and vii) NORTE-01-0145-FEDER-000005 – LEPABE-2-ECO-INNOVATION, supported by Norte 2020, under the Portugal 2020, through the ERDF, vii) project UID/EQU/00511/2019 - Laboratory for Process Engineering, Environment, Biotechnology and Energy – LEPABE funded by national funds through FCT/MCTES (PIDDAC).

©Seyedali Emami, 2017-2020

Laboratory for Process Engineering, Environment, Biotechnology and Energy

University of Porto – Faculty of Engineering

Rua Dr. Roberto Frias s/n, 4200-465 Porto, Portugal

ACKNOWLEDGMENTS

First of all I would like to thank Professor Adélio Mendes and Doctor Dzmitry Ivanou for all of their support during these years. Prof. Adélio is one of the most hardworking and smartest people I ever know. His constant support as an advisor and friend helped me to feel joyful and motivated throughout my PhD work. This work wouldn't be successful without all of those long and deep discussions with Adélio. Dzmitry, on the other hand, was always there for me in the lab to follow all the experiments and results. His critical guidance throughout the experimental work was always keeping me motivated and committed for achieving the goals for this thesis.

Special thanks to Prof. Joaquim Mendes and Prof. Fernão Magalhães for their help and support in mechanical engineering and material science related difficulties of my work. Thanks to Luísa Andrade for her assistance in the beginning of my PhD work. Thanks a million to D. Fátima Faustino for all of her amazing work and patience with me.

My biggest thanks to my colleagues at UPTEC for all of their help and support during these years. To the old gang, José Nogueira, Fernando Ribeiro, Ana Pereira, Joana Ângelo, and Bruna Amorim, you people have a special place in my heart. To the new kids, Rúben Madureira and Cristina Teixeira for all the fun time we had in the lab. To whatever group we can this next bunch of amazing people, Jorge Martins, Isabel Mesquita, António Vilanova, Paula Dias, and Rita Arnaldo, Salamti guys! You lovely people were like a family to me, kisses and hugs!

My special thanks to Jorge for all of his help on the sealing experiments, grande abraço! To Isabel for teaching me how to make cells and all of her assistance in the lab, beijinhos!

Cheers to all my wonderful friends in Porto, Aria, Behdad, João Carneiro, Erica, Diana, Bahareh, Mohammad Masudian, Mohsen, Negar, Ali Fotouhi and

Franak, for their friendship and love. To my lovely cousins, Morteza, Mohammad, Sara, Mahyar, Parsa and Saied, aunt Noushin, uncle Mansour, uncle Farhad, and uncle Mehdi, for their heart-warming moments through my entire life and during these years away from them. To grandma Maman Jon for all of her love and prayers. Though grandpa Baba Jon is not with me anymore, I am sure he is watching me from heaven the whole time.

To Aria for all the times we spent here in Porto away from home, not feeling alone because of having each other. Jigareto ghalandar!

To my brother Soleiman for always being there for me no matter what. To my beautiful sister Narges for her countless love and kindness. My biggest kisses to Reza, Marjan, Romina, and Elena for making us the happiest loving family.

To mom and dad, Baba and Maman, for their unconditional endless love and support in my life. Thank you both for giving me strength and teaching me how to become a better person.

To my lovely parents

PREFACE

The present work was developed at the Laboratory for Process Engineering, Environment, Biotechnology and Energy (LEPABE) facilities, in the Chemical Engineering Department of the Faculty of Engineering - University of Porto (FEUP), between 2017 and 2020 under the FCT (Foundation for Science and Technology) grant SFRH/BD/119402/2016. The work was supervised by Professor Adélio Mendes and Doctor Dzmitry Ivanou.

The findings of this work are published in four peer-reviewed scientific articles, one review article and one international patent.

This thesis is divided into five chapters: starting with a brief introduction; followed by three chapters describing the experimental work and results; and a final chapter with the general conclusions and perspectives for future work.

Chapters 1 and 2 are adopted from there articles and the patent, while chpater 3 and 4 are the reprint of two published artilces.

CONTENTS

ABSTRACT

Global energy demand is predicted to increase rapidly up to 50 % by 2050. To date, carbon-based fossil fuels are the primary energy source counting for more than 80 % of the global energy supply. The future of the planet relies on our actions towards the energy decarbonization routes of low-carbon footprint renewable energies. Among renewable energy sources, solar energy has been attracted enormous attention since there are no geographical limits for the collection of sunlight, comparing to other renewable sources such as wind and geothermal. Photovoltaic (PV) technology is expected to be one of the primary energy sources in near future. However, the electricity produced by PV technology is still straggling to economically compete with fossil fuels generated electricity. This work studies perovskite solar cells (PSCs) which are considered as one of, if not the most, promising third generation emerging PV technologies. The golden triangle of photovoltaic includes cost, efficiency and stability. The levelized cost of electricity (LCOE) for PSC was estimated to be *ca.* 3 times less compared to silicon solar cells. Moreover, lab size PSCs reached record power conversion efficiency (PCE) of 25.2 %, which is near the PCE of c-Si lab-size cells – 26.1 %. Thus, PSCs have already achieved the requirements for cost and efficiency. Currently, the only bottleneck keeping PSCs from commercialization is the poor stability of these PV devices.

For PSCs to become reliable candidates for competing with established PV technologies, devices stable for more than 20 years are required. The stability of PSCs is affected by two factors: i) external environmental (*i.e.* humidity, oxygen and temperature) and ii) operational condition (*i.e.* illumination and electrical load). The external environmental stability of PSC can be guaranteed by applying a hermetic encapsulation. The operational stability is achieved by materials and interfacial improvements.

The operational stability of these devices is being extensively researched by many material scientists. However, much less attention has been paid to the

external environmental stability of PSCs. This work focuses on technological solutions for reaching external environmental stability through the development and application of hermetic glass encapsulation to PSCs.

A novel laser-assisted glass frit sealing process was developed and optimized to perform encapsulation at extremely low process temperatures. A multi-layer glass frit configuration was used to seal two types of PSC device structures. The HTM-free devices were sealed at 100 °C using single laser beam while n-i-p cells were sealed at 50 °C using a dual laser beam encapsulation method. The hermeticity and long-term stability of the developed encapsulation was examined by IEC and MIL-STD standard test procedures.

The external environmental stability of the encapsulated PSCs was examined by submitting the sealed cells to 500 h humid air exposure test (85 % RH) and 50 thermal cycling tests of -40 °C to 85 °C. The HTM-free devices showed no performance losses after aging tests. However, the n-i-p PSCs showed *ca.* 16 % performance drop after thermal cycle test of -40 °C to 85 °C. XRD analysis revealed no perovskite decomposition and the performance loss was assigned to the thermal degradation of the HTM layer. In contrast, these cells showed no performance variations after humidity aging and thermal cycles of -40 °C to 65 °C.

The developed disruptive engineering approach, based on the very low process temperature laser-assisted glass encapsulation, is the missing puzzle piece for the future successful commercialization of emerging perovskite solar cells.

RESUMO

Prevê-se que as necessidades energéticas mundiais vão aumentar em 50 % até ao ano 2050. Até à data, os combustíveis fosseis são a principal fonte de energia primária, representando 80 % do abastecimento de energia global. O futuro do planeta depende de ações que levem à descarbonização energética das energias renováveis. Entre as fontes de energia renováveis, a energia solar tem atraído enorme atenção, uma vez que que não existem limites geográficos para a coleção da energia do sol, como é o caso da energia eólica e geotérmica. Num futuro próximo é previsto que as tecnologias fotovoltaicas sejam uma das maiores fontes de energia. Contudo, no presente, a eletricidade produzida por tecnologias PV ainda não consegue competir economicamente com a eletricidade produzida através de combustíveis fosseis.

O presente trabalho estuda as células solares sensibilizadas com perovskita (PSCs), uma das mais atrativas tecnologias fotovoltaicas de 3ª geração. O triângulo dourado das fotovoltaicas inclui o custo, a eficiência e a estabilidade. O custo normalizado de eletricidade (LCOE) das PSCs é aproximadamente 3 vezes inferior às tradicionais células solares de silício. Além disso, as PSCs de escala laboratoriais já atingiram a eficiência recorde de 25.2 %, valor muito próximo do das células solares de silício - 26.1 %. Assim sendo, as PSCs cumprem os requisitos em termos de custo e eficiência. Contudo, a sua estabilidade ainda é um dos fatores impeditivos da sua comercialização.

As PSCs necessitam de ser estáveis por mais de 20 anos para puderem competir com as atuais tecnologias fotovoltaicas existentes no mercado. A sua estabilidade é afetada por dois fatores: i) o ambiente externo (*i.e.* humidade, oxigénio e temperatura) e ii) as condições de operação (*i.e.* iluminação e potencial elétrico). A estabilidade ao ambiente externo é garantida através de um encapsulamento hermético. A estabilidade operacional pode ser alcançada por desenvolvimentos a nível dos materiais e das interfaces.

A estabilidade operacional das PSCs tem sido extensivamente estudada. Todavia, a estabilidade a ambientes externos tem recebido muito menos atenção. O presente trabalho visa alcançar esta estabilidade através do desenvolvimento de um encapsulamento hermético de vidro.

Um novo processo de selagem de frita de vidro assistido por laser foi desenvolvido e otimizado para temperaturas de operação extremamente baixas. Uma configuração de multicamada de fritas de vidro foi usada para selar dois tipos de estruturas de PSCs. Dispositivos sem camada transportadora de lacunas (HTM) foram selados a 100 °C usando um único feixe de laser. Células com a estrutura n-i-p foram encapsulados a 50 °C utilizando um sistema de duplo feixe de laser. A hermeticidade e a estabilidade do encapsulamento foram examinadas segundo os testes padrão IEC e MIL-STD.

A estabilidade das PSCs encapsuladas a ambientes externos foi estudada através do teste de exposição a ar húmido (85 % de humidade relativa) durante 500 h e 50 ciclos térmicos entre - 40 °C e 85 °C. Os dispositivos sem HTM não apresentaram perda de desempenho após os testes de envelhecimento. No entanto, dispositivos com a estrutura n-i-p tiveram uma perda de desempenho de aproximadamente 16 % após os ciclos térmicos entre -40 °C e 85 °C. Análise por difração de raios-X revelaram que a camada de perovskita não se decompôs e a perda de desempenho foi devido à degradação térmica da camada de HTM. Estes dispositivos não exibiram perda de desempenho quando submetidos a ciclos térmicos de -40 °C a 65 °C.

A disruptiva abordagem apresentada no presente trabalho e baseada no encapsulamento com frita de vidro assistido por laser a temperaturas processuais extremamente baixas, é a peça final para a futura comercialização das emergentes células solares sensibilizadas com perovskita.

چکیده

بر اساس پیش بینی‌ها، تقاضای انرژی جهان تا سال ۲۰۵۰ با رشد سریع ۵۰ درصدی روبرو خواهد شد. تا به امروز سوخت‌های فسیلی با ٪۸۰ سهم، منبع اصلی تامین انرژی جهانی هستند. آینده کره زمین در گرو اقدامات ما در زمینه کربن‌زدایی از فرآیند تولید انرژی از راه جایگزینی سوخت‌های فسیلی با نیروهای تجدیدپذیر است. در میان منابع انرژی تجدیدپذیر، انرژی خورشیدی به علت دسترسی بدون محدودیت جغرافیایی، در مقایسه با منابع تجدیدپذیر دیگر مانند انرژی بادی و انرژی زمین‌گرمایی (ژئوترمال)، توجه ویژه‌ای را به خود جلب کرده است. انتظار می‌رود که تکنولوژی فتوولتائیک در آینده نزدیک به یکی از اصلی‌ترین منابع تأمین انرژی تبدیل شود. اما در حال حاضر ارزان بودن تولید برق از طریق منابع سوخت فسیلی، یکی از بزرگترین موانع در مقابل توجیه اقتصادی استفاده از انرژی خورشیدی است. این پژوهش به مطالعه یکی از جدیدترین و جذاب‌ترین انواع سلول‌های خورشیدی نسل سوم به نام سلول خورشیدی پروسکایت، می پردازد. مثلث طلایی فتوولتائیک متشکل از سه رأس است: قیمت، بازدهی و پایداری. قیمت برق تولیدی توسط سلول های پروسکایت تقریبا سه برابر کمتر از سلول‌های سیلیکون است. در مورد بازده هم پروسکایت با رسیدن به رکورد ٪۲۵,۲ در مقابل ٪۲۶,۱ سیلیکون، در موقعیت بسیار خوبی قرار دارد. درنتیجه، سلول های پروسکایت هم اکنون نیز شرایط مطلوب بازدهی و قیمت را دارا هستند. تنها چالش پیش رو که در حال حاضر تولید انبوه و صنعتی سلول های پروسکایت با آن روبروست، پایداری این تجهیزات فتوولتائیک است.

سلول های پروسکایت تنها زمانی می‌توانند وارد عرصه رقابت با سلول های سیلیکون بشوند، که از پایداری لازم برای مدت حداقل ۲۰ سال برخوردار باشند. پایداری سلول های پروسکایت در مقابل دو فاکتور شکننده است: ۱) عوامل محیطی خارجی شامل رطوبت، اکسیژن و حرارت ؛ ۲) عوامل عملیاتی شامل روشنایی و بار الکتریکی. پایداری در مقابل عوامل محیطی خارجی سلول های پروسکایت با کپسوله کردن هرمتیک

(Hermetic Encapsulation) آنها، قابل تضمین است. پایداری عملیاتی این سلول ها از طریق علم مواد و ارتقاء سطوح تماس بین لایه ایی قابل حصول است.

پایداری عملیاتی سلول های پروسکایت به صورت گسترده توسط تعداد زیادی از دانشمندان علم مواد مطالعه شده است. با این وجود، تا امروز توجه بسیار کمتری به پایداری عوامل محیطی خارجی معطوف گشته است. تمرکز اصلی این پژوهش بر روی راه حل‌های فناورانه (تکنولوژیک) برای دستیابی به پایداری محیطی خارجی سلول‌های پروسکایت از طریق تحقیق و توسعه کپسوله کردن هرمتیک آنهاست.

فرآیند نوینی برای کپسوله کردن سلول‌های پروسکایت در دمای بسیار پایین به کمک لیزر مورد تحقیق، توسعه و بهینه‌سازی قرار گرفته شده است. برای این کار از سیلانت‌های ساخته شده از جنس شیشه استفاده شده و پرتو لیزر برای ذوب کردن این مواد، بکار گرفته شده است. سیلانت چند لایه شامل مواد شیشه‌ای گوناگون برای کپسوله کردن دو نوع ساختار سلول‌های پروسکایت به کار گرفته شده است. ساختار سه لایه متخلخل فاقد لایه حمل کننده حفره (HTM-free) در درجه حرارت ۱۰۰ درجه سلسیوس و با استفاده از یک پرتو لیزر، کپسوله شد. ساختار متداول n-i-p در درجه حرارت ۵۰ درجه سلسیوس و با استفاده همزمان از دو پرتو لیزر کپسوله سازی گشت. ضریب نفوذ و پایداری بلندمدت سلول های کپسوله شده از طریق استانداردهای IEC و MIL-STD مورد بررسی و آزمایش قرار گرفت.

پایداری محیطی خارجی سلول‌های کپسول شده از طریق آزمایش‌های پایداری تحت جریان هوای مرطوب ٪۸۵ برای ۵۰۰ ساعت و پایداری حرارتی تحت سیکل دما از ۴۰- تا ۸۵ درجه سلسیوس برای ۵۰ چرخه، مورد آزمایش قرار گرفت. ساختار فاقد لایه حمل کننده حفره، کارایی و بازده خود را بدون تغییر حفظ نمود. در مقابل، ساختار n-i-p ٪۱۶ از بازده خود را، پس از آزمایش سیکل حرارتی از ۴۰- تا ۸۵ درجه سلسیوس، از دست داد. مطالعات بلورشناسی پرتو ایکس (XRD) نشان داد که این افت بازده ارتباطی با تخریب لایه پروسکایت نداشته و به علت تخریب حرارتی لایه حمل کننده حفره میباشد. در عوض، اینگونه سلول‌ها پس از آزمایش پایداری رطوبت و سیکل حرارتی ۴۰- تا ۶۵ درجه سلسیوس، کارایی خود را حفظ کردند.

نتایج این نوآوری تحول‌آفرین مهندسی، براساس کپسول‌سازی شیشه‌ای با استفاده از لیزر در درجه حرارت بسیار پایین، قطعه گم شده پازل برای تولید و تجاری‌سازی موفق سلول‌های خورشیدی پروسکایت در آینده است.

LIST OF ABBREVIATIONS AND SYMBOLS

Symbol	Definition	Units
A	Area	m^2
c	Speed of light	$m\ s^{-1}$
C_p	Specific heat	$J\ kg^{-1}\ K^{-1}$
D	Laser beam diameter	mm
DOF	Depth Of Focus	mm
E	Energy	J
E_g	Band gap	eV
FF	Fill Factor	
FL	Focal Length	mm
h	Plank's constant	J s
HAZ	Heat Affected Zone	mm
J	Current	A
k	Thermal conductivity	$W\ m^{-1}\ K^{-1}$
L	Line length (pattern sealing)	mm
L	Equivalent leak rate in air	$atm\ cm^3\ s^{-1}$
LCOE	Levelized Cost of Electricity	$USD\ kWh^{-1}$
M	Molecular mass	$g\ mol^{-1}$
P	Power	W
P	Number of times that laser passes a given point (pattern sealing)	
p	Pressure	bar
P	Laser output power	W
p_b	helium bombing pressure	bar

PCE	Power Conversion Efficiency	%
Q	Heat transfer rate	W m^{-2}
R_L	Helium leak rate	atm cm^3 s^{-1}
S	Step length (pattern sealing)	mm
Spot ∅	Laser beam diameter	mm
T	Temperature	°C
t	Time	s
t_2	Dwell time between release of pressure (leak test)	h
t_b	Bombing time (leak test)	h
V	Voltage	V
V	Volume	m^3
v	Laser scanning velocity	mm s^{-1}
W	Laser beam waist	mm

Abbreviation	**Definition**
5-AVA	5-Ammonium Valeric Acid
a-Si	Amorphous silicon
BCB	Benzocyclobutene
BoS	Balance of System
CB	Conduction Band
CIGS	Copper Indium Gallium di-Selenide
DC	Direct current
DSC	Dye-sensitized Solar Cell
EIA	United States Energy Information Administration

ETL	Electron Transport Layer
FA	Formamidinium
FF	Fill Factor
FTO	Fluorine doped Tin Oxide (SnO_2: F)
GaAs	Gallium Arsenide
HOMO	Highest Occupied Molecule Orbital
HTE	Humidity and Thermal Exposure
HTL	Hole Transport Layer
HTM	Hole Transport Material
IEA	International Energy Agency
IPCC	Intergovernmental Panel on Climate Change
IRENA	International Renewable Energy Agency
LA	Laser-Added
MA	Methylammonium
meso	Mesoporous
NREL	National Renewable Energy Laboratory
Pc	Phthalocyanine
PI	Polyimide
PMMA	Poly (methyl methacrylate)
PSC	Perovskite Solar Cell
PTAA	Poly[bis(4-phenyl)(2,4,6- trimethylphenyl)amine]
PU	Polyurethane
PV	Photovoltaic
PVD	Physical Vapor Deposition
RSM	Response Surface Methodology
SCARA	Selective Compliance Assembly Robot Arm

SCN	Thiocyanate
spiro-OMeTAD	2,2′,7,7′-tetrakis(N,N-dimethoxyphenylamine)-9,9′-spirobifluorene
TCO	Transparent Conductive Oxide
TG	Thermogravimetric
TGA	Thermogravimetric Analysis
VB	Valance Band
XRD	X-Ray Diffraction

Greek symbols	**Definition**	**Unit**
λ	Wavelength	nm
α	Absorbance	%
ρ	Reflectance	%
τ	Transmittance	%

CHAPTER 1

INTRODUCTION

"عشق اگه روز ازل در دل دیوانه نبود تا ابد زیر فلک ناله مستانه نبود

نرگس ساقی اگه مستی صد جام نداشت سر هر کوی و گذر این همه میخانه نبود"

Hayedeh - *Afsaneh Hasti*

Adapted from review article

***S. Emami**, L. Andrade and A. Mendes, U. Porto Journal of Engineering, 2015, 1, 52-62.*

and international patent

*A. Mendes, J. Mendes, L. Andrade, **S. Emami**, J. Martins, et al., Laser-assisted hermetic encapsulation process and product thereof, WO/2017/221218, 2017.*

1 INTRODUCTION

One of the major concerns for the future of the human race on earth is climate change. In late 2018, the Intergovernmental Panel on Climate Change (IPCC) reported a 1.5 °C temperature increase due to Global Warming [1]. The mentioned report concludes that urgent action is required for the transformation of global energy use. Bearing in mind that more than 65 % of greenhouse gas emission is generated from energy-related sectors, the IPCC called for immediate use of renewable energy sources [1].

According to the 2019 report of the International Energy Agency (IEA), in 2017 fossil fuels such as oil, coal and natural gas were counting as the primary energy supply of world by *ca.* 81.3 %; while renewable energy sources (*i.e.* geothermal, solar, wind and heat) were only sharing 1.8 % of the world energy supply - **Figure 1.1**. Among renewable energy sources, solar energy has been attracting enormous attention since there are much less geographical limits for collection of sunlight, comparing to other geographical dependent renewable sources such as wind and geothermal [2].

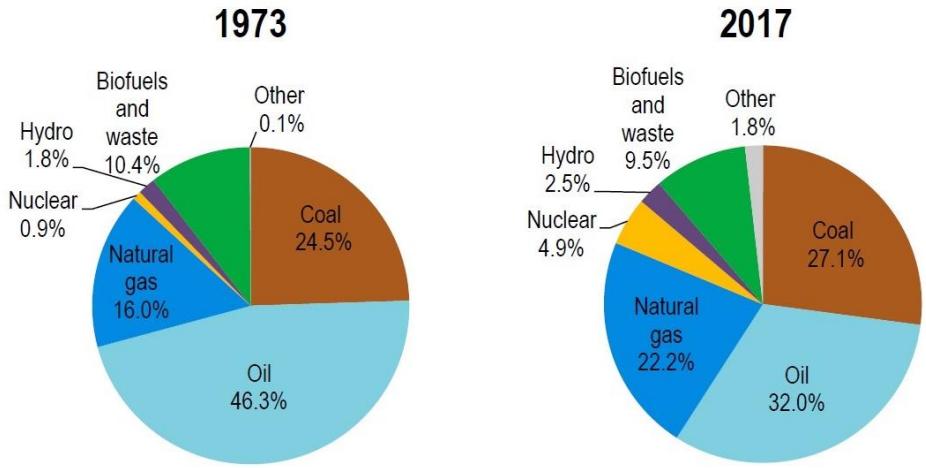

Figure 1.1. World total primary energy supply in 1973 and 2017. On the graph, peat and oil shale are aggregated with coal, and other energy sources include geothermal, solar, wind and heat; adapted from[2].

International Renewable Energy Agency (IRENA) analysis in 2019 showed that a combination of renewable energy and electrification can reduce the energy-related CO_2 emissions to 90 % [3]. In 2017, renewable energy resources filled 25 % of the share in the energy sector, and IRENA estimated an increase to 86 % by 2050 is reachable -**Figure 1.2**.

As shown in **Figure 1.1**, IRENA included technologies such as wind, solar photovoltaic (PV), solar thermal, geothermal, biomass, *etc.* as “Renewables”. “Energy efficiency” is considered as improving energy measure for application in sectors such as buildings, industrial and transport. Finally, “Electrification” represents the changing of fossil fuel burning equipment and machinery with similar electrified equipment, such as heat pumps in buildings and electric vehicles for transport sector [3].

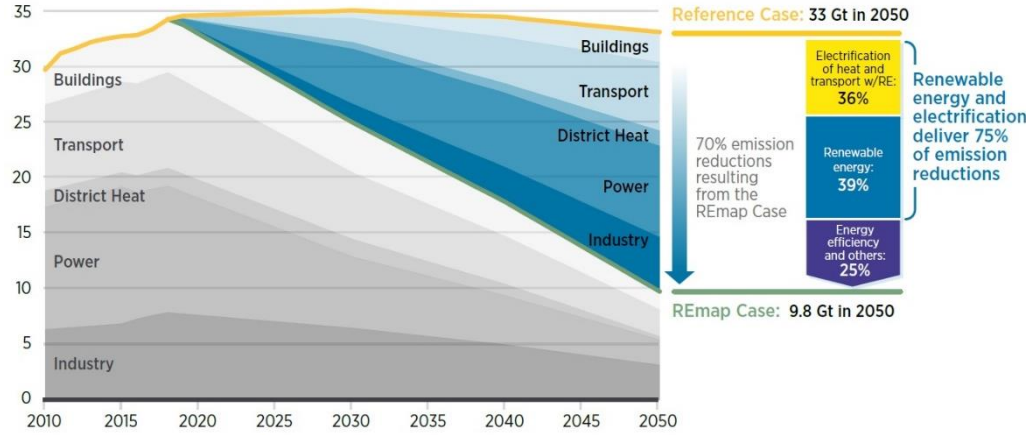

Figure 1.2. Annual energy-related CO_2 emission and reduction, 2015-2050 (Gt/yr), adopted from [3].

Among the renewable energy technologies, IRENA estimates that solar PV alone can decrease the CO_2 emissions up to 4.9 Gt in 2050. Thus, PV would count for 25 % of electricity generation worldwide. In 2018, solar PV has achieved a global total electricity power generation of 480 GW, which is expected to increase to 8519 GW by 2050 [4].

The installation cost and Levelized Cost of Electricity (LCOE) of solar PV in 2018 was 1210 USD/kW and 0.085 USD/kWh, respectively. The estimated value of 0.01 - 0.05 USD/kWh for LCOE in the year 2050, promises *ca*. 41 - 88 % of cost reduction. This decrease is foreseen due to intense worldwide effort in the field of solar PV research. These promising advancements would encourage average annual investment up to 192 USD billion/yr. **Figure 1.3** displays these predicted parameters for the future of solar PV by IRENA [4].

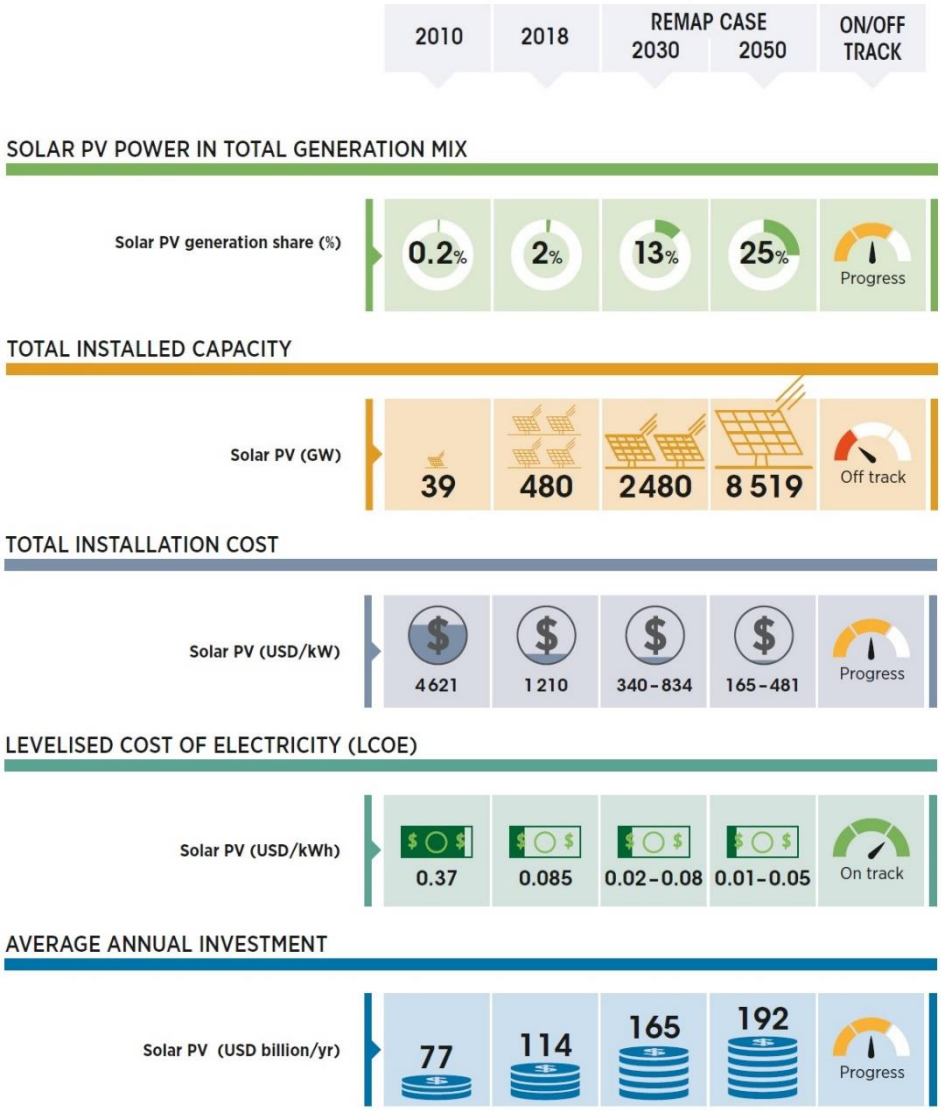

Figure 1.3. Current status and estimated future of solar photovoltaic technology by the year 2050, adopted from[4].

The power of the Sun is 380 × 10^{24} W, from which 170 × 10^{15} W reaches the earth outer atmosphere and 90 × 10^{15} W the earth's surface. Surprisingly, only 84 min solar radiation is enough for the world energy demand for one year. Most of the energy sources are originated from sunlight; for example oil, coal, natural

gas, and wood were originally formed through photosynthesis, and later transformed into these sources of energy through complex chemical reactions [5].

Solar energy can be utilized in a wide range of applications such as: water heating, thermal comfort, industrial process heat, solar power generation, desalination, photovoltaic and hydrolysis [6]. Photovoltaic panels are emerging as one of the most efficient processes for converting sunlight into readily used electricity.

1.1. PHOTOVOLTAIC TECHNOLOGY GENERATIONS

A photovoltaic system is built by interconnecting two main elements; a solar cell, and Balance of System (BoS) components. The solar cell converts the sunlight to electricity and BoS components are used for electrical connection, chemical protection and mechanical mounting of the cells to the PV panel [7]. The Direct Current (DC) electricity output of a solar cell can be consumed, stored, or inverted to Alternating Current (AC). In addition, a PV system includes other components for testing and monitoring as well as electronics - **Figure 1.4**.

Solar cells are typically categorized into three generations[7]:

- 1st generation: crystalline silicon cells;
- 2nd generation (thin-film): cadmium telluride (CdTe), copper indium gallium di-selenide (CIGS), amorphous silicon (a-Si), and single junction Gallium Arsenide (GaAs);
- 3rd generation: multi-junction and emerging solar cells (organic, dye-sensitized and perovskite).

Currently, only the first and the second generation solar cell technologies are commercially available. According to 2015 report from National Renewable Energy Laboratory (NREL), 1st generation technologies of multi-crystalline and mono-crystalline silicon hold 69 % and 24 % share of the PV market, while 2nd generation thin-film cells account for only 7 % (with 3 % for a-Si, 2.5 % CdTe,

and < 2 % CIGS) [7, 8]. China is the leading country for PV fabrication by holding 66 % share of the global solar module production, while Europe and the United States are only holding 6 % and 2 %, respectively [8].

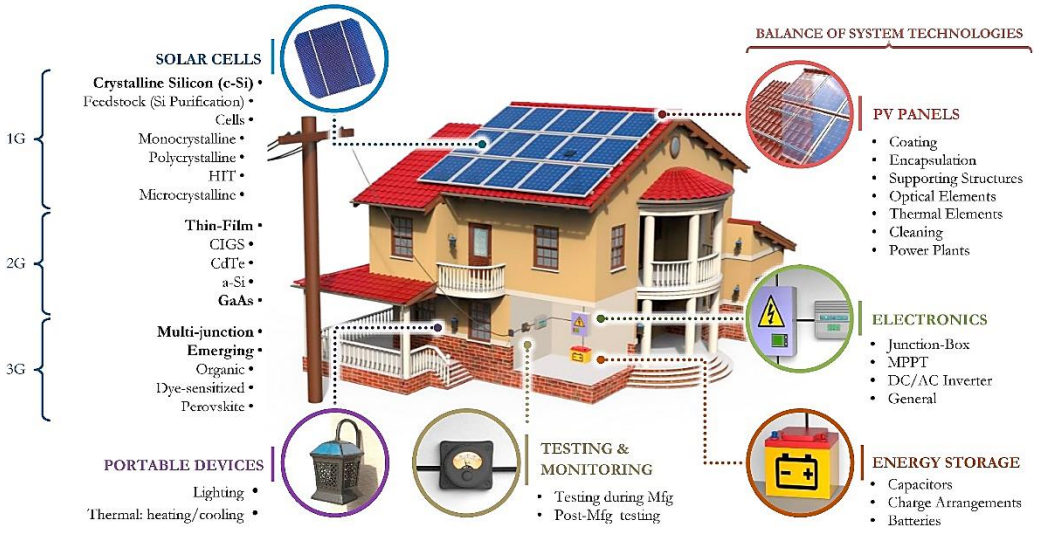

Figure 1.4. Schematic view of a solar photovoltaic system, adopted from[7].

The high fabrication costs of 3rd generation multi-junction PV technology and 2nd generation GaAs solar cells, only allows them to be used for aerospace power applications, where efficiency has priority over cost [9]. Finally, the emerging 3rd generation technologies are considered as the future market challengers for the traditional silicon solar cells.

Although the crystalline silicon cells are currently dominating the PV market, their high fabrication cost is an enormous disadvantage. During recent years, the manufacturing costs of 1st generation PV modules had decreased, however, the electricity produced by traditional fossil fuel energy sources such as coal and natural gas are still offering much lower prices. Apart from the necessity of changing fossil fuel-based energy sources with clean renewables, the cost is of the most importance for the final consumer. Therefore, for PV technology to

compete with fossil fuels, their production cost must be lowered as much as possible to ensure economic benefits for the consumers.

The 3rd generation emerging PV technologies such as Dye-sensitized Solar Cells (DSCs) and Perovskite Solar Cells (PSCs) can be fabricated by simple and cheap laboratory solution-based methods; their manufacturing cost is much lower comparing to silicon solar cells [10]. The current record efficiency of DSCs and PSCs is 12.3 % and 25.2 %, respectively[11]. Therefore, PSCs are perhaps the most suitable technology for the future of the PV produced electricity.

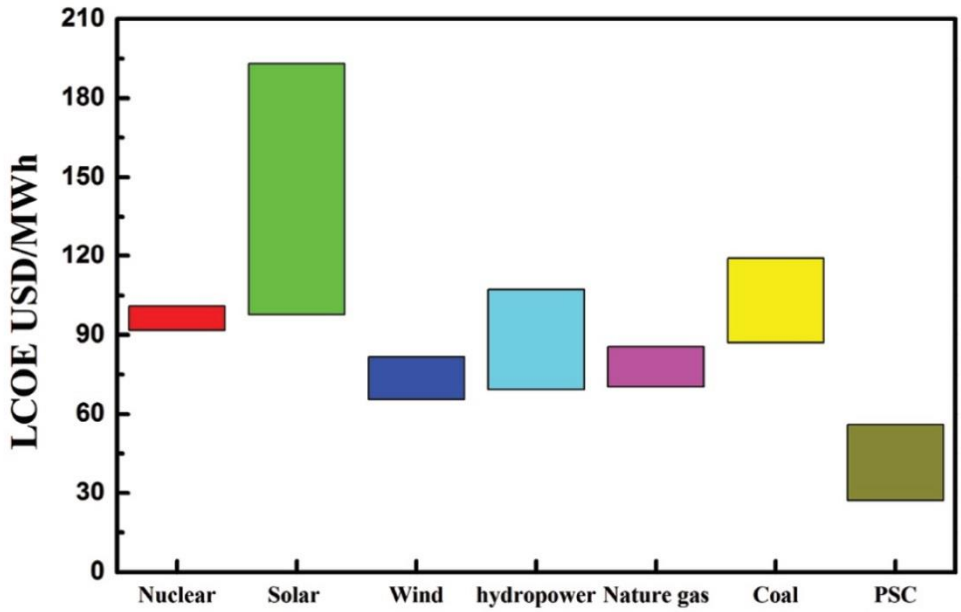

Figure 1.5. Comparison of LCOE for PSC to other sources for electricity production. The "Solar" category represents the 1st generation silicon solar cells. Adopted from [10].

In 2017, Cai *et al.* estimated the LCOE of perovskite solar cells and compared it to electricity produced by other energy sources reported by the United States Energy Information Administration (EIA). As shown in **Figure 1.5** the estimated LCOE for PSCs not only beats 1st generation solar cell ("Solar" category), but also overpasses the other energy production sources with a large margin. The

estimated LCOE was based on 15 years lifetime for 12 % efficient device which is a current scenario for PSCs. The calculated LCOE for this scenario yields 0.035 - 0.049 USD/kWh. This value is well in agreement with the 2050 goals defined by IRENA (**Figure 1.3**).

1.2. INTRODUCTION TO SOLAR CELL

A solar cell is a semiconductor diode that is designed to use sunlight to separate and collect electrons and holes and convert them to electrical current in a specific direction. Sunlight is an electromagnetic radiation and it is composed of photons with a particular quantity of energy. The photon energy is related to the wavelength (λ) and is defined by:

$$E_\lambda = \frac{hc}{\lambda} \qquad 1.1$$

where h is Plank's constant, λ is the wavelength and c is the speed of light. Photons with energies higher than the band gap (E_g) of the semiconductor are capable of exciting electrons in the valance band.

The sunlight radiation is spread over a wide wavelength of ultraviolet and visible to infrared. The surface temperature of sun is *ca.* 5762 K and its radiation spectra is approximately similar to a blackbody of that temperature. However, the earth atmosphere is affecting this by absorbing a fraction of the radiated light; ultraviolet region is absorbed by ozone, and CO_2 and H_2O of the atmosphere are also absorbing the light in other wavelengths. The air mass (AM) is a measure of these effects on the solar spectrum reaching the earth's surface and is defined by:

$$\mathrm{AM} = \frac{1}{\cos\varphi} \qquad 1.2$$

where φ is the zenith angle. The standard solar spectrum used for measuring power conversion efficiency for PV application is AM1.5G, for the irradiance of 1000 W m^{-2} at 25 °C. **Figure 1.6** shows the AM 1.5 G solar radiation spectrum.

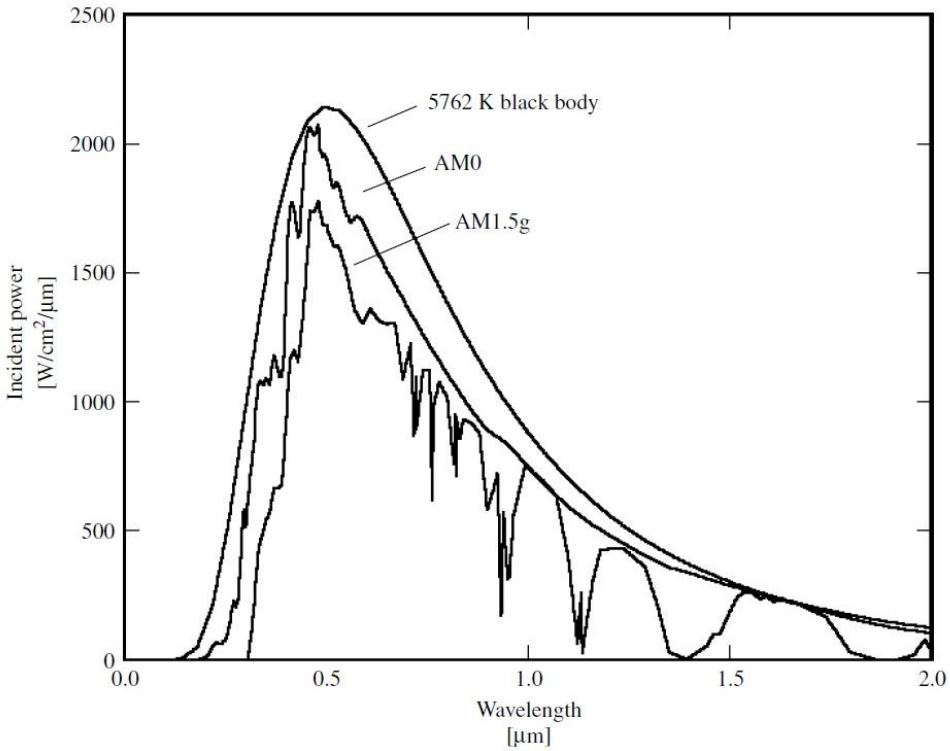

Figure 1.6. The radiation spectrum for a black body at 5762 K, compared to air mas zero and air mas 1.5 global, adapted from[12].

The power conversion efficiency (PCE) of a solar cell is the ratio of the maximum power output and light intensity:

$$\mathrm{PCE} = \frac{P_{\max}}{P_{\mathrm{in}}} \qquad 1.3$$

where P_{max} is the maximum power produced by the solar cell and P_{in} is the intensity of the incident light (1000 W m^{-2} for AM1.5 global). The fill factor (FF) is defined by the ratio of the maximum power (P_{max}) of the solar cell divided by its V_{oc} and J_{sc}:

$$\mathrm{FF} = \frac{P_{\max}}{V_{\mathrm{oc}}\, J_{\mathrm{sc}}} \qquad 1.4$$

where V_{oc} is the open-circuit photovoltage and J_{sc} is short-circuit current.

1.3. PEROVSKITE SOLAR CELLS

Perovskite is a term initially used for referring to a crystal structure identical to calcium titanate ($CaTiO_3$). The mineral was discovered in Russia and named after Russian mineralogist, Count Lev Alekseevich Perovskii (1792-1856). The general chemical formula for perovskite is ABX_3, where "A" and "B" are cations of very different sizes, and "X" is an anion [13].

The crystal structure of perovskite material is a simple cubic crystal system comprises of an anionic 3D network of corner-sharing $[BX_{6/2}]^-$ octahedra - **Figure 1.7**. The structure and physical properties of $CH_3NH_3MX_3$ (M= Pb or Sn, and X= Cl, Br or I) organometal halide perovskite material were first reported in 1978 [14]. These direct band gap semiconductors display a high light absorption coefficient in a wide range of wavelengths along with high charge-carrier mobility, appropriate for PV applications [15].

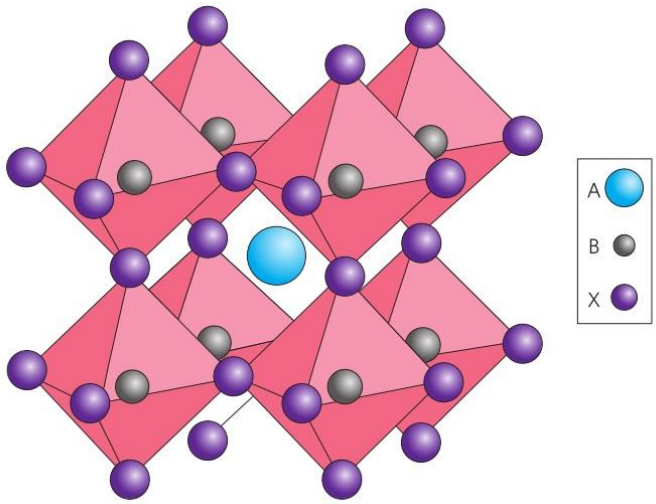

Figure 1.7. Crystal structure of perovskite material, reprinted from[16], Copyright 2014, Springer Nature.

Perovskite materials with more interest for solar cell applications are crystals with large cation A of methylammonium ($CH_3NH_3^+$), ethylammonium ($CH_3CH_2NH_3^+$), formamidinium ($NH_2CH{=}NH_2^+$), cesium (Cs^+), rubidium (Rb^+) or 5-ammonium valeric acid ($C_5H_{12}NO_2^+$) and small cation B of lead (Pb^{2+}) or tin (Sn^{2+}) and anion halogens X of commonly iodine (I^-), chlorine (Cl^-) or bromine (Br^-) [17-22].

The bandgap of semiconductor material for a single-junction photovoltaic cell should be ranging from 1.1 to 1.4 eV for efficient solar light conversion [12]. One of the most remarkable properties of perovskite material is that it could be tuned to different bandgaps by adjusting their chemical composition. For instance, by varying the iodide to bromide ions ratio in $CH_3NH_3Pb(I_{1-x}Br_x)_3$ (where, $0 \leq x \leq 1$), the bandgap changes from 1.2 to 2.3 eV [23]. Due to the possibility of fine-tuning of the bandgap the perovskite materials are favorable for construction multi-junction photovoltaic devices.

Perovskite solar cells (PSCs) have emerged in the PV community as one of the most promising candidates for direct competition with 1st generation crystalline silicon solar cells. The first reported PSCs had a PCE of 3.8 %[24] and in only 10 years the PCE of these cells has reached values as high as 25.2 % for single-junction and 28 % in monolithic tandem with silicon [11]. This rapid increase in PCE, along with the associated low production costs, makes PSCs suitable for the PV market. **Appendix A** shows the evolution and current status of all of the generations of solar cells from 1976 to the present (December 2019) reported by NREL.

In 2009 Miyasaka and co-authors, reported the first application of organometal halide perovskite materials in photochemical solar cells [24]. The device had a structure similar to DSCs, photoanode of TiO_2, $CH_3NH_3PbX_3$ (where X= Br, I) perovskite as light absorbing material, iodide/triiodide redox couple in the electrolyte, and platinum catalyst on the counter electrode. The best working cell displayed a PCE of 3.8 % but it was quite unstable when contacting air. This

pioneering work guided the research community to focus more on perovskites rendering in 2019 the PSC device with certified conversion efficiency as high as 25.2 %. **Figure 1.8** displays the progress in PCE of the 3rd generation solar cells.

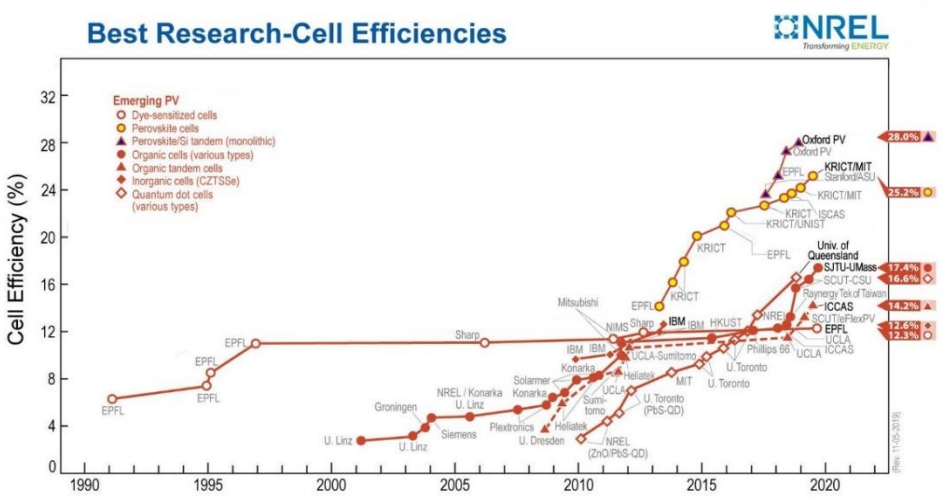

Figure 1.8. Best research cell efficiency chart for 3rd generation emerging solar cells from 1990 to 2019. This plot is courtesy of the National Renewable Energy Laboratory, Golden, CO[11].

A typical perovskite solar cell is a thin layered stack of several functional elements: (1) transparent substrate, typically made of glass, coated with transparent conductive oxide (TCO); (2) a compact layer of n-type semiconductor (blocking layer) as the electron transport layer (ETL); (3) a mesoporous scaffold layer (*i.e.* ETL); (4) a perovskite light absorbing layer; (5) a p-type semiconductor as the hole transport layer (HTL) also known as hole transport material (HTM) ; and (6) conductive back contact [25]. Depending on the structure and sequence of the layers in the perovskite photovoltaic stack the PSCs are categorized into three major groups[26];

- **Mesoporous**. This type of PSCs mimics the structure and working principle of the dye-sensitized solar cells. The perovskite light-absorber

is placed inside the mesoporous scaffold made from a large bandgap semiconductor, typically TiO_2. Photoelectron from the excited perovskite is injected into the mesoporous semiconductor scaffold and transferred through it to the TCO layer.

- **Planar**. In this structure, the perovskite light absorber is sandwiched between the ETL and HTL layers; no mesoporous layers of any other materials are used in the photovoltaic stack.
- **Triple mesoporous**. In this arrangement, the perovskite light-absorber is formed within a triple stack of mesoporous layers i) TiO_2 scaffold; ii) insulation layer (ZrO_2, Al_2O_3, SiO2, *etc.*) and iii) carbon back contact.

The mesoporous and planar structure of PSCs are further divided into two categories of conventional (formal) and inverted depending on their deposition sequence of the HTL and ETL layers- **Figure 1.9**.

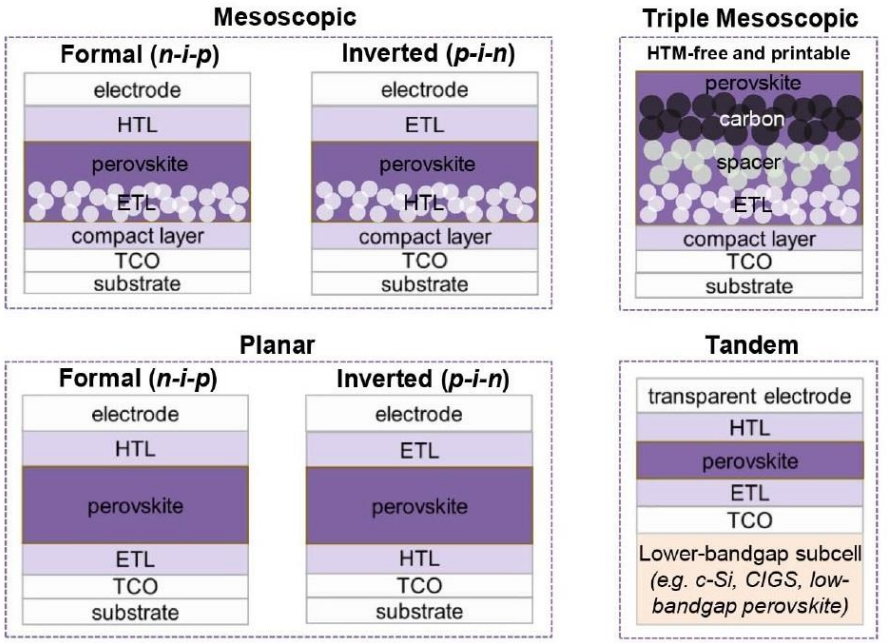

Figure 1.9. Perovskite solar cell device configurations, reprinted from[26], Copyright 2018, American Association of The advancement of Science (AAAS).

1.3.1. WORKING PRINCIPLE OF PEROVSKITE SOLAR CELLS

The working principle of a solar cell involves light absorption, charge separation, charge transport, and charge collection. Organometallic perovskites such as $MAPbI_3$ possess both electron and hole transport properties [27, 28]. Therefore, perovskite solar cells could be constructed both as p-n junction and p-i-n or n-i-p junction. There are 8 processes involved in the working principle of conventional mesoporous perovskite solar cells [29]:

a) Photoexcitation of perovskite absorber;

$$\text{Perovskite} + h\nu \rightarrow (\text{e}^- \cdots \text{h}^+)_{\text{Perovskite}} \quad 1.5$$

b) Electron injection;

$$(\text{e}^- \cdots \text{h}^+)_{\text{Perovskite}} \rightarrow \text{e}^-_{\text{cb}}\,[\text{TiO}_2] + \text{h}^+\,[\text{Perovskite}] \quad 1.6$$

$$\text{h}^+\,[\text{Perovskite}] \rightarrow \text{h}^+\,[\text{HTM}]$$

c) Hole injection;

$$(\text{e}^- \cdots \text{h}^+)_{\text{Perovskite}} \rightarrow \text{h}^+\,[\text{HTM}] + \text{e}^-\,[\text{Perovskite}] \quad 1.7$$

$$\text{e}^-\,[\text{Perovskite}] \rightarrow \text{e}^-_{\text{cb}}\,[\text{TiO}_2]$$

d) Photoluminescence;

$$(\text{e}^- \cdots \text{h}^+)_{\text{Perovskite}} \rightarrow h\nu' \quad 1.8$$

e) Non-radiative recombination;

$$(\text{e}^- \cdots \text{h}^+)_{\text{Perovskite}} \rightarrow \nabla \quad 1.9$$

f) Back electron transfer at TiO_2-perovskite junction;

$$\text{e}^-_{\text{cb}}\,[\text{TiO}_2] + \text{h}^+\,[\text{Perovskite}] \rightarrow \nabla \quad 1.10$$

g) Back charge transfer at perovskite-HTM junction;

$$e^- [\text{Perovskite}] + h^+ [\text{HTM}] \rightarrow \nabla \quad 1.11$$

h) Charge recombination at TiO_2-HTM interface;

$$e_{cb}^- [TiO_2] + h^+ [\text{HTM}] \rightarrow \nabla \quad 1.12$$

The overall efficiency of mesoporous PSC is determined by the above processes. To achieve high efficiencies, charge generation and transport (**1.5** - **1.7**) should occur faster than recombination (**1.8** - **1.12**) -**Figure 1.10**.

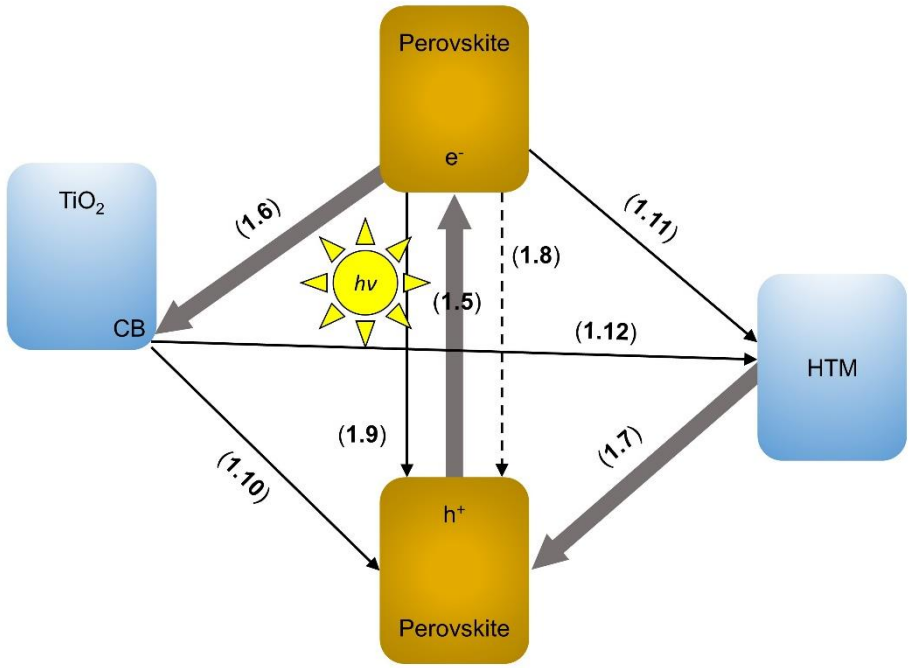

Figure 1.10. Scheme illustrating electron and hole transport in mesoporous PSC.

For efficient charge transfer, the energy levels of the electron and hole transport layers (ETL and HTL) must be aligned with the perovskite light-absorber and the contacts. For a conventional mesoporous PSC the conduction band (CB) edge of the perovskite absorber must be higher than the CB of TiO_2 while its valance band (VB) should be lower than the VB of the HTM layer [25]. Two device

structures are studied during the course of the present thesis: HTM-free triple mesoporous configuration and conventional n-i-p mesoporous structure. **Figure 1.11** illustrates the band diagram of two PSC device structures studied in the scope of the thesis.

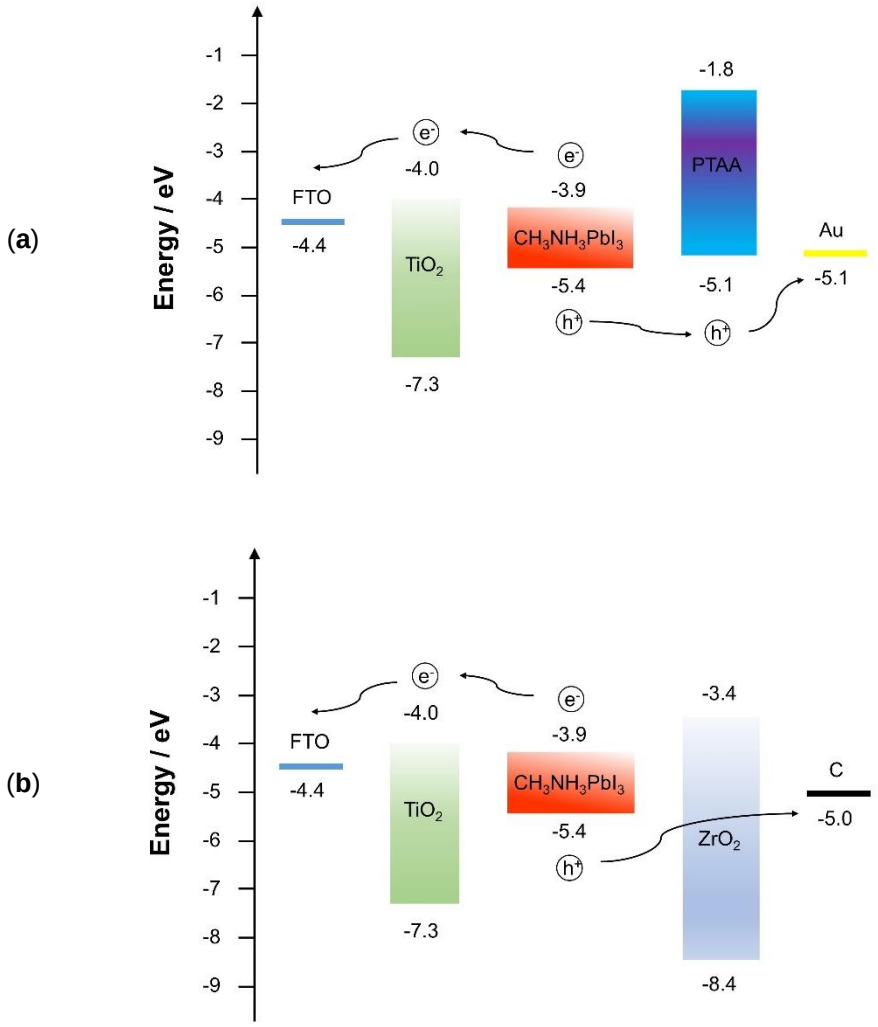

Figure 1.11. Band diagram for (a) conventional n-i-p mesoporous and (b) HTM-free triple mesoporous structure PSC.

The electron and hole transport in HTM-free triple mesoporous structure is based on the ambipolar behavior of perovskite absorber. The ambipolar transport nature of perovskite can be used for transporting both electron and hole [28]. Therefore, if the HTM layer is not included in the structure, the holes can be still collected at the back contact. However, in order to avoid short-circuit an insulating spacer layer (*e.g.* ZrO_2 or Al_2O_3) is required to separate the photo-electrode and back contact.

1.3.2. PEROVSKITE SOLAR CELL FABRICATION TECHNIQUES AND MATERIALS

There are various deposition methods for fabrication of perovskite solar cell components including spin-coating[30, 31], slot die[32, 33], chemical vapor deposition[34, 35], spray deposition[36, 37], screen-printing[38, 39] and inkjet printing[40, 41]. Among these methods, the most common one is the spin coating, which allows high-quality deposition for a small area (< 1 cm^2) lab-scale devices. To achieve a good quality of deposition in large-area devices, other aforementioned techniques are relevant.

From the structural point of view, two types of PSC arrangement were used in the thesis: mesoporous n-i-p and triple printable mesoporous. A brief description of the fabrication methods and most commonly used materials for making these architectures, is presented here. Fabrication methods for other structures of planar n-i-p[42], mesoporous p-i-n[43], planar p-i-n[44] and tandem configuration[45], can be found elsewhere[25, 26, 46].

In 2018, Rong *et al.* presented the evolution of PCE for various structures of perovskite solar cells[26]. As shown in **Figure 1.12**, mesoporous and planar n-i-p devices presented the highest PCE for small lab-scale devices of ≤ 0.1 cm^2 area, followed by p-i-n architecture and printable triple mesoporous HTM-fee devices, respectively. However, for larger device size of ≥ 1.0 cm^2 the mesoporous n-i-p and planar p-i-n devices display a relatively large PCE drop while planar n-i-p

and HTM-free devices are showing better adaptability for up-scaling. Perhaps, the main reason for the large PCE drop for n-i-p and p-i-n structures are due to the non-scalability of the deposition methods, while the scalable screen printed HTM-free devices display less drop of the PCE.

(**a**)

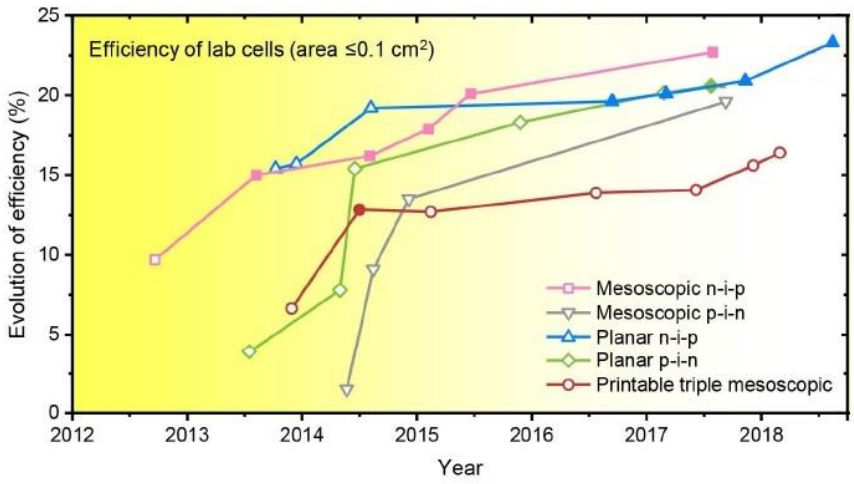

(**b**)

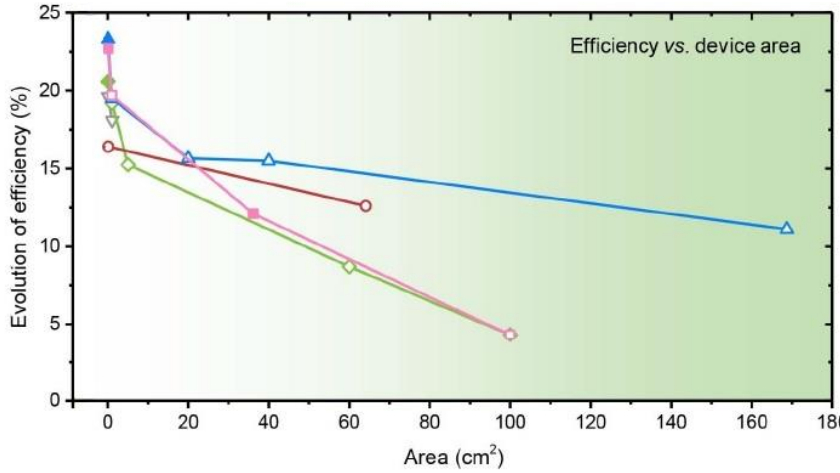

Figure 1.12. Evolution of PCE for (**a**) lab-scale and (**b**) large area perovskite solar cells. Solid and hollow symbols represent certified and uncertified measurements, reprinted from[26], Copyright 2018, AAAS.

Mesoporous n-i-p perovskite solar cells

The fabrication method for mesoporous n-i-p devices is based on the sequential deposition of the following layers on a TCO coated glass substrate:

- **a)** An n-type semiconductor compact layer (also known as blocking layer) - ETL;
- **b)** A mesoporous semiconductor or insulating scaffold layer;
- **c)** A perovskite absorber;
- **d)** A hole transport material - HTL;
- **e)** An electrical conductive back contact.

Mesoporous n-i-p PSC is fabricated on a substrate made of glass coated with a TCO layer. The most common TCO layer used for this device structure is SnO_2: F (fluorine doped tin oxide - FTO). The FTO-coated substrates are commercially available with various glass thicknesses (*e.g.* 1 mm, 2.2 mm and 3 mm) and sheet resistances (*e.g.* 7 Ω / □, 10 Ω / □ and 15 Ω / □). The optical transmittance of the substrate is defined depending on the glass thickness and sheet resistance. Since FTO layer is the front electrical contact of the cell lower sheet resistance is preferable. However, lower sheet resistance FTO substrates have less optical transmittance because of the thicker FTO layer. Therefore, a suitable TCO coating should have a balance between sheet resistance and optical transmittance. Thus, the most favorable option for the balance of sheet resistance and optical transmittance is 10 Ω / □.

PSCs are fabricated on a single substrate and the positive and negative charge terminals are separated through the removal of the TCO layer. This etching/scribing process can be achieved through various methods of mechanical, chemical, electrochemical or radiation (*i.e.* laser).

After appropriate substrate cleaning, the n-type ETL layer is deposited. This layer is also known as blocking layer or compact layer. There are two roles for the compact ETL: (i) transport generated electrons from the perovskite light

absorber to the external circuit and (ii) block the photogenerated holes from reaching the photo electrode [47]. Materials such as TiO_2 [48], SnO_2 [49], ZnO [50], *etc.* are typically used as compact ETL layer in n-i-p PSCs.

The next layer for mesoporous n-i-p PSC device is the mesoporous scaffold. The mesoporous scaffold is used to (i) assist the electron extraction from the perovskite absorber, (ii) decrease the electron charge transport length, and (iii) provide a scaffold to increase the quality of perovskite crystal formation [51]. There are two possible material groups for the scaffold layer; semiconductor and insulating. For semiconducting materials, the scaffold plays all the aforementioned roles, but for insulating materials, the scaffold only serves to ensure high surface area for perovskite. Although mesoporous layer has many positive advantages, however including it in the structure of the cell can lower the light absorbance of the perovskite at wavelength > 700 nm [52] and causes loss in V_{oc} [53]. The most common mesoporous scaffold layers for PSC is TiO_2 (semiconductor) and Al_2O_3 (insulating) [54].

The perovskite absorber is placed on top of the mesoporous layer. There are countless perovskite crystals with proper bandgap for application in PSC. As mentioned before, perovskite is a crystalline material with general chemical formula of ABX_3. The most common “A” cations are MA, FA and Cs, while “B” cation is mainly Pb or Sn. The anion “X” used can be I, Br, Cl or a mixture of these materials. Varying the composition of the cations and anion, results in different band gaps. The most commonly used $MAPbI_3$ crystal has a band gap of *ca.* 1.55 eV, 100 nm diffusion length and 66 $cm^2\ V^{-1}\ s^{-1}$ carrier mobility. The ambipolar $MAPbI_3$ displays charge transport properties range of 2 to 10 $cm^2\ V^{-1}\ s^{-1}$ and 5 to 12 $cm^2\ V^{-1}\ s^{-1}$ for electron and hole [55]. Another widely used perovskite is $FAPbI_3$ with 1.47 eV band gap. The incorporation of FA cation in the perovskite structure increases the thermal stability and phase transition point of the material [55]. Perovskite absorber is the heart of the cell, and its stability is the main concern for the future on these PV devices. Another alarming matter is the fact that so far the best performing crystals contain toxic Pb compounds.

The structure of n-i-p device is followed by deposition of the HTL. The terms HTM and HTL are often interchangeably used for referring to this layer. An ideal HTM layer must have (i) high hole mobility, (ii) good thermal stability and (iii) well-matched highest occupied molecule orbital (HOMO) or energy band level comparing to the perovskite absorber [55]. There are two main groups of HTL used in PSCs; organic, and inorganic. So far, the best performing cells are built with organic HTMs such as spiro-OMeTAD and Poly[bis(4-phenyl)(2,4,6-trimethylphenyl)amine] (PTAA) while inorganic materials such as Copper thiocyanate (CuSCN) and nickel oxide (NiO_x) display performance with moderate PCEs. Spiro is perhaps the best HTM for most n-i-p PSCs. This material displays well-matched band gap alignment with perovskite, good conductivity with dopants and well pore filling. CuSCN is a wide band gap p-type semiconductor with valance band edge of -5.3 eV. The hole mobility for CuSCN and spiro-OMeTAD is 10^{-2} cm^2 V^{-1} s^{-1} and 4×10^{-5} cm^2 V^{-1} s^{-1}, respectively. Although CuSCN has higher hole mobility comparing to spiro-OMeTAD, achieving uniform CuSCN layer is quite challenging [20]; therefore the cells fabricated with CuSCN show lower V_{oc}. Finally, PTAA has good hole mobility and band alignment level with perovskite, comparing to spiro-OMeTAD; PTAA displays a better thermal stability [55].

Finally, the n-i-p device is completed with a back contact conductive layer. The most commonly used material for back contact is gold. Other materials such as silver are not suitable for this terminal, as it can get damaged by exposure to light, heat or moisture. Au has a work function of -5.1 eV and electrical resistivity of 2.4×10^{-8} Ω m^{-1}, which makes it one of the best candidate for the top contact. However, the high cost of this material is a drawback for the PSCs [56].

Each one of the above-mentioned layers plays its specific role in controlling the efficiency of the solar cell [57]. These layers can be fabricated through various deposition techniques however, the methods used for the fabrication of PSCs during the present thesis are spin-coating, screen printing, thermal evaporation and spray pyrolysis.

Deposition techniques

Spray pyrolysis is a deposition method in which a precursor solution is sprayed on a heated sample to form a thin film deposition. This process follows several stages: (i) rapid evaporation of solvents, (ii) drying of the precipitated solute, (iii) annealing of the precipitated solute at the process temperature, (iv) formation of thin film, (v) sintering of the thin film [58, 59].

Spin coating deposition is based on centrifugal force to disperse a solution of a material on a substrate. Typically, the deposition requires three steps: (i) fixing of a substrate on the rotation plate and dropping of a solution in the center of the substrate, (ii) spinning the substrate at high rotation speed to remove the solvent, (iii) thin film formation on the substrate. The thickness of the final film is controlled by the surface tension, viscosity of the solution and the rotation time and speed [60]. The major disadvantage of this deposition method is the limited substrate size. For large substrates, achieving high rotation speed is more difficult, and the film quality and uniformity becomes low [61].

Thermal evaporation is a Physical Vapor Deposition (PVD) technique. A PVD is processed at high vacuum conditions, followed by generation of a vapor flux and its subsequent condensation of a thin film on a sample substrate. During thermal evaporation, a material (target) placed inside a crucible is heated to its evaporation point. Atoms or molecules are removed from the target in the form of vapor flux then condensates on the sample, forming a thin film [62].

Screen printing is a stencil deposition process where the material is only printed on the open areas of the screen. During printing, a paste including the target material is forced into the opening of the screen by a squeegee. The screen is made of a mesh covered with emulsion. For thin film application, materials such as polyester and metal meshes are used. The quality of the deposition is based on the mesh size; higher threads per cm, ensure better printing quality. Parameters such as mesh thickness and size, emulsion material and squeegee harness and shape define the thickness of the deposition [63].

(**a**)

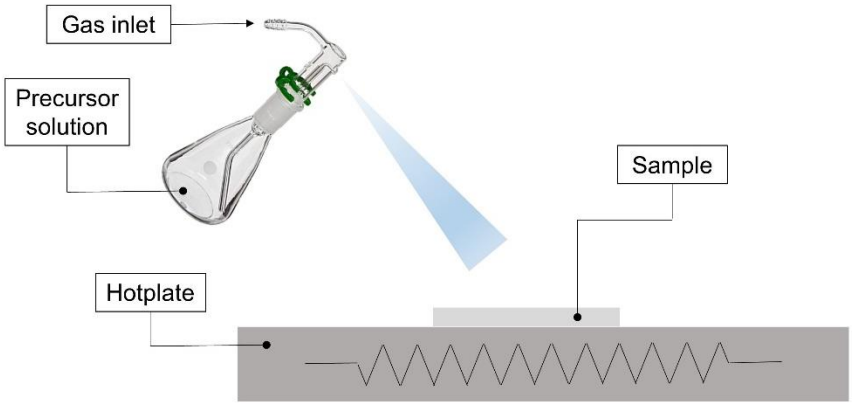
Gas inlet
Precursor solution
Sample
Hotplate

(**b**)

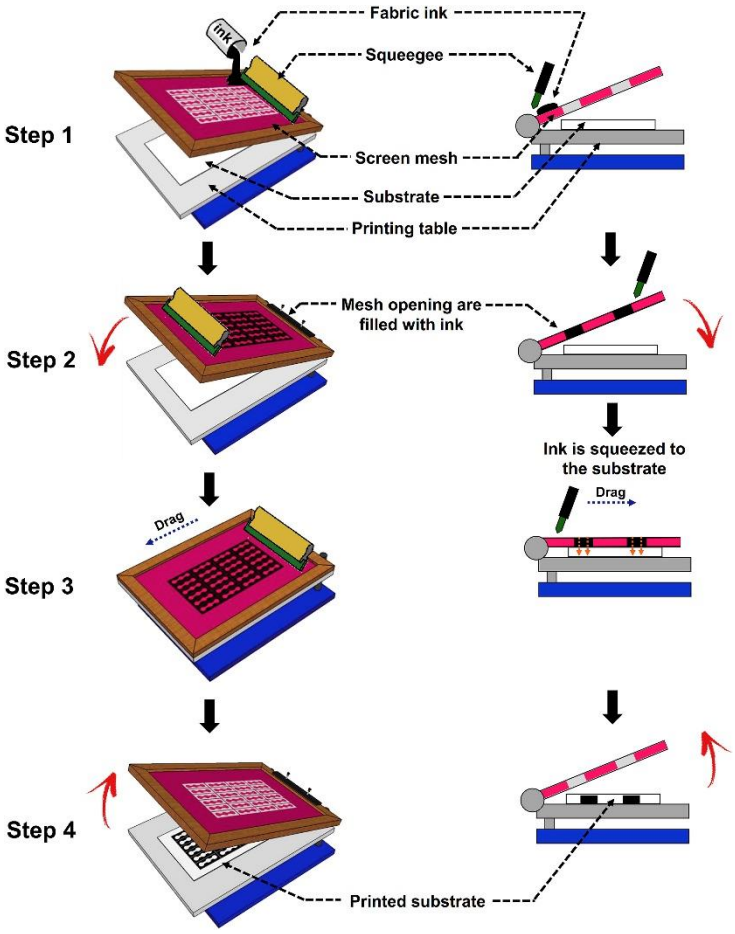
Fabric ink
Squeegee
Ink
Step 1
Screen mesh
Substrate
Printing table
Mesh opening are filled with ink
Step 2
Ink is squeezed to the substrate
Drag
Drag
Step 3
Step 4
Printed substrate

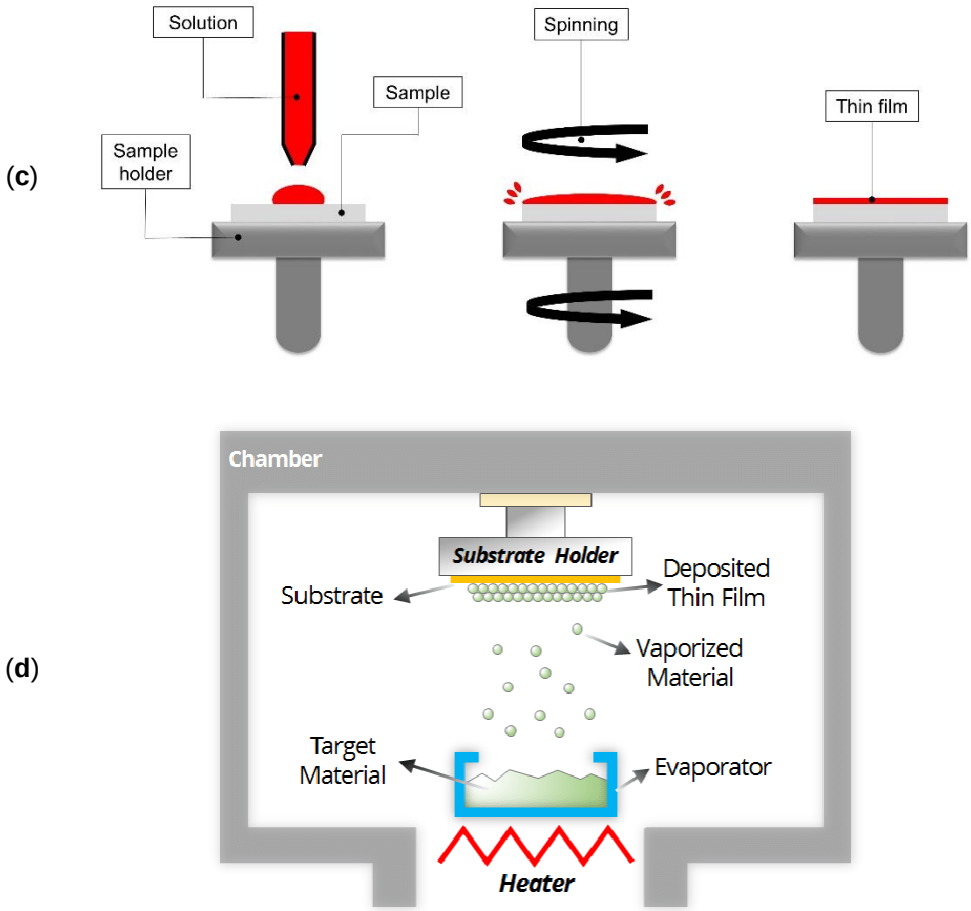

Figure 1.13. Schematic view of deposition methods for n-i-p mesoporous PSC; (**a**) spray pyrolysis, (**b**), screen printing (**c**) spin coating and (**d**) thermal evaporation. Reprinted from [64, 65] Copyright 2016, Springer Nature, Copyright 2019 Elsevier.

Figure 1.13 shows the schematic view of deposition methods for PSC fabrication. The fabrication of n-i-p mesoporous PSC involves steps at normal atmospheric conditions as well as controlled inert atmosphere. The perovskite absorber is known to decompose in contact with humidity and oxygen [66]. In order to avoid humidity exposure, most of the layers must be deposited at inert atmosphere filled glovebox (*e.g.* N_2, Ar) with water and oxygen level of < 1 ppm.

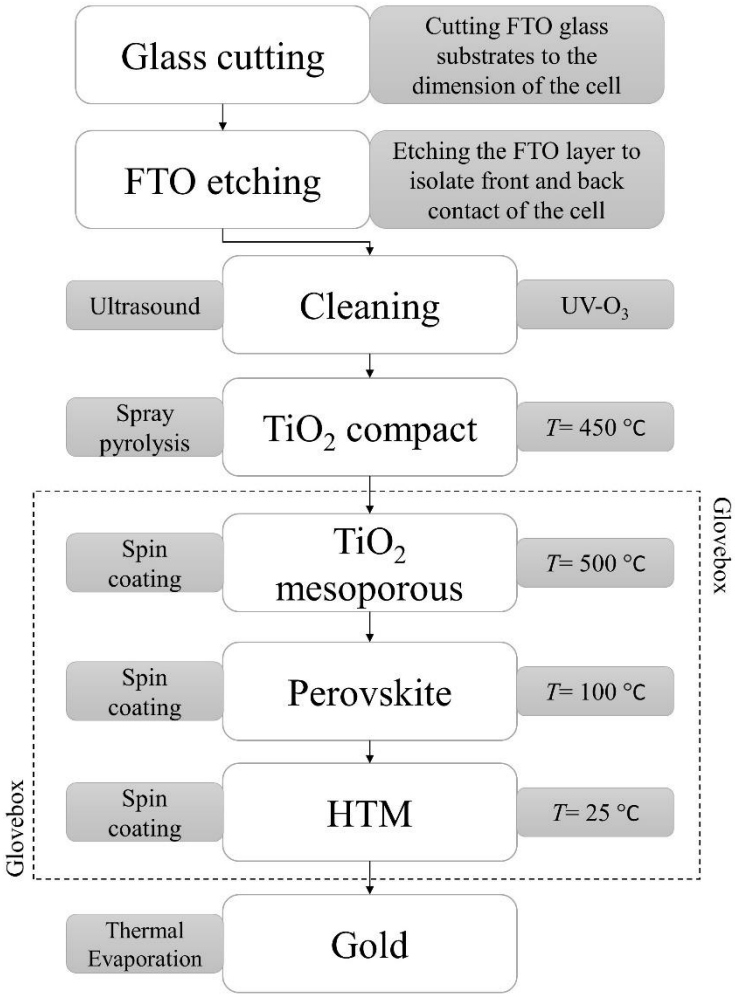

Figure 1.14. Fabrication steps for conventional n-i-p HTM-based perovskite solar cell.

Figure 1.14 shows the fabrication steps for conventional HTM based PSC, used in the thesis. After the first cleaning steps, *bl*-TiO_2 is deposited by spray pyrolysis with atmospheric air as a gas carrier. The spray deposition is performed at 450 °C and followed by sintering step for 45 min. After cool down, the samples are placed inside the glovebox and the *meso*-TiO_2 is spin-coated and dried at 100 °C. The mesoporous layer is then removed from the glovebox and sintered in a furnace at 500 °C. After cool down, to avoid humidity uptake in mesoporous

layer, the samples must be transferred to glovebox while they are still at temperature of > 100 °C. Then, the perovskite absorber is spin coated and sintered at 100 °C. The device fabrication is followed by spin coating of the HTM layer. Finally, the back contact of Au is deposited through thermal evaporation.

HTM-free triple printable mesoporous perovskite solar cells

Perovskite absorber displays ambipolar charge transport ability. Therefore, the solar cell can be fabricated without a HTM layer. These types of the devices were first reported in 2012 by Etgar and co-workers [27]. They achieved a PCE of 5.5 % for the device structure of *meso*-TiO_2 / $MAPbI_3$ / Au. It is important to mention that HTM layer plays two roles in the charge transport: (i) transporting hole charges and (ii) blocking the electrons from reaching the back contact. To avoid short-circuiting the TiO_2 with back contact, a spacer layer should be added in between [67]. The spacer layer is commonly made of insulating oxides such as ZrO_2, Al_2O_3, or SiO_2 [67]. For the insulating layer, ZrO_2 is the most suitable option, due to its suitable pore size matrix to host the perovskite crystal [68]. In 2013, Ku *et al.* reported a fully screen printed mesoporous device with the structure of TiO_2 / $MAPbI_3$ / ZrO_2 / C [69]. The authors replaced the expensive gold back contact with carbon black and achieved a PCE of 6.64 %. The breakthrough of fully printed PSCs occurred in 2014 [19]. A certified PCE of 12.8 % was reported by Mei *et al.* for a device with dual cation perovskite crystal of $(5\text{-AVA})_x(MA)_{1-x}PbI_3$. The addition of 5-AVA cation produced less defected perovskite crystals and favors the pore filling in the mesoporous scaffold.

As shown in **Figure 1.15**, the initial fabrication steps for the HTM-free PSC is similar to n-i-p devices. After the deposition of *meso*-TiO_2, the insulating layer of ZrO_2 is screen printed and sintered. The carbon back contact is also screen print deposited and sintered. The device is finished by dropping a precursor solution of perovskite absorber on top of the triple mesoporous structure. Therefore, perovskite crystals fill the pores of the entire mesoporous structure, building a matrix of semiconductor to transport both electron and hole charges. In this

structure, the hydrophobic carbon back contact prevents humidity entry to the mesoporous layers. Thus, unlike n-i-p PSCs, HTM-free devices are not required to be fabricated inside a glovebox, these structures can be made at normal atmospheric conditions.

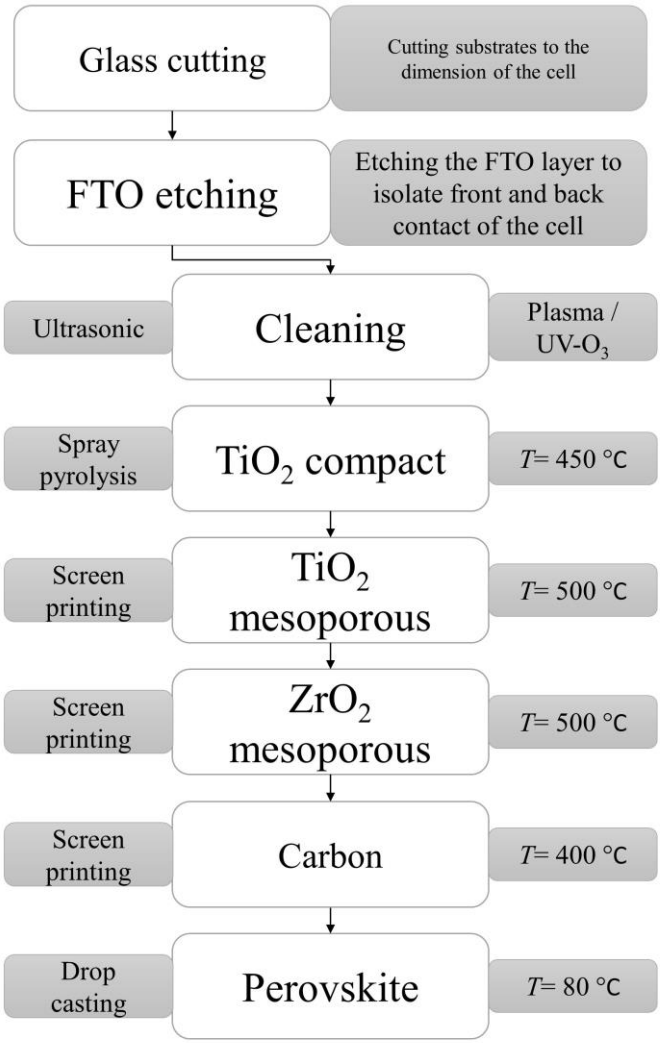

Figure 1.15. Fabrication steps for HTM-free triple mesoporous perovskite solar cell.

From fabrication point of view, solar cells should be built with simple, cheap and scalable methods. In this context, screen printing fits well with these requirements. The spin coating can only produce high-quality deposits in small areas. Vacuum deposition is expensive, time-consuming and not suitable for large-area devices. Thus, mesoporous n-i-p PSCs might not be a suitable candidate for industrialization. On the other hand, HTM-free PSCs with simple air processed screen printing deposition method are one of the strongest candidates to push perovskites into the PV market. For n-i-p devices to enter the commercialization route, different deposition methods must be considered.

1.4. STABILITY OF PEROVSKITE SOLAR CELLS

Although perovskite solar cells display promising high PCEs; their stability in various conditions is still a great concern. PSCs can degrade in contact with humidity, UV illumination and when exposed to high temperatures [70]. Degradation issues of perovskite solar cells is directly dependent on the structure of the device. For the device to have long term stability, the perovskite absorber layer must be stable. Other layers such as ETL and HTL can also contribute to the poor stability of the device. Therefore, the device structure must be tailored to the priority of perovskite stability. Stability issues of perovskite absorber layer are: (i) intrinsic, (ii) humidity and oxygen exposure, (iii) illumination and (iv) thermal exposure [71]. For mesoporous n-i-p devices other layers such as *meso*-TiO_2 and HTM are also responsible for the poor stability of the device during illumination and thermal exposure. The focus of the present thesis is to develop an encapsulation procedure to avoid humidity ingress stability issues for two device structures of HTM-free and mesoporous n-i-p. Therefore, here a brief description of stability related issues of perovskite absorber is presented along with some details on the thermal stability of other active layers of the device.

1.4.1. EFFECT OF HUMIDITY AND OXYGEN ON PEROVSKITE

Moisture can permanently decompose the perovskite light absorber. To date, most authors claimed that high humidity can decompose the crystal, but there are also reports on benefits of controlled humidity exposure for crystal growth [72]. **Reactions 1.13** to **1.16** show the $MAPbI_3$ decomposition pathway in the presence of moisture, oxygen and UV light.

$$CH_3NH_3PbI_3\ (s)\ \rightleftharpoons\ PbI_2\ (s) + CH_3NH_3I\ (aq) \quad 1.13$$

$$CH_3NH_3I\ (aq) \rightleftharpoons CH_3NH_2\ (aq)\ +\ HI\ (aq) \quad 1.14$$

$$4\ HI\ (aq) +\ O_2\ (g) \rightleftharpoons 2I_2\ (s)\ +\ 2\ H_2O\ (l) \quad 1.15$$

$$2\ HI\ (aq) \rightleftharpoons H_2\ (g)\ + I_2\ (s) \quad 1.16$$

Leguy and co-workers studied the humidity effect on $MAPbI_3$. They showed that the water uptake in the crystal structure of perovskite occurs both reversibly and irreversibly. The authors suggested that the irreversible decomposition of the crystal in the presence of water vapour only happens when the crystal is fully converted to its monohydrate phase [73]. The reversible hydration reactions of $MAPbI_3$ are presented in **reaction 1.17**.

$$4\ CH_3NH_3PbI_3 + 4\ H_2O\ \rightleftharpoons 4[CH_3NH_3PbI_3 \cdot H_2O] \rightleftharpoons\ (CH_3NH_3)_4PbI_6\ \cdot 2H_2O + 3PbI_2 + 2\ H_2O \quad 1.17$$

The monohydrate phase can be converted back to $MAPbI_3$ when exposed to dry atmosphere [74]. However, when the water vapour exposure is longer, the reaction tends toward the formation of the dihydrate phase along with lead iodide and release 2 water molecules. The released water molecules may be used to further react with $MAPbI_3$ and convert is to a monohydrate form. Finally, when the total conversion of $MAPbI_3$ is reached, the excess water is dissolving the MA, causing the irreversible decomposition of the perovskite material - **reaction 1.18**.

$$(CH_3NH_3)_4PbI_6\ \cdot 2H_2O\ (s) \xrightarrow{H_2O\ (l)} 4CH_3NH_3I\ (aq) +\ PbI_2\ (s) + 2H_2O\ (l) \quad 1.18$$

This irreversible decomposition of $MAPbI_3$ is visually identified by a colour change from dark brown to yellow due to the formation of yellow coloured PbI_2. This decomposition can also be identified by absorption spectroscopy at a wavelength range of 530 nm to 800 nm or crystallography XRD analysis [75].

1.4.2. UV LIGHT EXPOSURE EFFECT ON PEROVSKITE

As mentioned before, the most frequent mesoporous scaffold used for n-i-p PSCs is made from TiO_2. Titanium oxide is a semiconductor with a band gap of 3.2 eV, which can be used as a photocatalyst for oxidizing water and organic materials [76]. When TiO_2 based perovskite solar cell is exposed to light, the $MAPbI_3$ can decompose to PbI_2. Ito *et al.* proposed a decomposition mechanism at the interface of $MAPbI_3$ and TiO_2 mesoporous layer [77]:

$$2I^- \rightleftharpoons I_2 + 2e^- \quad \text{[at the interface of } TiO_2 \text{ and } MAPbI_3\text{]} \qquad 1.19$$

$$3CH_3NH_3^+ \rightleftharpoons 3CH_3NH_2 \uparrow + 3H^+ \qquad 1.20$$

$$I^- + I_2 + 3H^+ + 2e^- \rightleftharpoons 3HI \qquad 1.21$$

The $MAPbI_3$ contains ions of MA^+, Pb^{2+}, and I^-. At first step (**1.19**), TiO_2 can extract electrons from I^- ion to form I_2, resulting in the deconstruction of $MAPbI_3$ crystal. Although **reaction 1.20** is in equilibrium, in presence of water the forward reaction causes the evaporation of MA (boiling point of 17 °C) and constant production of H^+. Finally, the electrons extracted from **reaction 1.19** along with I_2 and I^- at the TiO_2 surface is reacted with H^+ (produced in **1.20**) to form HI [75].

To avoid UV illumination related issues of the TiO_2-based n-i-p PSCs, UV cut off filters can be used. Alternatively, the mesoporous layer of TiO_2 may be replaced by other scaffold materials such as Al_2O_3 [52] or coating of the TiO_2 nanoparticles with insulating layers of alumina-silicate shell [78].

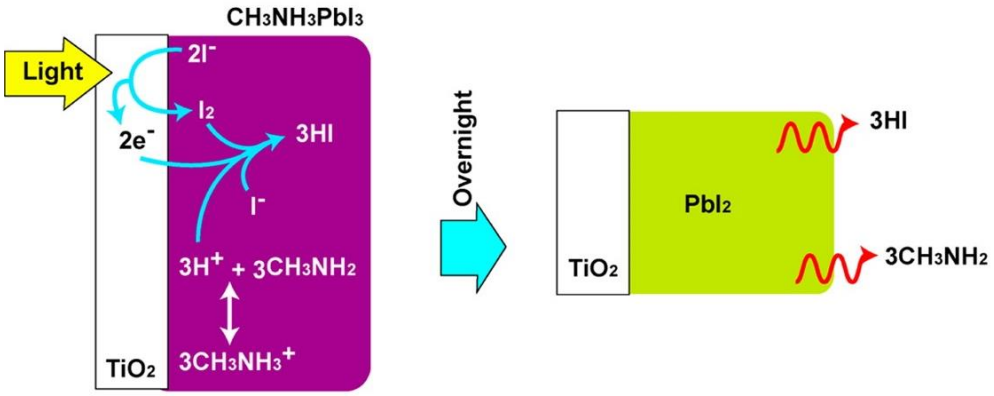

Figure 1.16. Schematic presentation of $MAPbI_3$ degradation upon light exposure at *meso*-TiO_2 interface. Reprinted from [77] Copyright 2014, ACS.

1.4.3. TEMPERATURE EFFECT ON PEROVSKITE

The perovskite absorber is mostly deposited in form of a solution. To remove the solvents and to initialize crystal formation, heat treatment is required. Grätzel *et al.* systematically studied the required annealing time for the formation of $MAPbI_3$ crystals [79]. They reported crystal conversion time of 3, 0.75 and 0.25 h at 80, 100 and 150 °C, respectively. At temperatures higher than 150 °C the conversion to perovskite was almost instantaneous and even at temperatures above 200 °C the colour of the material changed to yellow, which is the indication of PbI_2 formation. Samples annealed at 80 °C to 150 °C showed UV-vis absorption spectra quite similar to the spectrum reported for $MAPbI_3$ [54]. The highest absorbance behaviour was found for the sample annealed at 100 °C. Further increasing of the conversion temperatures resulted in lower absorbance along with a new absorption peak at 500 nm due to the formation of PbI_2. Finally, for annealed samples at 200 °C the spectra resemble to PbI_2 and no similarity to $MAPbI_3$ absorption characteristics -**Figure 1.17**.

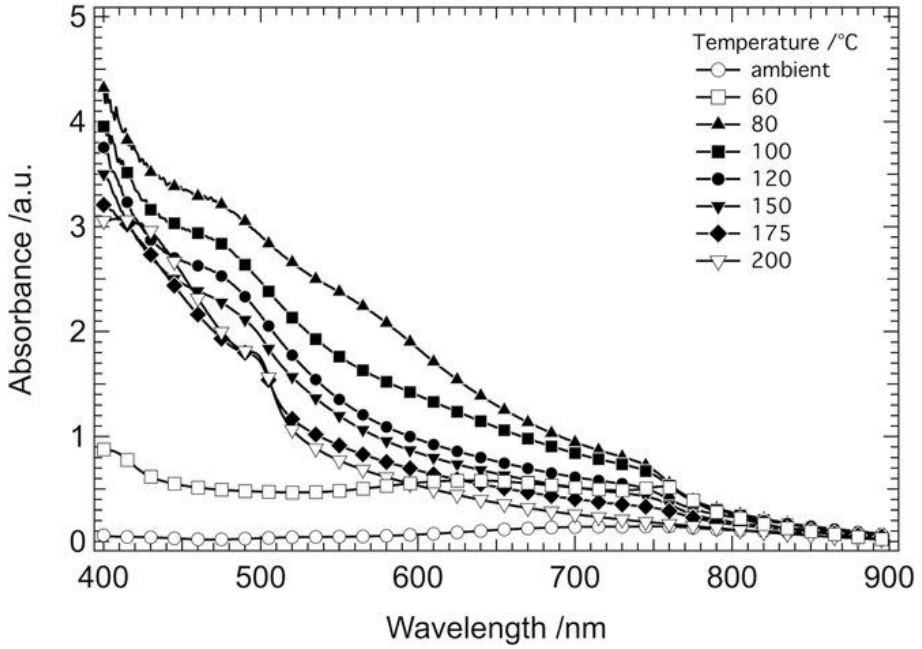

Figure 1.17. UV-vis absorption spectra for mesoporous TiO_2 films with $MAPbI_3$ perovskite annealed at various temperatures. Reprinted from [79], Copyright 2014 WILEY-VCH.

Reaction 1.22 describes the decomposition pathway of $MAPbI_3$ at a temperature range of 100 to 140 °C [80].

$$CH_3NH_3PbI_3 \xrightarrow{\Delta} PbI_2 + CH_3NH_2 + HI \qquad 1.22$$

To achieve better thermal stability for perovskite absorber, the MA cation may be replaced by FA. Song and co-workers studied the thermal stability of $FAPbI_3$ and $MAPbI_3$ with thermogravimetric (TG) analysis [81]. The authors associated the better thermal conductivity of FA based crystals due to enhanced bonding between FA cations and iodide ions. However, at room temperature, the crystal structure of $FAPbI_3$ tends to be in δ-phase (yellow). Although the α-phase (black) can be achieved by sintering heat treatment, the crystal tends to return to its δ-phase. This transition is even faster when the crystals are in contact with humidity [82]. Therefore, to avoid this phase transition, FA / MA mixture can be

used to stabilize the crystallinity of the perovskite and achieve better thermal stability. Another approach for improvement of crystal stability is through introducing small alkali cation such as Cs^+, Rb^+ or K^+, to the FA/MA mixture [83]. In this context, a triple cation perovskite with Cs/MA/FA showed thermal stability up to 130 °C [18].

The thermal stability of perovskite is particularly of most importance for the PSC to be able to pass industry standards. The most common thermal stress tests for PV involves temperature range of -40 to 85 °C. Therefore, perovskite absorber must be stable at these temperature ranges to ensure a long term stable device performance.

1.4.4. THERMAL STABILITY OF HTM LAYER

For n-i-p perovskite solar cells, the thermal stability of the device is mainly limited by the HTM layer. As mentioned, perovskite absorbers are mostly stable up to *ca.* 120 °C. To guarantee 20 years life time for a PSC device, the HTM must be thermally stable up to 85 °C. The most widely used spiro-OMeTAD hole transport layer has a glass transition temperature of 125 °C [84]. However, the additional electrical conductivity dopants to spiro-OMeTAD such as Li-bis(trifluoromethanesulfonyl) imide (Li-TFSI) and tert-butylpyridine (TBP) reduces the thermal stability of this HTM to temperatures lower than 85 °C. Domanski *et al.* concluded that back contacts made of gold can migrate to spiro-OMeTAD layer at temperatures of *ca.* 70 °C [85]. PTAA is the second most used organic HTM layer for n-i-p PSCs. This material showed 500 h thermal stability at 85 °C, under nitrogen atmosphere [17].

Mesquita *et al.* compared the in-situ thermal stability of n-i-p PSCs made with spiro-OMeTAD and PTAA HTMs. They showed that when the devices are heated to 80 °C, the performance of the spiro-based and PTTA-based cells, drop to 36 % and 48 % of their initial values, respectively. However, after letting the cells cool down to room temperature, spiro-based devices showed 21 %

irreversible PCE drop while PTTA-based displayed only 8 % irreversible performance loss [86].

Inorganic Cu-based materials are also good candidates for achieving better thermal stability for HTM layer. In this context, copper (I) thiocyanate (CuSCN) and copper phthalocyanine (CuPc) have been used in PSC devices to reach PCE of *ca.* 20 % [20, 87]. Similar to spiro-OMeTAD, CuSCN can also migrate to Au back contact. Therefore, a few nanometres layer of reduced graphene oxide or poly (methyl methacrylate) (PMMA) polymer is needed as a spacer layer to avoid the mentioned migration. CuSCN with PMMA spacer displayed 15 % efficiency loss after 1000 h of 85 °C, thermal stability test, while with reduced graphene oxide showed only 5 % drop after 1000 h at full sun illumination and 60 °C thermal stress [20]. On the other hand, CuPc based devices show no significant efficiency loss after 1000 h of thermal stress at 85 °C, with no required spacer layer. These devices have also remained stable after 50 thermal cycles of -45 °C to 85 °C [88].

1.5. ENCAPSULATION

Encapsulation is one of the most important steps for any PV device. While some photovoltaic devices are not sensitive to external environmental effects such as humidity and oxygen, for perovskite solar cells, encapsulation can effectively reduce the risk of such degradations. From an industrialization point of view, any sealing method used for PV application must display long-term stability towards temperature, humidity, mechanical stress, and light exposure.

Any given sealant is quantified by its leak rate assessment. There are two major levels for leak rate: gross and fine leak. A leak rate higher than 10^{-5} atm cm^3 s^{-1} is considered as a gross leak, while leak rates lower than *ca.* 5×10^{-8} atm cm^3 s^{-1} is defined as hermetic. Gross leak test is commonly performed by tracing a liquid penetration to the cavity of an encapsulation or bubble test, by observing bubbles through evaporation of a low boiling point indicator fluid at a temperature

of *ca.* 125 °C [89]. A fine leak test is examined by gas tracing techniques with gases such as helium or krypton-85. During fine leak measurement, the under study package is pressurized with the gas tracer for several minutes to force the entry of the tracer gas to the cavity of the device. After, the pressurized device is evacuated inside a vacuum chamber, where a mass spectrometer measures the flow of the tracer gas exiting the cavity of the package. MIL-STD-883 standard is the widely used procedure for leak rate measurement for electrical packaging purposes [90]. A detailed description of this method is included to **Chapter 2**.

For PV applications, the substrates are mostly made of glass, silicon or metal. There are two major bonding methods for the mentioned substrates: direct bonding and intermediate bonding. Direct bonding is obtained by joining two materials without having an intermediate layer between them. This method requires flat, clean and smooth surfaces on the joining materials. The direct bonding can be achieved at elevated annealing temperature during which a chemical bond is achieved between the two materials [91]. In contrast, the method of intermediate layer bonding uses an intermediate layer between two substrates. This intermediate layer can be made of a wide range of materials (*e.g*. metals, polymers, glass frits or composite materials).

Direct bonding can be achieved in both high (*ca.* 600 - 1200 °C) and intermediate temperatures (*ca.* 200 °C - 600 °C). The most common example of direct bonding is silicon and glass bonding. This method yields a hermetic and strong bond but the flatness of the surface plays an important role to achieve a high quality seal. The high temperature nature of the direct bonding makes it unsuitable for temperature sensitive devices. In contrast, intermediate temperature direct bonding requires pre-treatment of substrates such as plasma activation or involves ultra-high vacuum (*ca.* 10^{-10} mbar) to decrease the bonding temperature range to 200 °C - 400 °C [92]. The major disadvantage of this method is the requirement of expensive and complex technologies in order to achieve a lower temperature sealing.

Another common direct bonding is anodic bonding, which uses high DC voltage at intermediate temperatures. For instance, silicon can be bonded to alkali-containing glasses through applying 400 V – 1000 V at a hot plate (300 °C - 450 °C). The covalent bond formed through electrochemical reaction of silicon and glass produces a strong and hermetic seal [93].

Intermediate layer bonding can be categorized into two groups: electrically conductive and insulating interlayers. Common metallic interlayer methods are eutectic and solder bonding. Typically, these methods produce excellent hermeticity with high joint strength at medium to low temperatures but their application is limited to conductive joins due to the nature of the bonding materials. In contrast, insulating interlayer bonding techniques such as glass frit and adhesive bonding are suitable for insulating join applications.

In adhesive bonding, interlayers made of organic or inorganic materials are used for sealing. The adhesive bonding can be used to bond two different materials regardless of their coefficient of thermal expansion (CTE) difference. Adhesive bonding is quite cheap compared to other methods and the sealing temperature is low. Nevertheless, adhesive bonding is suitable for applications where hermeticity is not required since the bonding materials are long-term unstable and their bonding strength is relatively low. The most common adhesives used are made of photoresist, polyimide (PI), benzocyclobutene (BCB), and ionomers [94].

Ultrasonic bonding is a macroscale technique that can produce mechanical joining and fastening of both polymer and metal intermediate layers. This method yields a fast and low temperature bonding with high joint strength. Ultrasonic bonding uses ultrasonic energy and heat for the softening of the intermediate bonding layer. For the case of metal intermediate layer, the ultrasonic energy causes plastic deformation of metal layers which under compression diffusion of these layers generates the bonding. For example, glass and silicon ultrasonic bonding with indium (In) and gold (Au) can be achieved with bonding pressure

of *ca.* 15 MPa, power of *ca.* 25 W and vibration amplitude of *ca.* 1.5 µm. Localized heating of bonding material *via* ultrasonic energy is the advantage of this method which makes it suitable for temperature sensitive devices [95].

Glass frit bonding is another method of insulating bonding. However, in cases that a conductive join is required, conductive materials can be added to the bonding frit. Glass frits are commonly produced in a form of pastes, which mainly consist of glass materials mixed with solvents, binders, and fillers. Depending on the application the CTE of the sealant can be tailored to values close to the substrates, by mixing the paste with different additives [96].

1.5.1. ENCAPSULATION METHODS FOR PSCS

The encapsulation of PSCs can prevent their degradation by protecting them from external ambient factors, such as humidity and oxygen. According to IEC and MIL-STD standards, a long term stable hermetic encapsulation is required for PV application. The hermeticity of the encapsulation is determined with a fine He leak rate test described in MIL-STD-883 [90] and the long-term stability is examined with thermal and humidity freeze cycle test of IEC61646 [97]. The IEC humidity-freeze cycle is perhaps the most critical examination of both cell and the sealant since the cycle includes temperatures range of -40 °C to 85 °C and 85 % relative humidity (RH). Therefore, the sealing must be able to retain its hermeticity after this long term stability test and the cell components (*i.e.* perovskite and HTM) also should be able to withstand these conditions.

The encapsulation methods used for PSCs can be divided into two categories: thin film (*i.e.* on top of the active area) and edge seal (*i.e.* around the active area) encapsulation. The most common thin film encapsulation method consists in the application of hydrophobic films above the cell to protect the device from humidity and oxygen. The mentioned thin film should have a coefficient of thermal expansion (CTE) close to the components of the cell, to avoid possible damage to the cell during the thermal cycle tests [98]. The edge seal method uses

a perimeter sealing material around the cell and a cover substrate, the sealant bonds the substrate of the cell with the cover substrate [99]. **Table 1.1** summarises the encapsulated techniques reported in the literature.

In addition to encapsulation, other efforts such as applying inorganic ZnO and NiO_x as charge transport layers in device fabrication can improve the cell stability in the ambient conditions (10 % PCE loss after 60 days at 30-50 % RH, 25 °C) of cell [100]. HTM-free fully printable with carbon back contact [19] or incorporation of carbon single-walled nanotube [101] in fabrication can increase the moisture stability of PSCs, however, these approaches should be complemented by a proper encapsulation method.

Although thin film encapsulation methods are showing relatively good stability, Cheacharoen *et al.* reported that CTE related failures can raise concerns when tested for IEC standard [102]. In contrast, the edge sealing method displayed remarkable stability after thermal cycle, dry heat and damp heat stability, indicating that the 25 years lifetime is achievable [98]. Nevertheless, the edge sealing material should not affect the device performance during the sealing process or under stability aging tests. Epoxy resin sealing materials can affect the performance of the PSC after encapsulation due to the outgassing of the epoxy during thermal or UV curing step [103]. UV illumination can also cause degradation of TiO_2 mesoporous-based PSCs; to avoid this degradation the active area of the cell is typically masked during the UV epoxy cure process [104]. There is a lack of study on the epoxy resin stability tests such as damp heat, humidity, and thermal cycle tests. Therefore, epoxy resin based encapsulation methods are probably not strong candidates for the future of PSCs.

Table 1.1. Summary of reported thin film and edge seal encapsulated perovskite solar cells.

Encapsulation method	Sealant	Long-term stability test	Observations	ref.
Edge seal	Viewbarrier®	N/A	Sealed PSCs retained their initial PCE after 500 h at atmospheric humidity condition.	*105*
Edge seal and thin film	Al_2O_3 buffer layer and epoxy resin	N/A	Sealed cells with buffer layers had 5 % PCE drop after 350 h aging.	*106*
Edge seal	Thermo-plastic polymer	N/A	Sealed devices maintained 80 % of the initial PCE after 500 h under illumination at 45 °C.	*107*
Edge seal	UV cure epoxy	N/A	Sealed devices retained 80 % of their initial PCE after 36 h stability test under illumination at 85 °C.	*108*
Edge seal and thin film	SiO_2 protective layer and UV cure epoxy	N/A	20 % decrease in PCE of the sealed cell after 48 h stability test under illumination at 85 °C and 65 % RH.	*103*
Edge seal and thin film	Graphene oxide protective layer and UV cure epoxy	N/A	*ca.* 35 % decrease in PCE of the sealed cell after 48 h stability test under illumination at 85 °C and 65 % RH.	*103*
Edge seal and thin film	SiO_2 protective layer and AB epoxy glue	N/A	40 % decrease in PCE of the sealed cell after 48 h stability test under illumination at 85 °C and 65 % RH.	*103*
Edge seal	2 layers of Kapton polyimide (PI) tape with silicone adhesive	N/A	5 % PCE drop after 30 min water immersing test	*109*

Edge seal	Thermo-plastic (Surlyn)	N/A	58 % PCE decrease after 170 h (dark, 30 % RH).	*104*
Edge seal	UV cure glue	N/A	21 % PCE decrease after 170 h (dark, 30 % RH).	*104*
Edge seal	Xenon light cure glue	N/A	21 % PCE decrease after 170 h (dark, 30 % RH).	*104*
Edge seal	UV cure epoxy (selective UV illumination bonding)	N/A	15 % PCE drop during the encapsulation procedure and 25 % performance loss after 70 day at 30 °C and 50 % RH	*110*
Edge seal	Kapton PI adhesive (on active area), Xenon light cure glue edge seal and UV cure epoxy secondary (glass-glass) edge seal	N/A	No evident PCE decrease after 170 h (dark, 30 % RH), 22 % PCE drop after 102 h of stability test at 50 °C and 95 % RH and *ca.* 45 % PCE loss after 240 h of thermal stability at 85 °C, which is mainly due to the damage on the HTM (spiro-OMeTAD) of the cell other than the failure of the encapsulation.	*104*
Edge seal	UV cure adhesive	N/A	Encapsulated cells maintained 80 % of their initial PCE after 14 days of stability test aof 40 % RH at room temperature.	*111*
Thin film	UV cure fluoropolymer	N/A	Front and back coated fluoropolymer thin film encapsulated PSCs showed only 5 % PCE decrease after 90 days real outdoor stability test.	*112*
Thin film	Al_2O_3 and pV3D3 (poly (1,3,5-trimethyl-1,3,5-trivinyl cyclotrisiloxane)	N/A	Thin film protected PSCs displayed only 3 % loss in PCE after 300 h stability test of 50 % RH at 50 °C.	*113*
Thin film	Amorphous SiO_2	N/A	Devices showed only 3 % PCE drop after 1000 h at 25 °C and 10 % RH.	*114*

Thin film	Adamantane	N/A	Encapsulated PSC maintained 70 % of its initial PCE after 24 h stability test of 85 % RH at dark.	*115*
Edge seal	Polyurethane (PU) film	N/A	Encapsulated HTM-free devices retained their performance after 325 h at 85 °C. Real outdoor stability test of 2100 h showed only 2 % PCE loss.	*116*
Edge seal	Thermo-plastic (Surlyn) and secondary (glass-glass) edge seal of butyl rubber	200 thermal cycle (IEC standard)	Five sealed devices were subjected to 200 thermal cycles of -40 °C to 85 °C. Only 1 cell showed reasonable stability by maintaining 90 % of its initial PCE.	*102*
Edge seal	Thermo-plastic (ethylene vinyl acetate) and secondary (glass-glass) edge seal of butyl rubber	200 thermal cycle (IEC standard)	EVA (ethylene vinyl acetate) sealed devices retained 90 % of their performance after 200 thermal cycles of -40 °C to 85 °C.	*102*
Edge seal	Polyolefin “ENLIGHT” and secondary (glass-glass) edge seal of butyl rubber	1000 h dry heat (IEC standard)	Sealed PSCs retained 97 % of their initial PCE after 1000 h of aging test at 85 °C and 25 % RH.	*98*
Edge seal	Polyolefin “ENLIGHT” and secondary (glass-glass) edge seal of butyl rubber	1000 h damp heat (IEC standard)	Sealed PSCs retained 99 % of their initial PCE after 1000 h of aging test at 85 °C and 85 % RH.	*98*

Thermo-plastic sealing with bonding temperatures between 100 °C to 140 °C, used with thermally stable PSCs, are so far the strongest options for encapsulation. Among this group, Surlyn is probably the least appropriate material showing poor stability after cycle tests [102, 104]. EVA sealed PSCs showed perovskite degradation to PbI_2 after 20 h accelerated aging test at 120 °C and 100 % RH, which is likely to be caused by the transformation of EVA to acetic acid and reaction with perovskite [98]. The most highlighted work is by Cheacharoen *et al.*, who used polyolefin "ENLIGHT" and secondary (glass-glass) edge seal of butyl rubber. The sealed PSCs showed superior stability after 1000 h dry (25 % RH) and damp (85 % RH) heat test at 85 °C with negligible performance loss [102]. The only disadvantage of the mentioned encapsulation method is the relatively large secondary edge seal, which plays a key role in the stability and cannot be used in smaller dimensions.

A desired encapsulation method for perovskite solar cell application should be:

- *Hermetic*, to avoid humidity and oxygen induced instability issues of the cell;
- *Long-term stable*, to ensure a minimum 20 year lifetime of the PV device;
- *Compatible to the components of the cell,* to avoid any potential damage/degradation of the layer during the encapsulation process;
- *Adoptable to fabrication route of the cell*, to be easily integrated into the industrial production;
- *Scalable,* to ensure laboratory to commercial production transition.

Glass frit encapsulation method is one of the most promising options to fit all the above requirements.

Glass frit encapsulation

Glass frit encapsulation is one of the most promising technologies to achieve hermetic sealing [117]. Glass frits are generally produced in a form of glass pastes that are a mixture of glass powder (grain size of < 15 µm), solvents, binders, and

fillers; the latter can be tailored to match the final thermal coefficient of expansion (CTE) of the frit to various substrates (*e.g.* glass, metal, semiconductors)[118]. To reach high quality bonding, the CTE of the sealing glass frit and the substrates should be close to each other. The glass frit bonding includes the following steps: (i) glass frit deposition on the substrate(s) (commonly, through screen-printing); (ii) thermal treatment (pre-firing / sintering) of the paste to remove the volatile additives and reach a sintered bonding layer; (ii) bonding (sealing) process. The bonding is formed when the intermediate frit layer is heated to its sealing / bonding temperature. Various compositions of the glass frit offer wide range of sealing temperatures and CTEs.

The conventional glass frit bonding process is through thermo-compressive method in which the bonding is formed by application of pressure and temperature [119]. Generally, the sealing temperature of glass frits is above 380 °C and to reach the bonding through thermo-compressive method, the substrates should be held at the sealing temperature for several minutes inside a furnace. Therefore, thermo-compressive method is limited to encapsulation of electrical devices that can withstand temperature up to the sealing condition of the frit. Alternatively, the bonding process can be achieved through local melting of the glass frit *via* laser radiation. Laser-assisted bonding uses a laser beam to locally heat, melt, and join substrates. The only limitation of this process is that at least one of the substrates should be transparent at the wavelength of the laser. This method can be used for bonding of various intermediate layers such as glass frits, metals, and polymers. Laser-assisted technique was previously reported for wide range of substrates as well as bonding materials including borosilicate glass (Pyrex) to Si bonding with Al and Au [120], metal layers of Cr, Ta, Ti, and Au to seal borosilicate glasses [121], and even direct (with no intermediate layer) welding of Pyrex glass to Si [122]. Moreover, organic adhesives such as benzocyclobutene (BCB) are reported to weld Si to glass using a laser-assisted process [123-125]. Laser-assisted glass frit bonding of glass substrates is being investigated by several authors [126-133]; **Table 1.2** illustrates a summary of these reports until 2016.

Table 1.2. Summary of previously reported laser-assisted glass-glass sealing.

Substrates / CTE × 10^{-6} [K^{-1}]	**Laser wavelength [nm]**	**Process temperature [°C]**	**Bonding velocity [mm s^{-1}]**	**Device size [mm^2]**	**Ref.**
Borosilicate / 3.2	810	25	20 mm·s^{-1}	32 x 32	*127*
Soda-lime / 9	810	100 – 200	2 mm·s^{-1}	32 x 32	*127, 132*
Soda-lime / 9	808	25 – 100	20 mm·s^{-1}	Not closed area	*131*
Soda-lime / 9	1070	330	40	18.5 x 8.5	*128*
Soda-lime / 9	1070	390	40	140 x 13	*133*

Process temperature indicates an external heating source which is usually added to the laser-assisted method for bonding of glass substrates to minimize thermal shocks during the laser irradiation (*i.e.* crack, delamination, *etc.*). As shown in **Table 1.2**, glasses with lower CTE can be bonded at room temperature, while high CTE substrates can be joined at higher temperatures (> 100 °C). Moreover, the process temperatures are higher as the size of the device increases. Soda-lime glasses are the most inexpensive glass substrates in this topic and therefore more desirable for large-scale productions. The focus of research is mainly on low temperature sealing of large area devices constructed with low-cost materials.

1.6. SCOPE OF THE THESIS

In the state-of-the-art of the perovskite photovoltaics, the need for protecting the active components of the cell from exposure to the ambient is emerging for further commercialization of this technology. Glass-glass encapsulation of the PSCs by using glass frit sealants ensures the most hermetic and robust protection which is capable of passing harsh damp heat, humidity-freeze, and helium leakage standard tests for photovoltaics. However, the conventional process temperature for encapsulation with glass frit is typically above 380 °C and therefore not compatible to be applied to encapsulate perovskite solar cells. Glass frit encapsulation at temperatures below the decomposition point of the PSCs materials was an elusive objective, which was successfully overcome in this thesis using laser-assisted glass frit bonding.

This thesis aims at developing a laser-assisted glass frit encapsulation at process temperature lower than these two temperature limits (100 °C and 85 °C) with the objective to achieve a hermetic encapsulation capable of passing IEC and MIL-STD standard tests for PVs.

The potential of the developed glass sealing technology for glass encapsulation of the PSCs was demonstrated for PSC devices of two structural types: HTM-

free and mesoporous n-i-p. HTM-free structure is thermally stability up to *ca.* 100 °C, while n-i-p devices made with PTAA hole transport material, are reported to be thermally stable up to *ca.* 85 °C. Both of these two device structures have a potential to pass the IEC standard test of 85 °C, thermal stress test. The main reason to exclude spiro-OMeTAD as HTM layer at present thesis, was its thermal instability at temperatures higher than 65 °C.

Chapter 1 described the state of the art and background for perovskite solar cells and their encapsulation methods.

In **Chapter 2**, the experimental study and optimization of glass-to-glass encapsulation are summarized. This chapter includes the evolution of the laser-assisted sealing technique to achieve the lowest process temperature. The outcomes of this chapter would be used to encapsulate PSCs.

Chapter 3 discusses the fabrication of HTM-free perovskite solar cells. The laser-assisted sealed devices were tested with several industry-standard tests and in-house humidity stability tests to ensure the robustness of the developed encapsulation.

In **Chapter 4**, the lowest process temperature laser-assisted sealing method was used to glass encapsulate HTM-based (mesoporous n-i-p) perovskite solar cells. Similar to HTM-free perovskite solar cells, these devices were also subjected to external environmental stability tests.

Finally, **Chapter 5** reviews the findings and conclusions of the present thesis and suggests a future pathway for the encapsulation of PSCs.

The findings of this study are expect to drive the successful commercialization of perovskite solar cells for PV applications.

1.7. REFERENCES

1. Masson-Delmotte, V. P. Zhai, H. O. Pörtner, D. Roberts, J. Skea*, et al.*, *Global warming of 1.5°C.* , Intergovernmental Panel on Climate Change, 2018.
2. IEA, *Key world energy statistics* INTERNATIONAL ENERGY AGENCY, 2019.
3. IRENA, *Climate change and renewable energy* International Renewable Energy Agency, 2019.
4. IRENA, *Future of solar photovoltaic* International Renewable Energy Agency, 2019.
5. S. Kalogirou, *Solar energy engineering : processes and systems*, Academic Press, Boston, 2009.
6. S. A. Kalogirou, *Progress in Energy and Combustion Science*, 2004, **30**, 231-95.
7. M. H. Shubbak, *Renewable and Sustainable Energy Reviews*, 2019, **115**, 109383.
8. P. Beiter and T. Tian, *2015 Renewable Energy Data Book*, National Renewable Energy Lab. (NREL), 2015.
9. H. Yoon, J. E. Granata, P. Hebert, R. R. King, C. M. Fetzer*, et al.*, *Progress in Photovoltaics: Research and Applications*, 2005, **13**, 133-9.
10. C. Molang, W. Yongzhen, C. Han, Y. Xudong, Q. Yinghuai*, et al.*, *Advanced Science*, 2017, **4**, 1600269.
11. NREl, https://www.nrel.gov/pv/assets/pdfs/best-reserch-cell-efficiencies.pdf Accessed on: 2019/12/23, 2019.
12. S. H. Antonio Luque, *Handbook of Photovoltaic Science and Engineering*, second edn., 2003.
13. D. B. Mitzi, *Chemistry of Materials*, 1996, **8**, 791-800.
14. D. Weber, *Zeitschrift fur Naturforschung - Section B Journal of Chemical Sciences*, 1978, **33**, 1443-5.

15. C. C. Stoumpos and M. G. Kanatzidis, *Advanced Materials*, 2016, **28**, 5778-93.
16. M. A. Green, A. Ho-Baillie and H. J. Snaith, *Nature Photonics*, 2014, **8**, 506-14.
17. M. Saliba, T. Matsui, K. Domanski, J.-Y. Seo, A. Ummadisingu*, et al.*, *Science*, 2016.
18. M. Saliba, T. Matsui, J.-Y. Seo, K. Domanski, J.-P. Correa-Baena*, et al.*, *Energy Environ. Sci.*, 2016, **9**, 1989-97.
19. A. Mei, X. Li, L. Liu, Z. Ku, T. Liu*, et al.*, *Science*, 2014, **345**, 295-8.
20. N. Arora, M. I. Dar, A. Hinderhofer, N. Pellet, F. Schreiber*, et al.*, *Science*, 2017, **358**, 768-71.
21. H. S. Kim, C. R. Lee, J. H. Im, K. B. Lee, T. Moehl*, et al.*, *Sci Rep*, 2012, **2**, 591.
22. F. Hao, C. C. Stoumpos, D. H. Cao, R. P. H. Chang and M. G. Kanatzidis, *Nature Photonics*, 2014, **8**, 489-94.
23. J. H. Noh, S. H. Im, J. H. Heo, T. N. Mandal and S. I. Seok, *Nano Letters*, 2013, **13**, 1764-9.
24. A. Kojima, K. Teshima, Y. Shirai and T. Miyasaka, *Journal of the American Chemical Society*, 2009, **131**, 6050-1.
25. I. Mesquita, L. Andrade and A. Mendes, *Renewable and Sustainable Energy Reviews*, 2018, **82**, 2471-89.
26. Y. Rong, Y. Hu, A. Mei, H. Tan, M. I. Saidaminov*, et al.*, *Science*, 2018, **361**, eaat8235.
27. L. Etgar, P. Gao, Z. Xue, Q. Peng, A. K. Chandiran*, et al.*, *Journal of the American Chemical Society*, 2012, **134**, 17396-9.
28. G. Xing, N. Mathews, S. Sun, S. S. Lim, Y. M. Lam*, et al.*, *Science*, 2013, **342**, 344-7.
29. A. Marchioro, J. Teuscher, D. Friedrich, M. Kunst, R. Van De Krol*, et al.*, *Nature Photonics*, 2014, **8**, 250-5.
30. N. Ahn, D.-Y. Son, I.-H. Jang, S. M. Kang, M. Choi*, et al.*, *Journal of the American Chemical Society*, 2015, **137**, 8696-9.

31. N. J. Jeon, J. H. Noh, Y. C. Kim, W. S. Yang, S. Ryu*, et al.*, *Nat Mater*, 2014, **13**, 897-903.
32. D. Lee, Y.-S. Jung, Y.-J. Heo, S. Lee, K. Hwang*, et al.*, *ACS Applied Materials & Interfaces*, 2018, **10**, 16133-9.
33. K. Hwang, Y.-S. Jung, Y.-J. Heo, F. H. Scholes, S. E. Watkins*, et al.*, *Advanced Materials*, 2015, **27**, 1241-7.
34. M. Liu, M. B. Johnston and H. J. Snaith, *Nature*, 2013, **501**, 395-8.
35. M. M. Tavakoli, L. Gu, Y. Gao, C. Reckmeier, J. He*, et al.*, *Sci Rep*, 2015, **5**, 14083.
36. H. Huang, J. Shi, L. Zhu, D. Li, Y. Luo*, et al.*, *Nano Energy*, 2016, **27**, 352-8.
37. S. Bag, J. R. Deneault and M. F. Durstock, *Advanced Energy Materials*, 2017, **7**, 1701151.
38. K. Cao, Z. Zuo, J. Cui, Y. Shen, T. Moehl*, et al.*, *Nano Energy*, 2015, **17**, 171-9.
39. L. Zhang, T. Liu, L. Liu, M. Hu, Y. Yang*, et al.*, *Journal of Materials Chemistry A*, 2015, **3**, 9165-70.
40. Z. Wei, H. Chen, K. Yan and S. Yang, *Angew Chem Int Ed Engl*, 2014, **126**, 13455-9.
41. P. Li, C. Liang, B. Bao, Y. Li, X. Hu*, et al.*, *Nano Energy*, 2018, **46**, 203-11.
42. E. H. Anaraki, A. Kermanpur, L. Steier, K. Domanski, T. Matsui*, et al.*, *Energy & Environmental Science*, 2016, **9**, 3128-34.
43. K. Yao, F. Li, Q. He, X. Wang, Y. Jiang*, et al.*, *Nano Energy*, 2017, **40**, 155-62.
44. W. Chen, Y. Wu, Y. Yue, J. Liu, W. Zhang*, et al.*, *Science*, 2015, **350**, 944-8.
45. K. A. Bush, A. F. Palmstrom, Z. J. Yu, M. Boccard, R. Cheacharoen*, et al.*, *Nature Energy*, 2017, **2**, 17009.
46. H. S. Jung and N. G. Park, *Small*, 2015, **11**, 10-25.

47. B. Parida, A. Singh, M. Oh, M. Jeon, J.-W. Kang*, et al.*, *Materials Today Communications*, 2019, **18**, 176-83.
48. W. S. Yang, B.-W. Park, E. H. Jung, N. J. Jeon, Y. C. Kim*, et al.*, *Science*, 2017, **356**, 1376-9.
49. Q. Jiang, L. Zhang, H. Wang, X. Yang, J. Meng*, et al.*, *Nature Energy*, 2016, **2**, 16177.
50. R. T. Ginting, E.-S. Jung, M.-K. Jeon, W.-Y. Jin, M. Song*, et al.*, *Nano Energy*, 2016, **27**, 569-76.
51. J. Xiao, J. Shi, D. Li and Q. Meng, *Science China Chemistry*, 2015, **58**, 221-38.
52. T. Leijtens, G. E. Eperon, S. Pathak, A. Abate, M. M. Lee*, et al.*, *Nat Commun*, 2013, **4**, 2885.
53. N. Elumalai, M. Mahmud, D. Wang and A. Uddin, *Energies*, 2016, **9**, 861.
54. M. M. Lee, J. Teuscher, T. Miyasaka, T. N. Murakami and H. J. Snaith, *Science*, 2012, **338**, 643-7.
55. P. Tonui, S. O. Oseni, G. Sharma, Q. Yan and G. Tessema Mola, *Renewable and Sustainable Energy Reviews*, 2018, **91**, 1025-44.
56. J. Chen, X. Cai, D. Yang, D. Song, J. Wang*, et al.*, *Journal of Power Sources*, 2017, **355**, 98-133.
57. V. Stockhausen, I. Mesquita, L. Andrade and A. Mendes, *IEEE Journal of Photovoltaics*, 2018, **8**, 1029-38.
58. a. J B Mooney and S. B. Radding, *Annual Review of Materials Science*, 1982, **12**, 81-101.
59. T. V. Gavrilović, D. J. Jovanović and M. D. Dramićanin, in *Nanomaterials for Green Energy*, eds. B. A. Bhanvase, V. B. Pawade, S. J. Dhoble, S. H. Sonawane and M. Ashokkumar, Elsevier, 2018, pp. 55-81.
60. N.-T. Nguyen, in *Micromixers (Second Edition)*, ed. N.-T. Nguyen, William Andrew Publishing, Oxford, 2012, pp. 113-61.
61. N. Sahu, B. Parija and S. Panigrahi, *Indian Journal of Physics*, 2009, **83**, 493-502.

62. R. J. Martín-Palma and A. Lakhtakia, in *Engineered Biomimicry*, eds. A. Lakhtakia and R. J. Martín-Palma, Elsevier, Boston, 2013, pp. 383-98.
63. D. Novaković, N. Kašiković, G. Vladić and M. Pál, in *Printing on Polymers*, eds. J. Izdebska and S. Thomas, William Andrew Publishing, 2016, pp. 247-61.
64. S.-I. Park, Y.-J. Quan, S.-H. Kim, H. Kim, S. Kim*, et al.*, *International Journal of Precision Engineering and Manufacturing-Green Technology*, 2016, **3**, 397-421.
65. J. Sitanurak, N. Fukana, T. Wongpakdee, Y. Thepchuay, N. Ratanawimarnwong*, et al.*, *Talanta*, 2019, **205**, 120113.
66. M. Saliba, J.-P. Correa-Baena, C. M. Wolff, M. Stolterfoht, N. Phung*, et al.*, *Chemistry of Materials*, 2018, **30**, 4193-201.
67. M. Duan, Y. Hu, A. Mei, Y. Rong and H. Han, *Materials Today Energy*, 2018, **7**, 221-31.
68. T. Liu, Y. Rong, Y. Xiong, A. Mei, Y. Hu*, et al.*, *RSC Advances*, 2017, **7**, 10118-23.
69. Z. Ku, Y. Rong, M. Xu, T. Liu and H. Han, *Sci Rep*, 2013, **3**.
70. B. Salhi, Y. S. Wudil, M. K. Hossain, A. Al-Ahmed and F. A. Al-Sulaiman, *Renewable and Sustainable Energy Reviews*, 2018, **90**, 210-22.
71. D. Bryant, N. Aristidou, S. Pont, I. Sanchez-Molina, T. Chotchunangatchaval*, et al.*, *Energy & Environmental Science*, 2016, **9**, 1655-60.
72. J. You, Y. Yang, Z. Hong, T.-B. Song, L. Meng*, et al.*, *Applied Physics Letters*, 2014, **105**, 183902.
73. A. M. A. Leguy, Y. Hu, M. Campoy-Quiles, M. I. Alonso, O. J. Weber*, et al.*, *Chemistry of Materials*, 2015, **27**, 3397-407.
74. F. Hao, C. C. Stoumpos, Z. Liu, R. P. H. Chang and M. G. Kanatzidis, *Journal of the American Chemical Society*, 2014, **136**, 16411-9.
75. G. Niu, X. Guo and L. Wang, *Journal of Materials Chemistry A*, 2015, **3**, 8970-80.

76. A. Fujishima, T. N. Rao and D. A. Tryk, *Journal of Photochemistry and Photobiology C: Photochemistry Reviews*, 2000, **1**, 1-21.
77. S. Ito, S. Tanaka, K. Manabe and H. Nishino, *The Journal of Physical Chemistry C*, 2014, **118**, 16995-7000.
78. S. K. Pathak, A. Abate, T. Leijtens, D. J. Hollman, J. Teuscher*, et al.*, *Advanced Energy Materials*, 2014, **4**, 1301667.
79. A. Dualeh, N. Tétreault, T. Moehl, P. Gao, M. K. Nazeeruddin*, et al.*, *Advanced Functional Materials*, 2014, **24**, 3250-8.
80. T. Supasai, N. Rujisamphan, K. Ullrich, A. Chemseddine and T. Dittrich, *Applied Physics Letters*, 2013, **103**, 183906.
81. Y. Fu, H. Zhu, A. W. Schrader, D. Liang, Q. Ding*, et al.*, *Nano Letters*, 2016, **16**, 1000-8.
82. T. M. Koh, K. Fu, Y. Fang, S. Chen, T. C. Sum*, et al.*, *Journal of Physical Chemistry C*, 2014, **118**, 16458-62.
83. Z. Zhao, F. Gu, H. Rao, S. Ye, Z. Liu*, et al.*, *Advanced Energy Materials*, 2019, **9**, 1802671.
84. Y. Fang, X. Wang, Q. Wang, J. Huang and T. Wu, *physica status solidi (a)*, 2014, **211**, 2809-16.
85. K. Domanski, J.-P. Correa-Baena, N. Mine, M. K. Nazeeruddin, A. Abate*, et al.*, *ACS Nano*, 2016, **10**, 6306-14.
86. I. Mesquita, L. Andrade and A. Mendes, *ChemSusChem*, 2019, **12**, 2186-94.
87. T. Duong, J. Peng, D. Walter, J. Xiang, H. Shen*, et al.*, *ACS Energy Letters*, 2018, **3**, 2441-8.
88. Y. C. Kim, T. Y. Yang, N. J. Jeon, J. Im, S. Jang*, et al.*, *Energy & Environmental Science*, 2017, **10**, 2109-16.
89. Y. Tao and A. P. Malshe, *Microelectronics Reliability*, 2005, **45**, 559-66.
90. MIL-STD-883H, United States Department of Defense, 2010.
91. H. Kuisma, in *Handbook of Silicon Based MEMS Materials and Technologies*, eds. V. Lindroos, M. Tilli, A. Lehto and T. Motooka, William Andrew Publishing, Boston, 2010, pp. 501-4.

92. K. Henttinena and T. Sunib, in *Handbook of Silicon Based MEMS Materials and Technologies*, eds. V. Lindroos, M. Tilli, A. Lehto and T. Motooka, William Andrew Publishing, Boston, 2010, pp. 505-12.
93. A. Cozma Lapadatu and H. Jakobsen, in *Handbook of Silicon Based MEMS Materials and Technologies*, eds. V. Lindroos, M. Tilli, A. Lehto and T. Motooka, William Andrew Publishing, Boston, 2010, pp. 513-20.
94. C. T. Pan, P. J. Cheng, M. F. Chen and C. K. Yen, *Microelectronics Reliability*, 2005, **45**, 657-63.
95. J. Kim, B. Jeong, M. Chiao and L. Lin, *IEEE Transactions on Advanced Packaging*, 2009, **32**, 461-7.
96. R. Knechtel, in *Handbook of Silicon Based MEMS Materials and Technologies*, eds. V. Lindroos, M. Tilli, A. Lehto and T. Motooka, William Andrew Publishing, Boston, 2010, pp. 521-31.
97. IEC61646, International Electrotechnical Commission, 2008.
98. R. Cheacharoen, C. C. Boyd, G. F. Burkhard, T. Leijtens, J. A. Raiford*, et al.*, *Sustainable Energy & Fuels*, 2018.
99. R. Sastrawan, J. Beier, U. Belledin, S. Hemming, A. Hinsch*, et al.*, *Solar Energy Materials and Solar Cells*, 2006, **90**, 1680-91.
100. J. You, L. Meng, T.-B. Song, T.-F. Guo, Y. Yang*, et al.*, *Nature Nanotechnology*, 2015, **11**, 75.
101. S. N. Habisreutinger, T. Leijtens, G. E. Eperon, S. D. Stranks, R. J. Nicholas*, et al.*, *Nano Letters*, 2014, **14**, 5561-8.
102. R. Cheacharoen, N. Rolston, D. Harwood, K. A. Bush, R. H. Dauskardt*, et al.*, *Energy & Environmental Science*, 2018, **11**, 144-50.
103. Q. Dong, F. Liu, M. K. Wong, H. W. Tam, A. B. Djurišić*, et al.*, *ChemSusChem*, 2016, **9**, 2597-603.
104. F. Matteocci, L. Cinà, E. Lamanna, S. Cacovich, G. Divitini*, et al.*, *Nano Energy*, 2016, **30**, 162-72.
105. H. C. Weerasinghe, Y. Dkhissi, A. D. Scully, R. A. Caruso and Y.-B. Cheng, *Nano Energy*, 2015, **18**, 118-25.

106. S. Guarnera, A. Abate, W. Zhang, J. M. Foster, G. Richardson*, et al.*, *The Journal of Physical Chemistry Letters*, 2015, 432-7.

107. J. Burschka, N. Pellet, S. J. Moon, R. Humphry-Baker, P. Gao*, et al.*, *Nature*, 2013, **499**, 316-9.

108. F. Liu, Q. Dong, M. K. Wong, A. B. Djurišić, A. Ng*, et al.*, *Advanced Energy Materials*, 2016, **6**, 1502206-n/a.

109. B. Li, M. Wang, R. Subair, G. Cao and J. Tian, *Journal of Physical Chemistry C*, 2018, **122**, 25260-7.

110. E. Ramasamy, V. Karthikeyan, K. Rameshkumar and G. Veerappan, *Materials Letters*, 2019, **250**, 51-4.

111. L. Tan, C. Liu, Z. Huang, Y. Zhang, L. Chen*, et al.*, *Organic Electronics*, 2017, **48**, 308-13.

112. F. Bella, G. Griffini, J.-P. Correa-Baena, G. Saracco, M. Grätzel*, et al.*, *Science*, 2016, **354**, 203-6.

113. L. Y. Il, J. N. Joong, K. B. Jun, S. Hyunjeong, Y. Tae-Youl*, et al.*, *Advanced Energy Materials*, 2018, **8**, 1701928.

114. T. Liu, Y. Zhou, Z. Li, L. Zhang, M.-G. Ju*, et al.*, *Advanced Energy Materials*, 2018, **8**, 1800232.

115. J. Idígoras, F. J. Aparicio, L. Contreras-Bernal, S. Ramos-Terrón, M. Alcaire*, et al.*, *ACS Applied Materials & Interfaces*, 2018, **10**, 11587-94.

116. Z. Fu, M. Xu, Y. Sheng, Z. Yan, J. Meng*, et al.*, *Advanced Functional Materials*, 2019, **0**, 1809129.

117. R. Knechtel, M. Wiemer and J. Frömel, *Microsystem Technologies*, 2005, **12**, 468-72.

118. R. Knechtel, *Microsystem Technologies*, 2005, **12**, 63-8.

119. C. Dresbach, A. Krombholz, M. Ebert and J. Bagdahn, *Microsystem Technologies*, 2006, **12**, 473-80.

120. U. M. Mescheder, M. Alavi, K. Hiltmann, C. Lietzau, C. Nachtigall*, et al.*, *Sensors and Actuators A: Physical*, 2002, **97–98**, 422-7.

121. J. Haneveld, P. Tijssen, J. Oonk, M. Olde Riekerink, H. Tigelaar*, et al.*, 2014.

122. M. J. Wild, A. Gillner and R. Poprawe, *Sensors and Actuators A: Physical*, 2001, **93**, 63-9.
123. N. Lorenz, M. D. Smith and D. P. Hand, *Microelectronics Reliability*, 2011, **51**, 2257-62.
124. F. Bardin, S. Kloss, C. Wang, A. J. Moore, A. Jourdain*, et al.*, *Journal of Microelectromechanical Systems*, 2007, **16**, 571-80.
125. Q. Wu, N. Lorenz and D. P. Hand, *Microsystem Technologies*, 2009, **15**, 1051-7.
126. N. Lorenz, S. Millar, M. Desmulliez and D. P. Hand, *Journal of Micromechanics and Microengineering*, 2011, **21**, 045039.
127. S. Logunov, S. Marjanovic and J. Balakrishnan, *Journal of Laser Micro/Nanoengineering*, 2012, **7**, 326-33.
128. F. Ribeiro, J. Maçaira, R. Cruz, J. Gabriel, L. Andrade*, et al.*, *Solar Energy Materials and Solar Cells*, 2012, **96**, 43-9.
129. W. Wang, Y. Xiao, X. Wu and J. Zhang, *Optics & Laser Technology*, 2016, **77**, 111-5.
130. Q. Wu, N. Lorenz, K. M. Cannon and D. P. Hand, *IEEE Transactions on Components and Packaging Technologies*, 2010, **33**, 470-7.
131. M. Schmidt, F. Vollertsen, M. Merklein, H. Kind, E. Gehlen*, et al.*, *Physics Procedia*, 2014, **56**, 673-80.
132. S. L. Logunov and S. Marjanovic, Google Patents, 2010.
133. D. K. Ivanou, R. Santos, J. Maçaira, L. Andrade and A. Mendes, *Solar Energy*, 2016, **135**, 674-81.

CHAPTER 2

DEVELOPMENT AND OPTIMIZATION OF LASER-ASSISTED GLASS FRIT ENCAPSULATION

"Viver não é necessário. Necessário é criar."

Fernando Pessoa

Adapted from peer-reviewed articles

***S. Emami**, J. Martins, L. Andrade, J. Mendes and A. Mendes, Optics and Lasers in Engineering, 2017, 96, 107-16.*

and

***S. Emami**, J. Martins, R. Madureira, D. Hernandez, G. Bernardo, et al., Journal of Physics D: Applied Physics, 2019, 52, 074005.*

2 DEVELOPMENT AND OPTIMIZATION OF LASER-ASSISTED GLASS FRIT ENCAPSULATION

Glass frit encapsulation is widely used for electronic packaging applications. These technologies include: microelectromechanical system (MEMS) [1], organic light emitting diode (OLED) [2] and photovoltaic (PV) [3]. Glass frits are known to have excellent thermal, mechanical and chemical stability [3]. Thus, these sealants are strong candidates for achieving long-term stable encapsulation targets required for perovskite solar cell application.

Glass frit bonding is a thermo-compressive process in which the glass frit intermediate sealant is melted at high temperatures under mechanical force. Since glass frits generally display bonding temperatures of > 380 °C, the thermo-compressive bonding technique surpasses the 120 °C thermal stability of perovskite absorber and 85 °C for HTM layer. However, selective localized laser processing can be applied for achieving glass frit bonding at lower processing temperature range.

Laser processing can be used for applications such as alignment in automated assembly line, holography, analytical technique, medical, printing, heat treatment, among others [4]. In particular, laser beam as a heating source can be used for fast, cheap and reliable material processing. The most common lasers used for material processing include: CO_2, Nd:YAG and fiber lasers [4].

There are four main types of lasers: (i) gas lasers, (ii) solid-state laser, (iii) dye lasers and (iv) free-electron lasers. Lasers are categorized based on their output wavelength. While most of the lasers emit at a single wavelength, there are also lasers which can emit at a range of wavelengths. Lasers can be classified into two operation modes; continuous wave (CW) and pulsed - **Figure 2.1**.

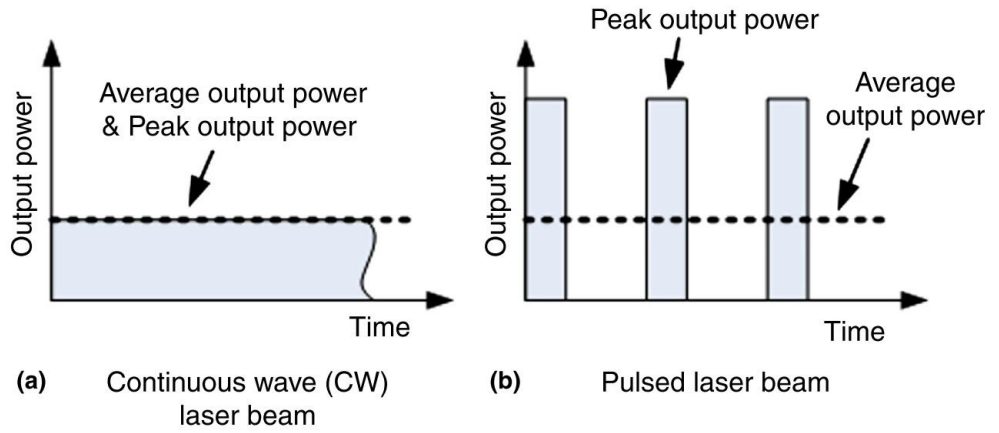

Figure 2.1. Average and peak output power for (**a**) CW and (**b**) pulsed laser. Reprinted from [5], Copyright 2014, Elsevier.

As shown in **Figure 2.1**, continuous wave output provides a stable power and peak output while pulsed lasers display a higher peak power for shorter time.

2.1 INTRODUCTION TO LASER-ASSISTED SEALING

Laser-assisted sealing of glass substrates was first reported by Wu *et al.* in 2010. The authors hermetically sealed Kovar to ceramic for MEMS application. Later, in 2012 the first application of glass frit laser-sealing for solar cells was reported by Ribeiro *et al.* at LEPABE research center [6]. The fundamental behind a laser-assisted sealing is fairly simple; a laser beam is emitted to glass frit (sealant) to melt and join the two substrates. However, there are many parameters involved for achieving a high-quality sealing.

Glass frit bonding is an intermediate bonding method, in which two substrates are bonded by heating the glass frit to its melting/bonding temperature to join the substrates. In this process the most important parameter is the coefficient of thermal expansion (CTE) of the substrates and sealant. A sealing structure configuration includes the substrates and sealant material. To avoid mechanical damage due to the expansion of materials during the thermal treatment, the CTE of the substrates and sealant must be in the same range.

As mentioned in **Chapter 1**, glass frit bonding is conventionally achieved through thermo-compressive technique. There are two parameters that have the most influence on thermo-compressive bonding: bonding temperature and bonding pressure. For example, if the bonding temperature is less than the sealing temperature, the frit stays solid and no bond is formed. Alternatively, for bonding temperatures higher than the recommended sealing temperature, the glass frit starts to flow on the substrate and the join can have voids since there are some areas free of glass frit. In other cases, when the bonding pressure is not enough, the frit may not wet the other substrate and no bond is formed. Finally, for higher pressures, the frit starts to flow on the substrate, resulting in low quality bonding. In contrast, laser-assisted sealing has the benefit of avoiding possible frit flow on the substrate since the joining takes place locally and frit melting only occurs on the spot that the laser is passing. **Figure 2.2** shows examples of sealing quality for the two methods.

(**a**)

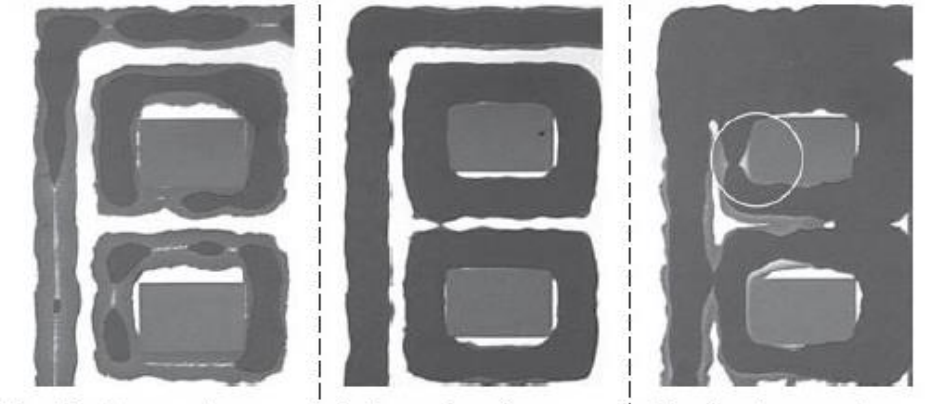

(**b**)

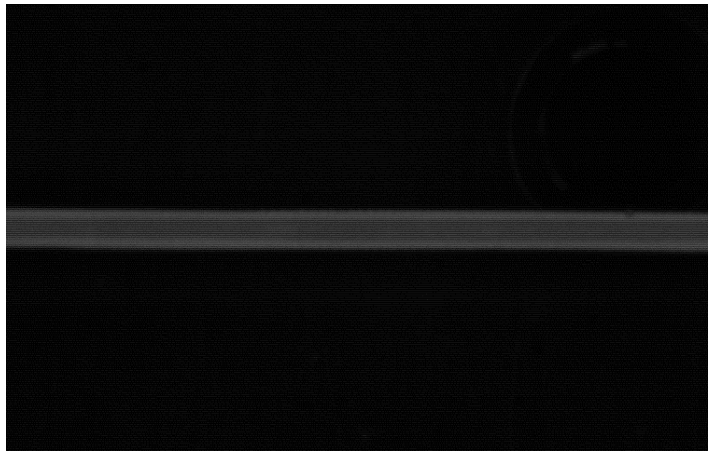

Figure 2.2. Quality of sealing (**a**) thermo-compressive *vs.* (**b**) laser-assisted. Reprinted from [7], Copyright 2012, Wiley.

Laser-assisted sealing technique can be used to avoid submitting the entire package to the sealing temperature. However, since the heat from laser beam melts totally or partially the bonding layer, as it thermally contracts during the solidification process eventually cracks or delamination at the sealing/substrate interface may occur; an external heating source should be added to minimize

the thermal shock between the bonding material and the substrates. The process temperature for laser-assisted bonding is commonly retained at minimum temperatures required to avoid disruptive thermal shocks on the substrates while laser heats the bonding material. Therefore, the entire device can be held at temperatures lower than the sealing/bonding temperature of the sealant while the laser beam locally heats up the bonding layer to its sealing temperature. The process temperature highly depends on the composition of the sealing configuration (*i.e.* substrates and sealant) and their thermal properties.

2.2 LASER-ASSISTED SEALING

The laser-assisted sealing apparatus consists of three main components;

- A laser source;
- A galvanometer scan head for beam movement;
- A heating source, providing the process temperature.

In addition, electrical cable and communication interfaces are required to accomplish the experiment on sealing. The laser source can be a CW or pulsed mode output at a wavelength transparent to glass substrates. For example, CO_2 lasers with emission wavelength at 10.6 µm are not suitable options. This output wavelength is mostly used for engraving of glass substrates since glass absorbs most of the emitted beam at that wavelength.

The glass substrates used for perovskite solar cells are made of soda-lime. The thickness of glass contributes to its thermal properties while the optical properties are quite similar for thickness of 1 mm to 3 mm. **Figure 2.3** shows the transmittance spectrum of a 2 mm soda-lime glass up to 4 µm wavelength. Glass is mostly opaque at wavelengths lower than 250 nm, while it transmits up to 80 % of the light in the wavelength range of 250 nm to 2750 nm. At higher wavelengths the transmittance drops to *ca.* 30 %.

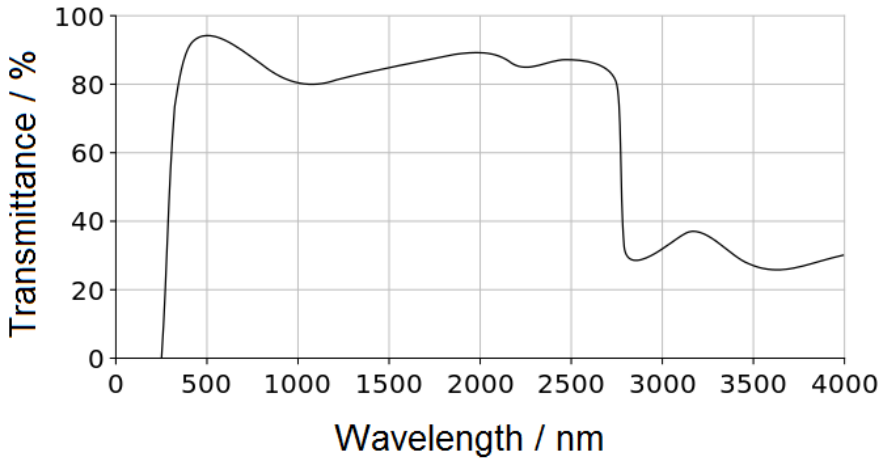

Figure 2.3. Transmittance spectra of 2 mm soda-lime glass. Adapted from [8] Copyright 2020 Wikimedia.

During laser-assisted sealing, the objective is for the laser beam to transmit from the glass substrate and get absorbed at the glass frit. Thus, the output laser beam wavelength suitable for accessing the glass frit material through glass substrates is in the high transmittance wavelength range region of glass. **Table 2.1** shows some selected laser types and their emission wavelength. Among these laser types, CO_2 and CO lasers are at wavelengths higher than 2750 nm, therefore not suitable for sealing glass substrates. Visible range diode lasers such as GaAs and ytterbium-doped fiber lasers are suitable for the wavelength region of glass. Diode lasers are commonly cheap with low and unstable beam power output. On the other hand, fiber lasers are mostly used for industrial applications which require a constant high-power beam output for a time duration of hour scale [9]. Therefore, the most suitable option for laser-assisted glass frit bonding is Y^{3+} doped fiber lasers.

Table 2.1. Example of output laser beam wavelength.

Type	Wavelength / nm
CO_2	10600
CO	5400
Tm^{3+} doped fiber	2080
Y^{3+} doped fiber	1070
Diode GaAs	750 - 870

Another aspect of laser to be considered is output power operation mode. As shown in **Figure 2.1**, CW mode delivers a constant average power while pulsed mode has a high intensity peak power. Both of the mentioned modes can be used for glass frit bonding purposes. However, the cost of CW lasers is generally lower than pulsed lasers. Therefore, CW mode can deliver powerful beam output required for achieving the required heat for bonding of glass frit.

Glass frit encapsulation is an edge sealing method. In the edge seal method, the sealant is deposited around a target area, in a closed geometric shape. Thus, for using a laser beam for reaching the sealant, the beam should be moved around the sealing shape. This can be achieved through various approaches; mechanical or optical or a combination of both. Mechanical beam movement can be achieved by using linear 2D positioning tools. The optical beam movement is through controlling mirrors by a galvanometer. The response time for a mechanical system is much slower than the optical systems. Therefore, for precision fast response laser beam delivery, optical systems are the best option.

The output beam from the optical moving system is then required to be focused by a lens before reaching the workpiece. There are two major types of lens for scanning a laser beam: spherical lens and flat-field scanning lens - **Figure 2.4**.

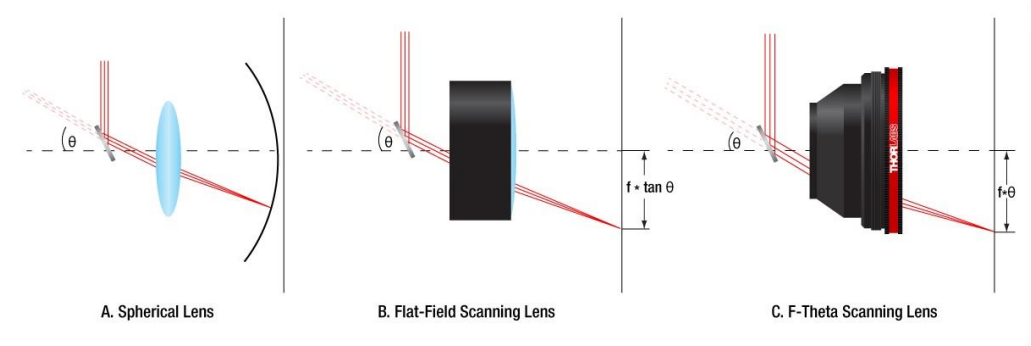

Figure 2.4. Types of lenses for laser beam focus and scanning: (**a**) spherical lens (**b**) and (**c**) flat-field and f-theta scanning lens. Reprinted from [10] Copyright Thorlabs.

The spherical lens produces a curved plan output beam, which is not suitable for high precision scanning. Flat-filed lens, on the other hand, focuses the beam on the workpiece in a flat plane. For flat-field lens - **Figure 2.4b** the position of the focused spot depends on the focal length (*FL*) and tangent of the deflection angle [11]. Lens can be designed to focus the beam based on the focal length and deflection angle; these lenses are called f-theta lens. For precision 2D material processing, f-theta lenses are the most suitable selection.

Laser beam array exiting a laser source are commonly collimated. A collimated beam consists of parallel arrays of beams with minimal divergence. The output collimated laser beam has a Gaussian distribution. The non-ideality of a laser beam compared to the ideal Gaussian behavior is defined by a parameter called M^2 factor. **Figure 2.5** shows a Gaussian distributed beam. The waist of a Gaussian beam (W) is defined at $1/e^2$ = 0.135 times the maximum intensity value.

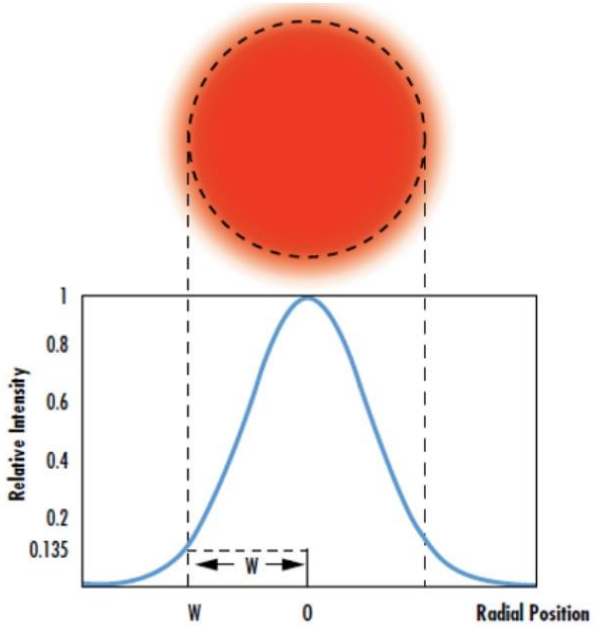

Figure 2.5. Gaussian beam intensity profile. Adapted from [12] Copyright Edmundoptics.

The focused spot diameter of the collimated laser beam exiting from an f-theta lens is calculated from [13]:

$$\text{Spot } \emptyset = C \times \lambda \times FL \times \frac{M^2}{D} \qquad 2.1$$

where, *C* is a constant (for a Gaussian beam *C* =1.27), λ is wavelength, *FL* is focal length and *D* is entrance beam diameter.

In practice, the actual spot size of the laser beam may differ from the nominal mathematically calculated value.

The last component of a laser-assisted sealing apparatus is a heating source. The heating can be simply provided to the process by using a hotplate, or for better thermal gradient uniformity a furnace can be used. **Figure 2.6** shows a scheme of laser-assisted sealing apparatus.

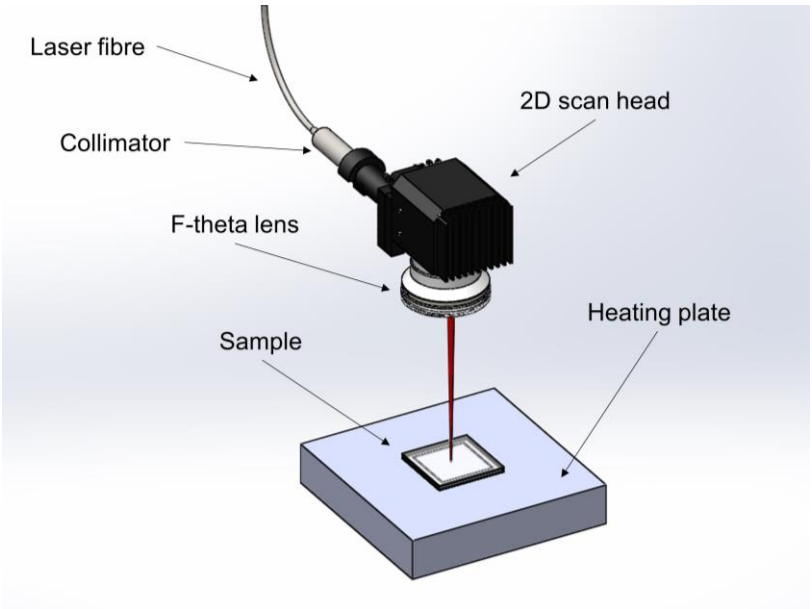

Figure 2.6. Schematic view of laser-assisted sealing apparatus.

As shown in **Figure 2.6**, a laser source provides the beam through a fiber cable delivered to a collimator. The collimated beam is then entering the 2D optical scan head for beam movement. The output beam from the scan head is then focused to the workpiece by an f-theta lens. A hotplate is used as a heating source to provide the process temperature. The laser beam is focused on the sealant (*i.e.* glass frit line) to locally melt and bond the substrates.

2.3 LASER-ASSISTED SEALING APPARATUS

The apparatus shown in **Figure 2.6** has the minimum requirements for performing laser-sealing experiments. In 2010, researchers at LEPABE assembled the first version of the sealing apparatus named "LaserBox" [6]. LaserBox was constructed according to the basic semi-automatic requirements indicated in **Figure 2.6**. Later, in 2014 an automated system was assembled to improve the process; this equipment is named "SealingStation". SealingStation is assembled for automated laser beam alignment. The 2D scan head of this

equipment is mounted on a SCARA (Selective Compliance Assembly Robot Arm) and the heating source used is a furnace with glass cover. In 2019, the SealingStation unit was further modified to operate with 2 scan heads; delivering two laser beams simultaneously. Through this upgrade, the second laser beam is used as a secondary heating source providing extra assistance to the process temperature generated by the furnace.

Table 2.2. Laser-sealing apparatus specification.

Apparatus	**LaserBox**	**SealingStation**	**SealingStation (*upgraded*)**
Laser Source	1070 nm / CW	1070 nm / CW	1070 nm / CW
Maximum laser Power / W	200	200 / 100	200 / 100 / 20
Scan head	2 dimension	2 dimension	(2 dimension) × 2
Lens	f-theta / *FL*= 387 mm	f-theta / *FL*= 494 mm	(f-theta / *FL*= 494 mm) × 2
Heating source	Hot plate	Furnace	Furnace and laser beam
System	Manual	Automatic	Automatic
Timeline	2010	2016	2019

All the developments prior to the year 2016, were made before the present thesis. SealingStation unit upgrade was done during the course of this thesis. The concept of 2 laser beam system was originated by the author. The part design and manufacturing of these upgrades were done by other members of the research team at LEPABE with mechanical engineering background.

As mentioned in **Table 2.2** , there are three available laser sources of 1070 nm continuous wave (CW) output with maximum power of 200, 100 and 20 W at LEPABE. Industrial laser sources are designed to operate at the output power

range of 10 % to 100 % of their maximum output power. Depending on the optical absorbance of the glass frit sealant, a laser beam with a wide range of maximum and minimum output power is desired for performing experiments. For example, dark colored glass frits tend to absorb more than 80 % of the laser beam while light colored frits only absorb 50 % or less.

LaserBox unit was the first system, in which the maximum output power required was initially unknown. Therefore, a 200 W source was purchased to ensure sufficient output power for laser-sealing experiments. It was later concluded that the maximum required laser power to achieve sealing was *ca*. 80 W. Therefore, the SealingStation was equipped with a laser source of 100 W maximum output power. These two laser sources are capable of delivering a minimum output power of 10 W and 20 W, respectively. These minimum thresholds are not suitable for high absorbing dark colored glass frits. Therefore, a new laser source of 20 W was purchased for operating at lower output power ranges.

Therefore, currently there are three laser beam delivery systems mounted on two apparatus; one fixed scan head at LaserBox and 2 moving (attached to SCARA arm) scan heads for SealingStation unit. All three laser sources are available to be used for both units.

The spot size of the laser beam is defined by the f-theta lens focal length. For LaserBox scan head and lens are fixed to produce a focused beam at workpiece. For SealingStation, the SCARA is a 4 axis robotic arm, which enables the user to change the position of the attached scan heads in x,y and z directions along with rotation axis. As shown in **Figure 2.7**, the collimated laser beam is converged after passing through the lens, until reaching the focal length of the lens. At the focal length the beam is at its highest quality followed by passing to the divergence zone. Thus, the highest beam quality is at the focal point of the lens, while at defocusing regions the beam would deliver less power density.

$$\text{Power density} = \frac{P}{A_{Beam}} \qquad 2.2$$

where, P is laser power and A_{Beam} is the area of the laser beam.

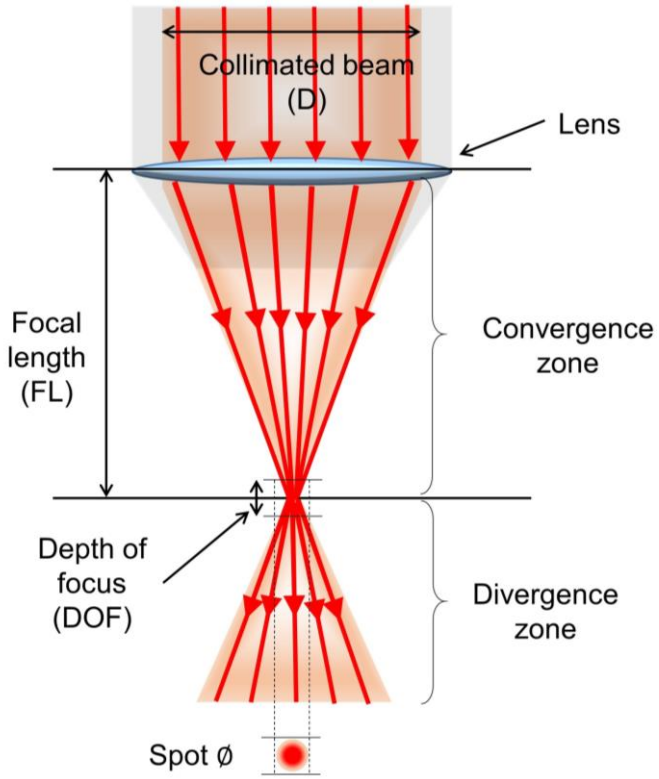

Figure 2.7. Schematic view of beam regions passing through a lens.

When considering the focus point of a laser beam exiting a lens, other than spot diameter, depth of focus (DOF) is required to be considered as well:

$$\mathrm{DOF} = \left(\frac{8\lambda}{\pi}\right) \times \left(\frac{FL}{D}\right)^2 \qquad 2.3$$

where, λ is wavelength, *FL* is focal length and *D* is entrance beam diameter. Mathematically, DOF is the distance where the beam is $\sqrt{2}$ larger than the beam waist (*W*) [13]. **Table 2.3** shows the nominal laser beam properties for the laser sources and f-theta lens used during the present thesis.

Table 2.3. Laser source beam quality and nominal focused laser beam parameters.

	Brand	Maximum power / W	M^2	*D* (Collimated) / mm
Laser source	IPG	200	1.05	5
	IPG	100	1.05	5
	Keopsys	20	1.1	5
	Brand	*FL* / mm	Spot ∅ / mm	DOE / mm
F-theta lens	QIOPIQ	387	0.055	4.10
	QIOPIQ	494	0.070	6.65

The parameters (output power, M^2, *D* and *FL*) shown in **Table 2.3** are provided by the manufacturers. The 5 mm collimated beam of the laser source is expanded 2 times before entering the lens. The calculated spot diameter and DOE are based on M^2 = 1.05, D = 10 mm for 1070 nm wavelength and FL of each f-theta lenses.

In practice, the laser spot diameter used for the sealing method is not at the *FL* distance. The values presented in **Table 2.3** for beam diameter are corresponding to spot $\emptyset_{FL}$. From geometry the working beam diameter spot $\emptyset_{WL}$ can be estimated from:

$$\frac{\text{spot } \emptyset_{WL}}{D} = \frac{FL-WL}{FL} \qquad 2.4$$

where, spot $\emptyset_{WL}$ is spot diameter at working length, *D* is collimated beam diameter, *FL* is the focal length of the lens and *WL* is the working length (distance from the lens to the workpiece)- **Figure 2.8**.

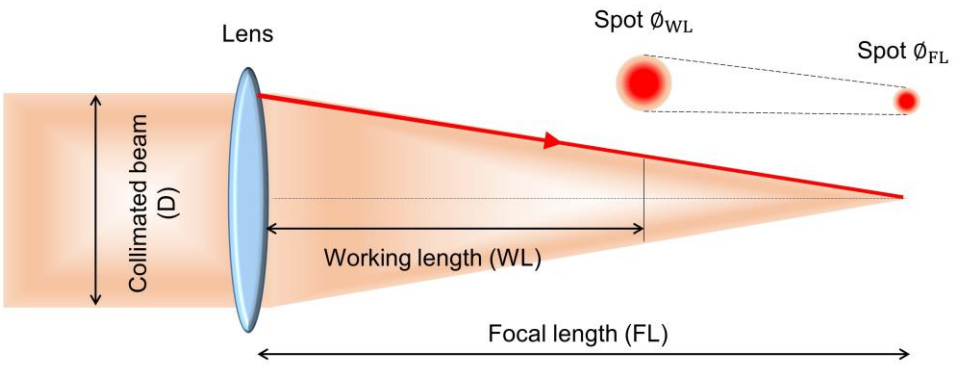

Figure 2.8. Schematic view of beam spot diameter relation with working length.

The spot diameter (also known as spot size) required for laser-assisted sealing is proportional to the width of the sealing line. Typically, the width of the glass frit sealant line used for the present work is 1 mm wide. Ideally, the laser beam spot size should cover at least *ca.* 60 % of the sealant width. The working lengths for collimated beam diameter of 10 mm of the two sealing apparatuses are presented in **Table 2.4**.

Table 2.4. Working length range for the two sealing machines.

Apparatus	*FL* (f-theta lens) /mm	WL range / mm	Spot $\emptyset_{WL}$ range / mm
LaserBox	387	364 (fixed)	0.59 (fixed)
SealingStation	494	490 - 430	0.07 - 1.30

The ideal spot diameter for LaserBox is at 364 mm distance from the f-theta lens. In case of SealingStation, the working length of the beam can be varied by the SCARA robotic arm *z*-axis. The *z*-axis of the robotic arm has a 60 mm movement range. At *z*=0 the *WL* is close to the *FL* of the lens, while at *z*=60 mm, the defocused beam can produce a spot size of 1.3 mm. The ideal spot size of 0.60 mm for SealingStation is at the *z*=30 of the SCARA arm.

There are several controlling components at LaserBox and SealingStation apparatuses including: scan head mirrors controller, temperature controller, SCARA robot controller. In addition, the laser beam movement is controlled by a software called “WaveRunner”. This software is the communication interface between the user, scan head controller and scan head mirrors. The heating for process temperature is achieved by LabVIEW interface communication with temperature controller and heating elements. The movement of the SCARA robot arm is also performed through LabVIEW interface. **Figure 2.9** shows a flowchart of the mentioned processes. The upgraded version of the SealingStation unit (**Table 2.2**) in addition to the components shown in **Figure 2.9b**; includes three additional components (scan head, scan head controller and laser source) for the second laser beam.

The laser beam alignment at LaserBox is a manual process performed by the operator. All of the three laser sources are equipped with a visible red laser pointer (guide laser). At LaserBox the operator uses the red guide laser to align the laser beam at the center of the glass frit line. The hotplate of this unit is mounted on a *x,y* moving stage, which enables the user to get better control in the *x* and *y* axis while the rotation is controlled manually.

At SealingStation the automated 4 axis SCARA robot is used for laser beam alignment. The *x*, *y* and rotation axis of the robotic arm is used for beam alignment, while the *z* axis is used for beam focusing.

(**a**) LaserBox

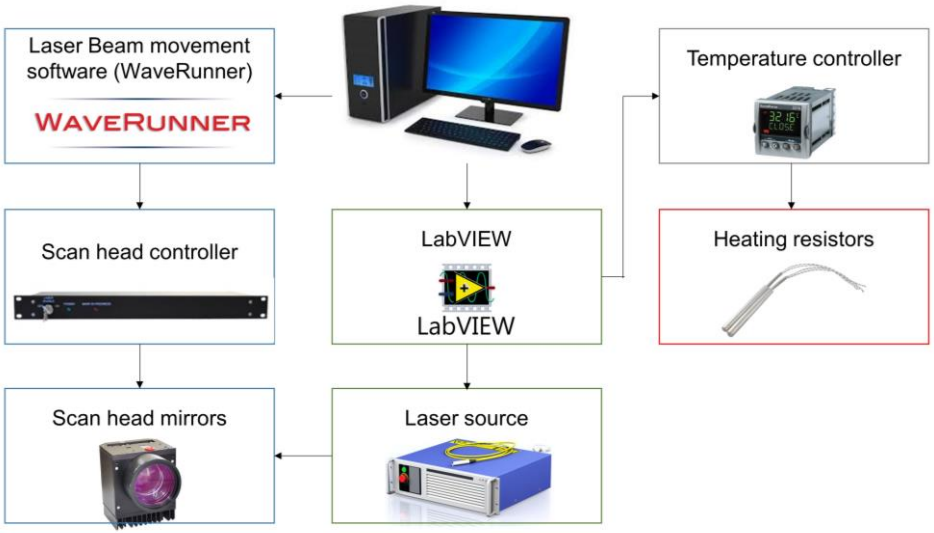
Laser Beam movement software (WaveRunner)
WAVERUNNER
Temperature controller
Scan head controller
LabVIEW
LabVIEW
Heating resistors
Scan head mirrors
Laser source

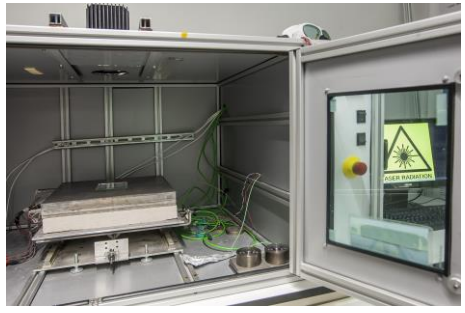

(**b**) SealingStation

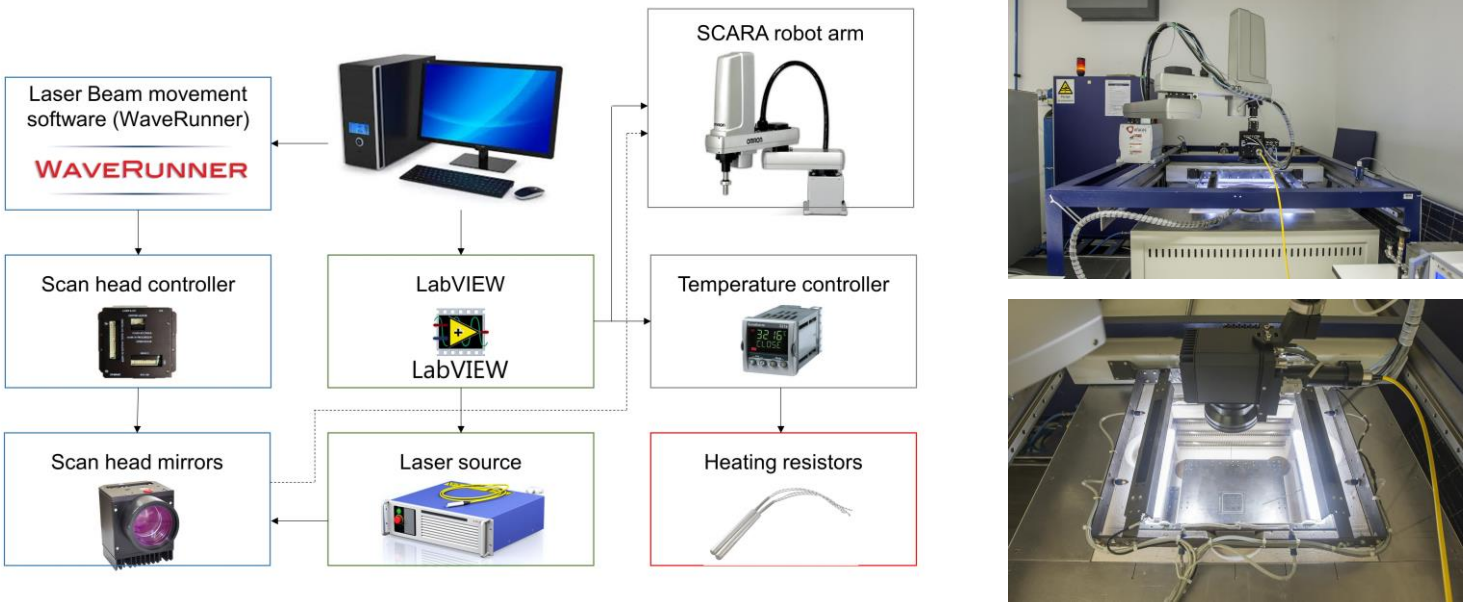

Figure 2.9. Flowchart and photograph for the controllers and communication interfaces of the laser sealing apparatuses: (**a**) LaserBox and (**b**) SealingStation. Images Copyrights, Nutfileld, National Instruments, IPG laser and Omron.

2.4 LASER-ASSISTED SEALING METHODS

Laser material processing is a dynamic method, in which a laser beam is moved on a workpiece to achieve the desired processing goal. As shown in **Figure 2.10** [14] laser sealing method can be categorized into:

- Contour bonding: a focused laser beam is moving slowly on the sealant to achieve the bonding.
- Mask bonding: an array of laser beams is radiated on a masked device; in which the laser only emits on the sealant to form the bonding.
- Quasi-simultaneous bonding: a focused laser beam is scanned at a very fast rate on the sealant for several loops to melt and join the substrates.
- Simultaneous bonding: multiple laser arrays are used to simultaneously melt the sealant.

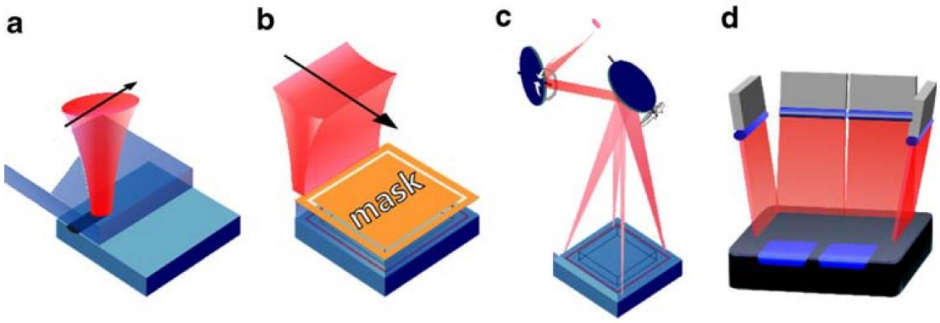

Figure 2.10. Laser bonding methods: (**a**) contour, (**b**) mask, (**c**) quasi-simultaneous and (**d**) simultaneous. Reprinted from [14], Copyright 2010, Springer.

Among these methods, array bonding methods cannot be applied using the available laser sources at LEPABE. These two methods are more common for applications in low melting temperature sealants such as thermal plastics, where the bonding is reachable with low laser power density. For glass frit sealants with bonding temperature of > 380 °C, a laser with higher power density is required.

Thus, contour and quasi-simultaneous bonding are the most suitable methods for glass frit bonding. The contour bonding method can be used for sealing experiments regardless of the size of the sample. On the other hand, the fast scanning speed for quasi-simultaneous method, limits its application to smaller area (< 50 × 50 mm^2) devices.

The most common method for laser processing is to use the laser beam in its spot shape (*i.e.* dot). However, by using fast scanning scan heads, the shape of the imaged beam at the workpiece can be modified into different geometrical shapes. For example, by fast scanning of a beam from position A to position B, a vector of $\overrightarrow{AB}$ is generated with a shape of an imaged line. The scanning speed depends on the mechanical features of the motors moving the mirrors in the laser scan head. The scanning area limitation of the quasi-simultaneous method is also related to this mechanical movement.

Hereafter, the two above methods would be mentioned as “dot” and “line” sealing. For achieving the required temperature for dot sealing, the beam should have a relatively slow velocity to reach the required temperature. On the other hand, if the laser beam hits the sealant for multiple times at a given position, the temperature increases in a more uniform manner. Therefore, through combining multiple lines passing a given point the holding time at the peak temperature is longer and the heating and cool down rates are more uniform. Hereafter, the term “pattern” sealing is referred to a “line” sealing which follows a repeating pattern.

A laser sealing “pattern” is a progressive line/arc configuration in which the laser passes a given point for several times. As shown in **Figure 2.11**, the sealing “pattern” comprises several “lines” with length “*L*” and each line proceeds to the next one by a step length “*S*”. The ratio between “*L*” and “*S*” defines the number of times “*P*” that the laser beam passes through a given point:

$$P = \frac{L}{S} \qquad 2.5$$

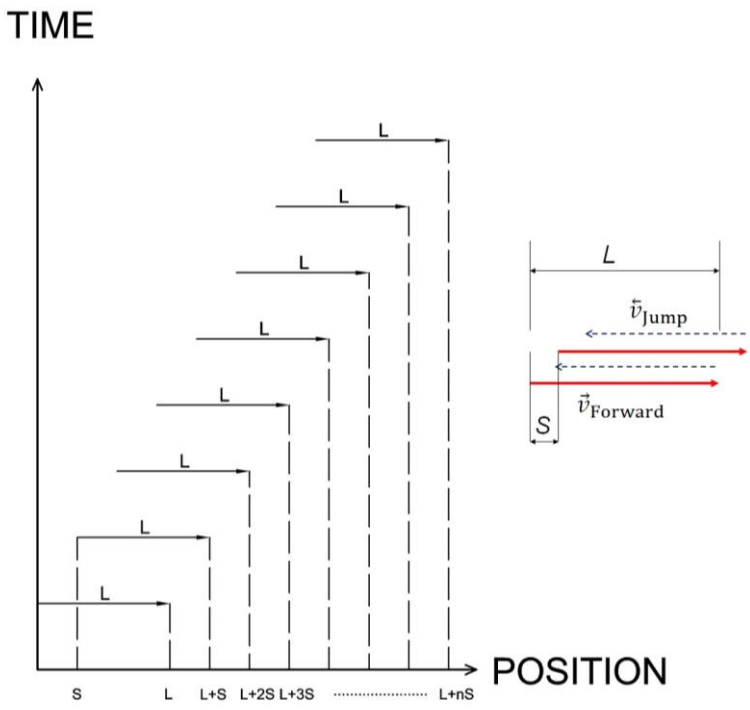

Figure 2.11. Position *vs.* time for laser sealing pattern.

The velocity of the beam in forward direction defines the scanning velocity, while for the reverse direction velocity is set to the maximum value that the scan head can deliver. The reverse direction velocity is commonly referred to as “jump” in the laser scanning equipment. For maximum velocity setting for v_{jump}, the reverse beam movement can be assumed to be instantaneous. Thus, following a movement pattern as shown in **Figure 2.11**.

The main advantage of using “pattern” sealing comparing to “dot” sealing method is its heating and cooling rate uniformity. **Figure 2.12** illustrates the beam tracking and temperature history for the two mentioned methods.

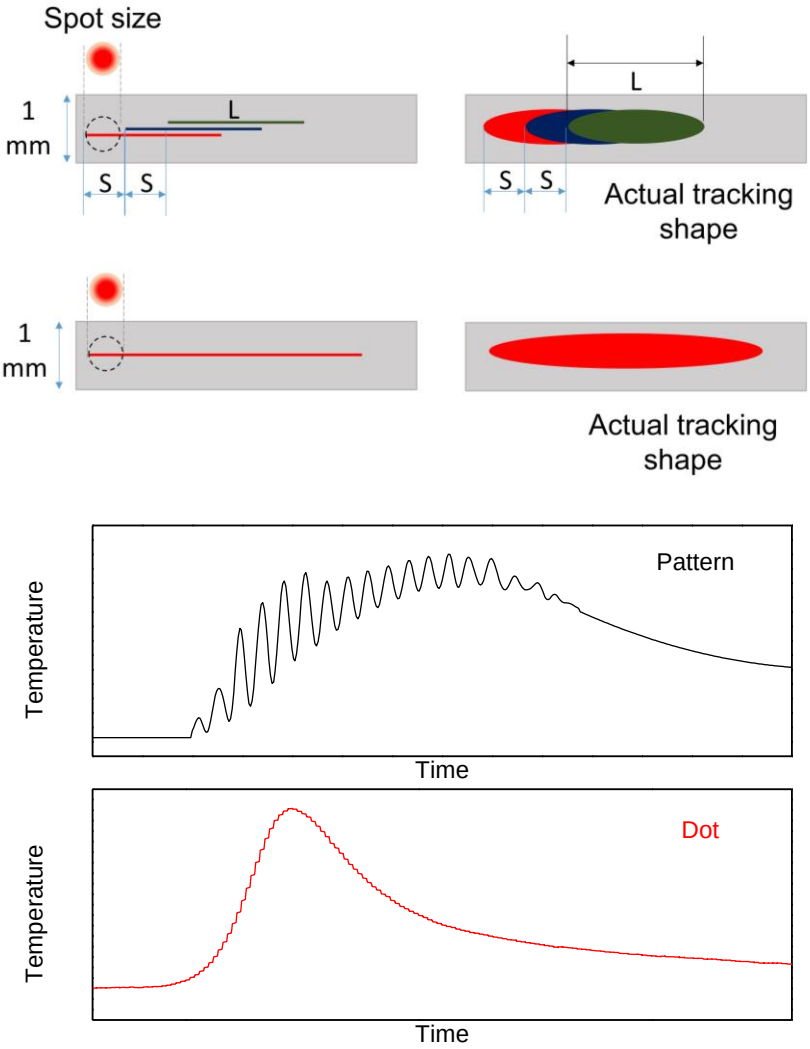

Figure 2.12. Laser beam radiation method; pattern *vs.* dot.

The heating rate for “dot” sealing is sharp and the time at pick temperature is short, therefore the mechanical stress on the sealant and substrates are high. For “pattern” sealing the temperature is gradually increased every time the beam passes on the sealant and the laser processing time and cool down are longer. The temperature history shown for pattern sealing in **Figure 2.12** is based on “*P*” value equal to 16 (**Equation 2.5**). The “pattern” sealing method can be used for contour and quasi-simultaneous bonding techniques.

2.5 GLASS FRIT

Glass frit is a composite material based on low melting point glass particles. These materials are commercially available in two forms: powder and paste. For close area (edge sealing) the paste form is more suitable since it can be deposited by screen-printing technique. Glass frit pastes are formed by mixing glass powder with additives (binders and solvents).

Before sealing, the additives must be removed from the printed glass frit paste through thermal treatment (sintering). Solvents are used in pastes to adjust the viscosity of the paste. Binders are added to keep the glass particles together to form a uniform pin-hole free glass matrix. The sintering process of a glass frit includes three steps:

- Solvent removal
- Binder burn out
- Glazing

The sintering condition of a glass frit can be optimized by thermogravimetric analysis (TGA). The sintering process of the glass paste plays a critical role not only on the adhesion of the paste to the substrates but also on the quality of sealing after laser bonding process. **Figure 2.13** shows the TGA and optimized sintering condition of a glass frit used during the present thesis.

The two most important characteristics of a glass frit are the CTE and bonding (sealing) temperature. For PSCs that are commonly fabricated on TCO coated soda-lime glass substrates, the CTE of the glass frit should be as close as possible to that of glass (*i.e.* 9×10^{-6} K^{-1}); glass frits with this CTE range have sealing temperatures >380 °C.

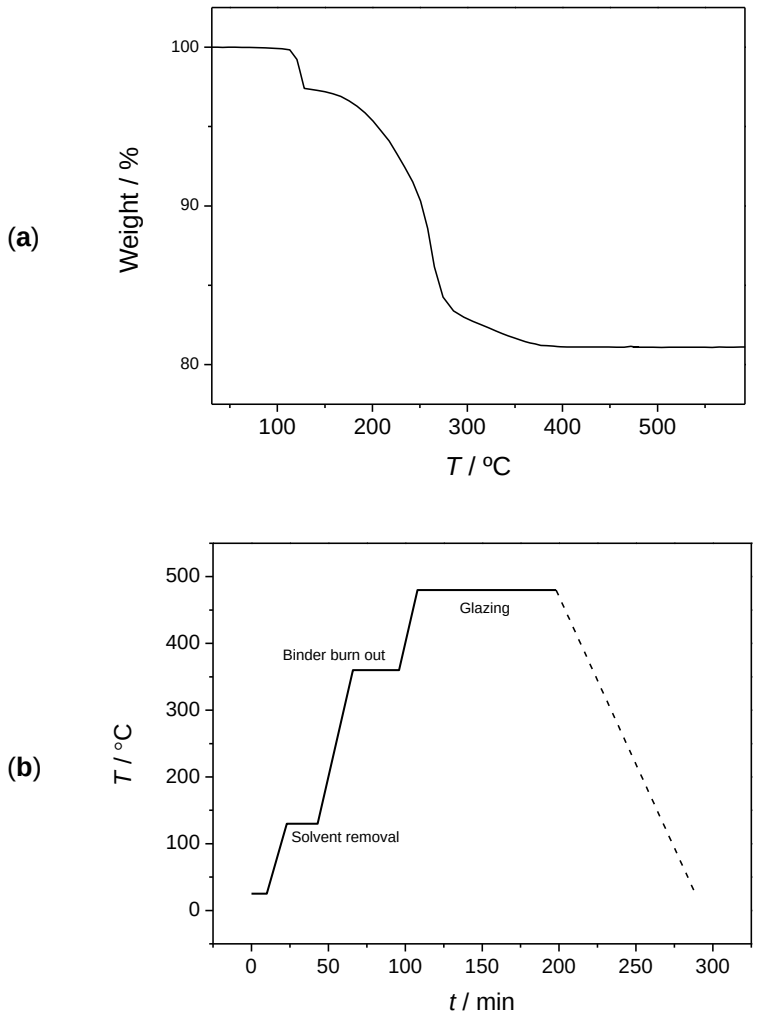

Figure 2.13. (**a**) TGA and (**b**) sintering condition for a glass frit used for the present work (glass frit C).

The mesh size for screen printing deposition is defined by the particle size of the glass frit. The printing resolution of the sealing line is dependent on selecting a proper mesh and emulsion for the screen. For example, if the mesh size of the screen is smaller than the particle size of the glass frit, during the deposition, glass particles may get stuck in the mesh. Moreover, the emulsion of the screen determines the final thickness of the deposited material. **Figure 2.14** displays an example of particle size distribution for a glass frit.

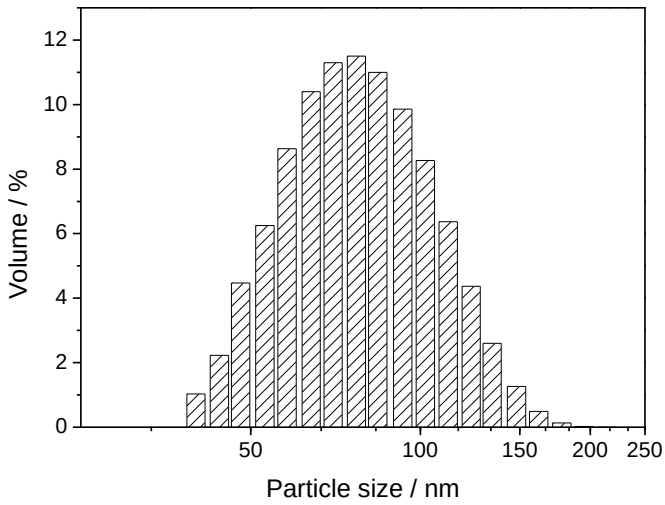

Figure 2.14. Particle size distribution of a glass frit used for the present work (glass frit C).

Within the present work various glass frits were studied to achieve low process temperature laser-assisted encapsulation. The sintering conditions for any given glass frit was optimized based on TGA study of the paste. Screen printing mesh size of 200 with “Azocol poly plus s” emulsion was used for the deposition of all of the glass frits. Depending on the composition of the glass frit, the final thickness of the sintered glass frit varied from *ca.* 13 to 25 µm.

For laser-assisted glass frit encapsulation method, there are two more parameters to be considered: (i) optical absorbance of the glass frit at the wavelength of the laser emission, and (ii) thermal shock resistance.

The transmittance and reflectance of glass frits and substrate (FTO coated soda-lime glass) were measured with a UV-VIS spectrophotometer to extract the absorbance of the glass frit. The absorbance was then calculated from:

$$\alpha = 1 - \rho - \tau \qquad 2.6$$

where α is the absorbance, is ρ the reflectance, and τ is the transmittance.

The thermal conductivity of the glass frits was compared by a simplified method (**Figure 2.15**) according to Fourier's law of heat conduction:

$$Q = -kA\frac{\Delta T}{\Delta x} \quad 2.7$$

where Q is the heat transfer rate, $\frac{\Delta T}{\Delta x}$ is the temperature gradient in the direction of the heat flow, A is area, and k is the thermal conductivity.

$$k = -\frac{Q\,\Delta x}{A}\frac{1}{\Delta T} \quad 2.8$$

For equal heat transfer rate and sample size, the thermal conductivity is proportional to the reciprocal of theΔT:

$$K \propto \frac{1}{\Delta T} \quad 2.9$$

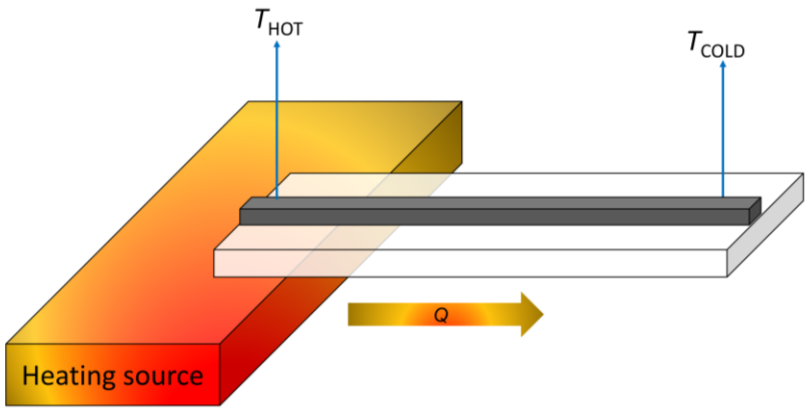

Figure 2.15. Schematic view of setup for thermal conductivity comparison measurements.

During the laser-assisted sealing processing, the minimum Laser-Added (LA) temperature difference required to achieve sealing is the difference between the bonding point of the sealant (*i.e.* glass frit) and laser-assisted process temperature;

$$\Delta T_{\mathrm{LA,minimum}} = T_{\mathrm{bonding}} - T_{\mathrm{process}} \quad 2.10$$

To achieve high quality bonding with no delamination and cracks, the ΔT_{LA} should not surpass the thermal shock resistance of the encapsulation configuration - **Figure 2.16**. The thermal shock resistance of a material depends on various properties such as CTE, thermal diffusivity, elastic modulus, tensile strength, thermal conductivity, fracture toughness, heat transfer coefficient, sample size and thermal shock duration [15].

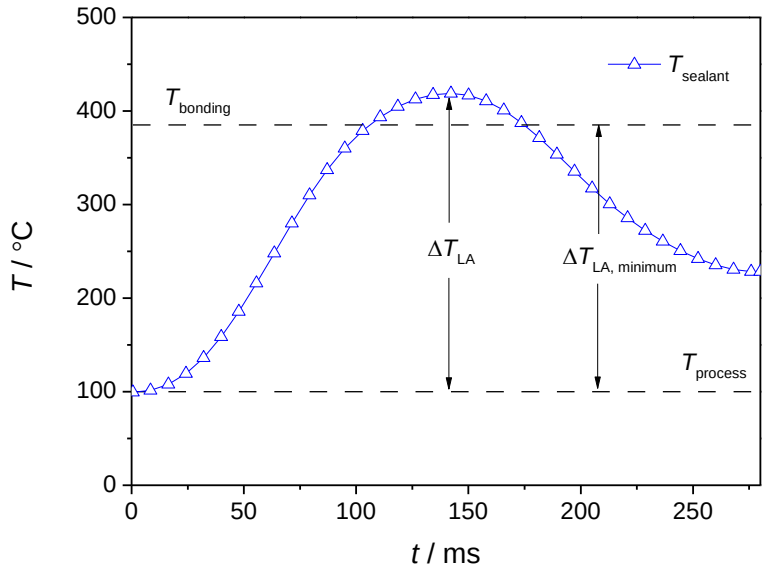

Figure 2.16. Temperature history of T_{sealant} (on the sealant) during a laser-assisted sealing process for T_{process} (i.e. device temperature) and T_{bonding} (melting/bonding temperature of the sealant) of 100 °C and 380 °C, respectively.

The encapsulation configuration comprises substrates and sealants. Since the thermal shock resistance of the substrates is limited to the soda-lime glass properties; the properties of the glass frit materials determine the overall resistance of an encapsulation configuration. The laser-assisted sealing method mechanism is based on the laser beam radiation absorbance of the glass frits. Since the glass substrate is transparent at the laser emission wavelength; the

glass frits are the main heat transfer media of the encapsulation configuration. Therefore, the thermal conductivity of glass frits defines the thermal shock resistance of the encapsulation configuration. Glass frits with higher thermal conductivity would provide higher thermal shock resistance to the sealing configuration.

Common glass frit compositions include oxide materials such as SiO_2, B_2O_3, Bi_2O_3, ZnO, V_2O_5 and PbO. The parameters with more influence on the sealing process temperature are, the bonding temperature and the thermal conductivity of the glass frits. A possible strategy for increasing the thermal conductivity of glass frits is to add silver nanoparticles to its composition. However, adding Ag to the frit would lead to electrical conductivity along the sealant. **Table 2.5** and **Table 2.6** present the properties of several studied glass frits and their laser-assisted sealing conditions. Note that the $T_{process}$ for encapsulation of HTM-free and n-i-p PSCs are required to be lower than 100 °C and 85 °C, respectively.

Glass frits A, B and C were selected to carry out the sealing experiments due to their good thermal conductivity or low bonding temperature. The highest thermal conductivity is displayed by glass frit C due to Ag nanoparticle. However, the electrical conductivity of this glass frit, limits its application for PSC encapsulation. Glass frit B has the lowest bonding temperature among all of the glass frits, therefore it can be used to achieve low processing temperature. Finally, glass frit A displays a suitable thermal conductivity and wettability to be used as a shock absorbing layer. During the present thesis three sealing configuration was optimized; C-C, C-B and C-BA, while other configurations were found to be not suitable for achieving low temperature sealing.

Table 2.5. Chemical composition and properties of the glass frits.

Glass frit	Composition	CTE × 10^{-6} / K^{-1}	Thermal conductivity / arb. Unit	Bonding temperature / °C
A	$SiO_2 \cdot B_2O_3 \cdot PbO$	7.8	++	430
B	$TeO_2 \cdot V_2O_5$	8.0	+++	380
C	$BaO \cdot SiO_2 \cdot PbO \cdot Ag$	9.0	++++	420
D	$BaO \cdot SiO_2 \cdot PbO$	7.9	++	450
E	$Bi_2O_3 \cdot ZnO$	7.7	+	440
F	$SiO_2 \cdot Bi_2O_3 \cdot ZnO$	7.5	+	450

Table 2.6. Laser-assisted sealing conditions for various encapsulation configurations.

Glass frit configuration	Overall thermal shock resistance	$T_{bonding}$ /°C	$T_{process}$ / °C	$\Delta T_{LA,minimum}$ / °C	Remarks
A-A	++	430	250	180	High $T_{process}$; not suitable for PSCs.

B-B	+++	380	120	260	Low sealing reproducibility.
C-C	+++++	420	25	395	Electrically conductive; not suitable for PSCs.
C-C	+++++	420	120	300	Electrically conductive; not suitable for PSCs.
D-D	++	450	250	200	High $T_{process}$; not suitable for PSCs.
E-E	+	440	330	110	High $T_{process}$; not suitable for PSCs.
F-F	+	450	330	120	High $T_{process}$; not suitable for PSCs.
C-B	+++	380	120	260	Suitable for HTM-free PSCs; major negative effect on device performance.
C-BA	++++	380	100	280	Suitable for HTM-free PSCs; minimal negative effect on device performance.
C-BA	++++	380	50	330	Suitable for n-i-p PSCs; minimal negative effect on device performance.

2.6 SEALING CHARACTERIZATION

For perovskite solar cell applications, the sealing should be hermetic. There are three levels of hermeticity for an encapsulation: i) gross leak, ii) non-hermetic and iii) hermetic. Gross leak test is commonly performed by tracing liquid penetration into the cavity of encapsulated sample immersed in a liquid (*e.g.* dye). A sample with no gross leak must be further examined with a gas (*e.g.* helium) for fine leaks. According to MIL-STD-883 standard, a sealing with helium leak rate lower than 5×10^{-8} atm cm^3 s^{-1} is considered as hermetic [16]. For samples that passed the gross leak test and failed the fine leak test, their hermeticity level is considered as non-hermetic.

In addition, the long-term stability of a hermetic sealing must be examined by simulated climatic tests to ensure > 20 years lifetime of the encapsulation. The long-term stability of sealing is commonly studied by environmental cycling tests as described in IEC61646 [17].

2.6.1 GROSS LEAK TEST

The sealed devices should be examined for gross and fine leaks. An in-house procedure was used to observe the gross leaks of the sealed devices:

- *Before sealing*, a permanent marker (Lumocolor® from Staedtler) containing an ethanol sensitive ink, was used to paint a mark inside the cavity of the cell.
- *After sealing*, devices with cavity size of ≤ 7 × 7 cm^2 were immersed in ethanol and pressurized at 2 bar of N_2 in a closed chamber overnight. Larger devices were immersed in ethanol at atmospheric pressure overnight.

A sample containing gross leaks allows ethanol vapor to diffuse through the sealing line (due to partial pressure differences) and this causes the solubilisation of ink mark inside the cell. If the sample contains no gross leaks,

then ethanol does not permeate the cell and the ink mark remains unchanged. Samples with no gross leaks are then subjected to fine leak test.

2.6.2 FINE LEAK TEST

The helium fine leak test was performed according to MIL-STD-883H standard, method 1014.13, A2 [16]. This test was accomplished inside two stainless steel chambers, *ca.* 17.5 × 17.5 × 6 cm^3, and comprehends two steps: i) pressurization (bombing) and ii) leak detection. In the pressurization step, the sealed devices are placed inside "chamber 1" and the chamber is vented and pressurized with helium. Depending on the tightness of the sealing line, helium permeates and build-up in the device cavity. After the pressurization step, "chamber 1" is depressurized to ambient pressure and the sample is transferred to "chamber 2", which is then evacuated. During this evacuation step, helium that had entered the device cavity is forced to leak out where the leak rate is quantified using a mass spectrometer attached to the "chamber 2". **Figure 2.17** shows the photograph of the two chambers and the mass spectrometer.

The A2 test condition of MIL-STD-883H standard allows choosing the bombing exposure time and the helium bombing pressure, as long as it is ≥ 2 bar. The mass spectrometer provides the He leak rate (R_L), and from the value of bombing pressure, bombing time and internal cavity volume of the devices, the equivalent air leak rate (L) in atm·cm^3·s^{-1} air can be computed [16]:

$$R_L = \frac{Lp_b}{p_{atm}}\left(\frac{M_{Air}}{M_{He}}\right)^{\frac{1}{2}}\left\{1 - e^{-\left[\frac{Lt_b}{Vp_{atm}}\left(\frac{M_{Air}}{M_{He}}\right)^{\frac{1}{2}}\right]}\right\} e^{-\left[\frac{Lt_2}{Vp_{atm}}\left(\frac{M_{Air}}{M_{He}}\right)^{\frac{1}{2}}\right]} \quad 2.11$$

where, R_L is measured leak rate of helium in atm·cm^3·s^{-1} He, L is equivalent leak rate in atm·cm^3·s^{-1} air, p_b is helium bombing pressure, p_{atm} is atmospheric pressure. M_{Air} is molecular mass of air (28.7 g·mol^{-1}), M_{He} is molecular mass of He (4 g·mol^{-1}), t_b is bombing time, t_2 is dwell time between release of pressure and leak detection, and V is the internal volume of device cavity. The samples

with equivalent air leak rates greater than the reject limit shown in **Table 2.7** are not hermetic. Mass spectrometer (ASM 142 from Adixen) with minimum detectable helium leak of 5 x 10^{-12} atm·cm^3·s^{-1} He was used for leak measurements.

Table 2.7. Reject limits for the equivalent leak rate according to MIL-STD-883H standard, method 1014.13, A2.

Internal cavity volume of the device / cm^3	Reject limit of equivalent leak rate (L) / atm·cm^3·s^{-1} air
≤ 0.01	5 × 10^{-8}
0.01 < V ≤ 0.4	1 × 10^{-7}
> 0.4	1 × 10^{-6}

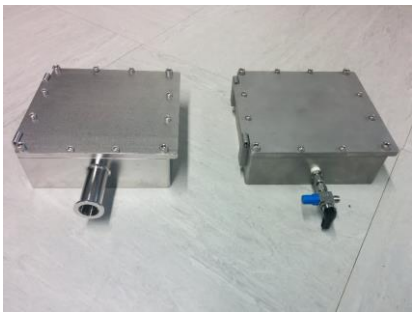

Figure 2.17. Photographs of helium leak test chambers and mass spectrometer.

2.6.3 LONG-TERM STABILITY CLIMATIC TESTS

The long-term stability of a hermetic sealing must be examined by simulated climatic tests to ensure the > 20 years lifetime of the encapsulation. The long-

term stability of sealing is commonly studied by environmental cycling tests (**Figure 2.18**) as described in IEC61646 [17]. These tests include:

- Thermal cycle test: -40 °C to 85 °C (no RH control);
- Humidity-freeze cycle test: -40 °C to 85 °C (with RH control);
- Damp heat test: 85 °C and 85 % RH.

(**a**)

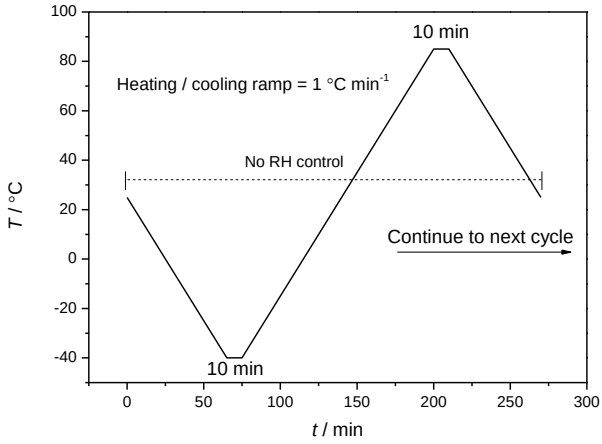

(**b**)

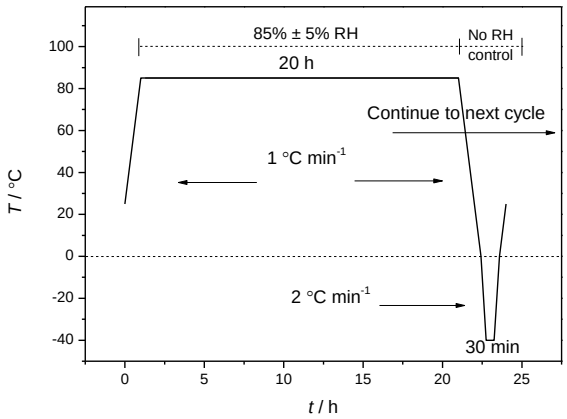

(**c**)

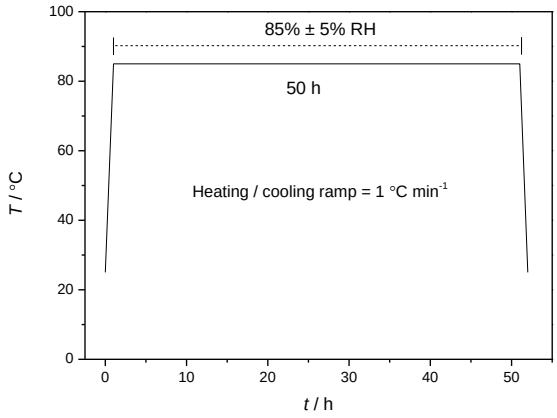

(**d**)

Figure 2.18. (**a**) Thermal cycle, (**b**) humidity-freeze cycle and (**c**) damp heat tests according to IEC61646 standard; (**d**) photograph of the climatic chamber.

The long-term stability of an encapsulation is, perhaps, even more critical than its initial hermeticity. Though several sealants display hermeticity initially, few of them can retain their hermeticity after stability tests.

2.7 SEALING RESULTS AND DISCUSSIONS

Although more than six glass frits were examined during the present thesis, only three glass frits were suitable for achieving the desired process temperature. The simplest configuration of glass frit structure is to use similar glass frit material printed on both top and bottom glass substrates. When using two different glass frits for bonding, the wettability of the frits plays an important role.

For example, even though glass frits C and D have similar chemical composition; C-D bonding is not possible due to poor wettability of both frits.

This section describes the optimization procedure for laser-assisted sealing of three glass frit configurations: C-C, C-B and C-BA for empty cells. Empty cell is a device made of two glass substrates (bottom/cell substrate and top/cover glass) sealed with a closed area edge glass frit with no active solar cell inside the cavity. The glass substrates are FTO-coated soda-lime glass suitable for PSC fabrication.

For laser-assisted sealing, the absorbance of the top glass frit where the laser beam is emitted, defines the amount of energy required from laser beam to melt and join the substrates. The transmittance and reflectance of the sintered glass frits on FTO-coated glass substrate were measured at the laser radiation wavelength of 1070 nm. **Table 2.8** shows the measured values for the two mentioned optical properties and the calculated optical absorbance (**Equation 2.6**) of the glass frits at the laser emission wavelength.

Table 2.8. Spectrophotometer analysis of the substrate and glass frits at a wavelength of 1070 nm.

Sample	Reflectance ρ / %	Transmittance τ / %	Absorbance α / %	Color
FTO coated glass	6.4	74.6	19.0	-
Glass frit A	15.4	6.1	78.4	Gray
Glass frit B	6.3	0.0	93.7	Black
Glass frit C	34.2	0.1	65.7	White

In a typical experiment, the sealing lines (1 mm width) were screen printed and sintered on both top (*i.e.* cover glass) and bottom (*i.e.* solar cell) substrates and the sealing procedure comprises the following steps:

- Positioning the top and bottom substrates so that the sealing lines of both substrates are perfectly aligned on each other and placing the sandwiched sample on the heating plate.
- Heating the sample to the desired temperature.
- Radiating the laser beam on the sealing line to locally bond the sample.

The glass frit configuration is coded with X-Y;

- X designates the glass frit printed on top/cover glass;
- "-" defines the laser-assisted sealing bonding interface;
- Y designates the glass frit deposited on bottom/cell glass.

For perovskite solar cell applications, the deposited glass frit on the bottom glass substrate must be electrically insulator to avoid short-circuiting the cell. Glass frit C is electrically conductive, however, its low absorbance at the wavelength of the laser beam and high thermal conductivity makes it the best candidate for achieving low process temperature sealing. Thus, the experimental study of glass frit configuration was started using C-C bonding. To avoid short-circuit of the device, C-B bonding was considered later. Finally, C-BA configuration was optimized to achieve < 100 °C process temperature for PSC application.

2.7.1 C-C BONDING CONFIGURATION

Glass frit C is a mixture of glass material (BaO SiO_2 PbO) with Ag nanoparticles. Silver nanoparticles provide outstanding thermal conductivity ability to this glass frit. Although its bonding temperature is relatively high (*ca.* 420 °C), glass frit C can be used to accomplish ≤ 120 °C laser-sealing process temperature.

After the sintering process, glass frit C has a white color. As shown in **Table 2.8**, the glass substrate reflectance is *ca.* 6.4 % while the glass frit reflectance is *ca.* 34.2 %. This indicates that the absorbance of the bonding material compared to common dark colored frits is relatively low and therefore the energy required for sealing should be higher.

The substrate absorbance is 19 % while the printed glass frit C on the substrate is 65.7 %. Hence, the estimated absorbance of the glass frit is 46.7 %. As mentioned before the substrates are FTO coated soda-lime glass. For a similar un-coated soda-lime glass, the transmittance and reflectance are 86.8 % and 6.9 %, respectively. Consequently, the absorbance of soda-lime glass is 6.3 % while a FTO coated soda-lime glass has 19 % absorbance. The FTO coating counts for 12.7 % absorbance at wavelength of 1070 nm, resulting in assisting the laser beam absorbance during sealing. Moreover, the FTO layer while absorbing a fraction of the laser beam before it reaches the glass sealing line allows a progressive temperature increase at the interfaces soda lime glass/FTO/glass sealing line, preventing thermal shock that would happen if the interface is just glass/glass sealing line.

Response surface methodology

The objective was to achieve laser-sealed devices using an optimized contour laser sealing method suitable for sealing empty devices regardless of their dimensions. A response surface methodology (RSM) model was followed for a process temperature of (120 ± 5) °C. RSM is a powerful statistical and mathematical tool used for optimizing multivariable processes [18]. Moreover, this methodology has been previously applied to laser-assisted sealing by Mendes *et al.* [6] and Wang *et al.* [19].

The main operating variables of the laser-assisted sealing process are: laser beam spot size, laser power, scanning velocity, and process temperature. The heating plate temperature was set to 120 °C for allowing to seal a broader variety of devices. On the other hand, based on pre-screen experiments the laser beam

spot size was set to *ca.* 600 µm. Therefore, the selected factors of the RSM model were laser scan velocity (*v*) and power (*P*) and the response was the sealing quality (*Q*). The factors and response ranges are summarized in **Table 2.9**.

Table 2.9. Interval levels for the factors and response of the RSM model of contour laser-assisted sealing.

Factor or response	Lower level	Higher level
v / mm·s^{-1}	35	250
P / W	20	70
Q / -	-10	10

The laser scan velocity is limited to a maximum value of 250 mm·s^{-1} due to the mirror movement of the scan head. The quality was rated based on visual inspection of the seal and the negative values correspond to delamination or crack on the substrates or glass frit, while positive values are considered for samples with no crack or delamination sealing. A set of 16 experiments (8 model runs and 8 leak of fit runs – **Appendix B**) was designed using *Design Expert 10* software. The factors were transformed to coded factors [18] ranging from -1 to +1:

$$x_1 = \frac{v-142.5}{107.5} \quad , \quad x_2 = \frac{P-45}{25} \qquad 2.12$$

The response model was well fitted to second order polynomial [18] with R^2 of 0.99, R^2_{Adj} of 0.98 and p-value < 0.0001.

$$y = \beta_0 + \sum_{i=1}^{2} \beta_i x_i + \sum_{i=1}^{2} \sum_{j=1}^{2} (\beta_{ij} x_i x_j + \beta_{ii} {x_i}^2) \qquad 2.13$$

where y is the sealing quality response, β_0, β_i, β_{ij} and β_{ii} are partial regression coefficients and x_i are the coded factors. The relevance of each factor,

interaction term and quadratic effects can be investigated with standard least square analysis and *p*-values. Whereas *p*-values lower than 0.05 have sufficient relevance, values in the range of 0.05 to 0.15 have marginal relevance, and finally values higher than 0.15 have insignificant effect on the model. The *p*-values for all the effects on the final model were ≤ 0.05 confirming that all of them have sufficient effect. The final quality response as a function of velocity and power is:

$$Q = -40.965 - 0.056\,v + 2.289\,P + 9.452 \times 10^{-4}\,vP + 9.78 \times 10^{-5}\,v^2 - 0.026\,P^2 \qquad 2.14$$

(**a**)

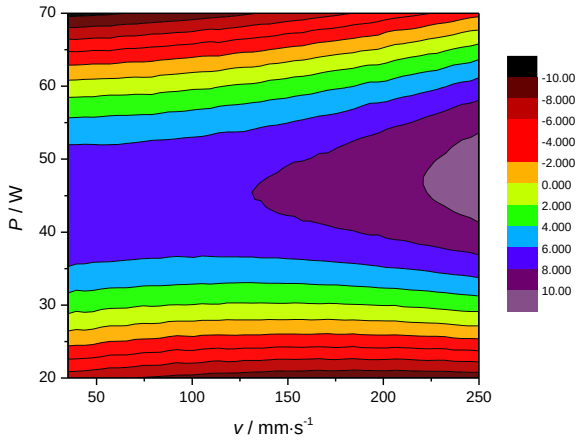

(**b**)

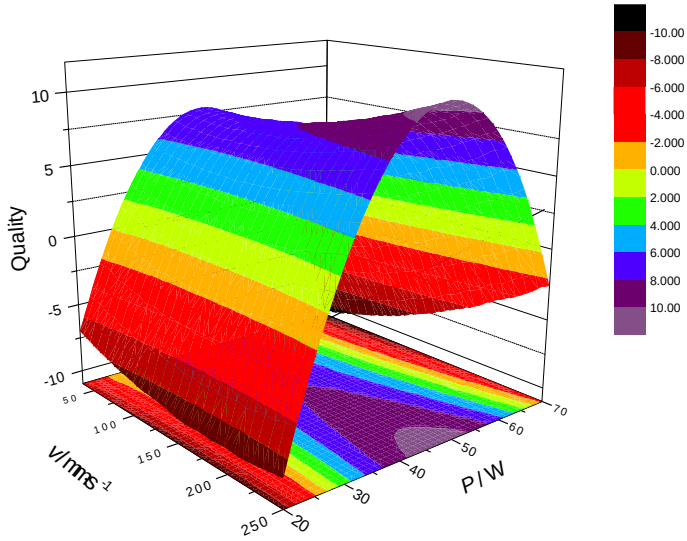

Figure 2.19. Predicted quality response based on the second order polynomial fitted RSM model: (**a**) contour plot, and (**b**) surface plot.

The RSM model fitted to contour laser-assisted at (120 ± 5) °C can be used to predict the sealing quality. **Figure 2.19** illustrates the predicted response surface of the model.

The negative values of the response in the lower laser power range correspond to no bonding, while for the higher power range is related to cracks or delamination. The positive response ranging from 8 to 10 is associated to the sealed devices with sufficient adhesion strength and high hermeticity.

The negative values of the response in the lower laser power range correspond to no bonding, while for the higher power range is related to cracks or delamination. The positive response ranging from 8 to 10 is associated to the sealed devices with sufficient adhesion strength and high hermeticity.

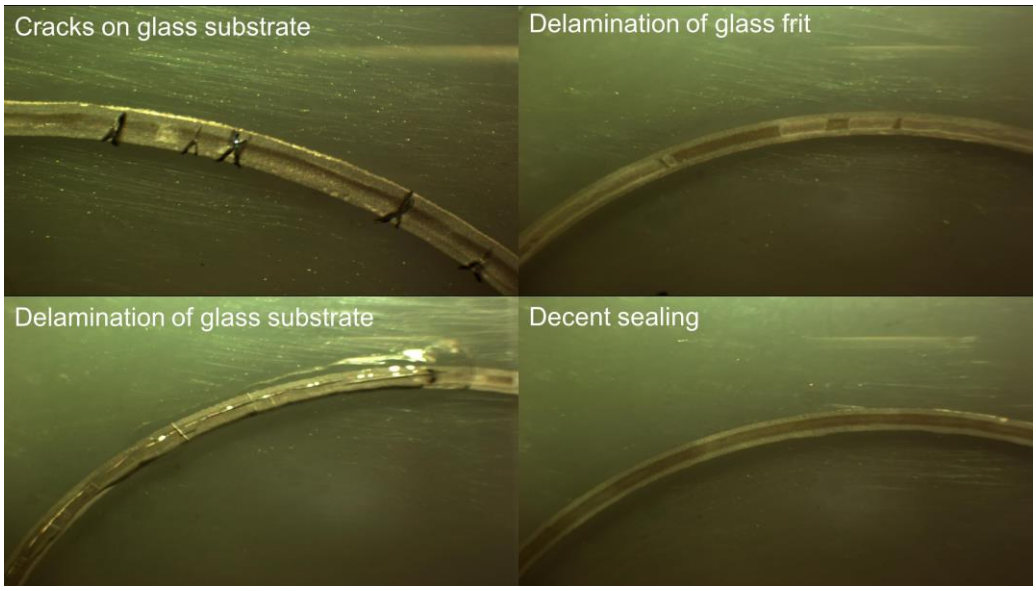

Figure 2.20. Microscopic images of the sealing quality response (*Q*) for various ranges.

Figure 2.20 shows examples of sealing quality response for:

- Negative response - 5 < *Q* < - 2 for cracks on the glass substrate;
- Negative response - 10 < *Q* < - 5 for delamination of the glass substrate;
- Negative response - 2 < *Q* < 0 for delamination of the glass frit;
- Positive response + 8 < *Q* < +10 for decent sealing.

The predicted sealing quality shows optimal results for laser power of *ca*. 47 W and scan velocity of 250 mm·s^{-1}. The contour plot (**Figure 2.19a**) of the model indicates that the process can be further improved by increasing the scan velocity. However, this improvement would be only possible if the galvanometer scanner is replaced by a faster scanning rate equipment. Hereafter these sealing conditions will be referred to as Optimal Sealing Condition (***OSC***) for laser spot size of *ca.* 600 µm and hot plate temperature of 120 ± 5 °C.

Sealing conditions

As mentioned before, there are two suitable sealing methods for glass frit bonding: contour and quasi-simultaneous. The maximum scan velocity of the scan head of LaserBox apparatus is 250 mm·s^{-1}. Since the quasi-simultaneous method requires fast scanning rates to achieve the sealing temperature of the frit, this method is limited to small area devices. In contrast, the contour method can be used to seal devices regardless of their dimension; **Table 2.10** illustrates the conditions used to seal C-C glass frits configuration.

Table 2.10. Laser-assisted sealing conditions for C-C glass frit configuration at room temperature (quasi-simultaneous) and 120 °C (contour) sealing.

Device size	Small	Large
Cavity shape	Circle	Square

Dimension	d = 3.5 mm	70 × 70 mm^2
Laser power / W	50	47
Laser scan velocity / mm·s^{-1}	150 - 220	250
Sealing method	Quasi-simultaneous	Contour
Laser beam radiation method	Pattern L= 3 mm, S=0.18 mm	Pattern L=3 mm, S=0.18 mm
Scanning loops	9	1
Heating plate temperature / °C	*ca.* 25 °C	(120 ± 5) °C

During the sealing process the temperature at a given position on the frit is directly related to the power and scanning velocity. Depending on the characteristics of the glass frit, its temperature would drop to its initial temperature in a matter of seconds. The scanning velocity for the quasi-simultaneous method should be optimized to avoid sudden thermal shocks on the glass substrates. For a given position in the sealing line, after the first pass of the laser, the frit cools down until the laser passes again. The temperature difference between the instant the laser passes and the instant the laser passes it again should be small, otherwise, during the next loop, there will be a thermal shock. It was experimentally concluded that the maximum time for each loop should be no larger than 200 ms for avoiding these thermal shocks.

Therefore, the scanning loops of quasi-simultaneous were optimized to keep this ratio and the sealing was reached in three steps: warm up, seal, and cool down at constant power. The optimal conditions were 3 warm up loops with scanning

velocities of 220 mm·s^{-1}, 200 mm·s^{-1} and 180 mm·s^{-1}, 3 sealing loops of 150 mm·s^{-1}, and 3 loops of cooling down of 180 mm·s^{-1}, 200 mm·s^{-1} and 220 mm·s^{-1} ,respectively to gradually lowering the temperature of the frit to room temperature.

Temperature history

The temperature profile of the ***OSC*** was measured by placing thin type K thermocouples (dia. 130 µm, *CHAL-005* from *Omega Engineering*) on three zones during contour laser-sealing of the device. The temperature zone and history are presented in **Figure 2.22**. The data was acquired with fast sampling rate data acquisition board (250 kS·s^{-1}, *NI USD-6221* from National Instrument). The obtained temperature signal was then smoothed with Fast Fourier Transform (FFT) filter for clarity of data presentation.

(**a**)

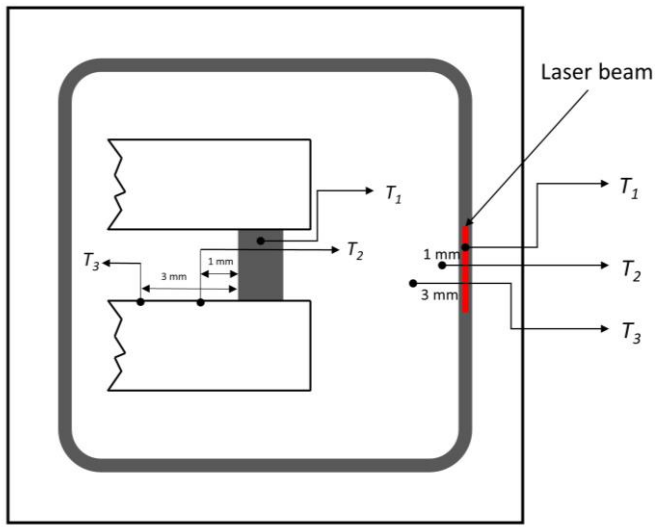

(**b**)

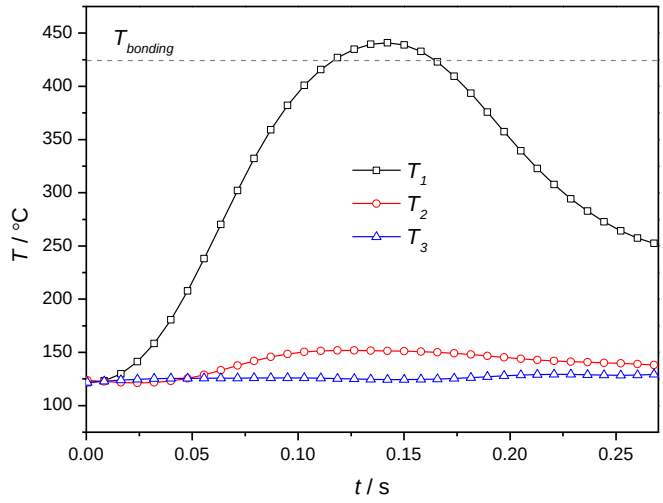

Figure 2.21. Thermocouples locations for temperature profile measurement, (**b**) temperature profile of T_1 (on the glass frit), T_2 (1 mm away from the frit) and T_3 (3 mm away from the frit).

The bonding (sealing) temperature of the glass frit C is *ca.* 420 °C. Therefore, few milliseconds of dwell time above the sealing temperature produces the bond. In contrast, temperature history at 1 mm and 3 mm away from the sealing line was measured to find the safe distance for the components of the PSC device. Thus, the Heat Affected Zone (HAZ) of the laser-assisted sealing is < 3 mm.

The applied FFT filter removes all high-frequency peaks related to pattern sealing method. As mentioned in **Table 2.10**, the laser beam radiation method of pattern with *L* and *S* of 3 mm and 0.18 mm was used. The *P* value (**Equation 2.5**) of *ca.* 16 corresponds to the number of times that the laser beam passed from a given position. The unfiltered temperature history data displays 16 peaks corresponding to the *P* value - **Figure 2.22**.

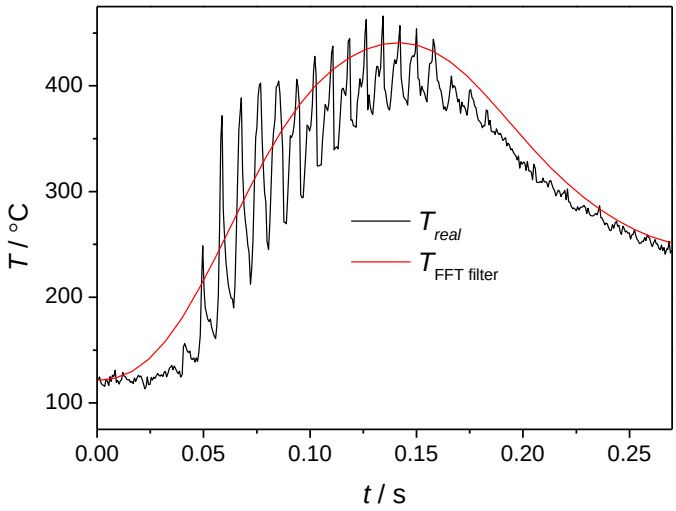

Figure 2.22. Temperature history of glass frit; real vs. FFT filtered.

SEM image analysis

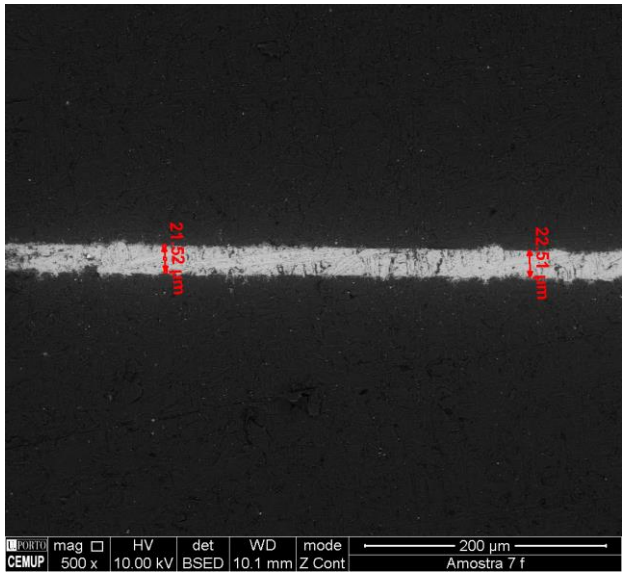

Figure 2.23. Cross-section SEM image of laser-assisted C-C glass frit bonding.

The quality of the bonding was analyzed by Scanning Electron Microscope (SEM). The cross-section morphology of the bond shows no cracks nor pin-holes on the laser-assisted sealed samples- **Figure 2.23**.

The thickness of the sintered glass frit on each soda-lime glass substrate is *ca.* 12 µm. However, the final thickness of the seal is reduced to *ca.* 22 µm which is related to the diffusion of the top and bottom frit into each other during laser bonding.

Fine leak test

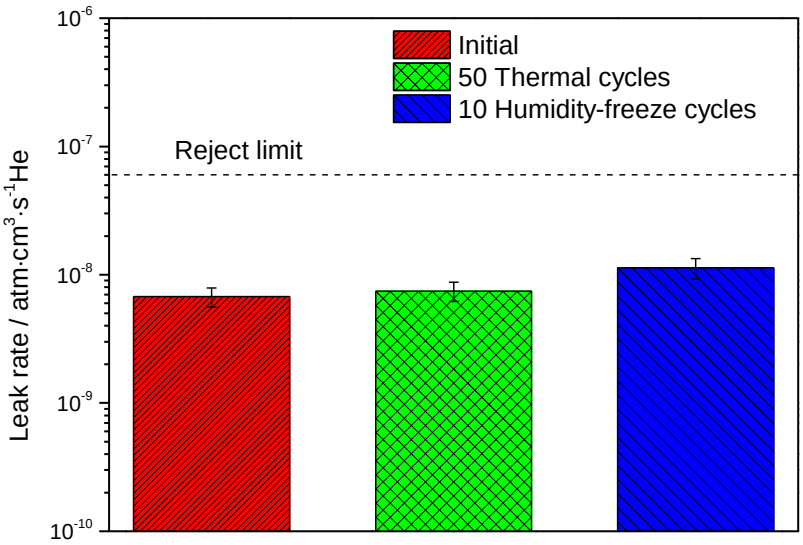

Figure 2.24. Helium leak rates for laser-assisted C-C glass frit bonding, initially and after climatic cycle tests.

A set of 4 devices (7 × 7 cm^2 internal area) were laser-sealed according to ***OSC*** and used for the helium leak rate test. The helium leak rate of the four devices was measured before and after each climatic aging tests – thermal cycling and humidity freeze. The initial helium leak rate was (6.74 ± 1.14) × 10^9 atm·cm^3·s^{-1}; after performing the 50 thermal cycles (IEC 61646) the helium leak rate was (7.46 ± 1.2) × 10^{-9} atm·cm^3·s^{-1}; and after performing the 10 humidity freeze cycles

(IEC 61646) it was (1.32 ± 0.21) $\times 10^{-8}$ atm·cm^3·s^{-1}. Therefore, the C-C sealing configuration showed helium leak rates lower than the reject limit of the MIL-STD-883H standard (5 $\times 10^{-8}$ atm·cm^3·s^{-1}) - **Figure 2.24**.

Bonding stress evaluation

To achieve a reliable laser-assisted sealing many parameters should be optimized. Among these parameters, sintering plays a critical role for the adhesion of the glass frit to the substrates. An optimized sintering process can improve the adhesion of the frit to the glass while poor sintering results in a weak bonding at the interface of the glass plate / bonding material. Therefore, the strength of the bonding not only depends on the sealing process but also on the previous adhesion of the frit to the glass. The recommended glazing step of the sintering process from the manufacturer is 10 min of dwell time at temperature of 450 °C. To achieve better adhesion of the glass frit to glass substrate the glazing step was modified to 60 min of dwell time at temperature of 480 °C.

The sealing strength can be assessed from examination of the fracture behavior of the sealed devices. The failure mode of the encapsulation may appear in four different manners (**Figure 2.25**):

I. in between the glass frit lines indicating partial sealing;

II. loss of adhesion at the interface of substrate and frit, due to poor sintering conditions;

III. break of the glass substrate in one side while the other side is still attached to the frit, showing sealing strength to be higher than the internal forces of the glass substrate;

IV. no break, showing a good adhesion.

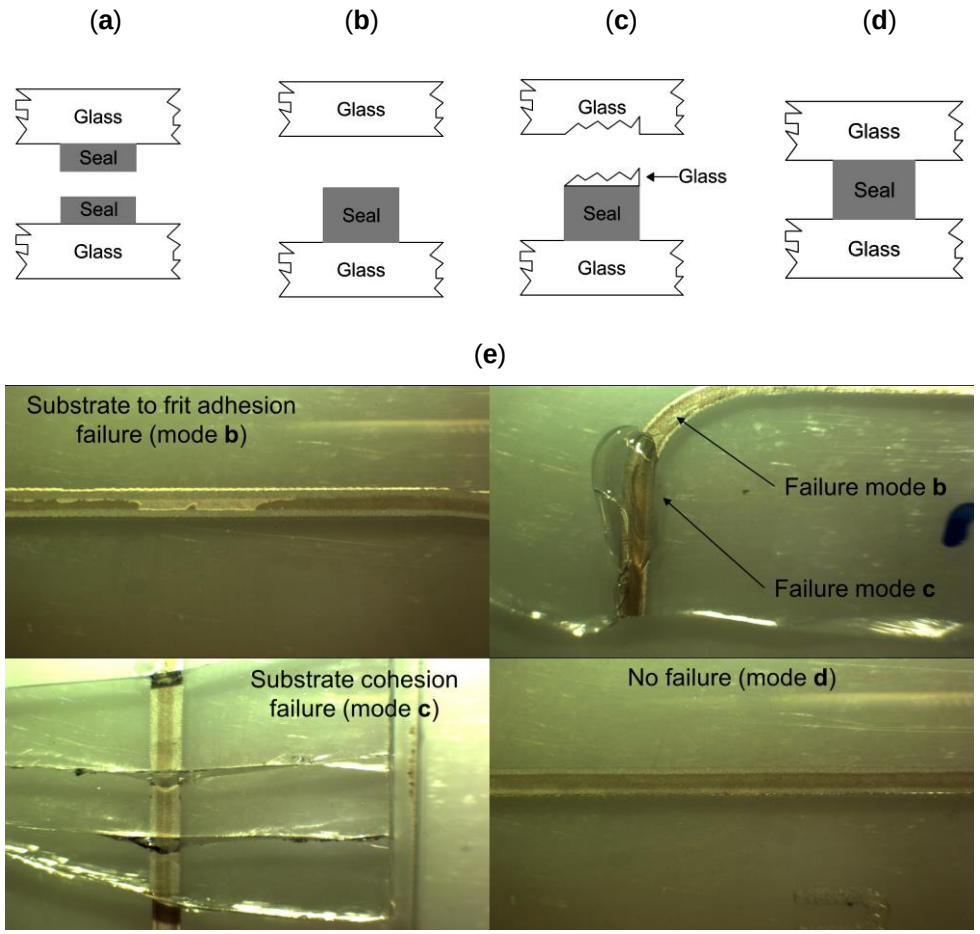

Figure 2.25. Failure mode for laser-assisted bonded C-C glass frit configuration; (**a**) frit cohesion failure, (**b**) substrate to frit adhesion failure, (**c**) substrate cohesion failure, and (**d**) no failure. (**e**) Microscopic images of fracture behavior showing various failure modes.

The failure mode of the laser sealed devices showed decent strength with either substrate cohesion failure (**Figure 2.25c**), or no failure (**Figure 2.25d**) that is the outcome of both suitable sintering and laser sealing conditions.

2.7.2 C-B BONDING CONFIGURATION

Glass frit B displays the lowest melting/bonding temperature among all the studied materials. This sealant is based on TeO_2 and V_2O_5, with CTE of *ca.* 8 × 10^{-6} K^{-1} and a bonding temperature of 380 °C. This eclectically insulating glass frit can be used on the cell substrate side without short-circuiting the cell.

Glass frit B has a dark black color aspect, after sintering step. As shown in **Table 2.8**, the calculated absorbance of glass frit C was 65.7 % while the glass frit B absorbance was 93.7 %. This, together with the fact that glass frit B has a lower melting temperature than glass frit C, clearly indicates that the laser energy required for melting glass frit B is lower than the laser energy required for melting glass frit C.

Laser-assisted bonding of B-B glass frit configuration requires a precise laser power control due the high absorbance of the frit at laser wavelength. As mentioned before, high power laser sources are designed to deliver power output of 10 % to 100 % of their maximum power, while having *ca.* 0.5 % to 1% output power precision control. Therefore, the 200 W and 100 W laser sources available at LEPABE are not suitable for laser-sealing of glass frit B as the top glass frit of the configuration. On the other hand, the 20 W laser source with minimum 2 W output power and 0.1 W precision control is appropriate for this application.

The laser-sealing experiments on B-B configuration showed a very narrow window for achieving a suitable bond. The sealing conditions used for bonding B-B configuration is shown in **Table 2.11**.

Table 2.11. Laser-assisted sealing conditions for B-B glass frit configuration.

Device size	Medium
Cavity shape	Square

Dimension	40 × 40 mm^2
Laser power / W	7
Laser scan velocity / mm s^{-1}	5
Sealing method	Contour
Laser beam radiation method	Dot
Process temperature / °C	120 ± 5

The “dot” sealing method with slow scanning velocity was used to achieve B-B bonding. The reproducibility of the sealing results was as low as 10 % mainly due to delamination of glass frit at the start and finish position of the laser processing.

The low bonding temperature of glass frit B provides vast benefits for laser-assisted sealing technique. The high absorbance of this glass frit makes it incompatible to be used as the top glass frit. In contrast, glass frit C has 34.2 % reflectance at the laser emission wavelength, which is favorable for controlling the laser inducted temperature change. The glass frit C can provide versatile benefits for laser sealing conditions, while glass frit B has the advantage of low bonding temperature along with being electrically insulating. Thus, the C-B glass frit configuration is an appropriate solution for PSC application.

Sealing conditions

Two substrates with sintered frit line are sandwiched together in a way that the sealing lines of each sample are aligned. The sandwiched device is then positioned in the furnace of the “LaserStation” and heated to 120 °C for 60 minutes dwell time, for temperature stabilization. Then the laser beam is emitted on the sealing line to locally melt the glass frit and join both substrates.

Devices of 7 × 7 cm^2 can be sealed using the scan head positioned in the center of the device; the laser beam is then directed to the sealing line using the mirrors of the 2D scan head. The scan head allows to seal devices up to 10 x 10 cm^2. Therefore, devices with dimension of 13 × 13 cm^2 are sealed by dividing the device in four identical sections of 6.5 x 6.5 cm^2 and sealing each section separately, as illustrated in **Figure 2.26**. In this method, the sealing is performed by positioning the scan head in the center of each section and bonding the corresponding sealing line segment.

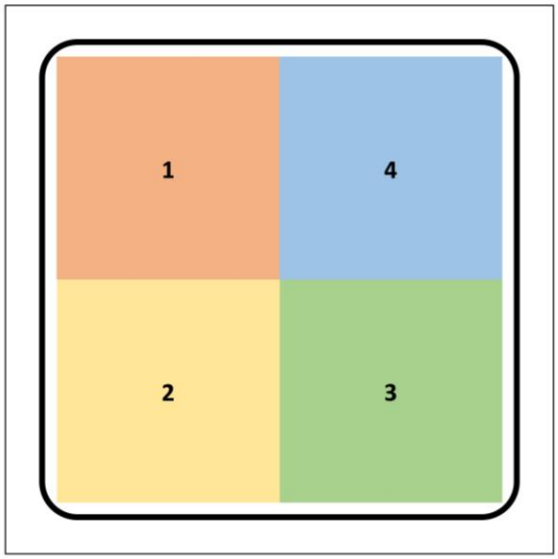

Figure 2.26. Schematic view of device segmentation for sealing 13 × 13 cm^2 devices.

The independent variables of the laser-assisted glass frit sealing process are: furnace temperature (process temperature), laser beam spot size, laser scanning velocity and laser power. The process temperature was set to 120 °C, compatible with the temperature requirements of HTM-free PSCs. The laser beam spot size was kept constant (*ca.* 0.6 mm). Hence, the two independent variables that were optimized, were the laser scanning velocity and the laser power. **Table 2.12** shows the optimized laser sealing conditions

Table 2.12. Optimized laser-assisted sealing conditions for C-B sealing configuration.

Device size	Large / Extra-Large
Cavity shape	Square
Dimension	70 × 70 mm^2 130 × 130 mm^2
Laser power / W	38
Laser scan velocity / $mm \cdot s^{-1}$	200
Sealing method	Contour
Laser beam radiation method	Pattern *L*=5 mm, *S*=0.525 mm
Furnace temperature / °C	(120 ± 5) °C

Application of glass frit C as the top sealant layer, resulted in successful bonding. In fact, the suitable wettability of glass frit B to glass frit C is another major factor for achieving the sealing. Through good thermal conductivity of glass frit C and pattern sealing method, the thermal shock on the substrates was minimized; resulting in high sealing reproducibility.

Temperature history

The temperature history during the sealing process was measured using a very thin type K thermocouple (dia. = 50 µm, CHAL-002 from Omega Engineering) placed between the two glass frit layers (**Figure 2.21a**). The signal was acquired

by *NI USB-6221* from National Instrument) and the temperature signal was smoothed with FFT filter for clarity of data presentation.

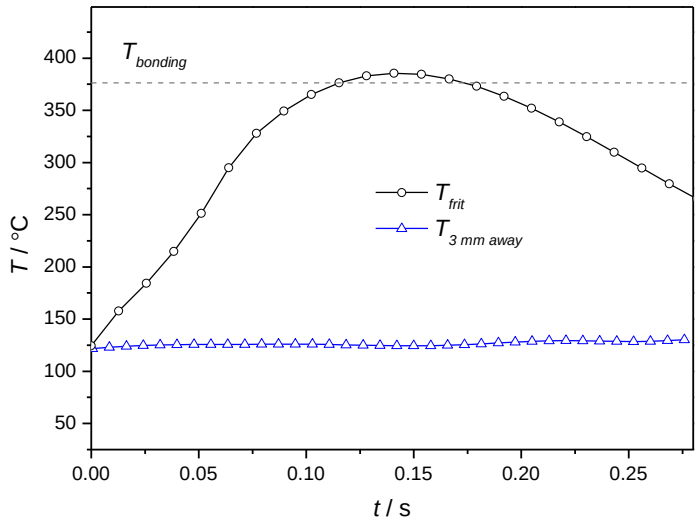

Figure 2.27. . Temperature history of the glass frit and substrate (3 mm away from the sealing line) during C-B configuration laser sealing process.

Figure 2.27 indicates that the maximum temperature of the glass frit during sealing is slightly above 380 °C and a few milliseconds is enough to achieve bonding. The heat affected zone of the laser-assisted sealing method was also measured and 3 mm away from the sealing line the temperature remained constant and equal to the process temperature. Therefore, the laser-assisted sealing method is compatible with PSCs manufacture when the cell component layer is deposited *ca*. 3 mm away from the sealing line.

Sealing quality analysis

The final quality of sealing depends on two factors: sintering conditions of the glass frit (before bonding), and laser sealing conditions. Sintering conditions of the glass frits plays an important role in the porosity of the glass frit before and after the bonding step. As mentioned before, glass frits are commonly available

in the form of printable pastes. These pastes contain solvents and organic binders, which should be removed during the sintering process. Improper sintering condition results in the presence of pores in the sealing line [20]. There are three factors that can cause pores in the sealing line:

- Organics trapped in the sealing line due to unsuitable burn out step: if the organic binders of the glass paste are not burn out properly, visual defects would appear after the laser assisted sealing process. The rapidly rise in temperature causes the organics to evaporate and the trapped gases pressure would force their release from the molten frit matrix originating defects.
- Insufficient glazing step: after the binder burn-out step, the glass frit is glazed for several minutes. Through the glazing step, the glass particles are melted, forming a compact pin-hole free glass matrix. Inadequate glazing step would originate voids in the sealing line. These voids can be identified from scanning electron microscopy (SEM) images.
- Not optimized laser sealing parameters: if the laser sealing parameters are not optimized, the glass frits would not bond properly, resulting in slit pores between the two glass frit layers.
- Reduction of metal oxide: during the bonding process reduction of metal oxides such as PbO and V_2O_5 by carbon releases gases such as CO and CO_2, which causes inevitably the formation of pores in the sealing line [20].

The quality of the sealing line was characterized by SEM – **Figure 2.28**. The absence of pore on the two glass frit layers is the result of appropriate sintering conditions. The cross-sectional SEM image shows a complete diffusion of the two glass frits, with no pinholes or cracks, which is characteristic of a high-quality sealing. The thickness of sintered glass frits C and B are *ca.* 13 µm and 25 µm respectively and the final sealing thickness is *ca.* 38 µm.

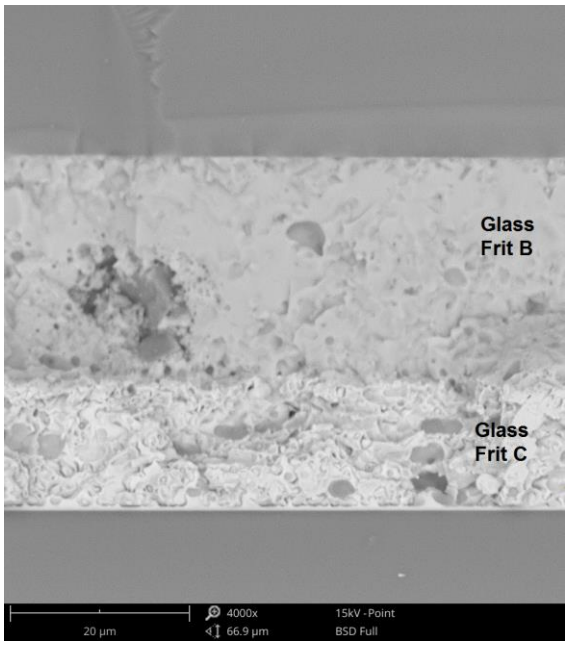

Figure 2.28. Cross-section SEM image of C-B sealing configuration.

Fine leak test

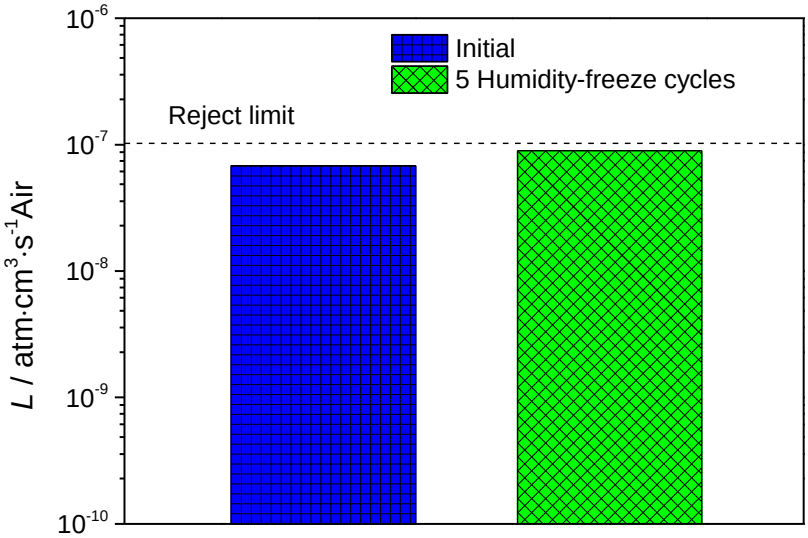

Figure 2.29. Leak rates of 70 × 70 mm^2 laser-assisted sealed C-B glass frit devices before and after five humidity-freeze cycle test.

The hermeticity of sealed samples, with cavity dimension of 7 x 7 cm^2, was measured according to MIL-STD-883H standard before and after five cycles of humidity-freeze test of IEC 61646. The initial helium leak rate was 6.81×10^{-8} $atm \cdot cm^3 \cdot s^{-1}$ air and after the humidity-freeze cycles the leak rate was 8.93×10^{-8} $atm \cdot cm^3 \cdot s^{-1}$ air – **Figure 2.29**. These measured leak rate values were lower than the reject limit of 1×10^{-7} $atm \cdot cm^3 \cdot s^{-1}$ air and therefore the encapsulation is not only hermetic but also long-term stable.

The gross leak test on extra-large sealed devices indicated no gross leaks. The fine leak test of the extra-large area devices was assessed according to the MIL-STD- 883 helium leak rate test (*i.e.* 2 bar He, 2 h). However, during the leak reading step of the test at "chamber 2" all of the sealed 13 x 13 cm^2 samples have displayed adhesion failure at the interface of the sealing line and the substrate, and no reading value could be obtained. During the leak reading step the tensile stress on the sealing line would cause mechanical tension on the sealing line; resulting is adhesion failure of the frit to substrate. Other authors also reported failures due to mechanical stress during the leak rate test [21-23]. Moreover, the applicability of MIL-STD-883 for testing fine leaks of packages with sub-micro cavity volumes was studied by other researchers and they found that the standard is not adequate for testing devices with cavity volume smaller than 10^{-2} cm^3 [24]. This shows strong limitations of MIL-STD-883 concerning its applicability to devices with small cavity volumes or large areas.

The main objective of sealing extra-large device were to assess the scalability of the laser-assisted method. These results showed that the method is scalable and suitable for industrialization.

2.7.3 C-BA BONDING CONFIGURATION

Glass frit A is based on SiO_2 B_2O_3 and PbO glass mixture. This glass frit displays a better thermal conductivity comparing to the glass substrate. Thus, the 120 °C

process temperature for C-B bonding can be further decreased by adding the glass frit A to the sealant configuration.

During laser-sealing process, the laser beam is radiated through the cover glass; therefore, the temperature required to achieve the bonding is the bonding temperature of glass frit B to melt and seal to glass frit C. Each of the triple layer glass frit plays a different role; glass frit C, with the highest thermal conductivity can withstand rapid thermal stress due to direct radiation of the laser beam; glass frit B has the lowest meting point to minimize the bonding temperature; finally, glass frit A acts as thermal shock absorbing layer.

Sealing conditions

The width of the screen-printed sealing line for glass frits B and C is 1 mm. The heat affected zone (HAZ) of C-B sealing configuration during the laser emission is < 3 mm. Therefore, during the laser process the temperature at the sealing line reaches values slightly higher than 380 °C, while *ca.* 2 mm away from the sealing line the temperature at the substrates is equal to the process temperature. Thus, to maximize the advantage of better thermal conductivity of glass frit A, this frit was deposited with 4 mm width.

There were two objectives to be reached for sealing of C-BA configuration: process temperature below 100 °C, and shorter dwell time at process temperature. In typical sealing experiments, the process temperature dwell time before laser sealing is *ca.* 60 min. This is due to the low thermal conductivity of soda-lime glass (1.05 W m^{-1} K^{-1}). However, the application of glass frit A in sealant configuration can improve the overall thermal conductivity of the sealing system. Therefore, in overall lower process temperature and shorter dwell times are reachable. The dwell time at process temperature directly effects the performance of the PSC device. The mentioned thermal effect is further discussed in **Chapters 3** and **4**.

Table 2.13. Single laser beam sealing conditions for C-BA sealing configuration.

Device size	Small / Medium
Cavity shape	Rectangle / Square
Dimension	20 × 25 mm^2 40 × 40 mm^2
Laser power / W	41
Laser scan velocity / $mm \cdot s^{-1}$	160
Sealing method	Contour
Laser beam radiation method	Pattern *L*=5 mm, *S*=0.525 mm
Process temperature / °C	(100 ± 5) °C

Table 2.13 shows the laser -assisted sealing condition for C-BA bonded with a single laser beam. This sealing can be achieved in both LaserBox and SealingStation units. Sufficient reproducibility and quality for sealing results at 100 °C, and *ca.* 35 min dwell time was achieved. These results are suitable for sealing of HTM-free devices.

For conventional n-i-p devices the process temperature of < 85 °C and even shorter dwell time is desired. Based on the sealing results presented in **Table 2.13**, C-BA configuration requires a process temperature of *ca.* 100 °C. However, this process temperature is only required for a short dwell time during laser emission. The upgrade on SealingStation was aimed at achieving short

process temperature dwell time by using a second laser beam. Thus, two laser beams are used for these sealing experiments.

- Heating laser beam ($Laser_{Heating}$): to increase the process temperature to 100 °C for a short dwell time < 5 min.
- Bonding laser beam ($Laser_{Bonding}$): to achieve the bonding.

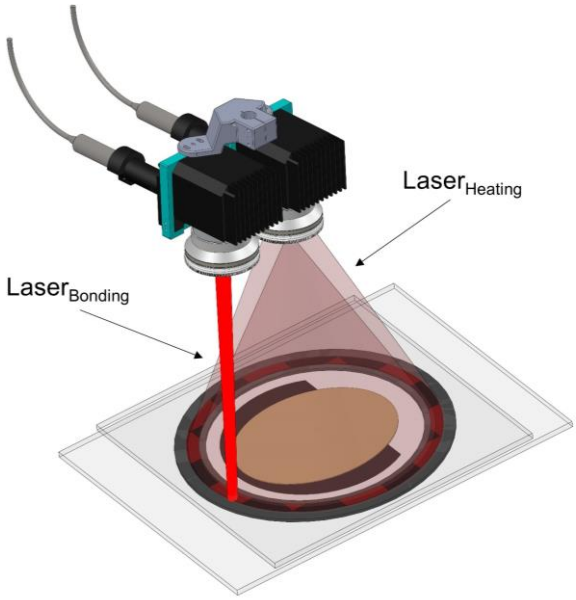

Figure 2.30. Schematic view of dual laser beam sealing method.

As shown in **Figure 2.30** the beam movement method of heating laser is quasi-simultaneous, while bonding laser is contour.

Table 2.14. Dual laser beam sealing conditions for C-BA sealing configuration

Device size	Small
Cavity shape	Rectangle / Circle
Dimension	20 × 25 mm^2 / d = 3 mm

Laser power / W	$Laser_{Bonding}$= 41 $Laser_{Heating}$ = 15 to 35
Laser scan velocity / mm·s^{-1}	$Laser_{Bonding}$ =210 $Laser_{Heating}$ = 250
Sealing method	Contour
Heating method (2nd laser)	Quasi-simultaneous
Laser beam radiation method	Pattern $Laser_{Bonding}$ L=5 mm, S=0.525 mm $Laser_{Heating}$ L= 6 mm, S=0.63 mm
Furnace temperature / °C	(50 ± 5) °C

As presented in **Table 2.14**, the temperature set point of the furnace at SealingStation is *ca.* 50 °C. Although the experiments can be performed at room temperature; the initial screening experiments showed that the tension on the bottom/cell substrate can be lowered through this slight thermal gradient.

Temperature history

The temperature profile for single laser beam sealing of C-BA, is similar to the one presented in **Figure 2.27**. The optimal condition for dual laser beam sealing was measure by placing a thin type K thermocouple (dia. 50 µm, CHAL-002 from Omega Engineering) at the interface of glass frits C and B. The temperature signal is then smoothed with FFT filter for clarity of data presentation.

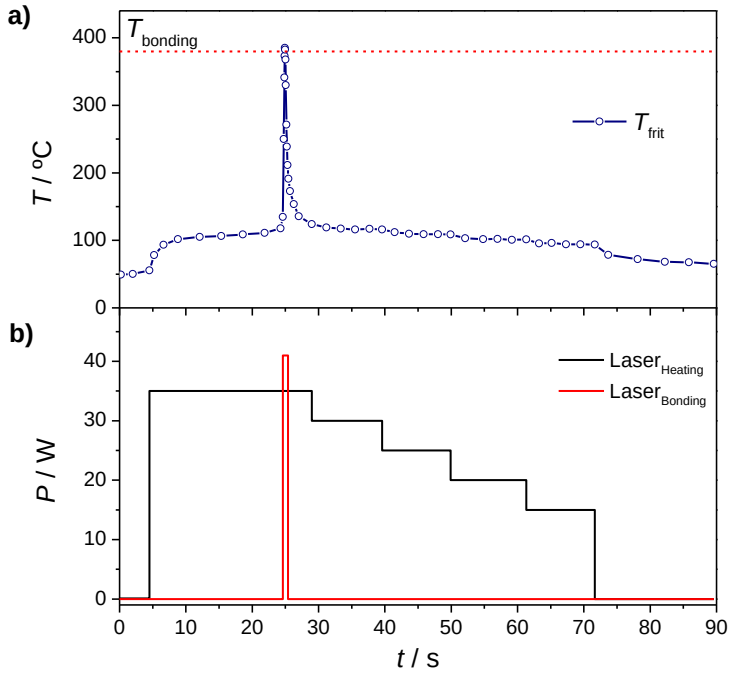

Figure 2.31. (**a**) Temperature and (**b**) Laser power history of the sealing during dual laser beam bonding of C-BA configuration.

As illustrated in **Figure 2.31** the temperature is 50 °C before the laser processing. The dwell time of temperature change from 50 °C to 100 °C, is *ca.* 90 s. The heating laser beam is emitted to the frit with 30 W power to increase the process temperature before the bonding laser beam performs the sealing. After achieving stabilized temperature of 100 °C, the bonding laser beam is radiated to join the glass frit B to C. Once the bonding is completed, the power on heating laser is maintained constant for a short period to (*ca.* 5 s) to avoid sudden thermal gradient. Afterwards, the power output of the heating laser is gradually decreased (5 W power every 10 s) to slowly cool down the frit. This method is suitable for encapsulation of conventional n-i-p PSC which can withstand short thermal exposure at *ca.* 100 °C - **Chapter 4**.

SEM image analysis

The thickness of screen-printed glass frits after sintering are *ca.* 17 µm, 22 µm and 13 µm for glass frits A, B and C, respectively. The total thickness of the encapsulation after laser-sealing process is *ca.* 52 µm.

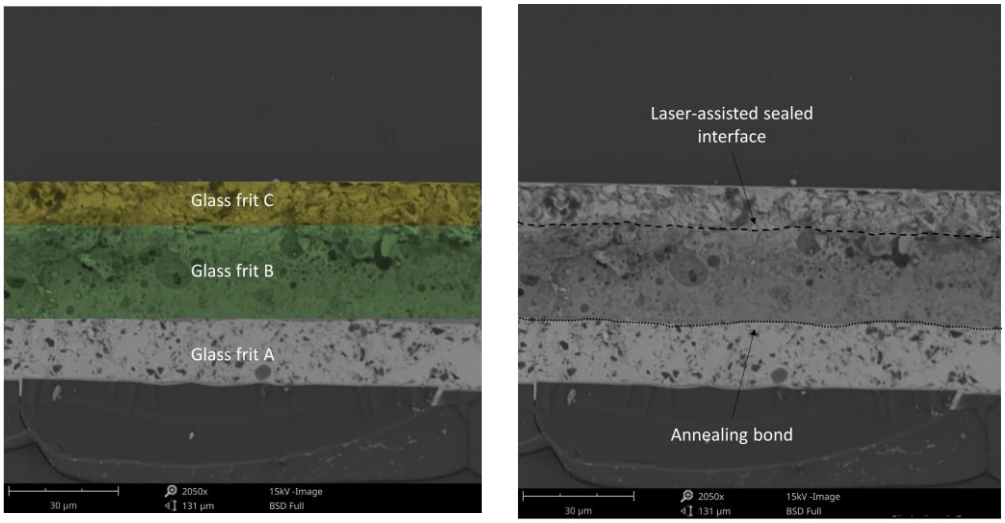

Figure 2.32. SEM image of laser-assisted glass frit C-BA bonding.

As shown in **Figure 2.32** there are no pin-holes in image of the sealing, which is the characteristic of high sealing quality.

Fine leak test

The hermeticity of the encapsulated packages measured according to A2 method of MIL-STD-883 standard (5 h of helium bombing at 2 bar). Two batches of encapsulated devices were used to perform the hermeticity test; i) optimized laser-assisted C-BA glass frit, and ii) thermal plastic. **Figure 2.33** compares the equivalent air leak rate (*L*) for the optimized laser-assisted glass frit sealed devices to devices sealed with a widely used thermoplastic named Surlyn™. The Surlyn™ sealed sample displayed leak rates higher than the reject limit and hence it was considered as non-hermetic.

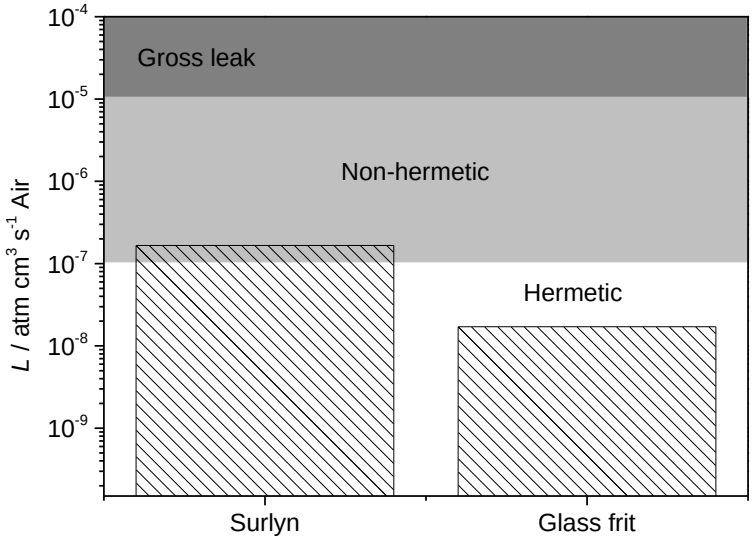

Figure 2.33. Fine leak rates for sealed devices of cavity size 2 × 2.5 cm^2 sealed with C-BA glass frit *vs.* Surlyn.

The C-BA sealing configuration displays a leak rate of 1.71 × 10^{-8} atm cm^3 s^{-1}; lower than the reject limit of the standard. The IEC standard long-term stability tests on C-BA sealing configuration was performed on devices with active perovskite solar cells. These results are presented in **Chapters 3** and **4**.

2.8 CONCLUSIONS

Encapsulation of perovskite solar cells is one of the most critical challenges for the future of this emerging PV technology. There are few studies on this topic and to the best of my knowledge, the present thesis is the first attempt on application of hermetic glass-glass encapsulation for PSCs.

The first optimized sealing configuration, using glass frit C deposited on the top and bottom glass substrates (C-C), was critical to achieve further developments. Small size encapsulation was achieved at room temperature *via* quasi-

simultaneous method with laser power of 50 W and 9 loops at a scanning velocity between 150 $mm \cdot s^{-1}$ to 220 $mm \cdot s^{-1}$. Larger (70 × 70 mm^2) devices were laser sealed using contour method at process temperature of *ca.* 120 °C. The contour sealing was optimized by RSM method to obtain optimal sealing conditions of 47 W and 250 $mm \cdot s^{-1}$ for laser power and scanning velocity, respectively. The fresh encapsulated devices showed helium leak rate of 6.74 × 10^{-9} $atm \cdot cm^3 \cdot s^{-1}$ and maintained their leak rates after 50 thermal cycles (7.46 × 10^{-9} $atm \cdot cm^3 \cdot s^{-1}$) and 10 humidity-freeze cycles (1.32 ×10^{-8} $atm \cdot cm^3 \cdot s^{-1}$) performed according to the IEC standard tests. Therefore, the C-C sealing configuration showed the hermeticity required for PSC application. However, the electrically conductive nature of glass frit C makes it incompatible for sealing perovskite solar cells.

The C-B sealing configuration was developed based on the unique thermal conductivity of glass frit C combined with the low melting temperature and electrical insulating properties of glass frit B. Two cavity size of large and extra-large dimension devices were sealed at 120 °C process temperature with 38 W laser power and 200 $mm \cdot s^{-1}$ scanning velocity. The 7 × 7 cm^2 sealed devices of C-B configuration displayed an initial leak rate of 6.81 × 10^{-8} $atm \cdot cm^3 \cdot s^{-1}$ air, and 8.93 × 10^{-8} $atm \cdot cm^3 \cdot s^{-1}$ air leak rate after 5 humidity-freeze cycle test, respectively; these values comply with the hermeticity requirements of the MIL-STD standard.

Although the C-B sealing configuration is suitable for encapsulating HTM-free PSCs, the 120 °C process temperature of this sealing configuration causes PCE drop of the cells. Addition of glass frit A to this sealing configuration improved the overall thermal conductivity of the sealing configuration.

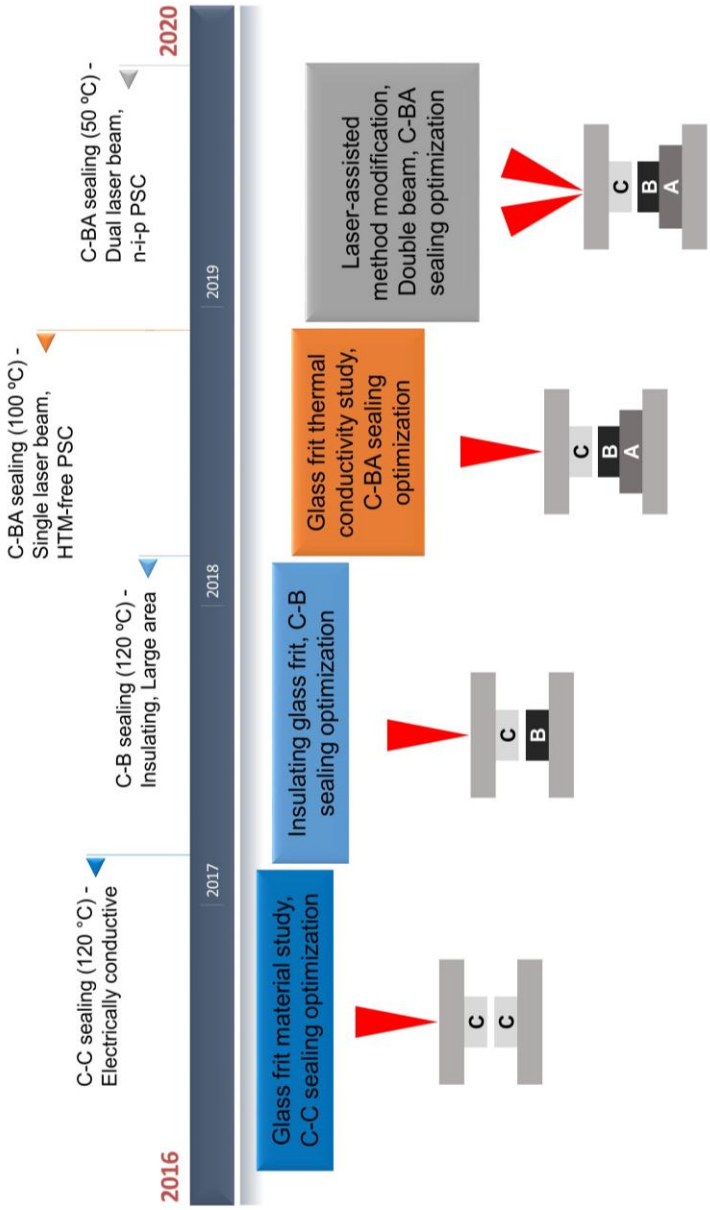

Figure 2.34. Timeline for evolution of the laser-sealing encapsulation method for PSC application.

The C-BA sealing configuration benefits from the two previously studied structures. The better thermal conductivity of glass frit A compared with the glass substrate, extends the overall thermal shock resistance of the sealing

configuration, therefore permitting process temperature below *ca.* 100 °C, and shorter dwell times. Conventional single laser beam contour sealing method with 41 W and 160 mm·s^{-1} scanning velocity achieved C-BA bonding at 100 °C, for dwell time of less than 40 min; appropriate for HTM-free perovskite solar cells. Dual laser beam sealing method of contour and quasi-simultaneous beam radiation was used to achieve the encapsulation at 50 °C furnace temperature and short 90 s dwell time at 100 °C, suitable for conventional n-i-p devices fabricated with HTM layers such as PTAA with good thermal stability. These sealed devices displayed high hermeticity with helium leak rate of *ca.* 1.71×10^{-8} atm cm^3 s^{-1}.

The laser-assisted sealing using glass frit was achieved at temperatures lower than the thermal decomposition limits required for PSC applications, ensuring no thermal damage to the cell. The heat affected zone of the laser-assisted sealing is *ca.* 3 mm; therefore, while the temperature of the glass frit sealant reaches *ca.* 380 °C, the temperature of the components of the PV device would be kept at below 100 °C.

2.9 REFERENCES

1. R. Knechtel, M. Wiemer and J. Frömel, *Microsystem Technologies*, 2005, **12**, 468-72.
2. Y. Lai, Z. Chen, Y. Huang and J. Zhang, *Proceedings - Electronic Components and Technology Conference*, 2012, 2036-41.
3. R. Sastrawan, J. Beier, U. Belledin, S. Hemming, A. Hinsch*, et al.*, *Solar Energy Materials and Solar Cells*, 2006, **90**, 1680-91.
4. W. M. Steen and J. Mazumder, *Laser material processing*, springer science & business media, 2010.
5. D. Zhang and L. Guan, in *Comprehensive Materials Processing*, eds. S. Hashmi, G. F. Batalha, C. J. Van Tyne and B. Yilbas, Elsevier, Oxford, 2014, pp. 125-69.
6. F. Ribeiro, J. Maçaira, R. Cruz, J. Gabriel, L. Andrade*, et al.*, *Solar Energy Materials and Solar Cells*, 2012, **96**, 43-9.
7. R. Knechtel, in *Handbook of Wafer Bonding*, 2012, pp. 1-17.
8. Wikimedia, *https://commons.wikimedia.org/wiki/File:Soda-lime_glass,_typical_transmission_spectrum_(2_mm_thickness).svg*, 2020.
9. W. Shi, Q. Fang, X. Zhu, R. A. Norwood and N. Peyghambarian, *Applied Optics*, 2014, **53**, 6554-68.
10. Thorlabs, *https://www.thorlabs.com/newgrouppage9.cfm?objectgroup_id=10766*, 2020.
11. SpecialOptics, *https://specialoptics.com/*, 2020.
12. Edmundoptics, *https://www.edmundoptics.eu/*, 2020.
13. A. Martínez-Conde, T. Krenke, S. Frybort and U. Müller, *Wood Science and Technology*, 2017, **51**, 943-66.
14. J. Holtkamp, A. Roesner and A. Gillner, *International Journal of Advanced Manufacturing Technology*, 2010, **47**, 923-30.
15. T. J. Lu and N. A. Fleck, *Acta Materialia*, 1998, **46**, 4755-68.

16. MIL-STD-883H, United States Department of Defense, 2010.
17. IEC61646, International Electrotechnical Commission, 2008.
18. D. C. M. Raymond H. Myers, Christine M. Anderson-Cook, *Response Surface Methodology: Process and Product Optimization Using Designed Experiments, 4th Edition*, John Wiley & Sons, Inc., 2016.
19. W. Wang, Y. Xiao, X. Wu and J. Zhang, *Optics & Laser Technology*, 2016, **77**, 111-5.
20. D. Sparks, *Chip Scale Review*, 2016, **20**, 36-9.
21. H. Greenhouse, R. Lowry and B. Romenesko, *Hermeticity of Electronic Packages*, Elsevier Inc., Oxford, 2012.
22. R. C. Kullberg and R. K. Lowry, IMAPS International Conference and Exhibition on Device Packaging - In Conjunction with the Global Business Council, GBC 2008 Spring Conference, 2008.
23. R. Clarke and A. Dermarderosian, Microelectronics 1998, 1998.
24. A. Goswami and B. Han, *Microelectronics Reliability*, 2008, **48**, 1815-21.
25. K. V. K. RAO, S. V. N. NAIDU and L. IYENGAR, *Journal of the American Ceramic Society*, 1970, **53**, 124-6.

CHAPTER 3

OPTIMIZATION OF LASER-ASSISTED GLASS FRIT ENCAPSULATION FOR HTM-FREE DEVICES

“I don't exactly know what I mean by that, but I mean it.”

J.D. Salinger - *The Catcher in the Rye*

Reprinted from peer-reviewed article:

***S. Emami**, J. Martins, D. Ivanou and A. Mendes, Journal of Materials Chemistry A, 2020, 8, 2654-62.*

3 OPTIMIZATION OF LASER-ASSISTED GLASS FRIT ENCAPSULATION FOR HTM-FREE DEVICES

Though perovskite solar cells (PSCs) are rapidly emerging into photovoltaic (PV) community, their long-term stability raises huge concerns for their future commercialization. PSCs are sensitive to humidity and temperature. A hermetic encapsulation is crucial for PSCs not only to prevent them from external environmental effects but also to avoid Pb-containing materials of the cells to leak out. An advanced laser-assisted glass-frit encapsulation method is developed to seal HTM-free PSCs. The long-term stability of the laser-sealed devices are examined at harsh environmental conditions of humidity and temperature exposure tests. The hermetically sealed PSCs have passed 70 thermal cycles (-40 °C to 85 °C) and 50 h damp heat (85 °C, 85 % RH) tests according to IEC61646 standard. Power conversion efficiency of hermetically encapsulated PSCs remained constant for 500 h under humid air feeding exposure (80 ± 5 % RH); non-hermetically encapsulated devices degraded after *ca.* 50 h. This work indicates that the hermeticity level of an encapsulation plays a key role on the stability of the devices at humid environment. Therefore, a hermetic encapsulation is vital for the industrialization of PSCs.

3.1 INTRODUCTION

Perovskite solar cells (PSCs) were first reported in 2009 by Kojima *et al.* [1] with power conversion efficiency (PCE) of 3.8 %. In only 10 years their PCE have reached to values as high as 25.2 % for a single junction and 29.1 % in monolithic tandem with silicon [2]. To date, most of the research effort is intensely focused on achieving high PCEs and little attention has been paid to long-term stability. High PCEs and simple fabrication method, allows perovskite solar cells to be a strong candidate for entering the photovoltaic (PV) market. However, the future commercialization of PSCs relies on long-term stability assurance. Most of the long-term stability research is dedicated to perovskite material and device structure modifications neglecting the PSCs encapsulation. Here, we show the crucial importance of hermetic encapsulation for long-term stability of PSCs.

The most common instability sources of PSCs are temperature and humidity [3]. To pass the requirements of the common PV standard tests such as IEC61646, PSCs must be stable at the temperature range of -40 °C to 85 °C and relative humidity of 85 % [4]. Therefore, the device should be fabricated with thermally stable materials and properly sealed to avoid humidity and moisture related issues. The thermal stability of PSC depends on its device structure. Common PSCs include electron transport layer (ETL), mesoporous scaffold, perovskite absorber, hole transport material (HTM) and back contact. While most ETLs and scaffolds are thermally stable, perovskite absorbers and HTMs decompose at elevated temperatures [5]. Perovskite absorbers are commonly synthesized with cations such as methylammonium (MA), formamidinium (FA) and Cs along with Pb. The most widely used $MAPbI_3$ is stable up to 120 °C [6] , while $FAPbI_3$ and $Cs_{0.10}FA_{0.90}Pb(I_{0.83}Br_{0.17})_3$ display better thermal stability [7, 8]. Nevertheless, all of the aforementioned perovskites are thermally stable at 85 °C; hence they would pass the requirements of the IEC standard. In contrary, widely used organic HTM such as spiro-OMeTAD (2,2´,7,7´-tetrakis(N,N-dip-methoxyphenyl-amine)9,9´ spirobifluorene decompose at *ca.* 70 °C [9]. Other HTMs such as PTAA (poly(triarylamine)) , CuSCN (copper (I) thiocyanate) and CuPC (copper

phthalocyanine) show thermal stability at 85 °C [8, 10-12]. In this context, HTM is the most vulnerable part of the device for passing industry related standards.

Since perovskite materials are capable of transporting both electrons and holes [13], PSCs can be fabricated without HTM layer [14, 15]. HTM-free structure is a promising candidate for commercialization of PSCs due to its simple air processed fabrication. These devices are fabricated by infiltration of perovskite crystals precursor into screen printed mesoporous stack layers of TiO_2 scaffold/ insulation layer (e.g. ZrO_2, Al_2O_3)/ back contact (e.g. Au, C). A fully screen printed HTM-free mesoscopic TiO_2/ZrO_2/C device with mixed cation perovskite of 5-ammoniumvaleric acid (5-AVA) and MA reached a certified PCE of 12.8 % and 1000 h stability in ambient air [16]. The hydrophobic carbon back contact in this structure improves the humidity stability issues of the cell, while the lack of HTM makes the devices stable up to the thermal stability of the perovskite absorber (*i.e*. above 85 °C). A study by Grätzel *et al.* showed that the performance of the HTM-free PSCs can be even further improved through humidity and thermal exposure (HTE) treatment [17]. They showed that *ca.* 115 h of 70 ± 5 % RH at 40 °C treatment of the cells would assist the crystal growth of perovskite at the TiO_2 scaffold [17]. The hydrophobic carbon back contact acts as a blocking mesh to avoid penetration of liquid water while permitting water vapor diffusing through ZrO_2 to assist the irreversible $(5\text{-AVA})_{0.05}(MA)_{0.95}PbI_3$ crystal growth not only in TiO_2 but also in the entire mesoporous media [17].

Although intense effort is being followed by many researchers for developing PSCs stable to humid environments, successful commercialization of these PV devices require encapsulation. Thus, the encapsulation plays a key role in the transition of PSCs from laboratory scale devices to real outdoor commercial panels. In this context, a suitable airtight encapsulation can be used to avoid humidity and oxygen exposure of the PSCs, regardless of the device structure. There are three levels of hermeticity for an encapsulation: i) gross leak, ii) non-hermetic and iii) hermetic. Gross leak test is commonly performed by tracing liquid penetration into the cavity of encapsulated sample immersed in a liquid

(*e.g.* dye). A sample with no gross leak must be further examined with a gas (*e.g.* helium) for fine leaks. According to MIL-STD-883 standard, a sealing with helium leak rate lower than 5×10^{-8} atm cm^3 s^{-1} is considered as hermetic [18].

In addition, the long-term stability of a hermetic sealing must be examined by simulated climatic tests to ensure the > 20 years lifetime of the encapsulation. The long-term stability of sealing is commonly studied by environmental cycling tests as described in IEC61646 [4]. These tests include:

- Thermal cycle test: -40 °C to 85 °C (no RH control);
- Damp heat test: 85 °C and 85 % RH.

The long-term stability of an encapsulation is, perhaps, even more critical than its initial hermeticity. Though several sealants display hermeticity initially, few of them can retain their hermeticity after stability tests [19].

To date, various sealant and sealing methods have been used for PSCs. The sealing method can be divided into two major categories: i) thin film in which a thin protective layer is deposited on top of the cell [20]; ii) edge seal in which the sealant is placed around the cell and it is bonded to a cover substrate [21]. For thin film encapsulation method, the coefficient of thermal expansion (CTE) of the protective layer should be close to the components of the cell, to avoid mechanical damage during stability tests [22]. In contrast, edge seal method is more reliable for stability tests; however, this method commonly requires additional thermal or light curing steps; therefore, the additional curing step should not affect the performance of the device.

The most widely used edge sealants for PSCs are epoxy resin and thermo-plastics. UV illumination can degrade perovskite solar cells containing TiO_2 layer [23]. Thus for UV curing of epoxy resin the active area most be masked to avoid performance losses on the device [21]. In the case of thermal curing epoxy sealants, the heating step can cause contamination to the cell due to outgassing

of the epoxy [24]. Thermo-plastic bonding is commonly achieved at *ca.* 140 °C in 10 min to 20 min under an applied mechanical force. In this context, sealants such as EVA (ethylene vinyl acetate) [22] and a combination of polyolefin "ENLIGHT" with butyl rubber [25], display superior performance after thermal and damp heat stability tests.

Glass frit encapsulation is an alternative edge sealant to thermo-plastic sealing. While common thermo-plastics are neither hermetic nor long-term stable, glass frit encapsulation displays a unique hermeticity even after stability tests according to IEC61646 [19]. Similar to thermo-plastics, glass frits bonding is achieved through thermal treatment. Most glass frits have a bonding temperature above 380 °C; higher than the thermal decomposition of the perovskite solar cells. To decrease the process temperature of the encapsulation a laser-assisted sealing method can be used. This method uses a laser beam to locally heat up the sealant material to its melting point while the device is kept at lower process temperature.

Laser-assisted material processing has been widely used for various industrial solutions. One of the highlighted advantages of laser-processing is its localized material processing feature. Therefore, for laser-assisted encapsulation of solar cells, the active area of the device is not required to be masked for avoiding performance losses due to sealant processing. Laser-assisted glass frit encapsulation for solar cells was first reported in 2012 by Mendes *et al.* for dye-sensitized solar cells (DSCs) [26]. A detailed description of laser-assisted sealing method was presented in **Chapter 2**. Laser-assisted glass frit sealing can produce long-term stable hermetic encapsulation [19, 27]. Moreover, the glass frit laser-sealing process can be applied to encapsulate large devices [27]. Therefore, this process can provide a scalable hermetic encapsulation for PSC application. A desired laser-assisted sealing for PSC application should be electrically insulating and should display a process temperature below the thermal decomposition of the components of the solar cell.

To date, the most effective encapsulation method reported is by McGehee *et al.* in which, the authors used a relatively wide sealant material (15 mm); therefore, current collectors were required for charge collection [25]. An industrially compatible encapsulation solution for PSCs must not affect the performance of the cells and should be as narrow as possible to minimize the cost.

The goal is to find a laser-assisted sealing configuration suitable for encapsulating HTM-free triple mesoporous PSCs. The main requirements include: i) electrically insulating glass frit configuration, ii) process temperature lower than the decomposition of perovskite absorber ($(5\text{-AVA})_{0.05}(MA)_{0.95}PbI_3$) and iii) compatible to the fabrication of the solar cell.

The thermal decomposition limit range of the double cation 5-AVA and MA perovskite is in the range of 100 °C to 140 °C. The decomposition rate of perovskite depends on the dwell time at the processing temperature. Thus at higher temperature threshold shorter dwell time is required for perovskite to decompose.

Among the three glass frit configuration reported in **Chapter 2**, C-C is not suitable due to electrical conductivity. C-B configuration maybe used, however the 120 °C process temperature of this configuration can cause perovskite decomposition at moderate dwell time range. Thus, the most suitable option is C-BA configuration with process temperature of 100 °C. The single laser beam sealing of C-BA configuration can achieve hermetic bonding at 100 °C and process dwell time range of 30 to 45 min. This scalable encapsulation method is compatible to the fabrication process of HTM-free PSCs and does not require additional current collectors. The current process temperature is compatible with HTM-free PSC while it can be also applied to any other PSC device configuration such as conventional HTM-based or inverted cells with superior thermal stability.

3.2 MATERIALS AND METHODS

3.2.1 DEVICE FABRICATION

HTM-free devices were fabricated by sequential screen print deposition of mesoporous layers of TiO_2, ZrO_2 and carbon back contact. The perovskite absorber is then infiltrated into the mesoporous structure by drop casting of the precursor solution on top of the carbon layer. Similar to TiO_2, ZrO_2 and C, glass frits are also required to be sintered after screen printing. Therefore, the sintering steps of the glass frits and components of the device must be compatible to avoid thermal degradation of both sealant and the cell components.

The substrates (2.2 mm TEC 7 from Greatcell Solar) were ultrasonically washed in distilled water and detergent. After drying, the substrates were further cleaned with UV-O_3 for 20 min. Then, a precursor solution of titanium diisopropoxide bis(acetylacetonate) in anhydrous 2-propanol was used to deposit a compact TiO_2 blocking-layer by spray pyrolysis at 450 °C. After, a 2 × 2.5 cm^2 rectangular shape with 4 mm linewidth of glass frit A was screen-printed and sintered at 500 °C. Then, the mesoporous layers of TiO_2 (T165/SP from Solaronix) and ZrO_2 (ZT/SP from Solaronix) were screen-printed and annealed at 500 °C, respectively. Afterwards, a 2 × 2.5 cm^2 rectangular shape with 1 mm linewidth of glass frit B was screen-printed and sintered at 400 °C. Then, the carbon back contact (Elcrocarb B/SP from Solaronix) was screen-printed and sintered at 400 °C. Finally, 5 µl of $(5\text{-AVA})_{0.05}(MA)_{0.95}PbI_3$ in GBL precursor solution (from Solaronix) was dripped on top of the mesoporous structure and sintered at 70 °C. The cover glass substrate was cleaned as described for cell substrates, before screen-printing and 450 °C sintering of a 2 × 2.5 cm^2 rectangular shape with 1 mm linewidth of glass frit C. For large area devices, the glass frit size and precursor solution volume were 4 × 4 cm^2 and 20 µl, respectively. The entire device fabrication process was performed at atmospheric condition with RH range 40 % to 60 %- **Figure 3.1**.

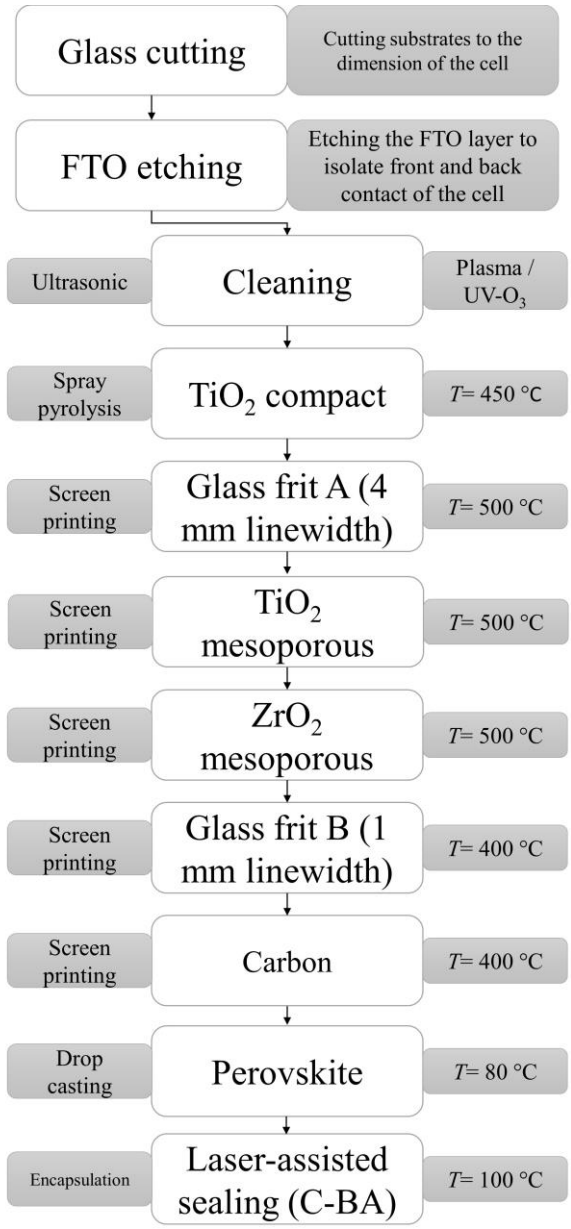

Figure 3.1. Fabrication steps for laser-assisted encapsulation of HTM-free perovskite solar cell devices.

Devices were treated with humidity and thermal exposure (HTE), to improve their performance. Saturated salt solution environment was used for HTE treatment

before encapsulation. Treatment was carried out by placing the cells inside a desiccator filled with a saturated solution of NaCl to achieve *ca.* 70 % RH at 40 °C inside a furnace- **Figure 3.2**.

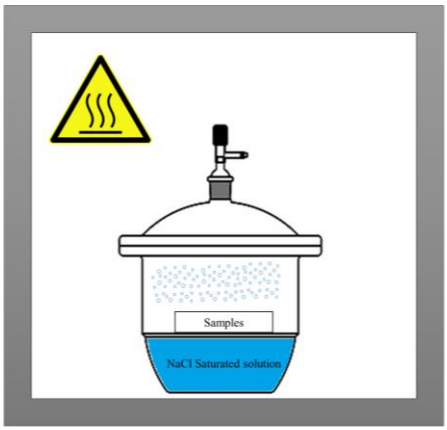

Figure 3.2. Schematic view of saturated salt solution environment for HTE treatment.

3.2.2 LASER-ASSISTED ENCAPSULATION

The sealing experiments were performed with LaserBox apparatus. Therefore, the conventional single laser beam method sealing was used for bonding C-BA glass frit configuration. The laser-assisted encapsulation process was carried out by heating the cells to the desired sealing process temperature for various dwell times. Design of experiments methodology was used to optimize the effect of encapsulation process on the performance of the PSC device. The optimal laser-sealing conditions were: 41 W of power and 210 mm s^{-1} scanning velocity at *ca.* 0.6 mm spot size. **Figure 3.3** illustrates the schematic view of glass frits configuration and PSC device structure.

(**a**)

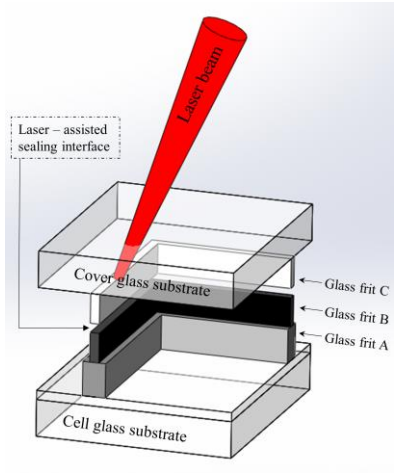

(**b**)

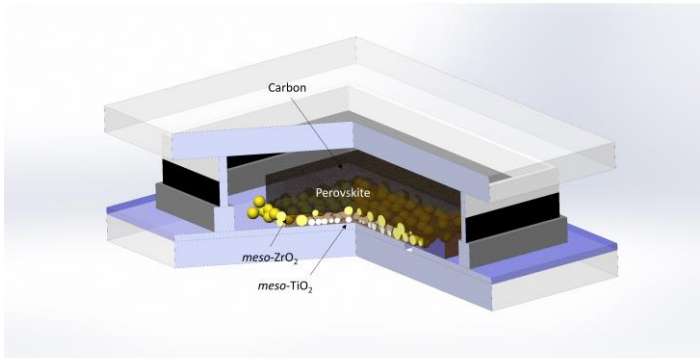

Figure 3.3. Schematic view of (**a**) the triple layer glass frit laser-assisted sealing C-BA configuration, and (**b**) encapsulated HTM-free PSC device.

3.2.3 HERMETICITY TEST OF ENCAPSULATED DEVICE

The hermeticity of the optimized encapsulation method was measured according to the MIL-STD-883 standard [18]. A previous study [27] showed that this test method is only valid for devices with internal cavity area of < 5.5 × 5.5 cm^2. The cavity area of the cells for the encapsulated cells are 2 × 2.5 cm^2 and 4 × 4 cm^2; therefore, the MIL-STD standard is valid. The leak rates of the encapsulated packages were measured according to method 1014.13, A2. For method A2 the leak rates must be reported in the equivalent air leak rate (*L*). The equivalent air leak rate (*L*) reject limit for the under study encapsulation is 1×10^{-7} atm cm^3 s^{-1}

Air. Leak rates higher than 1×10^{-5} atm cm^3 s^{-1} Air are considered as gross leakages. The test conditions for fine helium leak rate were 15 h of He bombing at 2 bar. More details on the leak rate measurement method can be found in **Chapter 2**.

3.2.4 EXTERNAL ENVIRONMENTAL STABILITY TESTS

The climatic tests according to IEC61646 was performed in an industrial climatic chamber (Fitoclima from Aralab). **Figure 2.18** shows the temperature and humidity history for the climatic tests. The humid air feed was produced by humidifying a 450 mL min^{-1} dry air feed to a cylindrical column filled with distilled water. The humid air was then fed to a 17.5 × 17.5 × 6 cm^3 stainless steel chamber where the devices were stored. The temperature of chamber was kept constant using a hotplate, and the humidity level was monitored with a humidity sensor.

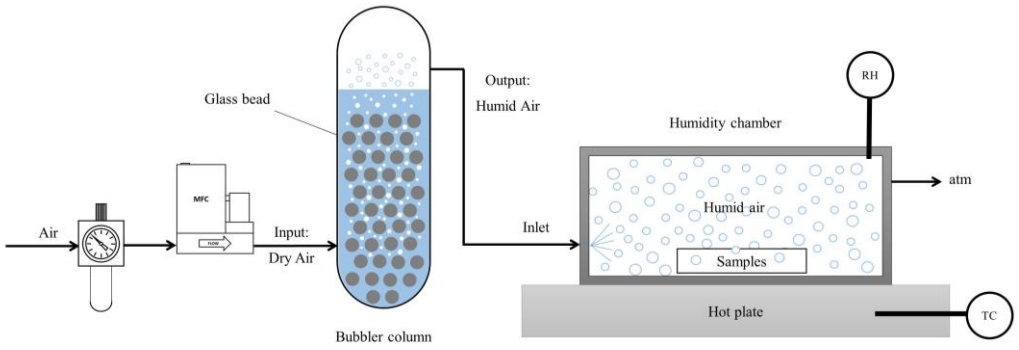

Figure 3.4. Schematic view of humid-air feeding chamber.

Figure 3.4 shows the scheme of the humid air exposure chamber apparatus. Three groups of devices (with different hermeticity level) were tested for humid air feeding exposure; no sealing, non-hermetic sealing and hermetic sealing. The quality of the laser-sealed devices depends on the laser emission power

and scanning velocity. Commonly, optimized laser condition produces a high quality crack-free sealing; however, in some cases the final sealing may include defects such as cracks and delamination. If a device with minor defects on the sealing passes a gross leak test, its hermeticity would be categorized as non-hermetic.

3.2.5 CHARACTERIZATION

The current-voltage (*J-V*) curves were recorded by an electrochemical workstation (Zahner Zennium) under AM1.5 illumination of 100 mW cm^{-2} using Oriel class ABA LED solar simulator (MiniSol LSH 732 from Newport). The illumination light was calibrated with a Si reference cell. The scan rate for *J-V* curve was 4 mV s^{-1} and the masked devices (*ca.* 0.2 cm^2 and 1 cm^2 mask area for small and large device size, respectively) were soaked with light for *ca.* 60 s before measurements. The reflectance spectra of the cells were measured with a UV-VIS-NIR spectrophotometer (Shimadzu UV-3600). The incident photon to current conversion efficiency spectra was recorded without biased light illumination using a semi-automatic station (Newport). The XRD spectra were collected on Philips X'Pert MPD diffractometer (Cu Kα radiation). The SEM images of the glass frit sealing were acquired with a benchtop microscope (Phenom XL).

3.3 RESULTS AND DISCUSSION

3.3.1 ENCAPSULATION OPTIMIZATION

The process temperature and dwell time of laser-assisted sealing procedure can affect the performance of the HTM-free PSC devices. Therefore, a response surface methodology (RSM) model with two-factor variables (sealing process temperature and heating dwell time) and three-factor response (sealing quality, sealing reproducibility and sealing process effect on performance of the PSC device) were considered, to minimize the mentioned effect. **Table 3.1** shows the

factors of the model; the intervals for sealing process temperature and heating dwell time were 80 °C < *T* < 120 °C, and 20 min < *t* < 60 min, respectively.

Table 3.1. Factors, intervals and goals for response surface methodology (RSM) method for sealing process optimization

Factor (variable/ response)		Interval		Optimization goal
		Lower limit	Upper limit	
Sealing process temperature / °C	Variable	80	120	In range
Sealing dwell time / min	Variable	20	60	In range
Sealing quality	Response	0	10	Maximize (weight = 0.375)
Reproducibility	Response	0	10	Maximize (weight = 0.125)
Effect on the PSC	Response	0	10	Minimize (weight = 0.5)

The responses interval range were 0 to 10. For sealing quality, the response was rated based on the visual inspection of the encapsulation after laser processing. For sealing reproducibility, the response was based on the reproducibility of the sealing experiments. Finally, the sealing procedure effect on the PSC performance was ranked by analyzing the photovoltaic parameters of the cell before and after the encapsulation. Design expert 10 software was used for fitting the responses of the model. **Equations 3.1** to **3.3** and **Figure 3.5** show the predicted response functions and their contour plots.

$$\text{Quality} = -76.02 + 1.82\,T + 0.57t - 7.53 \times 10^{-3}tT - 0.01T^2 - 4.26 \times 10^{-3}t^2 + 7.19 \times 10^{-5}T^2t - 7.67 \times 10^{-5}Tt^2 + 2.13 \times 10^{-5}T^3 + 8.67 \times 10^{-5}t^3 \qquad \{R^2_{Adj} = 0.97 | R^2 = 0.78\} \qquad 3.1$$

$$\text{Reproducibility} = -71.92 + 1.36T + 0.02t + 4.66 \times 10^{-4}tT - 6.16 \times 10^{-3}T^2 - 2.57 \times 10^{-3}t^2 \qquad \{R^2_{Adj} = 0.95 | R^2 = 0.87\} \qquad 3.2$$

$$\text{Effect on device} = 42.2 - 0.91T - 0.24t + 3.10 \times 10^{-3}tT + 4.88 \times 10^{-3}T^2 - 1.43 \times 10^{-4}t^2 \qquad \{R^2_{Adj} = 0.94 | R^2 = 0.88\} \qquad 3.3$$

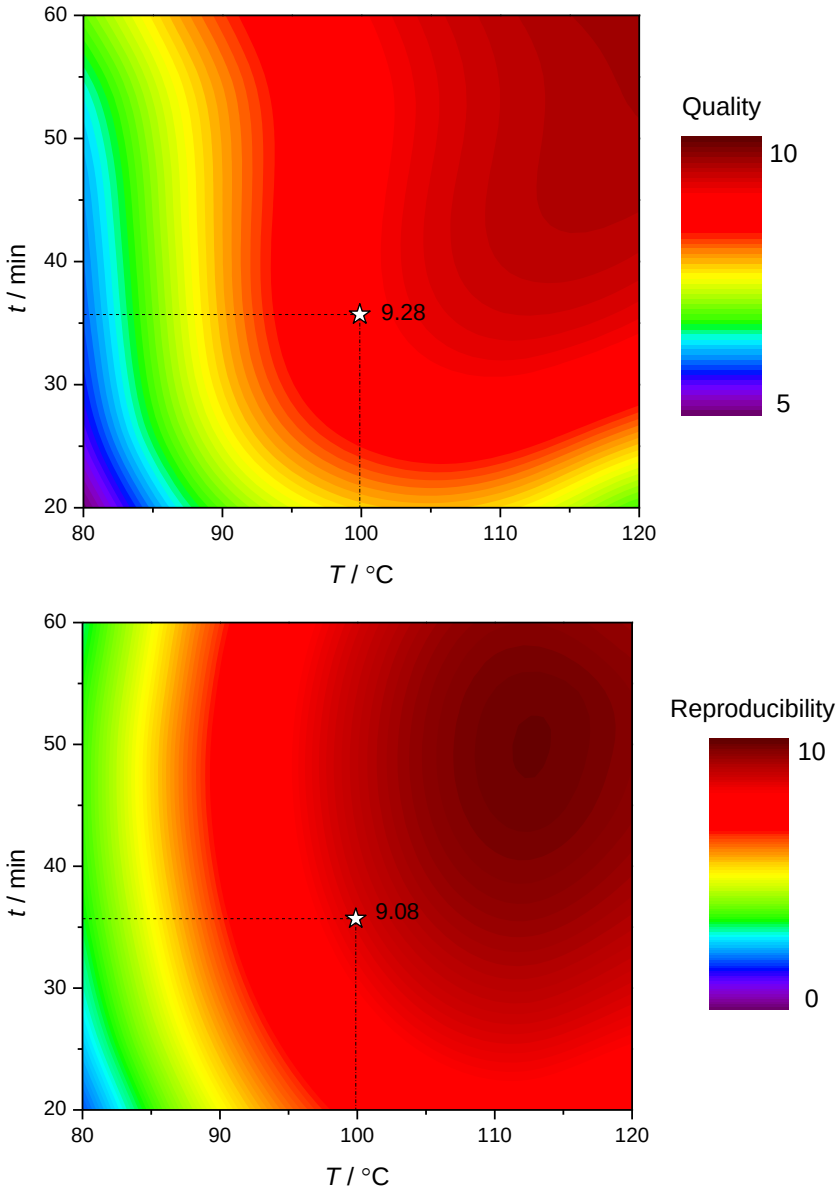

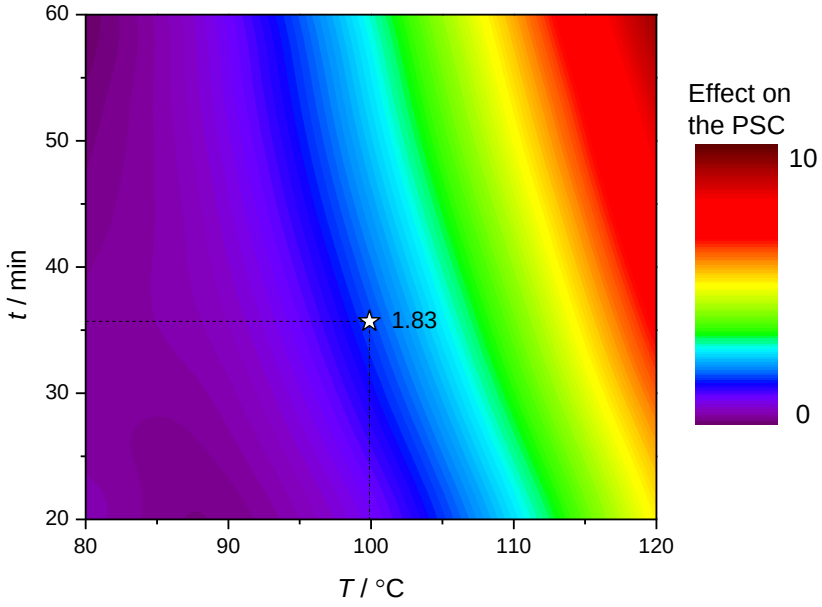

Figure 3.5. Contour plots for predicted response functions of the RSM model.

To optimize the multi response process, the desirability function was applied to the three responses of RSM model. The weight factors of the response for desirability function of sealing effect on the PSC, sealing quality and reproducibility were 0.5, 0.375 and 0.125, respectively. Therefore, the goal was set to minimize the performance loss of the cell and achieve high quality encapsulation with reasonable reproducibility rate. As shown in **Figure 3.6**, the highest desirability conditions can be achieved at 95 °C < *T* < 105 °C and 25 min < *t* < 40 min. The optimal condition is for *ca. T*= 100 °C and *t*= 35 min with a desirability value of 0.82.The optimal condition of RSM model is mostly valid for HTM-free devices with TiO_2/ZrO_2/C and $(5\text{-AVA})_{0.05}(MA)_{0.95}PbI_3$ perovskite absorber. As shown in **Figure 3.5** the highest encapsulation quality and reproducibility response are achieved at higher process temperature and dwell times, while the negative effect on the HTM-free PSC is more pronounced at temperatures higher than *ca.* 105 °C.

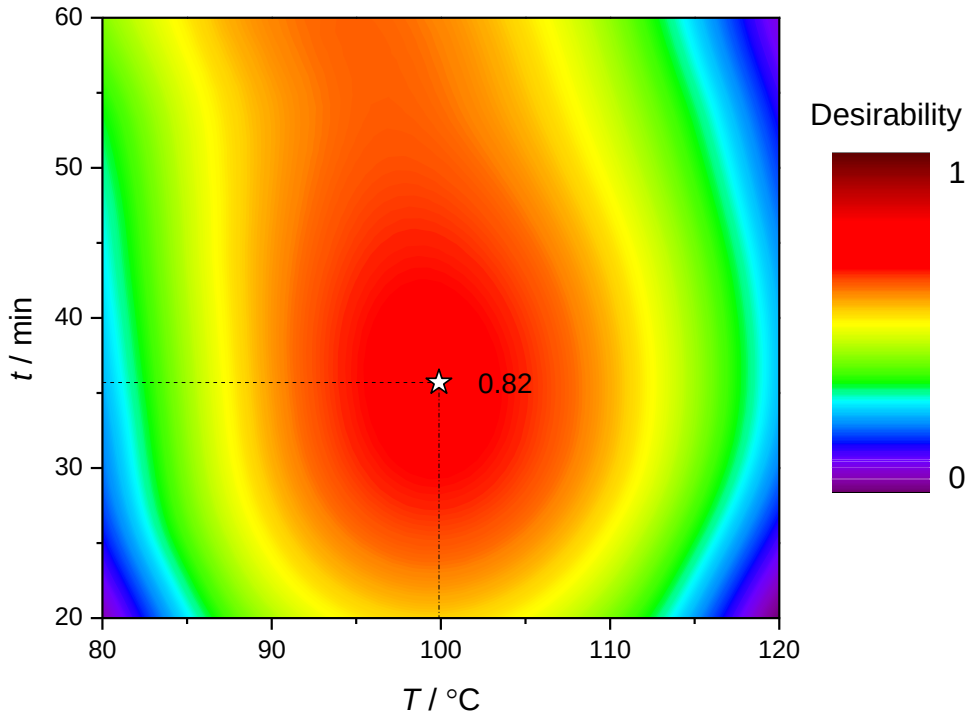

Figure 3.6. Contour plot of the desirability function of the responses for the RSM model to optimize the encapsulation procedure.

As mentioned, humidity and thermal exposure (HTE) improves the performance of HTM-free PSCs. **Figure 3.7** demonstrate the effect of HTE on the performance of the devices. While there was no change in the V_{oc} after the HTE treatment, a notable increase in the J_{sc} and PCE of the devices were achieved. For FF the results indicate a decrease after the HTE; however, since the *J-V* curves of fresh cells have a so-called “bump” (**Figure 3.7b**), the FF values for these cells should contain false positive errors while after HTE the results contain no such error. After the HTE treatments, the cells were sealed according to the optimal conditions of the RSM model.

(**a**)

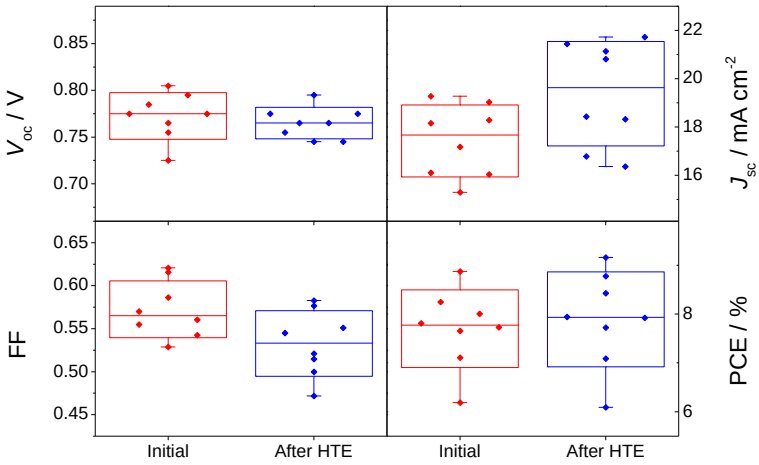

(**b**)

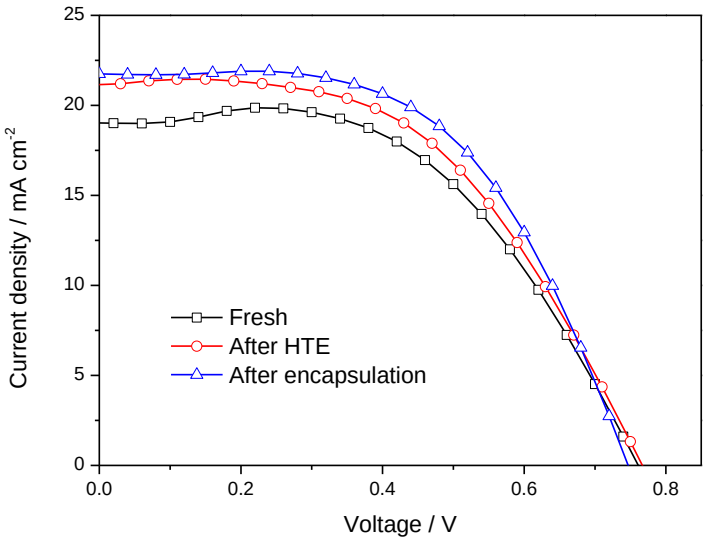

Figure 3.7. (**a**) 50 h of 70 % RH Humidity and temperature (40 °C) exposure (HTE) effect on the photovoltaic parameters of the devices, (**b**) *J-V* curve for a selected cell (4 mV s^{-1}, reverse bias); fresh, after HTE and after encapsulation.

As shown in the *J-V* curves of **Figure 3.7b**, the performance of the device remained unchanged after the encapsulation process. **Figure 3.8** presents the statics for the photovoltaic parameters (V_{oc}, J_{sc}, FF and PCE) of the tested devices before and after sealing.

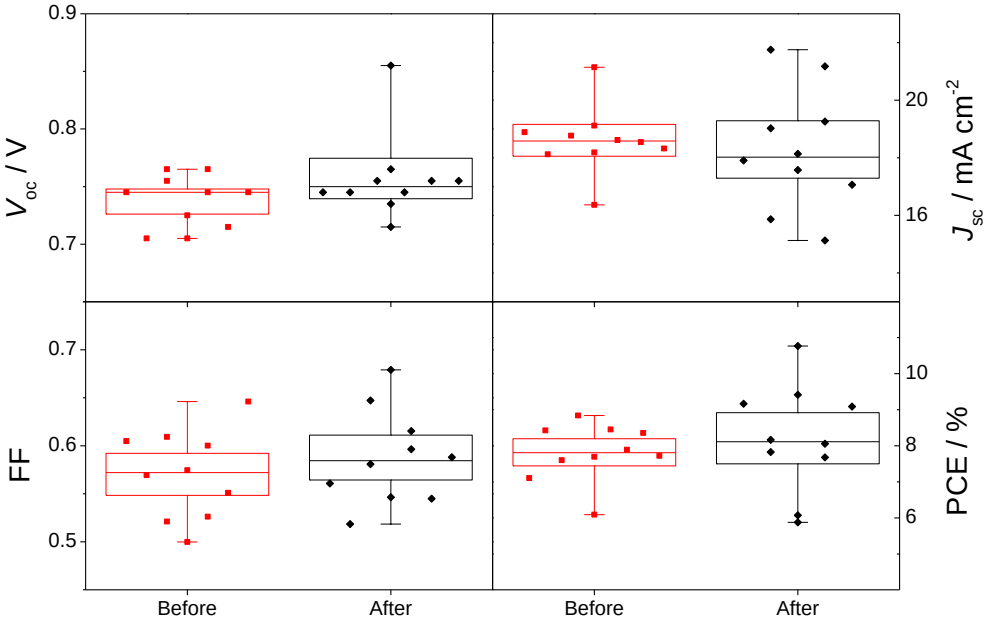

Figure 3.8. Statistics of photovoltaic parameters for a batch of 10 devices before and after encapsulation process (after stabilization of the cells). Boxes present the standard deviation and line bars indicate the maximum and minimum values.

To obtain stabilized cell performance, the results shown in **Figure 3.8** are for cells after *ca.* 7 days of their fabrication (or HTE treatment) and encapsulation process. The average results showed a slight improvement of V_{oc}, FF and PCE; and a minor decrease in J_{sc}. However, the standard deviation of the parameters after encapsulation has increased, which was assigned to the recrystallization of the perovskite during the heating step of the sealing process. The V_{oc} improved from 0.74 ± 0.02 V to 0.76 ± 0.04 V, the J_{sc} decreased from 18.61 ± 1.17 mA cm^{-2} to 18.29 ± 2.10 mA cm^{-2}, the FF improved from 0.57 ± 0.05 to 0.59 ± 0.05, and finally PCE improved from 7.82 ± 0.79 % to 8.21 ± 1.49 %. In general, the performance of HTM-free PSC improves during several days after their fabrication date [16]. Therefore, the overall improvement of the cells after encapsulation may be due to the combination of perovskite recrystallization

during the sealing process, and common stabilization improvements of the devices.

3.3.2 HERMETICITY

The hermeticity of the encapsulated packages measured according to A2 method of MIL-STD-883 standard. **Figure 3.9** shows the equivalent air leak rate (*L*) for the optimized conventional single laser beam C-BA glass frit sealed devices of small and large area size.

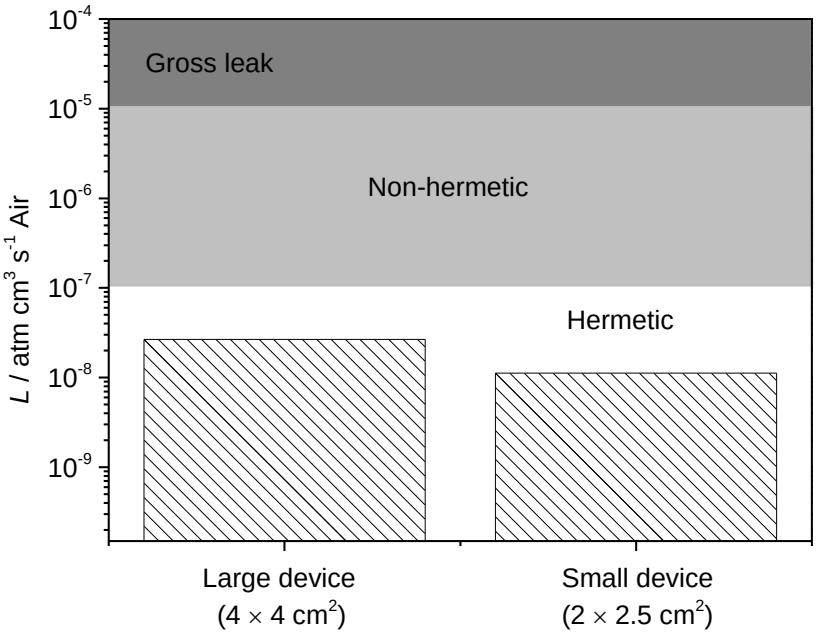

Figure 3.9. Leak rates for encapsulated devices (C-BA) of cavity size 2 × 2.5 cm^2 and 4 × 4 cm^2.

3.3.3 EXTERNAL ENVIRONMENTAL STABILITY

HTM-free devices similar to the present study display 1000 h operational stability under illumination without encapsulation [16]. Therefore, the stability of encapsulated devices of this structure was investigated under industry standard

tests and harsh humidity conditions. The long-term stability analysis was divided into two groups of experiments: i) ***climatic tests:*** stability of the hermetic encapsulation according to IEC61646 standard and ii) ***humid air feeding exposure:*** effect of humidity on hermetic and non-hermetic encapsulation.

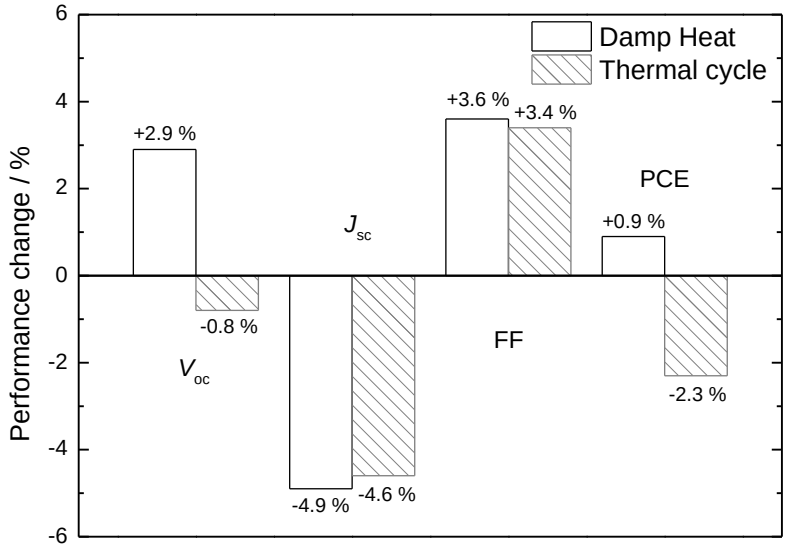

Figure 3.10. Changes in photovoltaic parameters of the hermetically encapsulated PSCs after thermal cycle and damp heat tests.

Climatic tests of 70 thermal cycles and 50 h damp heat according to IEC61646 standard were performed on hermetically laser-sealed devices. As shown in **Figure 3.10** the IEC standard tests had minimal effect on the hermetically sealed devices. Since the encapsulation is hermetic, there should be no humidity related effects on the cells during these tests. While the temperature during damp heat test is set to 85 °C, the temperature change from 85 °C to -40 °C of thermal cycle caused slight decrease in the PCE of the devices. This could be due to the CTE mismatch between components of the device (TiO_2, ZrO_2 and carbon), which can cause displacement of perovskite absorber in the scaffold and therefore grain boundary recombination. The CTE mismatch effect during

thermal cycle test has also been reported by other researchers [22]. The climatic test results showed that the encapsulation method is effective for elevated humidity and temperature cycling conditions.

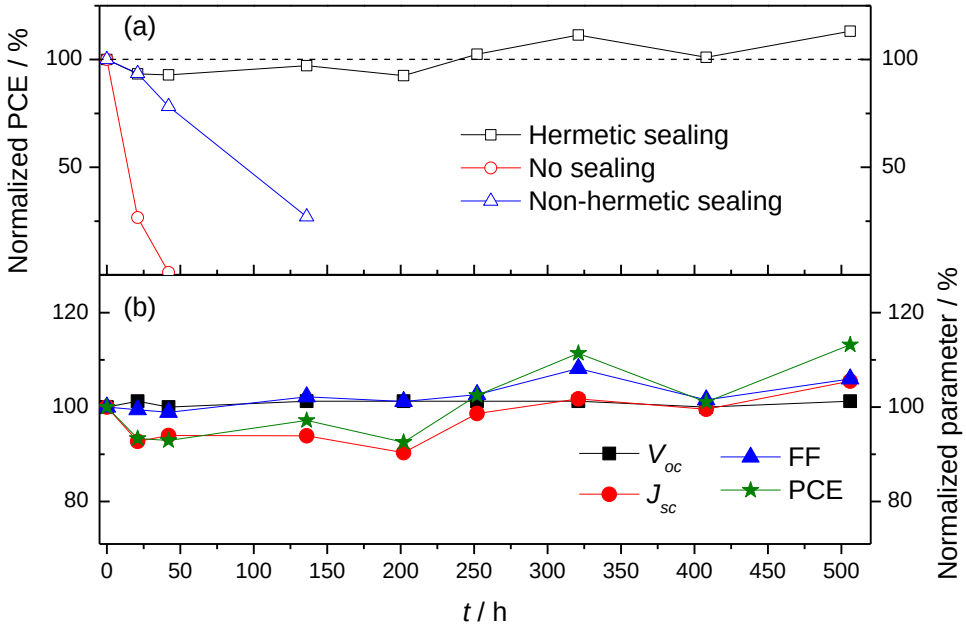

Figure 3.11. Humidity aging for 500 h of (**a**) hermetic, non-hermetic and no sealing devices; (**b**) photovoltaic parameters for a hermetically laser-assisted sealed PSC.

The effect of humidity on encapsulated devices with three hermeticity levels of "no sealing", "non-hermetic sealing" and "hermetic sealing" were investigated through humid air (80 ± 5 % RH) feeding exposure of the devices for 500 h. The humid air feeding procedure ensures the forced entry of humidity to the cavity of encapsulated devices under study. As shown in **Figure 3.11a** the performance of the "no sealing" devices rapidly dropped during the first hours of the humid air feeding test, while "non-hermetic sealing" cells showed losses after 50 h, and finally "hermetic sealing" PSCs retained their performance for 500 h. **Figure 3.11b** shows the 500 h history of the normalized photovoltaic parameters for a "hermetic sealing" device.

(**a**)

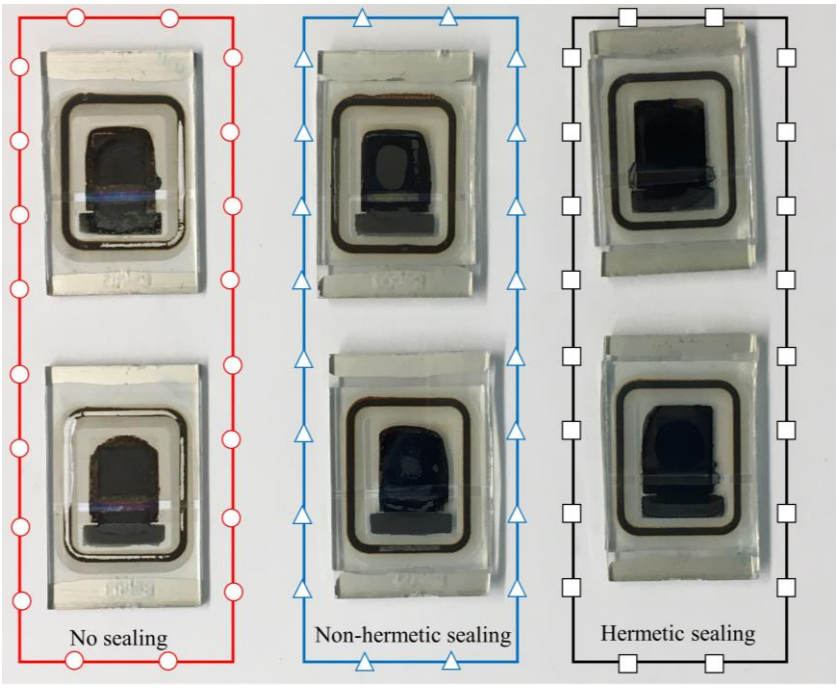

(**b**)

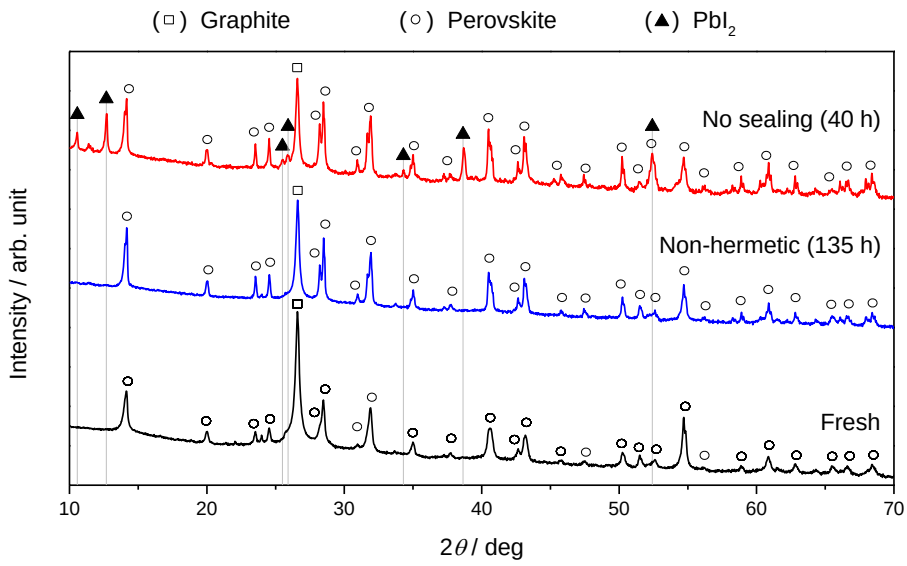

Figure 3.12. (**a**) Photograph of devices after the humidity aging test; no sealing (40 h), non-hermetic sealing (135 h) and hermetic sealing (500 h); (**b**) XRD patterns of complete device (glass/FTO/TiO_2/ZrO_2/$(5\text{-AVA})_{0.05}(MA)_{0.95}PbI_3$); fresh, "no sealing" and "non-hermetic" after 40 h and 135 h of humid air feeding test.

As shown in the photograph of **Figure 3.12a**, after 40 h of aging the dark black colored perovskite absorber of “no sealing” cells changed to yellowish color. The “non-hermetic sealing” cells showed a black to gray color change after 135 h of aging. The X-Ray Diffraction (XRD) of the “no sealing” sample indicates a strong PbI_2 peak, while the spectra for the “non-hermetic” device is quite similar to the fresh reference device - **Figure 3.12b**.

(**a**)

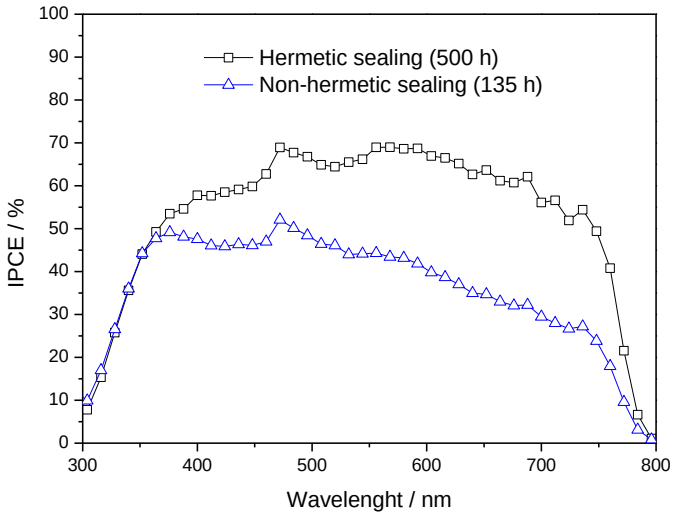

(**b**)

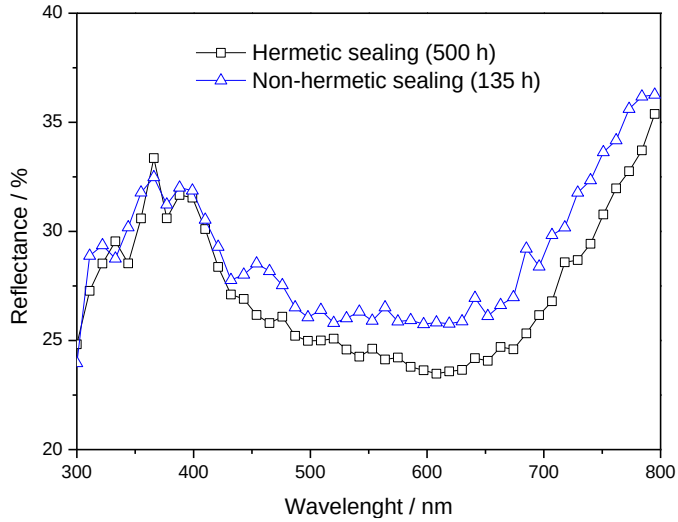

Figure 3.13. (**a**) IPCE (without biased light) and (**b**) reflectance for aged hermetic and non-hermetic sealing devices.

The Incident Photon-to-electron Conversion Efficiency (IPCE) for "non-hermetic" device shows a decrease of photocurrent quantum yield in the spectral region from 350 to 800 nm, which is the indication of partial decomposition of the perovskite to PbI_2 [28, 29] (**Figure 3.13a**). Furthermore, the grey colored perovskite and lead iodide mixture of the "non-hermetic" sample shows a higher reflectance value comparing to the pure black colored perovskite –**Figure 3.13b**.

(**a**)

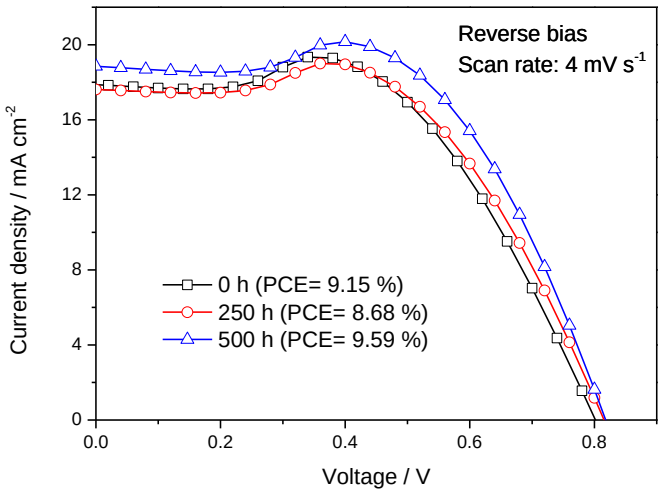

(**b**)

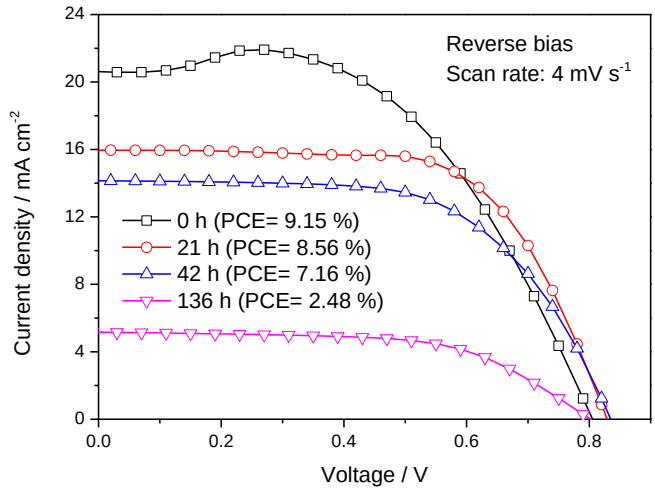

Figure 3.14. *J-V* curves for (**a**) hermetic and (**b**) non-hermetic sealed PSCs during humid air feeding stability test.

As mentioned before, the “bump” effect of *J-V* curve of fresh devices can be corrected through HTE treatment. Therefore, if a device is encapsulated without HTE treatment, the “bump” effect on the *J-V* curve can be corrected only if the sealing is “non-hermetic”. As shown in **Figure 3.14**, the humid air feeding affects the *J-V* curve of “non-hermetic” cell after 21 h of the stability test and gradually lowers the performance of the cell. In contrast, there are no changes in the *J-V* curves of the hermetically sealed device during 500 h stability test.

(**a**)

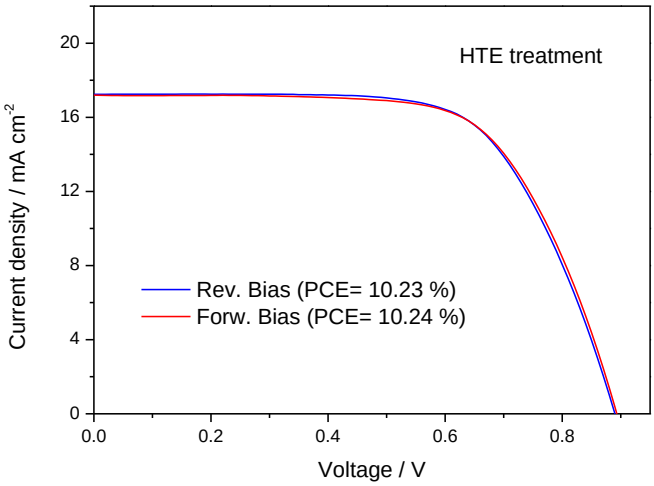

(**b**)

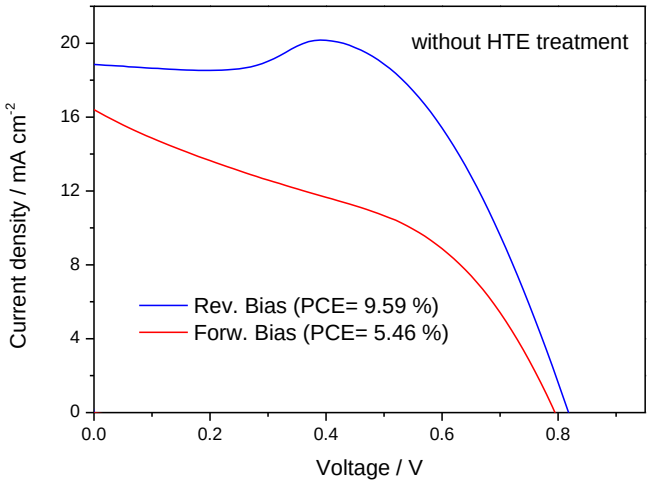

Figure 3.15. *J-V* curves (scan rate: 4 mV s^{-1}) for encapsulated device (**a**) with HTE (**b**) without HTE.

Regardless of HTE treatment before encapsulation, the performance of the cell should remain unchanged during the humidity stability test. However, the HTE treatment before sealing not only boost the performance of the devices but also results in hysteresis-free devices -**Figure 3.15**.

Figure 3.16 shows current *vs.* applied potential curves of a HTE treated hermetically sealed device before and after the humidity stability test.

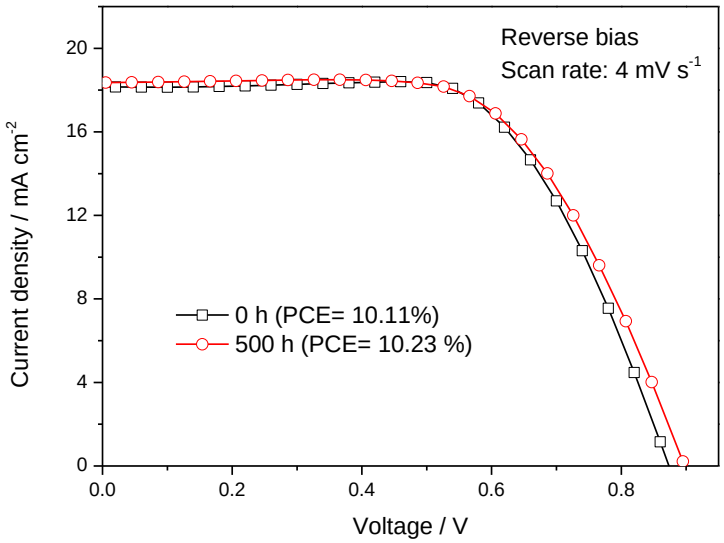

Figure 3.16. *J-V* curves of a hermetically sealed PSC, before and after 500 h humidity aging test.

3.3.4 LARGE-AREA DEVICE

The scale-up potential of the developed encapsulation method was shown by increasing the size of the devices from an internal cavity area of 2 × 2.5 cm^2 to 4 × 4 cm^2. Increasing the active area of the devices commonly results in PCE reduction due to the sheet resistance of the electrodes (FTO and carbon back contact). As shown in **Figure 3.17** the performance of the large area device remained unchanged after the encapsulation process, which confirms that the encapsulation is scalable.

(**a**)

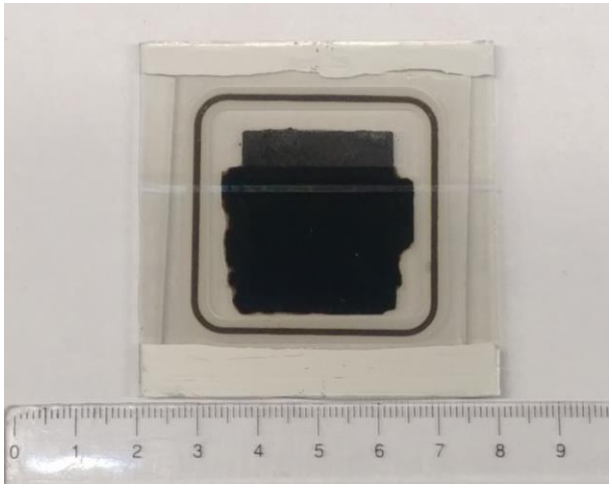

(**b**)

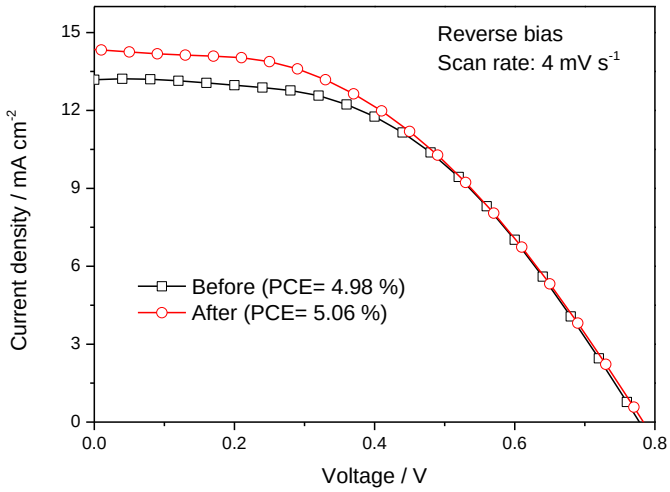

Figure 3.17. (**a**) Photograph and (**b**) *J-V* curve (scan rate: 4 mV s^{-1}) for a large area encapsulated device (before and after encapsulation).

3.3.5 HTM-BASED DEVICES

The optimal encapsulation condition (*ca. T*= 100 °C and *t*= 35 min) for single beam bonding of C-BA configuration were applied to encapsulate n-i-p HTM-based PSCs. Device structure *meso*-TiO_2 / $Cs_{0.10}FA_{0.90}Pb(I_{0.83}Br_{0.17})_3$ / HTM / Au with two HTM materials of PTAA and CuSCN were selected due to better thermal resistance. Despite the short thermal exposure time at 100 °C - 35 min,

the performance of the devices drastically dropped after the encapsulation - **Figure 3.18**. Since the annealing temperature of perovskite absorber ($Cs_{0.10}FA_{0.90}Pb(I_{0.83}Br_{0.17})_3$) is 100 °C, the performance loss of the n-i-p HTM-based is due to the thermal instability of HTM layers at 100 °C. As other authors reported a good thermal stability for HTMs such as PTAA [8], CuSCN[10] and CuPc[11] at 85 °C. Thus, through dual laser beam sealing method of C-BA configuration, with short dwell time at peak processing temperature; the negative effect of encapsulation on n-i-p devices can become minimal- **Chapter 4**.

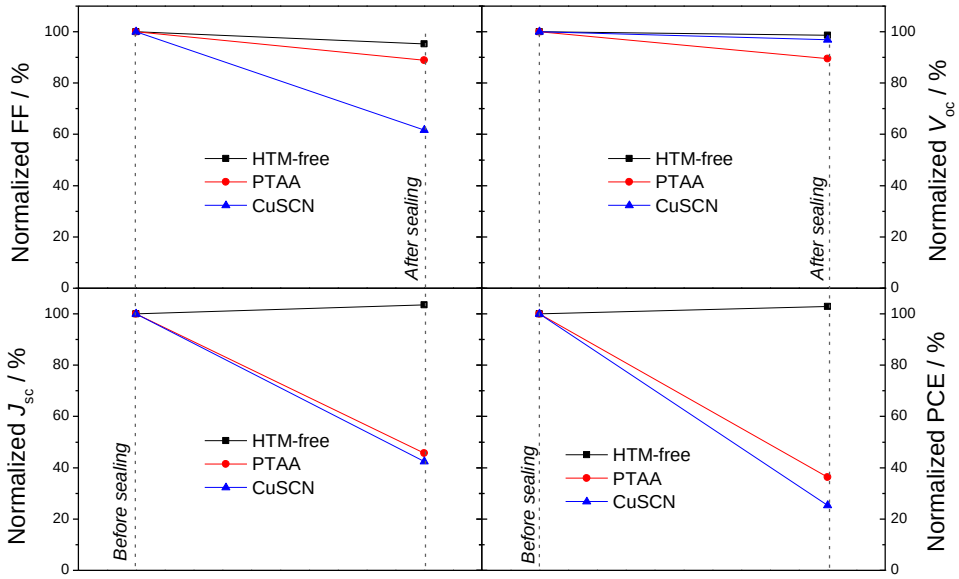

Figure 3.18. Effect of encapsulation process (100 °C, 35 min) on photovoltaic parameters of HTM-free *vs*. HTM-based PSCs.

3.4 CONCLUSIONS

In conclusion, this chapters findings showed that the hermetic encapsulation is critical for achieving long-term stability in PSCs. Although there are other reports on a long-term stable encapsulated PSC; to the best of my knowledge, this work is the first report on an encapsulation method capable of passing hermeticity requirements of the pertinent PV standard tests. The developed glass frit

encapsulation was optimized for not damaging the performance of the cells during sealing while achieving the highest hermeticity level. The hermetic sealing avoids both humidity penetrating to the cell and Pb leaking out. Moreover, the glass frit encapsulation process is compatible with PSC fabrication and does not require additional current collectors for charge extraction. The advanced encapsulation method uses a narrow 1 mm - 4 mm sealing line and the charge extraction is via TCO of the substrate. Finally, from industrialization point of view, the glass frit deposition is through screen-printing and hence scalable.

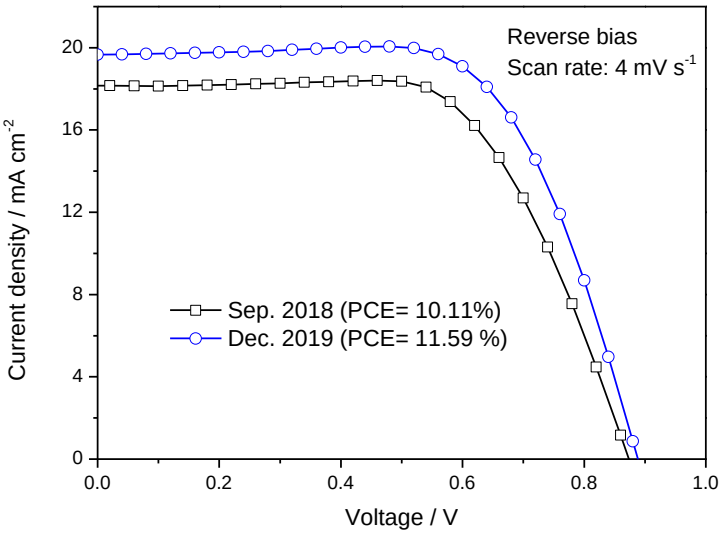

Figure 3.19. *J-V* curves for an encapsulated HTM-free device after 15 months of fabrication. The device was stored in dark at normal atmospheric condition.

The hermetically encapsulated HTM-free PSC devices showed no significant performance losses after thermal cycle and damp heat test according to IEC61646. Furthermore, the 500 h humid air feeding test indicated no performance change for hermetic devices, while non-hermetic devices showed degradation after the initial 50 h of the test; confirming the importance of hermeticity level of encapsulation. Finally, the performance of all encapsulated PSCs of the present work remained stable for more than 15 months. As shown

in **Figure 3.19**, there was even a gain in the performance of the cells which is due to stabilization of these devices for several days after fabrication date.

Although the HTM-free device are promising candidates for industrialization of perovskite solar cells, their relatively low PCE might be a drawback. In contrast, HTM-based (*e.g.* spiro-OMeTAD) devices with superior PCE are not yet ready to meet the thermal requirements of standard tests (-40 °C to 85 °C). Whenever, the HTM-based devices reach to that milestone, a hermetic encapsulation similar to the present work at process temperatures lower than 85 °C would grantee the successful commercialization of a highly efficient and stable PSC.

3.5 REFERENCES

1. A. Kojima, K. Teshima, Y. Shirai and T. Miyasaka, *Journal of the American Chemical Society*, 2009, **131**, 6050-1.
2. NREl, https://www.nrel.gov/pv/assets/pdfs/best-reserch-cell-efficiencies.pdf Accessed on: 2019/12/23, 2019.
3. D. Wang, M. Wright, N. K. Elumalai and A. Uddin, *Solar Energy Materials and Solar Cells*, 2016, **147**, 255-75.
4. IEC61646, International Electrotechnical Commission, 2008.
5. K. Qin, B. Dong and S. Wang, *Journal of Energy Chemistry*, 2019, **33**, 90-9.
6. A. Dualeh, N. Tétreault, T. Moehl, P. Gao, M. K. Nazeeruddin*, et al.*, *Advanced Functional Materials*, 2014, **24**, 3250-8.
7. G. E. Eperon, S. D. Stranks, C. Menelaou, M. B. Johnston, L. M. Herz*, et al.*, *Energy and Environmental Science*, 2014, **7**, 982-8.
8. M. Saliba, T. Matsui, J.-Y. Seo, K. Domanski, J.-P. Correa-Baena*, et al.*, *Energy Environ. Sci.*, 2016, **9**, 1989-97.
9. K. Domanski, J.-P. Correa-Baena, N. Mine, M. K. Nazeeruddin, A. Abate*, et al.*, *ACS Nano*, 2016, **10**, 6306-14.
10. N. Arora, M. I. Dar, A. Hinderhofer, N. Pellet, F. Schreiber*, et al.*, *Science*, 2017, **358**, 768-71.

11. Y. C. Kim, T. Y. Yang, N. J. Jeon, J. Im, S. Jang*, et al.*, *Energy & Environmental Science*, 2017, **10**, 2109-16.
12. I. Mesquita, L. Andrade and A. Mendes, *ChemSusChem*, 2019, **12**, 2186-94.
13. G. Xing, N. Mathews, S. Sun, S. S. Lim, Y. M. Lam*, et al.*, *Science*, 2013, **342**, 344-7.
14. L. Etgar, P. Gao, Z. Xue, Q. Peng, A. K. Chandiran*, et al.*, *Journal of the American Chemical Society*, 2012, **134**, 17396-9.
15. C. Tian, A. Mei, S. Zhang, H. Tian, S. Liu*, et al.*, *Nano Energy*, 2018, **53**, 160-7.
16. A. Mei, X. Li, L. Liu, Z. Ku, T. Liu*, et al.*, *Science*, 2014, **345**, 295-8.
17. S. G. Hashmi, D. Martineau, M. I. Dar, T. T. T. Myllymaki, T. Sarikka*, et al.*, *Journal of Materials Chemistry A*, 2017, **5**, 12060-7.
18. MIL-STD-883H, United States Department of Defense, 2010.
19. S. Emami, J. Martins, L. Andrade, J. Mendes and A. Mendes, *Optics and Lasers in Engineering*, 2017, **96**, 107-16.
20. L. Y. Il, J. N. Joong, K. B. Jun, S. Hyunjeong, Y. Tae-Youl*, et al.*, *Advanced Energy Materials*, 2018, **8**, 1701928.
21. F. Matteocci, L. Cinà, E. Lamanna, S. Cacovich, G. Divitini*, et al.*, *Nano Energy*, 2016, **30**, 162-72.
22. R. Cheacharoen, N. Rolston, D. Harwood, K. A. Bush, R. H. Dauskardt*, et al.*, *Energy & Environmental Science*, 2018, **11**, 144-50.
23. T. Leijtens, G. E. Eperon, S. Pathak, A. Abate, M. M. Lee*, et al.*, *Nat Commun*, 2013, **4**, 2885.
24. Q. Dong, F. Liu, M. K. Wong, H. W. Tam, A. B. Djurišić*, et al.*, *ChemSusChem*, 2016, **9**, 2597-603.
25. R. Cheacharoen, C. C. Boyd, G. F. Burkhard, T. Leijtens, J. A. Raiford*, et al.*, *Sustainable Energy & Fuels*, 2018.
26. F. Ribeiro, J. Maçaira, R. Cruz, J. Gabriel, L. Andrade*, et al.*, *Solar Energy Materials and Solar Cells*, 2012, **96**, 43-9.

27. S. Emami, J. Martins, R. Madureira, D. Hernandez, G. Bernardo*, et al.*, *Journal of Physics D: Applied Physics*, 2019, **52**, 074005.

28. A. M. A. Leguy, Y. Hu, M. Campoy-Quiles, M. I. Alonso, O. J. Weber*, et al.*, *Chemistry of Materials*, 2015, **27**, 3397-407.

29. J. Yang, B. D. Siempelkamp, D. Liu and T. L. Kelly, *ACS Nano*, 2015, **9**, 1955-63.

CHAPTER 4

OPTIMIZATION OF LASER-ASSISTED GLASS FRIT ENCAPSULATION FOR CONVENTIONAL N-I-P DEVICES

"An expert is a person who has made all the mistakes that can be made in a very narrow field."

Niels Bohr

Reprinted from peer-reviewed article

*J. Martins, **S. Emami**, R. Madureira, J, Mendes, D. Ivanou and A. Mendes, Journal of Materials Chemistry A, 2020, **8**, 20037-46.*

4 OPTIMIZATION OF LASER-ASSISTED GLASS FRIT ENCAPSULATION FOR CONVENTIONAL N-I-P DEVICES

Hermetic encapsulation protects perovskite solar cells (PSCs) from degradations induced by humidity and oxygen. A novel dual laser beam glass frit sealing is developed and optimized to hermetically encapsulate PSCs. A 3D transient phenomenological model of the laser-assisted encapsulation is developed, validated and used to optimize the glass sealing procedure. During the laser-sealing process, the cells are subjected to 65 ± 5 °C for a short time of < 60 s. This extremely low process temperature glass sealing procedure is applied to encapsulate n-i-p PSCs fabricated with poly[bis(4-phenyl)(2,4,6-trimethylphenyl) (PTAA) hole transport layer (HTL). The long-term stability of the encapsulated PSCs are examined at elevated humidity conditions and thermal cycle tests. No performance variations after 500 h of humidity aging at 85 % RH and 50 thermal cycles of -40 °C to 65 °C is observed. Though a 16 % PCE loss is observed after thermal cycles between -40 °C and 85 °C, XRD analysis revealed no perovskite decomposition and the performance losses are assigned to the thermal degradation of the HTL material. A hermetic encapsulation is a critical step for transition of PSCs from laboratory to market and this glass encapsulation ensures a successful path towards the commercialization of these emerging PV devices.

4.1 INTRODUCTION

First reported in 2009, perovskite solar cells (PSCs) reached in a decade a power conversion efficiency (PCE) of 25.2 % [1, 2]. PSCs are now entering into direct competition with commercial photovoltaics. However, the long-term stability of PSCs is still a challenge to overcome [3]. The stability of PSCs are affected by exposure to moisture, oxygen, heat and UV light [4].

PSCs are typically fabricated on glass substrates coated with a transparent conductive oxide (TCO) and comprise several layers: an electron transport layer (ETL); a mesoporous scaffold; the perovskite light absorber; a hole transport layer (HTL); and a back contact. Organometallic halides are the most common light absorbers in the PSCs and methylammonium (MA) lead iodide is the most frequently used one. Upon exposure to moisture $MAPbI_3$ vigorously decomposes to MAI and PbI_2. The degradation rate is faster when other factors such as heat and light are combined with moisture [5].

Performance losses due to oxygen exposure occur predominantly under UV light when TiO_2 is used as ETL and scaffold [6]. Surface defects on TiO_2 create trapping sites where oxygen is adsorbed, hindering charge transport. In addition, under UV light oxygen radicals are formed, causing degradation of organic layers of the cell [7]. To protect the PSC device from oxygen induced UV radiation effects, UV filter masks can be used or the TiO_2 layers can be replaced by others n-type semiconductors such as ZnO or SnO_2 [8].

An air-tight encapsulation protects PSCs from moisture and oxygen ingression [7] and it is a critical aspect towards industrialization of the PSCs [9]. The hermeticity of an encapsulation is categorized into two groups, depending on the size of their leak channels: gross and fine leaks. Leak rates are normally presented in $atm \cdot cm^3 \cdot s^{-1}$; values above 1×10^{-5} $atm \cdot cm^3 \cdot s^{-1}$ are considered as gross leaks. Fine leaks, in turn, are divided into: (i) non-hermetic with leak rates between 1×10^{-5} $atm \cdot cm^3 \cdot s^{-1}$ to 1×10^{-7} $atm \cdot cm^3 \cdot s^{-1}$ and (ii) hermetic, with values below $1 \times$

10^{-7} atm·cm^3·s^{-1}. A detailed description of leak rates can be found in **Chapter 2**. MIL-STD-883 describes the methods for leak rate measurements of electronic devices [10].

The long-term stability of PSCs is affected by two factors: (i) external environmental (*i.e.* humidity, oxygen and temperature) and (ii) operational (*i.e.* illumination and electrical load). The external environmental stability of a PSC is guaranteed through application of a hermetic encapsulation to a thermally stable cell. The operational stability is based on the properties of the device materials and interfaces, which should resist to the illumination and electrical bias. The most frequently used tests for assessing the long-term stability of PV devices are described in International Electrotechnical Commission (IEC) standards. Recently, an extensive multi-authored study [11] suggested IEC protocols are not suitable for PSCs. For IEC protocols the cells are required to retain 95 % of their initial PCE after the stability tests, which is challenging for PSCs. Therefore, the authors suggested to use a set of test protocols defined by International Summit on Organic Photovoltaic Stability (ISOS) for the examination of PSCs. The ISOS procedures are based on reporting the time required for the PCE of the cell to decay from its initial value to 80 % [11].

The external environmental factors of PSCs can be examined by either IEC or ISOS tests. However, the operational stability of PSCs characterized using ISOS protocols provide better insight concerning the degradation route of the cells. For encapsulation studies, the IEC 61215 standard test protocol is the most suitable procedure. The accelerated aging test methods described in IEC standard are intended to ensure > 20 years of lifetime for a PV device. The simulated environmental tests for long-term stability of PV devices include damp heat, thermal and humidity-freeze cycles [12]. A long-term stable encapsulation must retain its hermeticity after these tests.

The most commonly used encapsulations for PSCs are UV and thermal cure epoxy resins [13]. These materials are neither hermetic nor long-term stable. The

most effective reported encapsulation for PSCs uses a wide width (15 mm) sealant made of ethylene vinyl acetate (EVA) and "ENLIGHT" polyolefin [14]. Although organic based sealants may be able to provide relatively good short-term stability, their robustness lifetime of 20 years is a challenge which needs to be discovered in real outdoor tests.

In contrast, glass frit encapsulation is known to display excellent long lifetime hermetic encapsulation characteristics [15]. Glass frits are inert materials composed of low melting point glass particles with high wettability to most surfaces [16]. The outstanding hermeticity and robustness of these materials make them unique where a narrow width sealant perimeter is desired [17]. Glass frits are used to encapsulate several type of devices such as micro-electromechanical systems (MEMS) [18, 19], organic light-emitting device (OLED) [20], perovskite solar cells [21] and dye-sensitized solar cells (DSCs) [22, 23].

Thermo-compression technique is the conventional method to perform glass frit bonding. In this process the bonding is achieved by heating the device under mechanical load up to the melting temperature of the glass frit, typically higher than 380 °C, for several minutes [16]. Temperature sensitive devices, such as PSCs, cannot be sealed using this approach. The perovskite light absorber and the HTL are the two most temperature sensitive components of a PSC; $MAPbI_3$ light absorber is thermally stable up to 120 °C [24] and the most common HTLs, 2,2',7,7'-tetrakis(N,N-di-p-methoxyphenylamine)-9,9'spirobifluorene (spiro-OMeTAD) and poly[bis(4-phenyl)(2,4,6-trimethylphenyl) (PTAA) show thermal degradation at 70 °C and 85 °C, respectively [25-27].

Laser-assisted glass frit bonding is an alternative method to thermo-compression [22]. This technique uses a laser beam to locally heat the glass frit material to its melting temperature, while the entire device is kept at lower processing temperature [28]. During laser bonding, the generated thermal gradient causes mechanical stress on the encapsulation package. Thus, an external heating source (*e.g.* hot plate or furnace) is used to reduce the stress on the

device [29]. The process temperature of laser-assisted method is defined by the temperature provided by the external heating source and the dwell time is the duration that the device is exposed to heat. To date, the reported process temperature for glass frit laser-assisted bonding range from 100 °C to 330 °C for dwell time of 35 min to 3 hours.

In **Chapter 3**, an encapsulation method for HTM-free PSCs using laser-assisted glass frit technique, was reported. The PSCs were encapsulated at the process temperature of 100 °C for a dwell time of 35 min, the maximum thermal operating conditions allowed by perovskite absorber. However, to encapsulated conventional n-i-p PSCs containing HTLs, the process temperature and dwell time must be reduced. The present work describes a novel dual laser beam encapsulation approach to encapsulate temperature sensitive HTL-based conventional n-i-p PSCs at 65 °C ± 5 °C with a dwell time of < 60 s.

4.2 MATERIALS AND METHODS

4.2.1 DEVICE FABRICATION

The FTO layer on the glass substrates (1.1 mm, 10 Ω/□ from VisionTek Systems Ltd.) was chemically etched to separate front and back contacts. The substrates were then ultrasonically washed in detergent and distillated water, respectively. After drying the glass substrates were treated with UV-ozone cleaner for 20 min. The TiO_2 compact layer was deposited by spray pyrolysis at 450 °C using a precursor solution of titanium diisopropoxide bis(acetylacetonate) in anhydrous 2-propanol, followed by 45 min sintering step. The mesoporous TiO_2 layer was then deposited by spin coating for 10 s at 5000 rpm with a ramp of 2000 $rpm \cdot s^{-1}$, using a 30 nm particle paste (Greatcell Solar 30 NR-D) diluted in ethanol with a mass concentration of 1:6. After the spin coating, the substrates were dried at 100 °C for 10 min and sintered at 500 °C for 30 min. For the deposition of this layer, the cell substrate was masked with Kapton tape from 3M, which was removed before the sintering step.

A 28 mm diameter circle shape of glass frit A was then screen printed on the device substrate with a linewidth of 4 mm and sintered at 500 °C. A second glass frit (glass frit B) with a linewidth of 1 mm was then screen printed on top of the first glass frit (glass frit A) and sintered at 400 °C. A third glass frit (glass frit C) with 28 mm diameter circle shape and linewidth of 1 mm was screen printed on the cover glass substrate and sintered at 450 °C.

The perovskite solution was prepared by mixing a precursor solution of formamidinium iodide (FAI, 1 M), lead iodide (PbI_2, 1.1 M), methylammonium bromide (MABr, 0.2 M) and lead bromide ($PbBr_2$, 0.2 M) in a mixture of anhydrous N,N-dimethylformamide/dimethyl sulfoxide (DMF:DMSO, 4:1 v/v). The dual cation perovskite precursor was then mixed with 5 wt. % cesium iodide (CsI, 1.5 M in DMSO) to prepare a $Cs_{0.05}(MA_{0.17}FA_{0.83})_{0.95}Pb(I_{0.83}Br_{0.17})_3$ triple cation perovskite precursor solution. Before the deposition of the perovskite and HTM layers, the cell substrate was masked with Kapton tape to protect the glass frits and contacts from contamination. The perovskite layer was spin coated for 10 s at 1000 rpm, followed by 30 s at 6000 rpm; 15 s before the end of the second step, anti-solvent (chlorobenzene) was dropped on the spinning substrate. The substrates were then annealed at 100 °C for 40 min. After annealing, the substrates were cooled down to room temperature before the deposition of the HTM. A solution of PTAA (Ossila) (10 mg/mL) in toluene was prepared and doped with 1.6 µL of bis(trifluoromethylsulfonyl)imide lithium solution (Li-TFSI, Sigma-Aldrich) (1.8M) in acetonitrile and 2 µL of 4-tert-Butylpyridine (tBP, Acros Organic, 96%). The PTAA solution was then spin-coated at 4000 rpm for 20 s. Then, the Kapton mask was removed and a new Kapton mask was used to pattern the device for gold back contact deposition. A 60 nm of gold back contact was deposited by thermal evaporation. A schematic flowchart diagram of the device preparation is illustrated in **Figure 4.1**. Perovskite and HTM preparation and deposition was performed inside is N_2 filled glovebox, while the other steps were carried out at normal atmospheric conditions (40 % to 60 % RH).

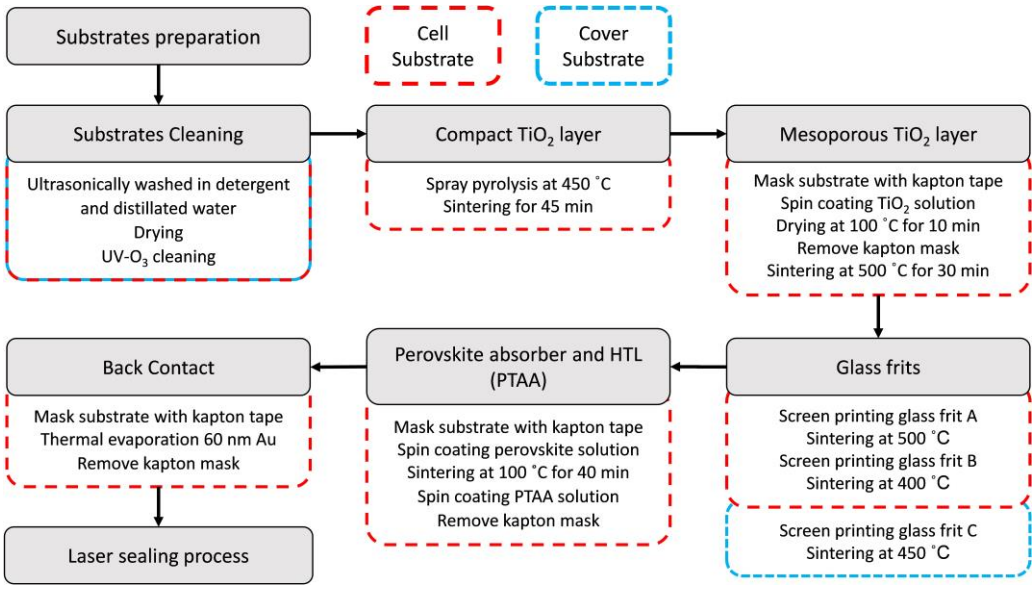

Figure 4.1. Flowchart diagram showing the fabrication steps for laser-sealed n-i-p PSCs.

4.2.2 SEALING PROCEDURE

A multi-layer glass frit configuration comprising three glass frits was used to encapsulate the devices. The triple layer structure includes glass frit A and B on the device glass substrate and glass frit C on the cover glass. After sintering, the thicknesses of glass frits A, B and C are *ca.* 17 µm, 22 µm and 13 µm, respectively. Each glass frit layer plays a specific role during laser-assisted sealing; a detailed description of the triple layer glass frit configuration can be found in **Chapter 2** and **3**. Briefly, in this sealant configuration (C-BA) the bonding is achieved by joining glass frit B to glass frit C. Glass frit C with high ductility and thermal conductivity serves for dissipating the thermal stresses build up at the cover glass when laser radiation is absorbed. Glass frit B, with low melting temperature, is used to achieve the bonding at *ca.* 380 °C. Glass frit A minimizes the thermal stress on the device glass substrate.

The laser-assisted glass frit encapsulation was performed using an in-house made apparatus named “LaserStation” described in **Chapter 2**. This equipment

was modified to accomplish sealing experiments using two laser beams. The upgraded system comprises two 1070 nm continuous wave (CW) laser sources with maximum output of 100 W and 200 W; two optics sets of 2D scan head/*f*-theta lens, one for each laser source. A four-axis Selective Compliance Assembly Robot Arm (SCARA) is used to position the optics sets above the workpiece. A furnace with a glass lid transparent at the laser beam wavelength is used as an external heating source – **Figure 4.2**.

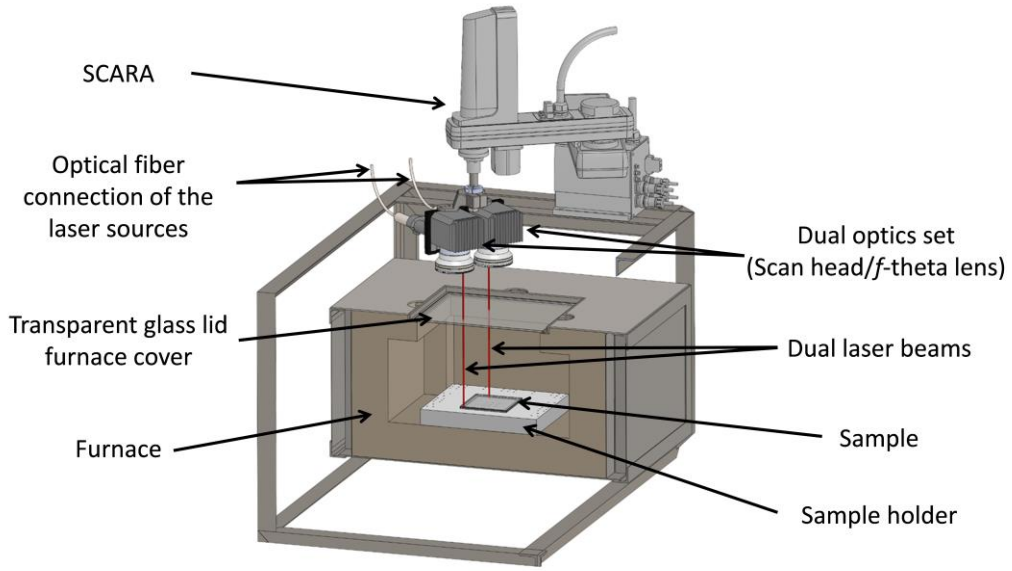

Figure 4.2. Schematic view of "LaserStation" with dual laser beam configuration used for the laser assisted glass encapsulation.

Samples were prepared by sandwiching the bottom (cell) and top (cover) substrates together, in such a way that sealant lines of glass frits C and B are aligned. The prepared device is then placed inside the furnace at 50 °C and maintained for 60 min, for temperature stabilization before performing laser-sealing process. The SCARA arm aligns the optic sets with sealant perimeter

and during laser bonding the laser beams are focused on the glass frit C with a spot size of *ca.* 0.6 mm.

4.2.3 EXTERNAL ENVIRONMENTAL STABILITY TESTS

Humid air exposure and thermal cycling tests were performed on the encapsulated PSC devices. For humid air exposure, the samples were stored in a 17.5 × 17.5 × 6 cm^3 stainless steel chamber and submitted to a humidified air flow - **Figure 3.4**. The humid air was produced by feeding 200 $mL \cdot min^{-1}$ dry air through a cylindrical column filled with distilled water. The humidity level inside the chamber was measured using a humidity sensor and kept at *ca.* 85 % relative humidity (RH). The mentioned test was performed at room temperature (*ca.* 20 °C) for 500 hours. The thermal cycling test was carried out inside an industrial climatic chamber (Fitoclima; Aralab). Two climatic simulated tests were performed; (i) 50 thermal cycles from −40 °C to 85 °C, according to IEC 61215 and (ii) 50 cycles from −40 °C to 65 °C - **Figure 2.18a**. The heating/cooling rate was 1 $°C \cdot min^{-1}$ and each cycle had a 10 min dwell time at maximum and minimum temperatures.

4.2.4 CHARACTERIZATION

The photocurrent-potential (*J-V*) curves were recorded with an electrochemical workstation (Zahner; Zennium) by applying an external potential bias in a reverse scan mode with a rate of 10 $mV \cdot s^{-1}$. The masked cells (*ca.* 0.2 cm^2 active area) were measured using an Oriel class ABA LED solar simulator (MiniSol LSH 732; Newport) calibrated for AM1.5G illumination of 100 $mW \cdot cm^{-2}$. The optical reflectance spectra of the cells were measured with a UV-VIS-NIR spectrophotometer (Shimadzu UV-3600). The XRD spectra were obtained with Siemens D5000 X-ray diffractometer (Cu Kα radiation).

4.3 RESULTS AND DISCUSSION

As shown in **Chapter 3** laser-assisted glass frit encapsulation can be achieved at a process temperature of 100 °C, using a single laser beam and a glass frit with a bonding temperature of 380 °C. The objective of this chapter is to further reduce the process temperature to *ca.* 50 °C for achieving glass frit encapsulation compatible with n-i-p temperature-sensitive PSCs.

During laser-assisted sealing, the glass frits and glass substrates are locally heated up from the process temperature ($T_{process}$) to the bonding temperature ($T_{bonding}$); after the sealing is accomplished, the temperature relaxes from $T_{bonding}$ to $T_{process}$. The minimum laser added temperature to accomplish the sealing is defined as $T_{LA} = T_{bonding} - T_{process}$. The temperature changes induce stresses in both glass substrates and glass frits. Stress may be generated due to coefficient of thermal expansion (CTE) differences at the substrate/glass frit interface or due to thermal gradient along the bodies of the substrates or the glass frits. Excessive stress causes defects such as cracks and delamination. Defects produced during and after laser-sealing are caused by thermal or residual stresses, respectively. To minimize the thermal stress of a very high laser added temperature, T_{LA} = 330 °C, two approaches were considered: (i) using a second laser to locally increase the temperature of the sealant for short dwell time and (ii) using glass substrates of different thicknesses.

In dual laser beam configuration (**Figure 4.3**), one laser beam (LB_{heat}) is used to locally heat the sealant material from the process temperature of 50 °C to operating temperature of 100 °C - 120 °C for a short time of < 2 min, while the other laser beam (LB_{bond}) is used to achieve the bonding temperature *ca.* 380 °C ($T_{bonding}$). LB_{heat} scans the entire sealant perimeter at a fast scanning velocity (4000 mm·s^{-1}). LB_{bond} moves at a slower scanning velocity of 210 mm·s^{-1} along the sealing line to bond the substrates.

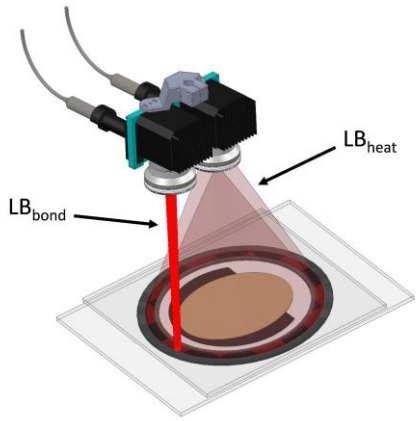

Figure 4.3. Scheme of the laser-assisted glass frit sealing process with dual laser beam configuration.

4.3.1 PHENOMENOLOGICAL SIMULATION OF LASER-SEALING[1]

The heat transfer at the encapsulation components, *i.e.* glass frit layers and glass substrates, during the laser-sealing process, is a 3D-transient thermal phenomenon which can be described by Fourier's Law (**Equation 4.1**) [30]:

$$\frac{\partial^2 T}{\partial x^2} + \frac{\partial^2 T}{\partial y^2} + \frac{\partial^2 T}{\partial z^2} + \frac{q}{k} = \frac{\rho C_p}{k}\frac{\partial T}{\partial t} \qquad 4.1$$

$$\int_v \dot{\varepsilon}^T [C_{ep}] \dot{\varepsilon}\, dv + \int_v \dot{\varepsilon}^T \gamma \dot{T}\, dv = \int_v V^T \dot{f}\, dv + \int_S V^T \dot{p}\, dS$$

$$\int_v (\rho_0 C_p + \bar{\gamma}) T^T \dot{T} dv - \int_v \bar{\beta}^T \dot{\varepsilon}\, T\, dv = \int_v D\, T^T\, dv + \int_v Q(r) T\, dv + \int_v T_i^T\, [k]\, T_j\, dv + \int_S q^T n T dS \qquad 4.2$$

[1] The simulation studies were performed by Ruben Madureira from LEPABE – supervisor Prof. Joaquim Mendes. The reported work was a joint research involving the author of the thesis, Ruben Madureira and Jorge Martins.

where ε is the strain, $[C_{ep}]$ is the elastic-plastic matrix, $[k]$ is the thermal conductivity matrix, D is the thermoplastic coupling factor, T is the temperature, ρ is the specific mass, q is the heat flux, γ is the generalized thermal modulus, C_p is the specific heat, β is the thermal modulus tensor, Q is the heat generation, V the rate of displacement, f is the body forces and p is the surface tractions.

The coupled thermo-elastic-plastic (**Equation 4.2**) differential equations describe the stress and strain distribution at the encapsulation components [31]. Software Ansys Mechanical 2020 was used to solve the model.

Main assumptions of the model

The following main assumptions were considered: i) air convection at the sides of the substrates are negligible; ii) emissivity of the glass substrate is 1, and there is no radiation or convection in the space between the two substrates; iii) the laser beam is absorbed at the top of glass frit and the laser beam absorption in the cover substrate is negligible; iv) the glass frit is bonded to the both substrates; v) materials are isotropic and thermal and mechanical properties are constant with temperature; this includes the three layers of glass frit here treated as made of a single material.

Quadratic mesh elements were considered, with mesh sizes of < 25 μm for the glass frit and < 1 mm for the rest of the bodies. The properties of the glass frit and substrates are presented in **Table 4.1**.

3 different operating conditions were analyzed assuming glass substrates of 1.1 mm and of 2.2 mm thickness: a) furnace temperature of 50 °C with single laser beam heating (T_{LA}= 330 °C); b) furnace temperature of 110 °C with single laser beam heating (T_{LA}= 270 °C); c) furnace temperature of 50 °C with local heating (LB_{heat}) of the glass frit to operating temperature of 100 °C - 120 °C (dual laser beam configuration, T_{LA}= 330 °C).

Table 4.1. Properties of the glass frit and substrates used in the thermal stress simulation.

Parameter	Glass frit	Substrate
ρ [kg m^3]	5000	2500
CTE [10^{-6} °C^{-1}]	8	8.5
E [GPa]	80	50
Poisson's ratio	0.3	0.18
Thermal Conductivity [W °C^{-1} m^{-1}]	3	1.4
Specific Heat [J kg^{-1} °C^{-1}]	600	750

Figure 4.4 shows the model results for the maximum stress observed in the substrates during the laser-sealing. Decreasing the furnace temperature from 110 °C to 50 °C results in increasing stress for 13.3 %. This trend is observed for both 1.1 mm and 2.2 mm glass substrates. Local heating of the glass frit from furnace temperature of 50 °C to operating temperature of 110 ± 10 °C, using the secondary laser beam, decreases the stress by 10.2 % for the 2.2 mm substrates and by 8 % for 1.1 mm glass substrates. Thus, the dual laser beam configuration provides considerable effect in reducing the thermal stresses.

Reducing the glass substrate thickness from 2.2 mm to 1.1 mm decreases the stress for all studied operating conditions, 15.5 % for the case of furnace temperature of 50 °C and 110 °C, and 13.5 % for the case with local secondary laser heating. Reducing the substrate thickness decreases the thermal inertia of the substrate. This means that for equal conditions, the temperature of the substrate increases faster, therefore decreasing the thermal gradient of the body for this transient situation. The simulation results clearly show that the stress on the substrates, during the laser-assisted process, can be reduced by using dual laser beam configuration and 1.1 mm glass substrates.

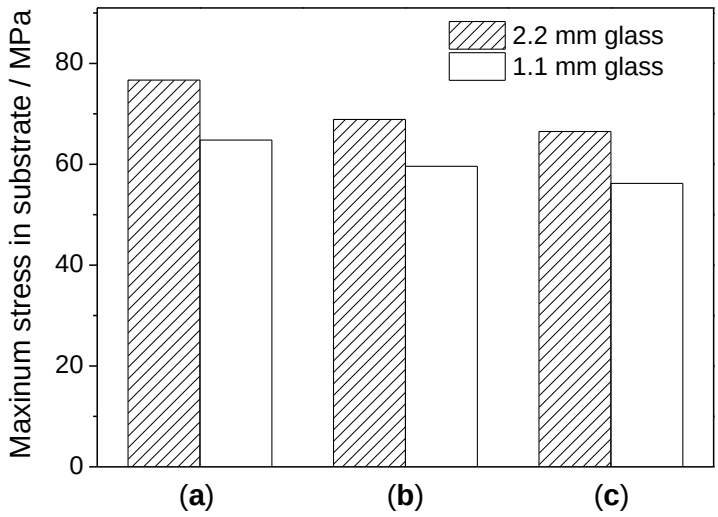

Figure 4.4. Maximum stress for 2.2 mm and 1.1 mm FTO glass substrates for a) furnace temperature of 50 °C; b) furnace temperature of 50 °C and local secondary laser heating to operating temperature of 110 ± 10 °C and; c) furnace temperature of 110 °C.

The simulated temperature profiles for the glass frits and substrates during the dual laser beam sealing of 1.1 mm glass are presented in **Figure 4.5a**. **Appendix C** shows the simulated temperatures in the cross section of the glass frit and substrates during the laser-sealing process. The laser-sealing process can be divided into 5 steps: I) the device is placed in the furnace at the process temperature of 50 °C until a homogeneous temperature is reached (temperature stabilization period is not represented); II) LB_{heat} radiates and the sealant temperature increases up to 110 ± 10 °C; III) LB_{bond} is emitted, raising the temperature in the glass frit up to > 380 °C, bonding the substrates; IV) LB_{bond} is turned off and LB_{heat} continues emitting, maintaining the sealant material at 110 ± 10 °C; V) laser-sealing finishes, LB_{heat} is turned off and the temperature in the sealant decreases to the process temperature. The mentioned 5 steps are illustrated in **Figure 4.5**.

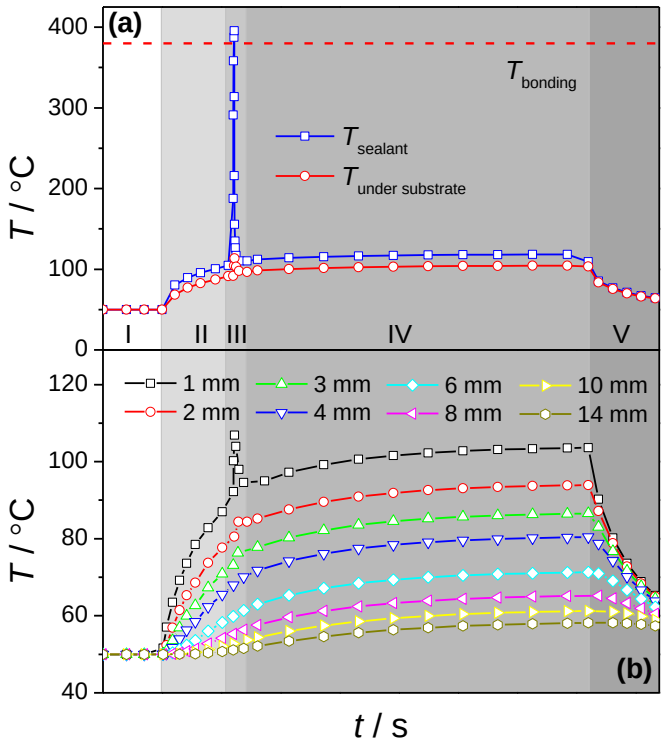

Figure 4.5. Simulated temperature profiles for **(a)** sealant and at the rear side of the cell substrate and **(b)** the cell substrate at 1, 2, 3, 4, 6, 8, 10 and 14 mm distance from the center of the glass frit.

The heat affected zone (HAZ) of the LB_{heat} may cause thermal damage to the active layers of the PSC device. Although the dwell time of this heating is shorter than 120 s, the heat flows inward the cell, reaching the device active layers mainly through the bottom glass substrate. The temperature profiles in the cell substrate, bottom glass substrate, at different distances from the center of the glass frit are presented in **Figure 4.5b**. This simulated data is particularly important to establish the safe distance between the glass frit sealing line and the active layers of the PSC. At 1 mm from the center of the glass frit line, the cell substrate temperature reaches temperatures above 100 °C, as well as being affected by the LB_{bond}. The temperature reaches a maximum value of 80 °C and 70 °C, at 4 mm and 6 mm distance away from the center of the glass frit line,

respectively. As mentioned before, the most temperature sensitive component of a PSC device is the HTM. The simulated results indicate that 4 mm away from the center of the sealing line, the temperature reaches 80 °C, the thermal stability threshold at which PTAA can be used as HTM. For the case of using spiro-OMeTAD as HTM, the safe distance should be 6 to 8 mm. Thus, the selected HTM layer must consider the mentioned aspects to ensure suitable implementation of the laser-sealing process to the device geometry.

4.3.2 EXPERIMENTAL VALIDATION OF DUAL LASER SEALING

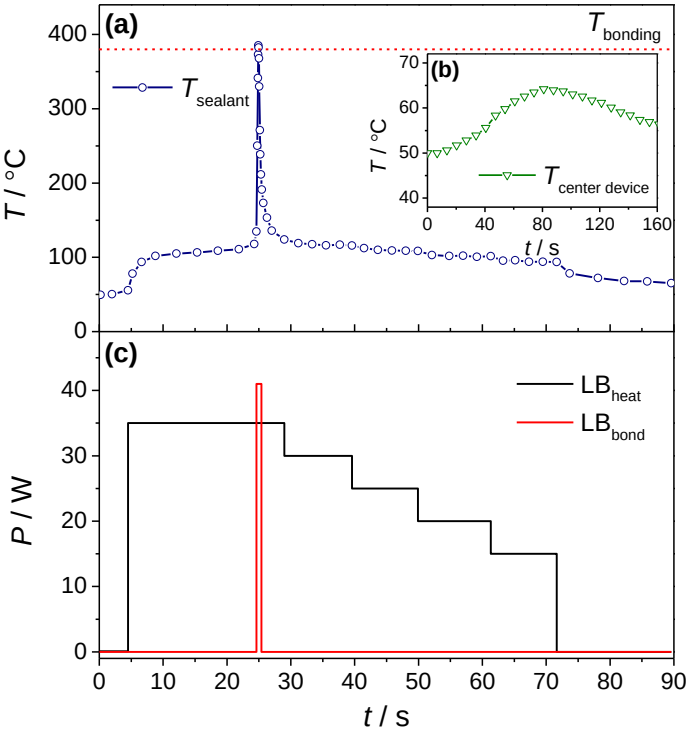

Figure 4.6. Temperature history of the **(a)** sealant and **(b)** center of the cell substrate during laser encapsulation process; **(c)** Power timeline of the two laser beams.

The mathematical model was validated by comparing simulated to experimental results. **Figure 4.6a** shows the actual temperature history of the sealant for optimized sealing conditions, measured by thermocouples. **Figure 4.7** illustrates

the position of thermocouples on the device. The sealing process starts when laser LB_{heat} is radiated at 35 W with scanning velocity of 4000 mm·s^{-1}. The temperature at the sealant gradually increases and stabilizes at 110 ± 5 °C, after *ca.* 20 seconds of laser emission. At this moment, LB_{bond} is emitted at 41 W with a scanning velocity of 210 mm·s^{-1}. The temperature of the sealant raises rapidly above 380 °C, melting the glass frit and bonding the substrates. After bonding, the LB_{heat} power is gradually reduced, slowly decreasing the temperature of the sealant – **Figure 4.6c**. The total laser processing time is *ca.* 65 seconds.

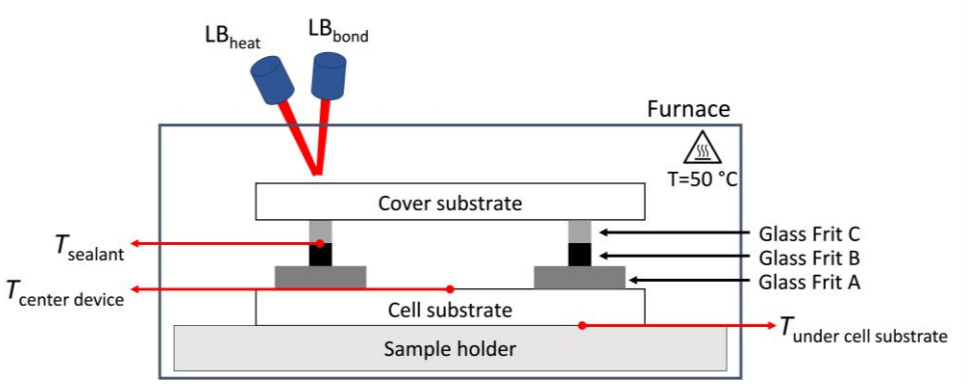

Figure 4.7. Thermocouples positions for temperature measurement during dual laser sealing process.

The temperature increases at the center of the device (14 mm distance from the glass frit) to maximum of 65 ± 5 °C for a short dwell time of < 60 s – **Figure 4.6b**. Although the simulated temperature at the center of the device was slightly lower, *ca.* 60 °C (**Figure 4.5b**), the experimental results display a suitable agreement with the simulation. Therefore, the 4 mm distance from the center of glass frit sealing line required for not reaching temperatures above 80 °C, obtained by the simulation, was considered for the deposition of the PSC active layers. As predicted by the model, the screening experimental results showed that the temperatures of the laser process can cause thermal decomposition of the spiro-OMeTAD HTM, while PTAA-based HTM devices showed no performance losses. A similar thermal decomposition behavior is reported by

Mesquita *et al.* where spiro-OMeTAD based devices presented high irreversible performance loss when submitted to 70 ± 5 °C, while PTAA-based devices displayed only minor losses of performance [27].

Figure 4.8 shows the experimental temperature profile under the bottom cell substrate. During the sealing process, the temperature increase at the rear side of the cell substrate is faster for the 1.1 mm substrate, compared with the 2.2 mm substrate, thus showing the reduced thermal inertia of the thinner glass substrate.

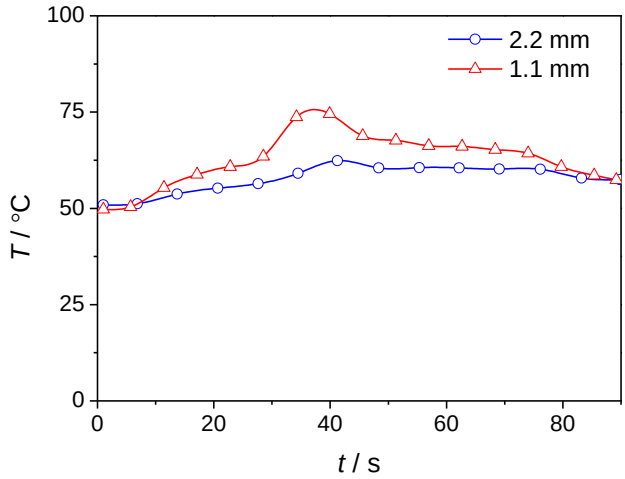

Figure 4.8. Temperature history at the rear side of the glass (*i.e.* under cell substrate) for 2.2 mm and 1.1 mm thick glass substrates.

A batch of 14 PSCs was encapsulated according to the above described process. The performance of the devices was measured before and after the sealing and are compared in **Figure 4.9**.

The average open circuit voltage (V_{oc}) remained unchanged after sealing process at 0.91 ± 0.03 V; the short circuit current density (J_{sc}) increased from 19.62 ± 0.77 mA·cm^2 to 19.80 ± 0.88 mA·cm^2; the fill factor (FF) decreased from 0.52 ± 0.04 to 0.50 ± 0.04 and the PCE decreased from 9.35 ± 0.89 % to 9.03 ±

0.66 %. The devices presented an average PCE loss of 3.4 %, which is a minor variation.

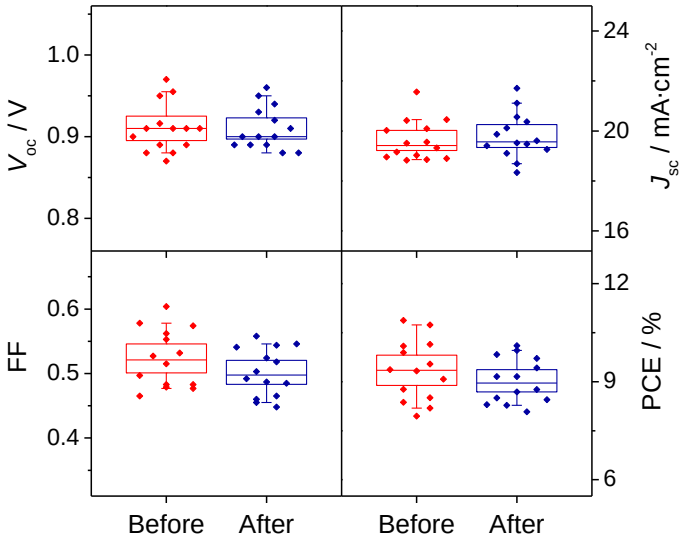

Figure 4.9. Photovoltaic parameters of PSCs before and after encapsulation process; boxes represent standard deviation; lines show 10-90 percentile.

The focus of the present study is to develop a low temperature hermetic encapsulation process suitable to thermal sensitive conventional PSCs. Fabricating highly efficient solar cells was beyond the scope of the present study. However, the effect of incorporating the glass frit sealants into the manufacturing steps of the PSC device was studied to identify fabrication constraints and methods. As shown in **Figure 4.1**, during device preparation there are many masking steps to avoid cross contamination between layers (PSC components and glass frits). The spin-coating deposition technique requires flat and uniform substrates to achieve a high quality film [32]. Therefore, masking the substrate during the spin-coating deposition of active layers affects the quality of this deposition and namely the thickness uniformity. Three groups of PSC devices were fabricated to compare the masking and sealant effect: (i) masked with sealant (*M&S*), (ii) masked without sealant (*M*) and (iii) no sealant and no mask

(*NS&NM*). There was a PCE loss of *ca.* 23 % and 8 % for *M&S* and *M* devices, when comparing to *NS&NM* group – **Figure 4.10**. The drop in PCE is due to a decrease in the V_{oc} for *M* devices, while for *M&S* devices is caused by a lower V_{oc} and FF. Lower V_{oc} and FF are indicators of high charge recombination caused by non-uniform films. The defects in these films create recombination sites for the generated charge at the interface between PSC layers [33, 34]. Therefore, the performance of the cells of *M&S* group can be improved by applying different deposition techniques such as screen printing for mesoporous TiO_2 layer and spray deposition for perovskite absorber and HTL layers. Alternatively, deposition techniques such as inkjet or slot-die should also be considered for the PSC fabrication. The mentioned improvements are beyond the scope of the present thesis and it can be investigated in a future study.

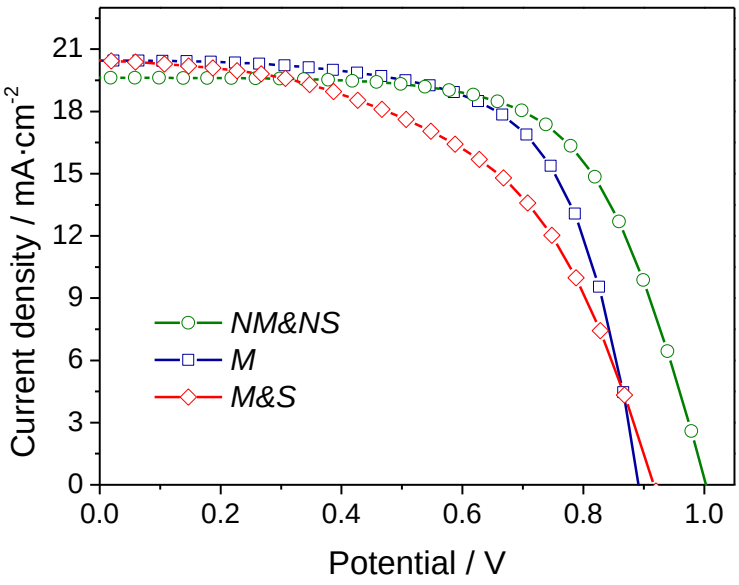

Figure 4.10. Current density *vs*. potential curves of *NS&NM*, *M* and *M&S* devices.

4.3.3 EXTERNAL ENVIRONMENTAL STABILITY

Humid air exposure

The stability of the encapsulated devices was assessed by exposing the devices to humid air (85 % RH) for 500 hours. The devices were characterized during the test and the performance parameters history are shown in **Figure 4.11a**. During the humidity aging test, V_{oc} remained stable, J_{sc} decreased while FF increased resulting in a small increase in the PCE. The encapsulated devices are considered hermetic according to MIL-STD-883 standard with average leak rate value of 1.71×10^{-8} atm·cm^3·s^{-1}, therefore protecting the PSCs devices from moisture and oxygen exposure during the stability test. The current density *vs* potential curve (*J*-*V*) of a hermetically encapsulated cell, after 500 h of humid air exposure, as well as the *J*-*V* curves before and after encapsulation are presented in **Figure 4.11b**. The slight J_{sc} improvement after the sealing was assigned to the re-crystallization of the perovskite absorber and perovskite/HTM interface enhancement during the thermal conditioning steps of the sealing. However, the stabilized performance of the cell after 500 h, indicates that the cells undergo various interfacial improvements to achieve better performance.

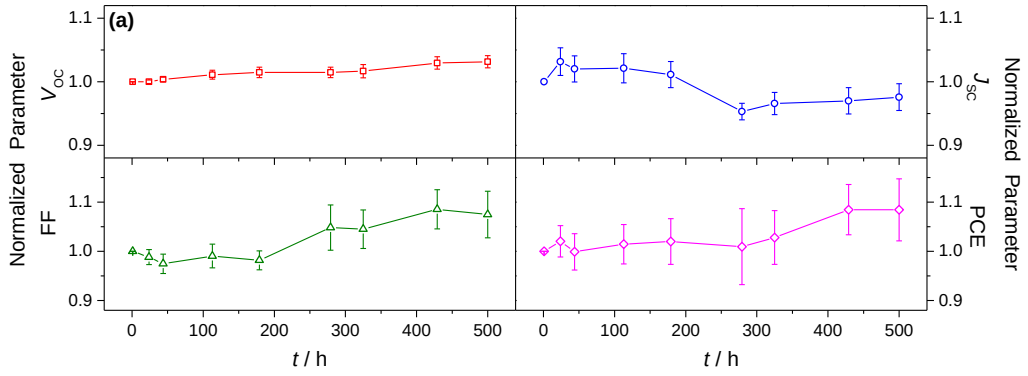

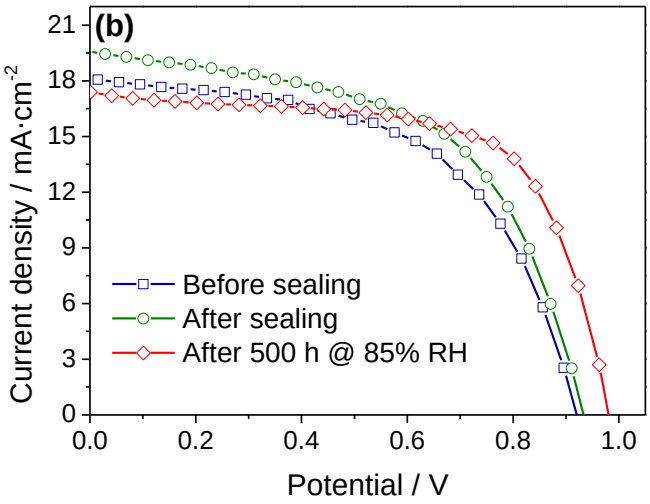

Figure 4.11. (a) Normalized photovoltaic parameters of hermetically encapsulated PSCs submitted to 500 h humid air exposure test; **(b)** Current density vs potential curves of a PSC before and after the sealing process and of a hermetically encapsulated device after 500 h of humid air exposure.

The effect of hermeticity level of the glass encapsulation during humidity aging test was studied by comparing the performance of a hermetically encapsulated device with a device with non-hermetic encapsulation – **Figure 4.12**.

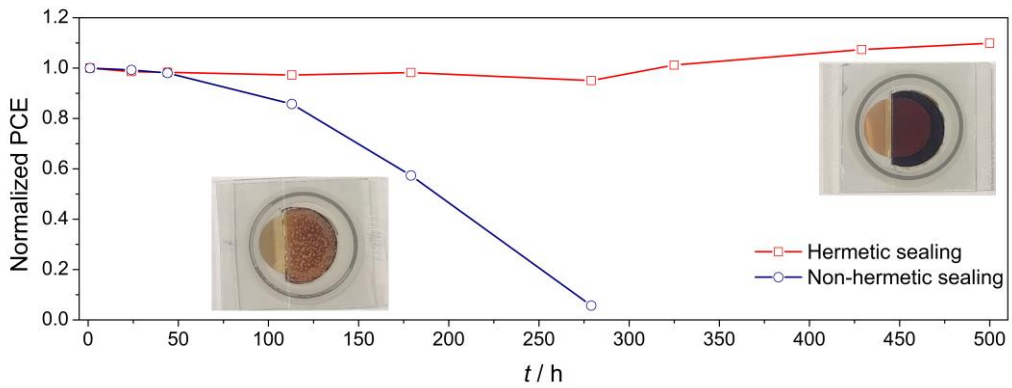

Figure 4.12. Normalized PCE of devices with hermetic and non-hermetic encapsulation submitted to 500 h of humid air exposure test.

The reproducibility rate for achieving a hermetic encapsulation for the dual laser-assisted sealing method of the present work is > 80 %. The unsuccessful encapsulation results are related to the organic contamination of the frits during spin-coating of cell layers or due to the incorrect alignment of the laser beams during sealing. These remaining 20 % of the sealed sample present crack and loss of adhesion at the interface of glass frit/glass substrate; the hermeticity level of these devices (with no gross leaks) are considered as non-hermetic. The performance of the non-hermetic encapsulated device has dropped to 50 % after 200 h of the aging test.

After 500 h of stability test, the non-hermetic encapsulated device showed a higher optical reflectance spectrum, when compared to the hermetically encapsulated device, due to perovskite decomposition – **Figure 4.13**.

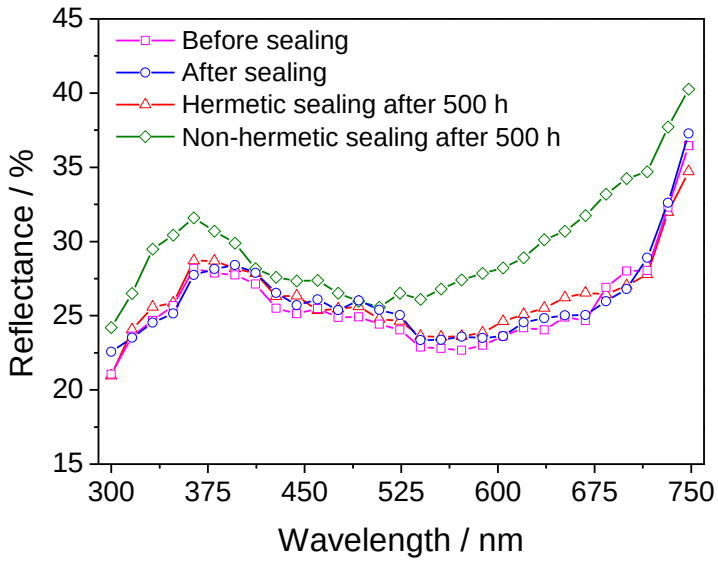

Figure 4.13. Reflectance spectra of a PSC before and after sealing process; and for a hermetically and a non-hermetically encapsulated devices, after 500 h of humid air exposure.

The X-Ray diffraction (XRD) spectrum of the non-hermetic device displayed PbI_2 and $PbBr_2$ peaks associated with the moisture induced degradation of the perovskite absorber – **Figure 4.14**. The reflectance spectrum and XRD pattern of a hermetically encapsulated PSC remained similar to a fresh fabricated. Since the XRD patterns presented in **Figure 4.14** are from different batches of prepared cells, few peak variations can be identified. The reflexes associated to Cs-Pb-halide compounds for hermetically sealed devices were assigned to unreacted salts during the perovskite precursor preparation; while similar peaks are not identified for fresh devices, prepared in a different batch.

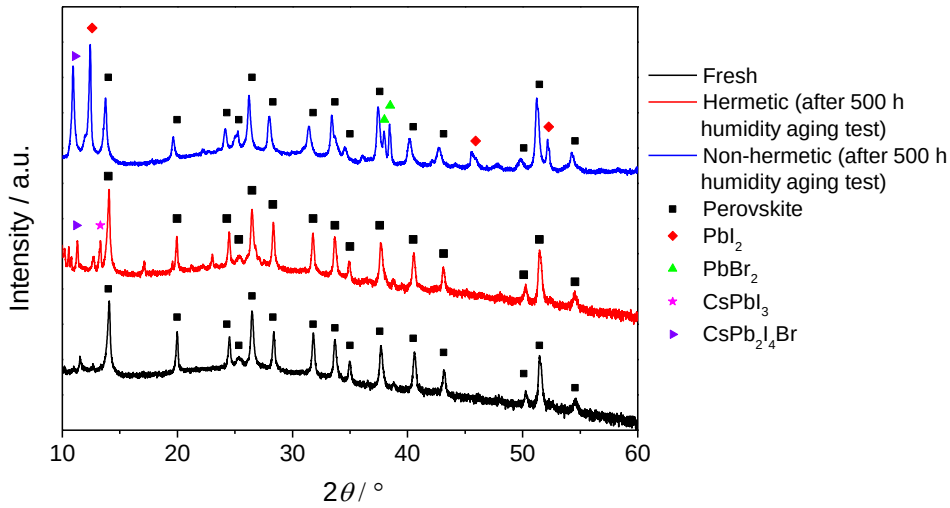

Figure 4.14. XRD pattern for a fresh device, hermetic and non-hermetic encapsulated devices after 500 h of humid air exposure test.

Thermal cycling

Hermetically encapsulated devices were submitted to thermal cycling test from −40 °C to 85 °C, according to the IEC 61215 standard. Although there is no humidity control during this test, RH can reach up to 85 %. The purpose of this standard test is to simulate the outdoor climatic conditions required to ensure the stability of more than 20 years for PV devices. The long-term stability of devices during the thermal cycling test depends on the hermeticity level of the

encapsulation and the thermal stability of the solar cell components. As shown in **Chapter 2** and **3** the hermeticity of the glass frit sealant remained unchanged after this test. Thus, the instability source for the PSCs during the thermal cycling test should be assigned to the thermal stability of solar cell layers.

As shown in **Figure 4.15**, the devices display a major performance loss after 50 thermal cycles. There was 28.9 ± 4.4 % decrease in the J_{sc} of the devices, while V_{oc} showed minor improvement (2.45 ± 0.79 %). The large drop in current density and small voltage increase causes an improvement in FF. Finally, the devices displayed a 15.46 ± 6.54 % PCE drop. Since the PCE loss is more than 5 %, according to IEC standard, the long-term stability results are considered as failure.

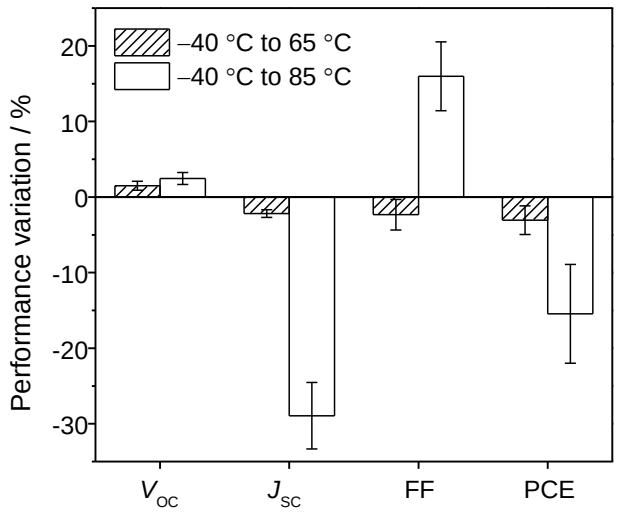

Figure 4.15. Performance variation of devices after thermal cycling tests of −40 °C to 65 °C and of −40 °C to 85 °C.

In contrast, when a moderate 50 thermal cycles between -40 °C to 65 °C were applied to examine the thermal stability of the PSC components, there were no major performance variations. There was a slight increase in V_{oc}, while other parameters displayed minor decreases. The PCE of the devices showed

3.06 ± 1.89 % drop, which was considered a rather small performance loss - **Figure 4.15**.

The XRD analysis of the devices showed no onset of perovskite degradation after the -40 °C to 85 °C thermal cycling test – **Figure 4.16**. Therefore, the performance drop should be related to the degradation of HTM or mechanical damages at the interface of layers due to CTE mismatch of the solar cell components [35]. The results of the -40 °C to 65 °C cycling test also indicate no thermal degradation and the XRD pattern confirms no structural changes of perovskite absorber – **Figure 4.16**. The minor performance variation should then be assigned to minor performance degradation of the PSC active layers, which can be induced by the temperature stress as well as the mechanical stress induced by the CTE mismatch.

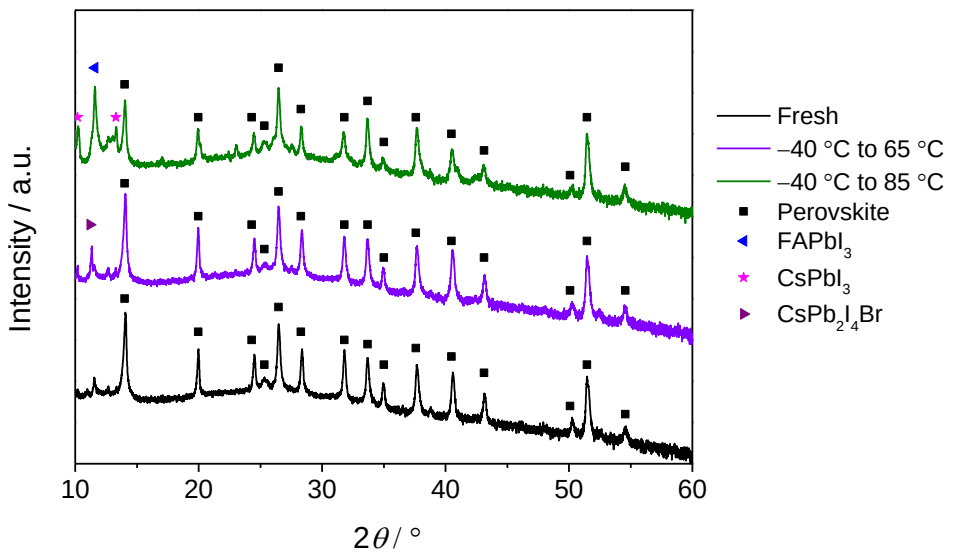

Figure 4.16. XRD pattern for a fresh device *vs.* hermetic encapsulated devices after 50 cycles of -40 °C to 65 °C and of −40 °C to 85 °C.

Similar to the humidity aging test, the effect of the hermeticity level on the encapsulation was studied for thermal cycle tests. For non-hermetic encapsulated PSCs tested for -40 °C to 85 °C and -40 °C to 65 °C cycling tests,

the XRD analysis indicates perovskite decomposition due to humidity (*i.e.* reaching up to 85 % RH) – **Figure 4.17**.

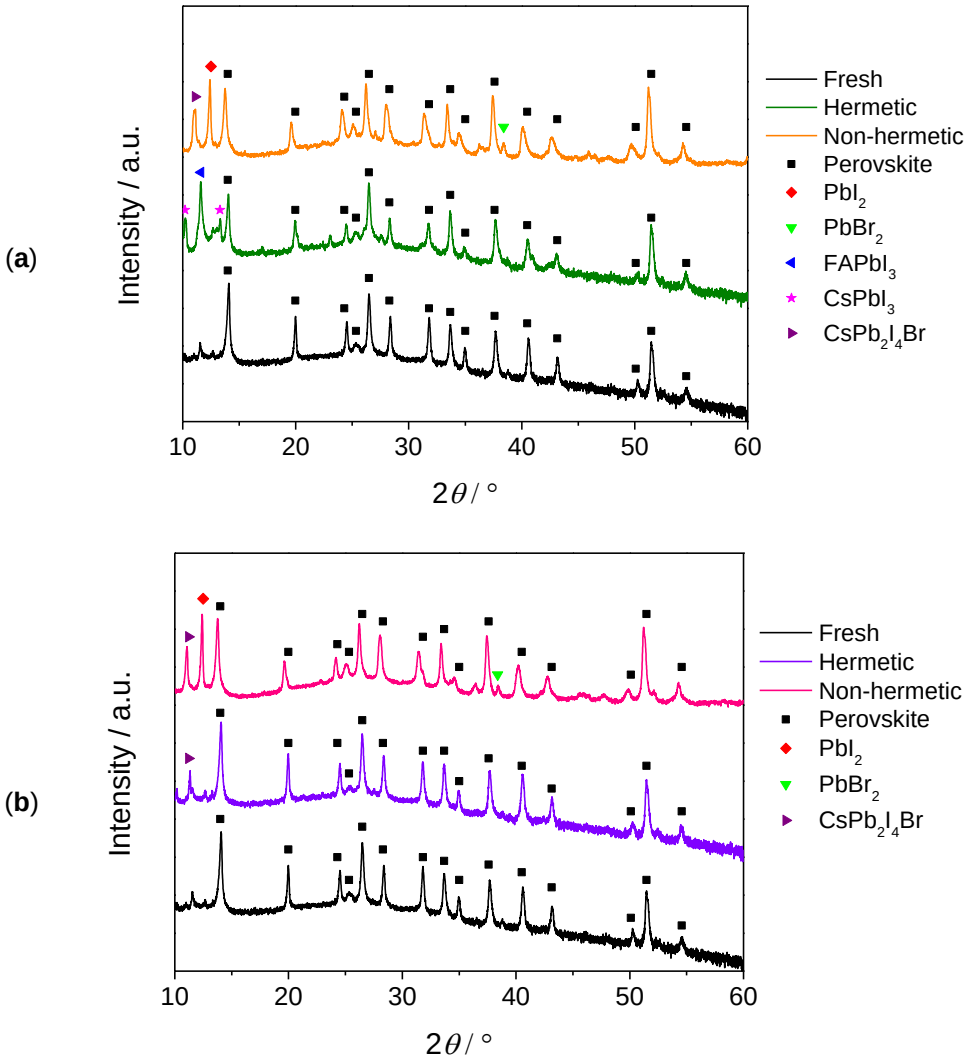

Figure 4.17. XRD pattern for a fresh device and for hermetically and non-hermetically encapsulated devices, after the thermal cycling test between (**a**) −40 °C to 85 °C, and (**b**) −40 °C to 65 °C.

4.4 CONCLUSIONS

The hermetic encapsulation is a critical feature on improving the long-term stability of PSC devices; hermetic encapsulation is effective to prevent moisture and oxygen related degradation concerns. Conventional PSCs are fabricated with temperature sensitive HTMs and the previously reported laser-assisted glass frit sealing technique cannot be used to encapsulate these types of devices due to high process temperature and long dwell times. In the present work, a novel laser-assisted glass frit encapsulation method was developed that can be used to hermetically encapsulate HTM-based conventional PSCs. The technique uses a dual laser beam configuration where one laser beam preheats the glass frit material from 50 °C up to 110 ± 10 °C, while the other laser beam melts the glass frit and bonds the glass substrates.

A dynamic phenomenological 3D model was developed, validated and used to analyze and optimize the dual laser beam glass-sealing process. Using two laser beams, the simulation results indicate a thermal stress decrease of *ca.* 9.1 %, during the laser sealing process, when compared with laser sealing with a single laser beam, for a process temperature of 50 °C. Furthermore, the thermal stress decreases for *ca.* 13.8 % by reducing the thickness of glass substrates from 2.2 mm to 1.1 mm.

The PSC layers were deposited 4 mm away from the glass frit sealant, and the maximum temperature recorded at the center of the device was 65 ± 5 °C for 60 s. The dual laser-sealing process caused no notable performance losses to PSC devices fabricated with PTAA as HTM.

Hermitically encapsulated devices submitted for 500 hours to humid air at 85 % RH showed no performance losses, while non-hermetic devices displayed 50 % of PCE loss after 200 h. XRD analysis showed the presence of Pb halides, associated with moisture induced decomposition of the perovskite absorber, in the non-hermetically encapsulated devices. In contrast, no evidence of Pb halides were found in the devices hermetically sealed.

The long-term stability of the encapsulated PSC devices was further tested according to the thermal cycling test of IEC 61215 standard. The tested devices show a PCE loss of *ca.* 16 %. This loss of performance was assigned to the temperature sensitivity of the HTM (PTAA) since no perovskite decomposition was observed in the XRD patterns. A moderate thermal cycling test between -40 °C to 65 °C showed a minor PCE drop of 3.4 %.

In conclusion, a novel advanced dual laser beam sealing process was developed to encapsulate temperature sensitive HTM-based PSCs, which provided long-term stability towards humidity and moderate thermal cycling tests. The present work suggests future research should focus on developing more stable HTM materials to grant the long-term thermal stability of PSCs according to IEC 61215 standard. The combination of the present encapsulation and thermally stable materials will ensure a successful commercialization of perovskite solar cells.

4.5 REFERENCES

1. NREl, https://www.nrel.gov/pv/assets/pdfs/best-reserch-cell-efficiencies.pdf Accessed on: 2020/05/29, 2019.
2. A. Kojima, K. Teshima, Y. Shirai and T. Miyasaka, *Journal of the American Chemical Society*, 2009, **131**, 6050-1.
3. T. Leijtens, G. E. Eperon, N. K. Noel, S. N. Habisreutinger, A. Petrozza*, et al.*, *Advanced Energy Materials*, 2015, **5**, 1500963-n/a.
4. M. I. Asghar, J. Zhang, H. Wang and P. D. Lund, *Renewable and Sustainable Energy Reviews*, 2017, **77**, 131-46.
5. J. A. Christians, P. A. Miranda Herrera and P. V. Kamat, *Journal of the American Chemical Society*, 2015.
6. A. Farooq, I. M. Hossain, S. Moghadamzadeh, J. A. Schwenzer, T. Abzieher*, et al.*, *ACS Applied Materials & Interfaces*, 2018, **10**, 21985-90.

7. T. A. Berhe, W.-N. Su, C.-H. Chen, C.-J. Pan, J.-H. Cheng*, et al.*, *Energy & Environmental Science*, 2016, **9**, 323-56.
8. H.-S. Kim, J.-Y. Seo and N.-G. Park, *ChemSusChem*, 2016, **9**, 2528-40.
9. D. Wang, M. Wright, N. K. Elumalai and A. Uddin, *Solar Energy Materials and Solar Cells*, 2016, **147**, 255-75.
10. MIL-STD-883H, United States Department of Defense, 2010.
11. M. V. Khenkin, E. A. Katz, A. Abate, G. Bardizza, J. J. Berry*, et al.*, *Nature Energy*, 2020, **5**, 35-49.
12. IEC61646, International Electrotechnical Commission, 2008.
13. F. Matteocci, L. Cinà, E. Lamanna, S. Cacovich, G. Divitini*, et al.*, *Nano Energy*, 2016, **30**, 162-72.
14. R. Cheacharoen, C. C. Boyd, G. F. Burkhard, T. Leijtens, J. A. Raiford*, et al.*, *Sustainable Energy & Fuels*, 2018.
15. D. K. Ivanou, R. Santos, J. Maçaira, L. Andrade and A. Mendes, *Solar Energy*, 2016, **135**, 674-81.
16. R. Knechtel, *Microsystem Technologies*, 2005, **12**, 63-8.
17. R. Knechtel, in *Handbook of Wafer Bonding*, 2012, pp. 1-17.
18. M. Esashi, *Journal of Micromechanics and Microengineering*, 2008, **18**, 073001.
19. N. Lorenz, S. Millar, M. Desmulliez and D. P. Hand, *Journal of Micromechanics and Microengineering*, 2011, **21**, 045039.
20. R. M. Morena, J. F. Bayne, J. T. Westbrook, S. Widjaja and L. Zhang, in *Handbook of Organic Light-Emitting Diodes*, eds. C. Adachi, R. Hattori, H. Kaji and T. Tsujimura, Springer Japan, Tokyo, 2018, pp. 1-22.
21. S. Emami, J. Martins, D. Ivanou and A. Mendes, *Journal of Materials Chemistry A*, 2020, **8**, 2654-62.
22. F. Ribeiro, J. Maçaira, R. Cruz, J. Gabriel, L. Andrade*, et al.*, *Solar Energy Materials and Solar Cells*, 2012, **96**, 43-9.
23. R. Sastrawan, J. Beier, U. Belledin, S. Hemming, A. Hinsch*, et al.*, *Solar Energy Materials and Solar Cells*, 2006, **90**, 1680-91.

24. A. K. Jena, Y. Numata, M. Ikegami and T. Miyasaka, *Journal of Materials Chemistry A*, 2018, **6**, 2219-30.
25. M. Saliba, T. Matsui, K. Domanski, J.-Y. Seo, A. Ummadisingu*, et al.*, *Science*, 2016.
26. K. Domanski, J.-P. Correa-Baena, N. Mine, M. K. Nazeeruddin, A. Abate*, et al.*, *ACS Nano*, 2016, **10**, 6306-14.
27. I. Mesquita, L. Andrade and A. Mendes, *ChemSusChem*, 2019, **12**, 2186-94.
28. S. Emami, J. Martins, L. Andrade, J. Mendes and A. Mendes, *Optics and Lasers in Engineering*, 2017, **96**, 107-16.
29. S. Emami, J. Martins, R. Madureira, D. Hernandez, G. Bernardo*, et al.*, *Journal of Physics D: Applied Physics*, 2019, **52**, 074005.
30. T. L. Bergman, F. P. Incropera, D. P. DeWitt and A. S. Lavine, *Fundamentals of heat and mass transfer*, John Wiley & Sons, 2011.
31. T.-R. Hsu, *The finite element method in thermomechanics*, Springer Science & Business Media, 2012.
32. Y. Zhang, S.-W. Ng, X. Lu and Z. Zheng, *Chemical Reviews*, 2020, **120**, 2049-122.
33. T. S. Sherkar, C. Momblona, L. n. Gil-Escrig, J. Ávila, M. Sessolo*, et al.*, *ACS Energy Letters*, 2017, **2**, 1214-22.
34. M. B. Johnston and L. M. Herz, *Accounts of Chemical Research*, 2016, **49**, 146-54.
35. R. Cheacharoen, N. Rolston, D. Harwood, K. A. Bush, R. H. Dauskardt*, et al.*, *Energy & Environmental Science*, 2018, **11**, 144-50.

CHAPTER 5

GENERAL CONCLUSIONS AND OUTLOOK

“Many of life's failures are people who did not realize how close they were to success when they gave up.”

Thomas Edison

5 GENERAL CONCLUSIONS AND OUTLOOK

The main motivation for the present thesis was to address the stability of perovskite solar cells through hermetic encapsulation. The commercialization of emerging PSCs is dependent on the development of devices with more than 20 years stability. Therefore, a reliable airtight sealing should assure a successful laboratory to industry transition.

This chapter reviews the main conclusions obtained during the course of the present thesis. In addition, an outlook for the future of encapsulation along with the challenges for PSC technology is presented. Finally, few future work plans are proposed for forthcoming status of the PSC research.

5.1 MAIN CONCLUSIONS

Perovskite solar cells are now entering into a new era. Small (< 0.2 cm^2) and large (module < 6500 cm^2) area PSCs have been reached record power conversion efficiency of 25.2 % and 16.1 %, respectively[1]. This fast-growing emerging PV technology is now ready for commercialization.

To date, most of the research attention was focused on achieving highly efficient solar cells, and the importance of encapsulation was overlooked. For a PV technology to be used in real outdoor conditions, the encapsulation is one the most important factors to be considered before commercialization. In particular, since perovskite solar cells are highly sensitive to oxygen and humidity[2], encapsulation is even more critical. Therefore, an airtight encapsulation is the missing puzzle for PSCs to enter the PV market.

The importance of the hermeticity level of encapsulation, limits the choice of sealant materials to a very narrow group. Polymer based thermal plastics[3], epoxy resin[4] or thin film[5] encapsulations cannot ensure long lifetime stability for PSCs. In contrast, glass frit sealant has shown remarkable long-term stable hermetic characteristics[6], required for PSC application.

However, since the conventional thermo-compressive glass frit bonding method with thermal processing above 400 °C, is not suitable for thermally sensitive components; a laser-assisted sealing method was used to encapsulate PSCs. The previously reported laser-assisted sealing for dye-sensitized solar cells (DSCs) with process temperature of 250 °C, available at LEPABE, was further studied and optimized to reduce the process temperature below 120 °C.

The optimization of laser-sealing parameters was carried out driven by experimental studies of the temperature history at the bonding zone. A novel laser pattern sealing method allowed to achieve high-quality sealing results with no thermal damage to the substrates and glass frit. The laser output power, spot

size and sealing pattern parameters were optimized following a response surface methodology.

More than 6 glass frits and 15 frit bonding configurations were studied to achieve the low process temperatures suitable for PSC encapsulation. The glass frits were deposited on both bottom and top glass substrates. In addition, more than one glass frit layer can be applied to the substrate by sequential deposition. The glass frit configuration was coded with X-Y; the coded configuration from left to right designate the glass frits position from top to bottom in encapsulation structure, and "-"defines the bonding interface.

Although the first low temperature encapsulation bonding was obtained using a C-C configuration, this was not used for the encapsulation of cells due to the electrical conductivity of glass frit C; despite, this glass frit has a quite high thermal conductivity. To ensure no electrical conductivity on the bottom substrate, C-B bonding was optimized for process temperature of 120 °C. The final frit configuration of C-BA allowed laser-assisted low process temperatures; in which each frit layer plays an essential role in achieving the high-quality bonding. Glass frit C, with high ductility and thermal conductivity, serves for dissipating the thermal stresses build up at the cover glass when laser radiation is absorbed. Glass frit B, with low melting temperature, is used to achieve the bonding at *ca.* 380 °C. Finally, glass frit A minimizes the thermal stress on the bottom glass substrate.

The material properties of the glass frits and glass substrates were studied to achieve a high-quality bonding. Apart from the main parameters of CTE, melting point and optical absorbance, it was concluded that the thermal conductivity is the most important factor for obtaining a low process temperature laser assisted glass encapsulation. In addition, the thickness of the glass substrates plays a critical role in dissipating mechanical tensions during the sealing. Considering the mentioned parameters and using statistical design of experiment tools, the

laser-assisted sealing operating and design variables were fully optimized to produce hermetic encapsulation.

The hermeticity of empty cells with bonding configurations C-C, C-B and C-BA were measured according to MIL-STD-883 standard test[7]. All of these encapsulation configurations showed helium leak rates lower than the reject limit (5×10^{-8} atm cm^3 s^{-1}). The stability of the encapsulation was examined based on climatic tests according to IEC61646 standard[8]. These tests included thermal and humidity-freeze cycling. The developed sealing retained its hermeticity after the climatic tests, confirming that the sealing is capable of providing the minimum required 20 years lifetime for PSC applications.

The scalability of the developed encapsulation method was studied by sealing empty cells of various sizes. Device sizes up of 7 × 7 cm^2 were bonded by conventional laser-sealing method, which considers a scan head positioned in the center of the device and the sealing is performed by the mirrors of the 2D laser scan head. The field area of the scan head allows to seal devices up to 10 x 10 cm^2. Therefore, larger devices with dimension of 13 × 13 cm^2 were sealed by dividing the device in four identical sections of 6.5 x 6.5 cm^2 and sealing each section separately. In this method, the sealing was obtained using a robot arm for positioning the scan head in the center of each section and bonding the corresponding sealing line segment. Therefore, the developed encapsulation showed a great potential to be used for the fabrication of large-area perovskite solar cells.

The single laser beam method was used to encapsulate HTM-free PSCs at process temperature of 100 °C and processing dwell time of *ca.* 35 min. The hermetically encapsulated HTM-free PSC devices showed no significant performance losses after 50 thermal cycles of -40 °C to 85 °C and 50 h damp heat test of 85 °C / 85 % RH according to IEC61646. The 500 h humid air feeding test indicated no performance change for hermetic devices, while non-hermetic

devices showed degradation after the initial 50 h of the test, confirming the importance of hermeticity level of encapsulation.

The novel dual laser beam sealing method, where one laser pre-heats the sealant perimeter and the other melts the glass frit, was used for sealing conventional n-i-p PSCs at process temperature of 50 °C. For these devices, thinner glass substrates were used to achieve better sealing reproducibility. The thermal stress on the encapsulation was slightly reduced (*ca.* 14 %) by reducing the glass thickness from 2.2 mm to 1.1 mm. The hermetically sealed n-i-p devices have successfully passed external environmental stability tests including 50 thermal cycles of -40 °C to 65 °C and 500 h of humid air feeding. However, the inferior thermal stability of PTAA caused 16 % performance loss after thermal cycle of -40 °C to 85 °C.

As mentioned before, the stability of PSCs is affected by two factors: i) external environmental (*i.e.* humidity, oxygen and temperature) and ii) operational (*i.e.* illumination and electrical load). The developed glass-glass encapsulation of the present thesis effectively prevents PSCs from humidity and oxygen-based degradation. However, the thermal stability of the device active components (in most cases HTM), must be well improved to ensure successful external environmental stability of PSCs.

The operational stability of PSCs under illumination and electrical load was not fully addressed. A maximum power point tracking (MPPT) algorithm was developed and programmed in LabVIEW platform to measure the stabilized PCE of the devices under constant illumination. **Appendix D** shows the LabVIEW control panel interface of the programmed MPPT. **Figure 5.1**, compares the stabilized PCE measured under MPPT conditions to the PCE measured by conventional *J-V* curves for the laser-encapsulated PSCs fabricated during the present thesis. The HTM-free devices remained stable over >300 s MPPT, while the conventional n-i-p cell showed a rapid PCE loss.

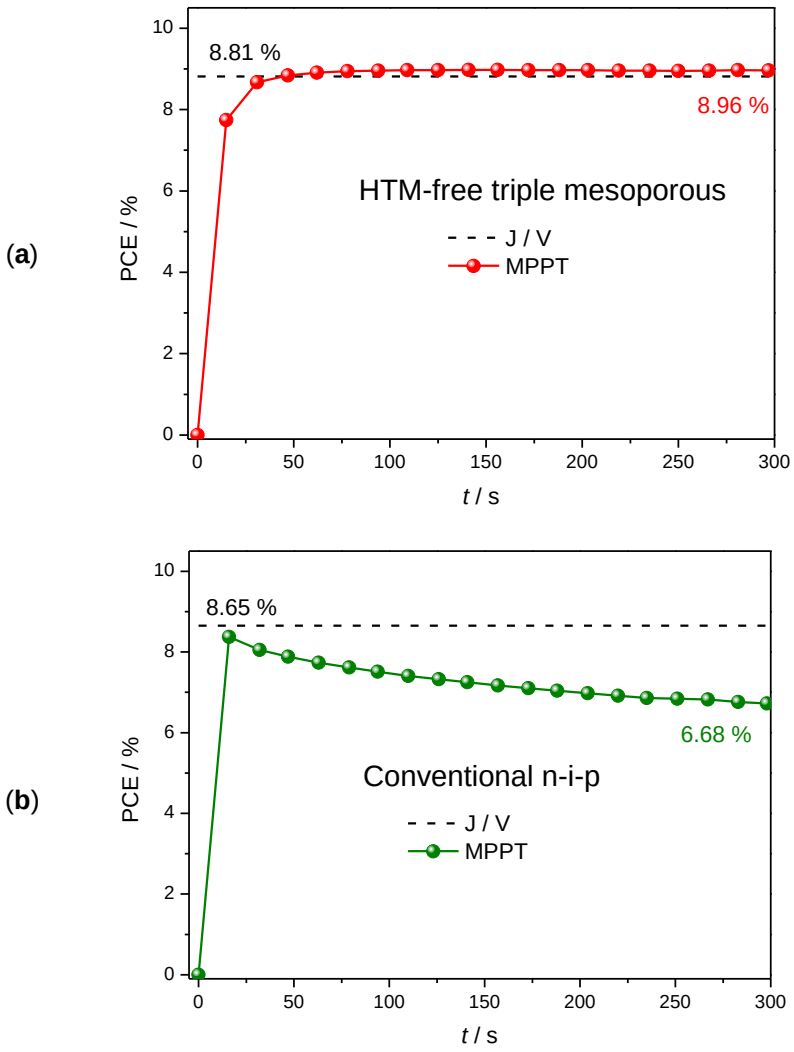

Figure 5.1. Maximum power point tracking for 300 s, to assess the PCE stability of laser-sealed devices (**a**) HTM-free and (**b**) conventional n-i-p (PTAA) PSCs.

In general, the operational stability under illumination of PSCs is affected by physical mechanisms including internal polarization caused by modulation of the permittivity, trapping/detrapping at the interfaces, band bending and ferroelectric polarization due to ion migration[9]. The transient behavior of PSCs is therefore controlled by interfacial trap states and ion migration. Interface engineering by

passivation layers and higher quality perovskite crystallization is the key to minimize these issues[10]. The loss of PCE for n-i-p devices during MPPT was assigned to two factors: i) poor crystallization of the perovskite layer causing trap states and ii) charge accumulation at the meso-TiO_2 and perovskite interface.

Studies on interfacial engineering and improvement of perovskite crystallization must be conducted in a future work.

5.2 OUTLOOK OF PEROVSKITE SOLAR CELLS

Since the discovery of perovskite solar cells, this PV technology has shown a great potential to end the market dominance of silicon solar cells. Although, the production costs of the silicon solar cells have been decreasing rapidly in the past few years; studies showed that the levelized cost of electricity (LCOE) for a PSC module displaying a PCE of 12 % and 15 years lifetime, is 3 times lower compared to Si photovoltaics[11].

The present thesis has successfully proved that the external environmental stability of PSCs is feasible through hermetic encapsulation. The operational stability has been widely addressed by other research groups. Therefore, combining the two factors, highly efficient, stable and low cost PSC devices can be reached. By combining the present 16 % efficient large area PSCs module with a hermetic sealing of the present study, a lifetime of more than 20 years can be accomplished. Thus, the LCOE of this emerging PV devices would be much lower than previous anticipated studies.

Another current major challenge of PSCs is that the in the most efficient perovskite devices are fabricated with Pb-based absorbers. According to RoHS regulation the allowed amount of lead content is 0.1 % per mass in homogeneous materials. From the point of commercialization, the amount of lead in PSC glass-glass modules ranges from 0.005 to 0.03 %[12]. Although not a very satisfying arguments, the lead-based PSCs can pass the required limits for the regulations.

To ensure maximum environmental safety, two possible routes for the future of PSCs is foreseen: i) reducing the Pb content by either using Pb/Sn absorbers or Sn-based perovskites[13]; and ii) implementing lead mitigation strategies to avoid possible lead leakage in case of glass breakage[14].

For perovskite solar cells, the golden triangle of photovoltaics, which includes cost, efficiency and stability, must be updated to become the golden pentagon, where sustainability and safety must be added. The future for PSC technology should aim at maximizing the safety and minimize the environmental impact, while optimizing the PCE and stability at the lowest costs.

Finally, I believe that the most suitable option, among the available PSC configurations, is the fully printable HTM-free mesoporous device structure. Although these devices are not exhibiting the highest achievable PCEs within the perovskite solar cells, they are the most favorable devices for large area fabrication. These devices are showing better operational stability over conventional n-i-p cells and their fabrication method of screen printing is much easier to scale-up comparing to spin-coating method of conventional n-i-p PSCs. By joining a robust hermetically glass sealed HTM-free modules to an effective lead mitigation strategy, the commercialization of PSCs would be easily achieved.

5.3 REFERENCES

1. NREl, https://www.nrel.gov/pv/assets/pdfs/best-reserch-cell-efficiencies.pdf Accessed on: 2020/05/29, 2019.
2. A. M. A. Leguy, Y. Hu, M. Campoy-Quiles, M. I. Alonso, O. J. Weber*, et al.*, *Chemistry of Materials*, 2015, **27**, 3397-407.
3. J. Maçaira, L. Andrade and A. Mendes, *Solar Energy Materials and Solar Cells*, 2016, **157**, 134-8.
4. F. Matteocci, L. Cinà, E. Lamanna, S. Cacovich, G. Divitini*, et al.*, *Nano Energy*, 2016, **30**, 162-72.
5. J. Idígoras, F. J. Aparicio, L. Contreras-Bernal, S. Ramos-Terrón, M. Alcaire*, et al.*, *ACS Applied Materials & Interfaces*, 2018, **10**, 11587-94.
6. S. Emami, J. Martins, L. Andrade, J. Mendes and A. Mendes, *Optics and Lasers in Engineering*, 2017, **96**, 107-16.
7. MIL-STD-883H, United States Department of Defense, 2010.
8. IEC61646, International Electrotechnical Commission, 2008.
9. A. Gagliardi and A. Abate, *ACS Energy Letters*, 2018, **3**, 163-9.
10. Y. Shao, Z. Xiao, C. Bi, Y. Yuan and J. Huang, *Nat Commun*, 2014, **5**, 5784.
11. C. Molang, W. Yongzhen, C. Han, Y. Xudong, Q. Yinghuai*, et al.*, *Advanced Science*, 2017, **4**, 1600269.
12. L. Wagner, S. Mastroianni and A. Hinsch, *Joule*.
13. X. Jiang, F. Wang, Q. Wei, H. Li, Y. Shang*, et al.*, *Nat Commun*, 2020, **11**, 1245.
14. X. Li, F. Zhang, H. He, J. J. Berry, K. Zhu*, et al.*, *Nature*, 2020, **578**, 555-8.

APPENDIX

Appendix A. NREL's best research efficiency chart for photovoltaics

Appendix B. RSM table for C-C glass frit bonding optimization

Appendix C. Simulated temperature during dual laser beam sealing

Appendix D. Developed LabVIEW control panel interface for MPPT

APPENDIX

APPENDIX A

Best research-cell efficiency chart for photovoltaic technologies from 1976 to December 2019. This plot is courtesy of the National Renewable Energy Laboratory, Golden, CO”

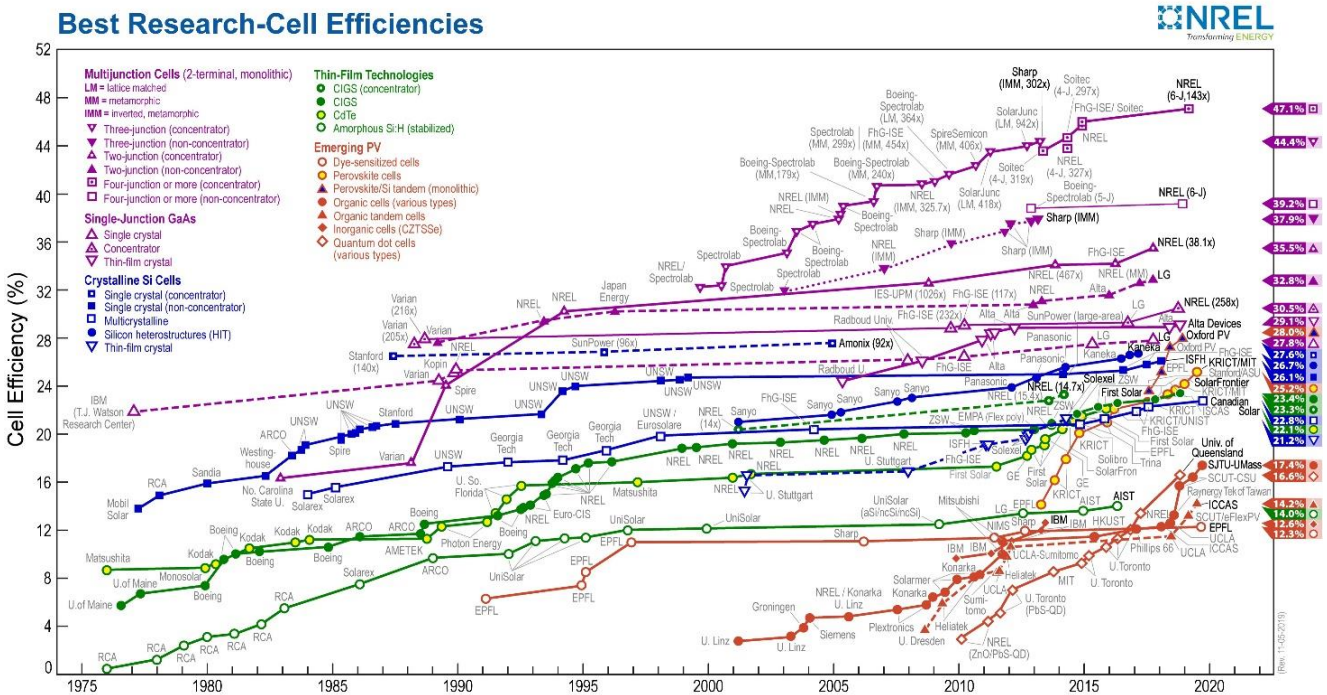

APPENDIX B

Experimental matrix design, response, and model parameters for the RSM of contour laser-assisted sealing, C-C glass frit configuration.

Run	Leverage	Space Type	Build Type	v / mm·s^{-1}	P / W	Q	x_1 (-1,1)	x_2 (-1,1)	y_{pred}	Residual
1	0.3472	Edge	Model	35	47.25	6.5	-1	0.09	7.510673	-1.01067
2	0.5949	Vertex	Model	35	20	-7.5	-1	-1	-7.00794	-0.49206
3	0.6648	Vertex	Model	250	20	-8.5	1	-1	-9.05678	0.556781
4	0.4113	CentEdge	Model	142.5	70	-8.5	0	1	-7.718	-0.782
5	0.2219	Interior	Lack of Fit	179.546	25.75	-3	0.344614	-0.77	-2.2418	-0.7582
6	0.391	Edge	Lack of Fit	124.225	20	-9	-0.17	-1	-8.95577	-0.04423
7	0.7397	Vertex	Model	250	70	-2	1	1	-2.53155	0.531554

8	0.208	Interior	Lack of Fit	182.275	55	7.8	0.37	0.4	6.913613	0.886387
9	0.1659	Interior	Lack of Fit	93.5432	32	3.8	-0.45541	-0.52	3.466654	0.333346
10	0.4031	Edge	Model	250	47	10	1	0.08	10.99539	-0.99539
11	0.2106	Interior	Lack of Fit	87.675	62.75	-1.85	-0.51	0.71	-1.07715	-0.77285
12	0.6739	Vertex	Model	35	70	-10	-1	1	-10.644	0.643998
13	0.1957	Interior	Lack of Fit	97.35	48.9954	7.75	-0.42	0.159816	7.277455	0.472545
14	0.3188	Edge	Lack of Fit	35	33.25	5.9	-1	-0.47	4.988839	0.911161
15	0.217	Interior	Model	142.5	39.6621	8	0	-0.21352	7.282124	0.717876
16	0.236	Interior	Lack of Fit	228.5	34	5.5	0.8	-0.44	5.698242	-0.19824

APPENDIX C

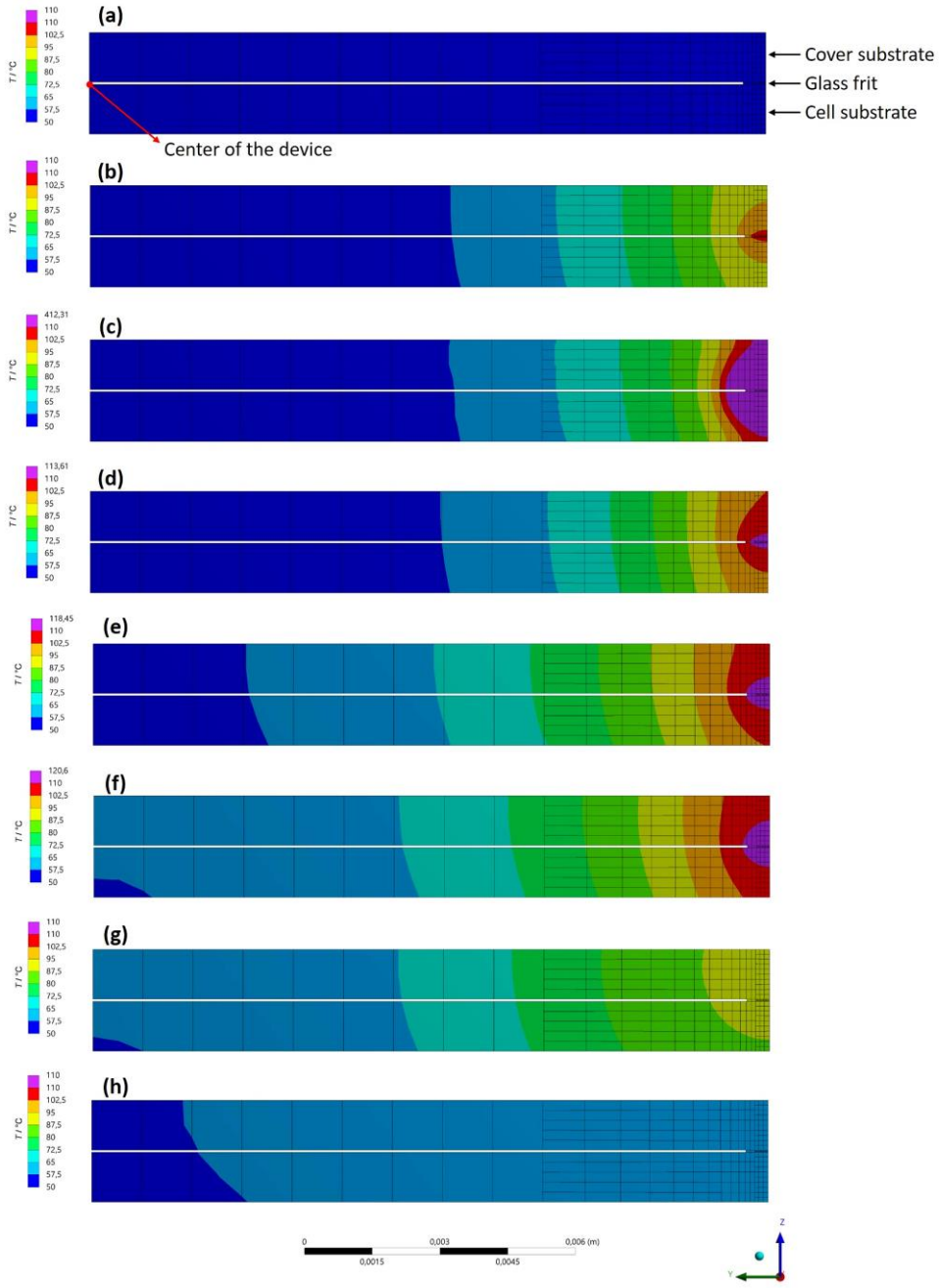
(a)
Cover substrate
Glass frit
Cell substrate
Center of the device
(b)
(c)
(d)
(e)
(f)
(g)
(h)
T / °C
0
0,003
0,006 (m)
0,0015
0,0045
Z
Y

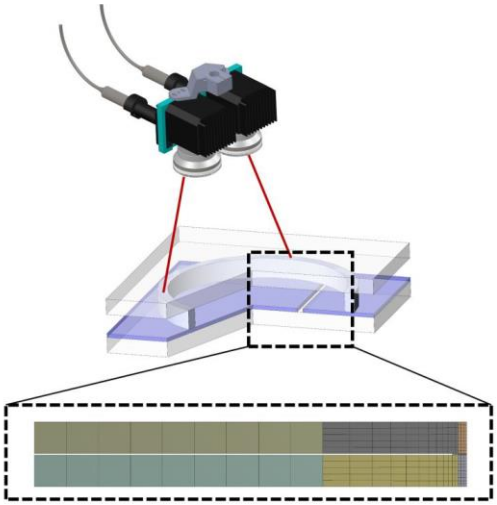

Simulated temperature during the sealing process at the glass frit and substrates. (**a**) the device is placed in the furnace at the process temperature of 50 °C until a homogeneous temperature is reached (temperature stabilization period is not represented), (**b**) LB_{heat} starts to radiate and the temperature in the sealant increases up to 110 ± 10 °C (**c**) LB_{bond} is emitted and the, temperature in the glass frit reaches up to > 380 °C, bonding the substrates, (**d**, **e** and **f**) LB_{bond} is turned off and LB_{heat} continues emitting, maintaining the sealant material at 110 ± 10 °C, (**g** and **h**) laser-sealing conclusion, LB_{heat} is turned off and the temperature in the sealant decreases to the process temperature.

APPENDIX D

LabVIEW control panel interface for the MPPPT algorithm.